NTNU

Norwegian University of
Science and Technology

Dynamic response of a multi-span suspension bridge with floating pylons

Anders Lessø Mjaaland
Audun Mathias Øvstebø

Civil and Environmental Engineering
Submission date: June 2017
Supervisor: Ole Andre Øiseth, KT
Co-supervisor: Yuwang Xu, IBM

Norwegian University of Science and Technology
Department of Structural Engineering

Department of Structural Engineering
Faculty of Engineering Science and Technology
NTNU- Norwegian University of Science and Technology

ACCESSIBILITY
(+47) 47 28 88 75
(+47) 95 42 13 07

MASTER THESIS 2017

SUBJECT AREA:	DATE:	NO. OF PAGES:
Structural Dynamics	11.06.2017	192 (30+137+25)

TITLE:

Dynamic response of a multi-span suspension bridge with floating pylons

Dynamisk respons av en flerspenns hengebro med flytende pyloner

BY:

Anders Lessø Mjaaland

Audun Mathias Øvstebø

SUMMARY:
The Norwegian Public Roads Administration is currently investigating the possibility of crossing the 500 m deep and 5 km wide fjord, Bjørnafjorden, located in Norway. Several concepts have been developed on behalf of the Norwegian Public Roads Administration. A multi-span floating suspension bridge, with pylons resting on tension leg platforms, is considered in this thesis. A parametrized FE-model, which includes the hydrodynamic properties of the bridge, has been developed and used to obtain the standard deviations from a coupled buffeting and wave analysis, performed in modal coordinates in the frequency domain.

From the modal buffeting analyses, it is discovered that the wind loading is the dominating loading with respect to the STD compared to the wave loading. It is discovered that second order wave forces could be important for high-frequency response.

Load combinations with a 100 year return period are estimated by the contour surface method. The extreme short-term response and the extreme long-term response, based on the probability density function of the environmental loading, have been estimated and compared for lateral displacement at the middle of the central span. From the extreme value assessment, it is found that wind loading is the dominant contributor to the lateral displacement. Swell waves increase the extreme response by 15 \%, while the contribution from wind waves are of little importance.

The motion induced instability, with empirical derived aerodynamic derivatives, is found to be a combination of the second vertical mode and the first torsional mode. The corresponding critical velocity is 85.09 m/s. In a parameter study of damage to different components of the bridge, it has been found that unsymmetrical top cable damage severely alters the vertical modes of the bridge.

For the further research and development of this bridge project, it is, in particular, recommended to develop a realistic probability distribution of the environmental conditions in the Bjørnafjorden area.

RESPONSIBLE TEACHER: Associate Professor Ole Øiseth

SUPERVISOR(S): Associate Professor Ole Øiseth, PhD Candidate Yuwang Xu

CARRIED OUT AT: Department of Structural Engineering, Norwegian University of Science and Technology

Sammendrag

Staten Vegvesen utreder muligheten for å krysse den 500 m dype og 5 km brede fjorden, Bjørnafjorden, lokalisert i Norge. Flere konsepter har blitt utviklet på oppdrag fra Statens Vegvesen. En flerspenns hengebro, med pyloner som hviler på strekkstagplattformer, er undersøkt i denne oppgaven. En parametrisert modell, som inkluderer de hydrodynamiske egenskapene til broa, har blitt utviklet og brukt til å finne standardavviket i en koblet buffeting- og bølgeanalyse, utført i modale koordinater i frekvensdomenet.

Fra den modale buffetinganalysen er det funnet at vindlasten, sammenlignet med bølgelasten, er den dominerende lasten med tanke på bidraget til standardavviket. Det fremkommer at andre ordens bølgekrefter kan være viktig med tanke på høyfrekvent respons.

Lastkombinasjoner med en 100 års returperiode er estimert ved bruk av konturplott-metoden. Ekstremverdier for laterale forskyvninger av midtpunktet på midtspennet fra korttids og langtids responsanalyser er beregnet basert på sannsynlighetsfordelingen til miljølastene. Korttids og langtidsresponser har blitt sammenlignet med hverandre. Fra ekstremverdianalysen er det funnet at vind gir det dominerende bidraget til den laterale forskyvningen av midtpunktet på midtspennet. Dønnings-bølger øker den laterale forskyvningen med 15 %, mens bidraget fra vindbølger er funnet til å være av liten betydning.

Bevegelsesindusert instabilitet, basert på empirisk utledet aerodynamisk deriverte, er en kombinasjon av andre vertikalmode og første torsjonsmode. Den korresponderende kritiske hastigheten er 85.09 m/s. I en parameterstudie som omhandler skade på ulike komponenter av broa er det funnet at usymmetrisk skade på toppkabel kan drastisk endre vertikalmodene til broa.

For videre forskning og utvikling av dette brokonseptet, anbefales det spesielt å utvikle en realistisk sannsynlighetsfordeling for miljølastene i Bjørnafjorden.

Abstract

The Norwegian Public Roads Administration is currently investigating the possibility of crossing the 500 m deep and 5 km wide fjord, Bjørnafjorden, located in Norway. Several concepts have been developed on behalf of the Norwegian Public Roads Administration. A multi-span floating suspension bridge, with pylons resting on tension leg platforms, is considered in this thesis. A parametrized FE-model, which includes the hydrodynamic properties of the bridge, has been developed and used to obtain the standard deviations from a coupled buffeting and wave analysis, performed in modal coordinates in the frequency domain.

From the modal buffeting analyses, it is discovered that the wind loading is the dominating loading with respect to the STD compared to the wave loading. It is discovered that second order wave forces could be important for high-frequency response.

Load combinations with a 100 year return period are estimated by the contour surface method. The extreme short-term response and the extreme long-term response, based on the probability density function of the environmental loading, have been estimated and compared for lateral displacement at the middle of the central span. From the extreme value assessment, it is found that wind loading is the dominant contributor to the lateral displacement. Swell waves increase the extreme response by 15 %, while the contribution from wind waves are of little importance.

The motion induced instability, with empirical derived aerodynamic derivatives, is found to be a combination of the second vertical mode and the first torsional mode. The corresponding critical velocity is 85.09 m/s. In a parameter study of damage to different components of the bridge, it has been found that unsymmetrical top cable damage severely alters the vertical modes of the bridge.

For the further research and development of this bridge project, it is, in particular, recommended to develop a realistic probability distribution of the environmental conditions in the Bjørnafjorden area.

Preface

This master thesis constitutes the work carried out the spring semester of 2017 and represents the completion of the Master degree's program, Civil and Environmental Engineering, at the Norwegian University of Science and Technology in Trondheim. The work of this thesis has been carried out by Anders Lessø Mjaaland and Audun Mathias Øvstebø at the Department of Structural Engineering under the supervision and guidance of Associate Professor Ole Øiseth and Ph.D. candidate Yuwang Xu and in cooperation with the Norwegian Public Roads Administration.

We would like to thank Associate Professor Ole Øiseth for interesting discussions and valuable input and comments to our thesis. We would also like to express our deepest gratitude to Ph.D. candidate Yuwang Xu who has tirelessly been helping and guiding us throughout this thesis. In addition, we would like to thank the Norwegian Public Roads Administration for funding this thesis and providing us with relevant documentation, in particular, we would like to thank Simen Hellgren Holtberget who has been our contact at the Norwegian Public Roads Administration.

Trondheim, June 12, 2017

Anders Lessø Mjaaland

Audun Mathias Øvstebø

Table of Contents

List of Tables

List of Figures

Abbreviations

ae	Aerodynamic
COB	Centre of buoyancy
COG	Centre of gravity
DOF	Degree of freedom
EOM	Equation of motion
FE	Finite element
FEA	Finite element analysis
FEM	Finite element modelling, finite element method
FORM	First Order Reliability Method
IFORM	Inverse First Order Reliability Method
MDOF	Multiple degree of freedom
MSL	Mean sea level
NPRA	Norwegian Public Roads Administration
QTF	Quadratic transfer function
SDOF	Single degree of freedom
STD	Standard deviation
TLP	Tension leg platform
VAR	Variance

Notation

Mathematical operators

e	Euler's number
∇	Del operator
∇^2	Laplace operator

Imaginary quantities

i	Imaginary unit
Re	Real part of a complex value
Im	Imaginary part of a complex value

Matrix and vector notation

Matrices are bold, upper case Latin or Greek letters, unless stated otherwise.
Vectors are bold, lower case Latin or Greek letters, unless stated otherwise.

Superscripts and bars above symbols

H indicates the Hermitian operator.
T indicates the Transpose.
A tilde ($\tilde{}$) above the symbol indicates a modal quantity.
A bar ($\bar{}$) above the symbol indicates an averaged value.
A hat ($\hat{}$) above the symbol in hydrodynamics indicates a coordinate system fixed in space and coincides with a body fixed coordinate system at rest.
A prime ($'$) above a symbol indicates a derivative with respect to a variable.
A dot or two dots ($\dot{}$) or ($\ddot{}$) above a symbol indicates the time derivatives.

Latin letters

Aerodynamic and Dynamics

$\mathbf{a}_f(\omega)$	Fourier transformation of the loading
$\mathbf{a}_r(\omega)$	Fourier transformation of the displacement
$\mathbf{a}_1$, $\mathbf{a}_2$, $\mathbf{a}_3$, $\mathbf{a}_5$	Empirical determined coefficients from wind tunnel testing
$A_1^* - A_6^*$	Aerodynamic derivatives related to the motion in torsion
$\hat{\mathbf{b}}$	Mean wind load coefficient vector
B	Width of the cross-section

$\mathbf{B}_q$, $\hat{\mathbf{B}}_q$	Buffeting load matrix
$C_D(\alpha)$, $C'_D(\alpha)$, $\bar{C}_D$	Quasi-static load coefficients
$C_L(\alpha)$, $C'_L(\alpha)$, $\bar{C}_L$	Quasi-static load coefficient
$C_M(\alpha)$, $C'_M(\alpha)$, $\bar{C}_M$	Quasi-static load coefficient
$\mathbf{C}$	Damping matrix
$\tilde{\boldsymbol{C}}$	Modal damping matrix
$\mathbf{C}_{ae}$	Aerodynamic damping matrix
$\hat{\mathbf{C}}_{ae}$	Aerodynamic damping matrix based on non-dimensional ADs
dU	Step size for the wind velocity in the instability analysis
d_1, d_2	Empirical determined coefficients from wind tunnel testing
D	Height of the cross-section
$\mathbf{f}(t)$	load vector
$\tilde{\boldsymbol{f}}(t)$	Modal load matrix
$\mathbf{F}(\omega)$	Fourier transformation of the load matrix
$\mathbf{F}_{ae}(\omega)$	Aerodynamic load matrix in the frequency domain
h	Height above MSL
$H_1^* - H_6^*$	Aerodynamic derivatives related to the motion caused by across-wind
$\mathbf{H}(\omega)$	Transfer function
$\mathbf{K}$	Stiffness matrix
$\mathbf{K}_{ae}$	Aerodynamic stiffness matrix
$\tilde{\boldsymbol{K}}$	Modal Stiffness matrix
$\hat{\mathbf{K}}_{ae}$	Aerodynamic stiffness matrix based on non-dimensional ADs
$\mathbf{M}$	Mass matrix
$\tilde{\boldsymbol{M}}$	Modal mass matrix
$P_1^* - P_6^*$	ADs related to the motion caused by along-wind
$q(t)$	Wind load
q_D, q_M, q_L	Components of the wind load vector at cross-sectional level
$q_D(x,t)$	Drag due to wind loading
$q_L(x,t)$	Lift due to wind loading
$q_M(x,t)$	Moment due to wind loading
q_y, q_z, q_θ	Components of the total wind load vector at cross-sectional level
$\mathbf{q}_{tot}(x,t)$	Total wind load vector at cross-sectional level
$\bar{\mathbf{q}}$	Static part of wind load vector a cross-sectional level
$r_x(x), r_y(x), r_z(x)$	Components of the dynamic response/displacement vector along the x-axis
$\mathbf{r}(t)$	Displacement
$\mathbf{r}(x,t)$	Cross-sectional rotational/displacement vector
$\dot{\mathbf{r}}(t)$	Velocity
$\ddot{\mathbf{r}}(t)$	Acceleration
$S_{ff}(\omega)$	General load spectrum
$S_{rr}(\omega)$	Displacement spectrum
$S_{uu}^+(\omega)$, $S_{ww}^+(\omega)$, $S_{uw}^+(\omega)$	Spectral densities of the wind field
$u(x,t)$, u	Fluctuating along-wind horizontal velocity component
$U(t), U(h), U$	Mean wind velocity
$U(x,t)$	Total wind velocity along the x-axis
U_{cr}	Critical wind velocity in the instability analysis
U_{rel}	Instantaneous relative wind velocity
$\hat{U}$	Reduced velocity
$\mathbf{u}$	Wind velocity vector containing fluctuating components
w, $w(x,t)$	Fluctuating along-wind vertical velocity component

Hydrodynamics

A_{kj}	Added mass coefficient associated with DOF k and direction of motion j
A_m	Complex amplitude of the n^{th} regular wave
A^3	Complex wave amplitude of third order
B_{kj}	Added damping coefficient associated with DOF k and direction of motion j
$\overline{BM}$	Distance from COB to the metacentre
C	A constant
$\mathbf{C}_h(\omega)$	Hydrodynamic added damping matrix
C_{kj}	Hydrostatic coefficient associated with DOF k and mode j
$d\mathbf{Z}_r(\omega)$	Spectral process associated with the response vector $r(t)$
$D(\theta)$	Frequency independent wave directional distribution function
$D(\omega, \theta)$	Directional wave distribution function
$F_{exc,k}$	The wave excitation force for the force direction k
$F_{pk}^{(2)\pm}$	Potential second order force vector for force direction k
$F_{rad,k}$	Radiation force associated with DOF k
$\mathbf{F}$	Hydrostatic and hydrodynamic force vector
$\mathbf{F}_{exc}^{(1)}(\omega)$	Wave excitation force vector
$\mathbf{F}_{tot}^{(1)}(\omega)$	First order hydrodynamic load vector
$\mathbf{F}_{exc}^{(2)}$	Second order wave excitation force vector
$\mathbf{F}_{p}^{(2)}$	Second order potential
$\mathbf{F}_{q}^{(2)}$	Second order quadratic interaction of the first order solution
g	Acceleration of gravity
$\overline{GM}$	Distance from COG to the metacentre
H_s	Significant wave height
$\mathbf{H}$	The second order component of T^t
$\mathbf{i}$, $\mathbf{j}$ and $\mathbf{k}$	Unit vectors in the Cartesian coordinate system
$\mathbf{K}_h$	Hydrostatic stiffness matrix
m	Mass of the displaced volume
$\mathbf{M}$	Hydrostatic and hydrodynamic moment vector
$\mathbf{M}_{exc}^{(2)}$	Second order wave excitation moment vector
$\mathbf{M}_h(\omega)$	Hydrodynamic added mass matrix
n_k	Normal vector of the submerged body associated with k
$\mathbf{n}$	Normal vector of a submerged body
$\hat{\mathbf{n}}$	Instantaneous unit normal vector of the submerged body
$\mathbf{P}(\hat{\mathbf{x}})$	Fluid pressure given by Bernoulli's equation
$Q_{k,m}^{(1)}$	First order transfer function associated with force direction k and wave m
$Q_{mn}^{(2)\pm}$	Second order quadratic transfer function
$\mathbf{Q}_r^{(1)}(\omega, \theta)$, $\mathbf{Q}_s^{(1)}(\omega, \theta)$	Directional first order wave exciting transfer functions associated with the points r and s
s	Spreading parameter
S	Body surface
S_0	Area of the water plane
S_{ii}	Second moment of area of the water plane about axis i
S_B	Wetted mean body surface
S_F	Free surface
$\hat{S}_B(t)$	Instantaneous submerged body

$S^{(2)}_{p_r p_s}(\mu)$	Drift force spectrum
$\mathbf{S}^{(1)}_{p_r p_s}(\omega)$	Hydrodynamic load cross-spectral density
$\widetilde{\mathbf{S}}^{(1)}_{PP}(\omega)$	Modalized first order environmental wave load spectra
$\widetilde{\mathbf{S}}^{(2)}_{PP}(\omega)$	Modalized second order environmental wave load spectra
$S_\eta(\omega)$	One-sided empirical wave spectra, e.g. JONSWAP or Pierson–Moskowitz
$S_\eta(\omega, \theta)$	Autospectral density of the waves
$S_{\eta_r \eta_r}(\omega, \theta)$, $S_{\eta_s \eta_s}(\omega, \theta)$	Two-dimensional spectral density with respect to r and s
t	Time
T_p	Peak wave period
$\mathbf{T}$	Transformation matrix
$\mathbf{U}$	Velocity vector of a submerged body
V_w	Volume of the submerged body
wl	Waterline
wp	Water plane
$\mathbf{x}$	Body fixed coordinate system in space
$\mathbf{x}_{sea}$	A location in space, related to the sea surface elevation
$\hat{\mathbf{x}}$	Fixed coordinate system in space, which coincides with the body fixed coordinate system at rest
$X_{m,k}$	Force coefficient associated with force direction k and wave m
$X^{\pm}_{mn}$, $X^{\pm}_{q,mn}$, $X^{\pm}_{p,mn}$	Second order force coefficients associated with waves m and n
z	Water depth
z_B	z-coordinate of the COB
z_G	z-coordinate of the COG
$\hat{z}$	z-coordinate of $\hat{\mathbf{x}}$
Z_0	z-coordinate of the origin of $\hat{\mathbf{x}}$
$Z_\eta(\{\kappa\}, \omega)$	Spectral process related to η

Probability theory

a_i, b_i, e_i,f_i and k_i	Coefficients of $f_{U,H_s,T_p}(u,h,t)$, $i = 1, 2, 3$
c_1, c_2, c_3	Coefficients in the Lonowe model
d_1, d_2, d_3	Coefficients in the Lonowe model
E_i	Predicted value
$f(x)$	Discrete probability distribution
$f(x; \alpha, \beta)$	Weibull distribution
$f(x; \mu, \sigma)$	Lognormal distribution
$f_{H_s}(h)$	Marginal distribution of the wave height from the Lonowe model
$f_{H_s \mid U}(h \mid u)$	Probability distribution of H_s given U
$f_{T_p \mid H_s}(t \mid h)$	Marginal distribution of the wave period given the wave height from the Lonowe model
$f_{T_p \mid U, H_s}(t \mid u, h)$	Probability distribution of T_p given H_s and U
$f_U(u)$	Probability distribution of U
$f_{U,H_s,T_p}(u,h,t)$	Joint probability distribution of U, H_s and T_p
$F(x)$	Cumulative distribution function
$F_{H_s \mid U}(h \mid u)$	Cumulative distribution of the wave height given the wind velocity
$F_{T_p \mid U, H_s}(t \mid u, h)$	Cumulative distribution of the wave period given the wind velocity and the wave height
$F_U(u)$	Cumulative distribution of the wind velocity
$F_{\hat{X}}(H_s, T_p, \xi)$	Short-term CDF of the extreme value $\hat{X} = \hat{X}(T)$
$F_{\hat{X}}(\xi)$	Long-term CDF of the extreme value $\hat{X} = \hat{X}(T)$

$g(X_d, H_s, T_p, U; x_{crit})$	Limit state function
h	Wave height
O_i	Observed quantity
p	Probability at an evaluated point
p_i	Discrete probability associated with i
$\hat{p}_f(x_{crit})$	Design probability associated with x_{crit}
r_i	Residuals between observations and predicted values
R^2	R-squared
SSE	Error sum of squares
SST	Total sum of squares
T	Long-term period
T_s	Natural period in surge
u_1, u_2, u_3	Coordinates in the U-space
U	U-space, standard Gaussian nonphysical space
VAR	Variance
x	Discrete variable
x_{crit}	Critical value in the limit state function
x_i	Discrete variable i
X_d	d-hour maximum response value within a sea state
y_i	Measured quantity
$\hat{y}_i$	Predicted value
Y	Normal distributed random variable

Greek letters

Aerodynamic and Dynamics

α	Angle of incidence
α_{power}	Power law wind profile exponent
$\boldsymbol{\alpha}$	Rotational displacements of $\mathbf{x}$
ϵ	Convergence criteria in the instability analysis
ζ	Structural damping ratio for the complex eigenvalue problem
ζ_j	Damping ratio for the complex eigenvalue problem
η_n	Generalized coordinate associated with mode n
$\boldsymbol{\eta}(t)$	Displacement vector in generalized coordinates
$\dot{\boldsymbol{\eta}}(t)$	Velocity vector in generalized coordinates
$\ddot{\boldsymbol{\eta}}(t)$	Acceleration vector in generalized coordinates
κ	Constant in the spectral density for wind equation
λ_j	The solution to the quadratic eigenvalue problem associated with mode j
$\boldsymbol{\lambda}$	Matrix containing the solution to the quadratic eigenvalue problem
μ_{crit}	Critical real part of the quadratic eigenvalue problem
μ_j	Real part of the quadratic eigenvalue problem associated with mode j
ρ	Density of air
ϕ_{Cr}	Critical eigenvector in the quadratic eigenvalue problem
$\phi_{flutter}$	Simplified fluttering mode shape
ϕ_n	Eigenvector n
Φ_{Modes}	All modes included in the instability analysis
$\boldsymbol{\Phi}^T$	Eigenvector matrix
ω	Angular frequency
ω_{cr}	Critical response frequency for motion induced instability
ω_{guess}	Initial iterative angular frequency in the instability analysis
$\omega_i(U)$	Resonance frequency with respect to mode shape i
ω_{it}	Iterative angular frequency in the instability analysis
ω_j	The frequency of the quadratic eigenvalue problem associated with mode j
ω_n	Natural frequency
ω_p	Peak frequency

Hydrodynamics

α	Phillips constant (To use in the Pierson–Moskowitz spectrum)
γ	Peakedness parameter to use in the JONSWAP spectrum
Δx	Distance along the x-axis between two point, e.g. two pontoons
Δy	Distance along the y-axis between two point, e.g. two pontoons
$\eta(\{x\}, t)$	The ocean surface
θ	Wave direction
θ_0	Angle of the mean wave direction
θ_i	Heading angle associated with incident wave i
θ_j	Heading angle associated with incident wave j
κ	Modulus of the wave number
$\boldsymbol{\kappa}$	Wave number vector
μ	Wave frequency
ξ_j	Translational and rotational displacement of the oscillating body in excitation mode j

$\boldsymbol{\xi}$	Translational displacements of $\mathbf{x}$
ρ	Density of the fluid
$\tilde{\sigma}$, $a(\omega)$, $\tilde{\sigma_a}$, $\tilde{\sigma_b}$, $\tilde{\alpha}$	Parameters in the JONSWAP spectrum
$\phi(x, y, z, t)$	Velocity potential
$\phi_{ij}^{+}(x, y, z,)$	Second order sum potential associated with the incident waves i and j
$\phi_{ij}^{-}(x, y, z,)$	Second order difference potential associated with the incident waves i and j
$\phi_j(x, y, z,)$	Complex velocity potential associated with incident wave j
ϕ_j	Velocity potential for a body oscillating with a unitary speed for jth exciation mode
ϕ_t	Partial derivative of the velocity potential with respect to time
ϕ_D	First order diffraction potential
$\phi_D^{\pm}$	Second order diffraction potential
ϕ_I	First order incident wave potential
$\phi_I^{\pm}$	Second order incident wave potential
ϕ_R	First order radiation potential
$\phi_R^{\pm}$	Second order radiation potential
$\phi_{R,j}^{\pm}$	Second order velocity potential associated with radiation for mode j
$\phi_{R,k}$	First order radiation potential associated with force direction k
ϕ_S	First order scattering potential
$\phi_S^{\pm}$	Second order scattering potential
$\phi^{(1)}(x, y, z, t)$	Total first order velocity potential
$\phi^{(2)}(x, y, z, t)$	Total second order velocity potential
ω	Angular frequency of the wave
ω_i	Circular frequency of incident wave i
ω_j	Circular frequency of incident wave j

Probability

α, β	Parameters in the Weibull distribution
α_U, β_U, θ, γ	Parameters used in the joint probability distribution of U, H_s and T_p
β	Radius of the failure sphere in the U-space
κ	Scaling parameter for the North Sea PDFs
μ	Mean value associated with discrete variables
ν	Degree of freedom (statistics)
ξ	Global extreme response value
σ	The standard deviation associated with discrete variables
σ, μ	Parameters in the lognormal distribution
σ_{LHM}, μ_{LHM}, α_{HM} and β_{HM}	Parameters in the Lonowe-model
σ_X	Standard deviation of the variable X
$\sigma_{\dot{X}}$	The derivative of the standard deviation of the variable X
$\Phi(\quad)$	Gaussian distribution function
χ^2	Chi-squared

Chapter 1

Introduction

The Norwegian Public Roads Administration (NPRA) is currently investigating the possibilities of carrying out several fjord crossings on the Coastal Highway Route E39, in the western part of Norway. This thesis compass a floating multi-span suspension bridge that is considered for the 5 km long crossing of Bjørnafjorden. The floating multi-span suspension bridge is developed by several private companies on behalf of NPRA. In this regard, the authors of this thesis, have gained access to a large part of the documentation manufactured. This includes CAD-drawings of the concept, environmental data measurements from Bjørnafjorden and analysis reports about the different aspects of the bridge, e.g. aerodynamic stability, design basis, structural analysis reports and so forth.

This thesis is written in cooperation with NPRA. Thus, it is appropriate to some extent compare the finite element analysis results with the results reported in the NPRA-reports.

The authors have been free to include, with advice from the supervisors, Associate Professor Ole Øiseth and PhD candidate Yuwang Xu, what they have deemed interesting to investigate.

1.1 Description of the problem

To assess the behaviour of the bridge, it is necessary to establish numerical models that are able to reproduce the dynamic properties of the bridge. The models are to be verified, and the effect of the environmental conditions need to be considered.

1.2 Scope of the thesis

Based on the presumptions above, the main scope of this thesis was selected to be the development of a parametrized finite element model of a floating multi-span suspension bridge with tension leg

platform floaters. The finite element model has been exposed to environmental loading from wind and waves.

Much time has been spent on the development of the parametrized finite element model, as the complicated geometry, properties and boundary conditions of the bridge were taken into account. This also includes the hydrodynamic properties of the pontoons. To evaluate how the pontoon design influences the bridge behaviour, basic analyses are performed for two suggested hull alternatives.

The coupled effect of wave and wind loading on the suggested suspension bridge is quite unique and is studied through a coupled buffeting and wave analysis performed in modal coordinates in the frequency domain. Spectral densities and the standard deviation along the bridge is presented for various load cases and assumptions.

To the best knowledge of the authors of this thesis, this particular combination of top cables and the tethers employed as structural components to a multi-span suspension bridge, have never been carried out anywhere in the world to this day. These interesting components are studied in a parameter study regarding the effects on the spectral densities and the standard deviation of the response due to damage on either some of the tethers or some of the top cables.

By using standard deviations from the buffeting analysis, a horizontal displacement with a 100 year return period at the middle of the central main span, is investigated in an extreme value analysis. By using a self-established probability distribution function (PDF) representing the environmental loading in Bjørnafjorden, based on numerical and actual measurements of the conditions in the fjord, and other available PDFs, estimations of the critical long-term load conditions and the long-term response is found and discussed.

This bridge includes three extremely long and slender spans. For this reason, the critical velocity for the instability phenomenon, flutter, is obtained and discussed. Also, a simplified illustration of the flutter mode shape is presented.

A great deal of the effort put into this thesis has been made to develop, adapt and understand MATLAB scripts.

1.3 Structure of the report

1. **Chapter 2 - The Bridge** An overview of the project, Coastal Highway Route E39, will be presented and a summary of the bridge concept, including selected technical drawings, will be given.
2. **Chapter 3 - Theory** The theory that serves as a basis for this thesis will be presented.
3. **Chapter 4 - Methods** The methods used to assess the problems are given and described.
4. **Chapter 5 - Finite Element modelling in ABAQUS** How the bridge was modelled in ABAQUS along with the assumptions made will be presented. A verification of the model is presented.

5. **Chapter 6 - Modelling in HydroD and GeniE** A presentation of the assumptions made when modelling the concrete floater and steel floater is given. A verification of the models is presented.
6. **Chapter 7 - Results and Discussion** The results from the analyses carried out are presented and discussed.
7. **Chapter 8 - Conclusions** A summary of the work is presented and conclusions are made.
8. **Chapter 9 - Further Work** Suggestions for further work and research are given.

Chapter 2

A Description of the structural design of the bridge concept

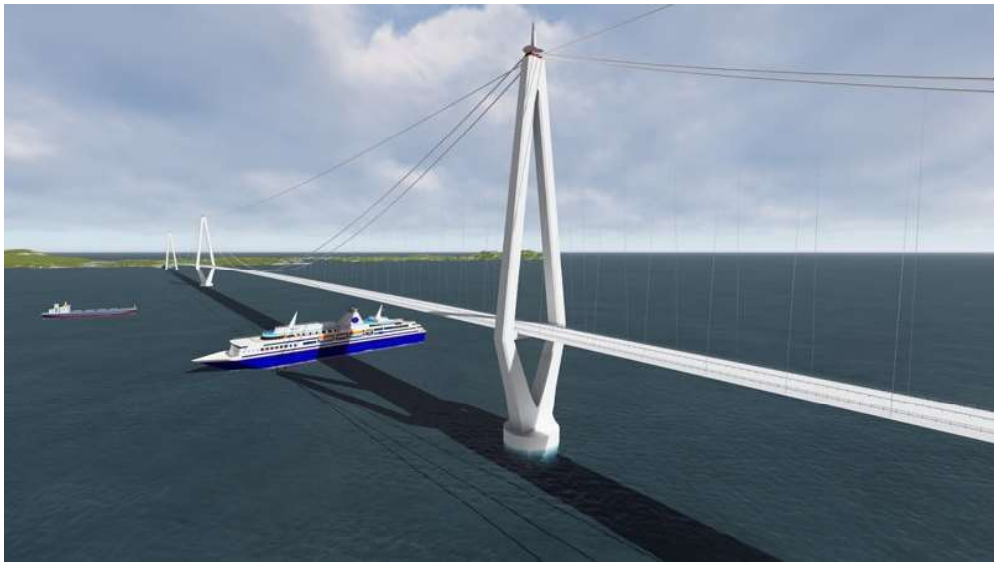

Figure 2.1: The suggested design of the Bjørnafjorden bridge (NPRA, 2016o)

2.1 The Coastal Highway Route E39

The Coastal Highway Route E39, see figure 2.2, is a project that aims at replacing the ferry crossings along the west coast of Norway south of Trondheim within the next 20 years. The route stretches from Trondheim in the north to Kristiansand in the south and will be 1100 km long. As

a part of this project, several pioneering fjord crossings has to be made (NPRA, 2016u). One of those fjords that have to be crossed is Bjørnafjorden, south of Bergen.

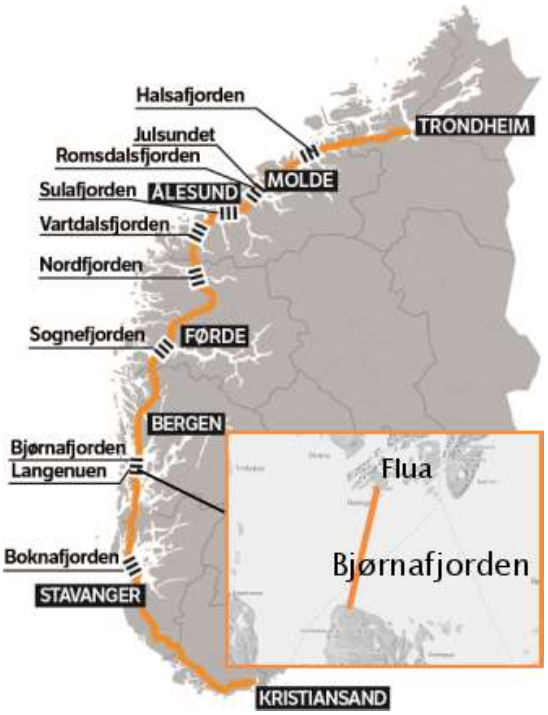

Figure 2.2: The figure shows the Coastal Highway Route E39 and the Bjørnafjorden crossing, (Statens vegvesen, 2017)

2.2 Challenges related to the crossing of Bjørnafjorden

The crossing of Bjørnafjorden will demand the development of a bridge that is first of its kind. For this reason, several concepts are being developed in parallel, and in this thesis, the concept concerning a multi-span suspension bridge on tension leg platforms (TLP) will be considered and discussed. The crossing requires the bridge to be 4748 m long, with three suspension-spans that range from 1325 m to 1385 m and a side span with a length of 653 m. The two floating pylons are supported by TLPs, anchored at water depths of 550 m and 450 m. It is also introduced a top cable to prevent large deformations connecting the four pylons at the pylon tops. A general layout of the bridge is presented in figure 2.3.

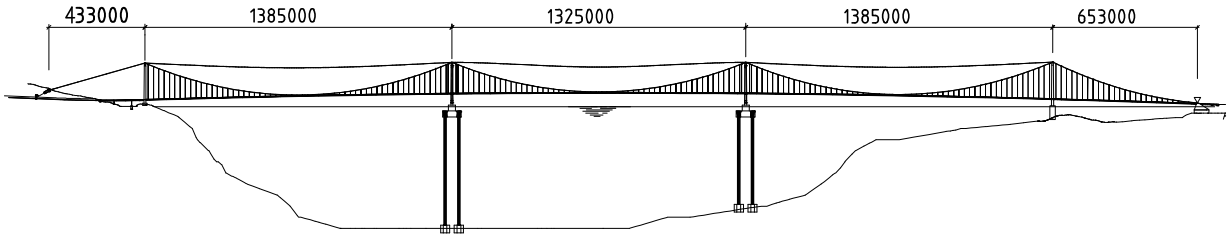

Figure 2.3: General layout of the bridge, (NPRA, 2016j)

The Bjørnafjorden fjord crossing requires a bridge with remarkable features. The concept has been developed by combining existing offshore and bridge technology in a new fashion. The massive scale of the bridge regarding length and slenderness combined with floating pylons standing on straight TLPs will give rise to large deformations.

Two different concepts have been considered for the pontoons that support the floating pylons, a reinforced concrete hull, and a steel hull. In this thesis, the concrete alternative has been studied in detail, while the steel hull alternative has not been assessed as thorough.

2.3 The floaters

2.3.1 Concrete hull

The main dimensions of the concrete hull are as follows (NPRA, 2016b, 3.1), see figure 2.4a and 2.4b. The hull consists of a cylindrical caisson with a cylinder with a smaller diameter placed on top of it. The diameter of the caisson is 84.2 m, and the top plate of the caisson is resting 20 m below MSL. There are 16 tethers attached to the caisson in groups of 4. The total prestressing of the tether is equal to 300 MN. The draught of the hull is 47.5 m. The top cylinder on the caisson has a width of 31.6 m, and the top is 6 m above MSL. The bridge pylon is connected to the upper part of the concrete cylinder. The interior consists of 50 compartments, where most of them are ballast tanks. The ballast in each concrete pontoon is equal to 24 500 tonnes and the pontoon weights 86 000 tonnes.

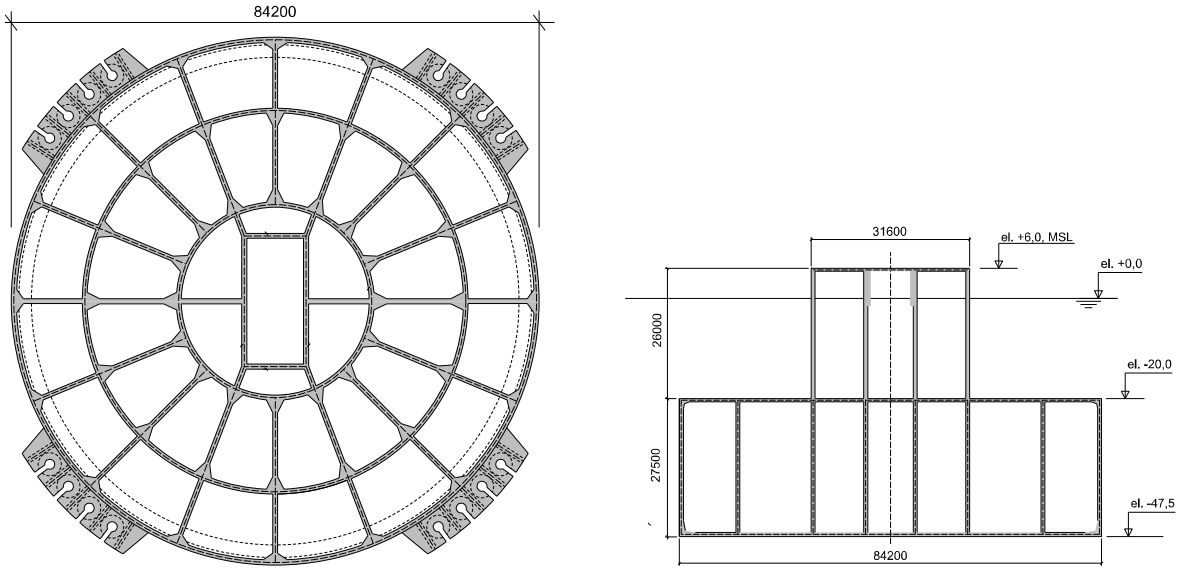

(a) Horizontal section of the concrete hull.

(b) Vertical section of the concrete hull.

Figure 2.4: The horizontal and vertical section of the concrete hull, (NPRA, 2016k).

2.3.2 Steel hull

The lower part of the steel hull consists of a 20 m tall hexagonal box, with three tethers attached at each corner of the hexagonal. The total height of the structure is 56 m with a draft of 50 m. The upper part of the hull consists of one top cylinder with a diameter of 30 m and a cone split horizontally with a bottom diameter of 40 m. The hexagon is 70 m between the parallel sides. The bridge is connected at the same vertical coordinate to the steel pontoon as with the concrete pontoon. The steel hull also contains compartments. It weights 19 500 tonnes. The steel hull has 12 tethers attached to it, in groups of 2. The total prestressing force in the tethers is equal to 225 MN.

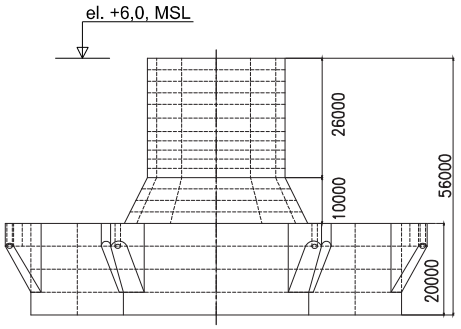

(a) Vertical section of the steel hull, (NPRA, 2016l)

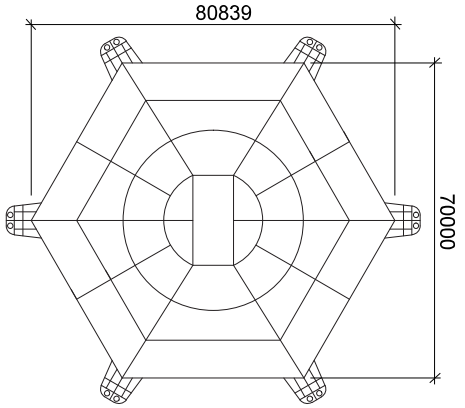

(b) Horizontal section of the steel hull, (NPRA, 2016l)

Figure 2.5: Horizontal and vertical sections of the steel hull.

2.4 Cable system

2.4.1 Suspended cable

The main cable system comprises of two suspended cables, both which are skew and inclined inwards. The inclination inwards provides a unique angle for each hanger pair along the length of each of the bridge. At the main span of the bridge (the three spans ranging from 1325-1385 m) the suspended cable diameter is equal to 0.605 m. At the side span (the northern span between the north-most fixed tower and the shore) the cable diameter is 0.655m. The reason for the bigger suspended cable diameter is that the top cables are only present at the main spans. For all the suspended cables the air void is about 20 %. The sag to span ratio for the suspended span is 1:10. The suspended cables are made with the parallel wire strand method, whereas there are 87 strands consisting of 127 wires in the main span suspended cables and 102 strands consisting of 127 wires in the side span suspended cables, (NPRA, 2016p). The wires are equal to 5.15 mm.

2.4.2 Top cable

A top cable has been introduced between the pylon tops of the bridge, to increase the in-plane stability of the suspension bridge and reduce vertical displacement of the bridge deck, (NPRA, 2016p).

The top cables are anchored at the concrete pylon tops and are not continued into the side spans, but there are added additional strands to the suspended cables in both side spans to accommodate for the anchorage of the top cables in the pylon tops. The top cable is anchored at each pylon top horizontally by anchoring each strand individually, see figure 2.6. The sag of the top cable over the central span is calculated to be 23.1m for a steel cable and 26.6m for a cable which also comprises the protection or wrapping of the cable, (NPRA, 2016p). The top cable is a ten strand cable, where the strands consist of 55 wires each.

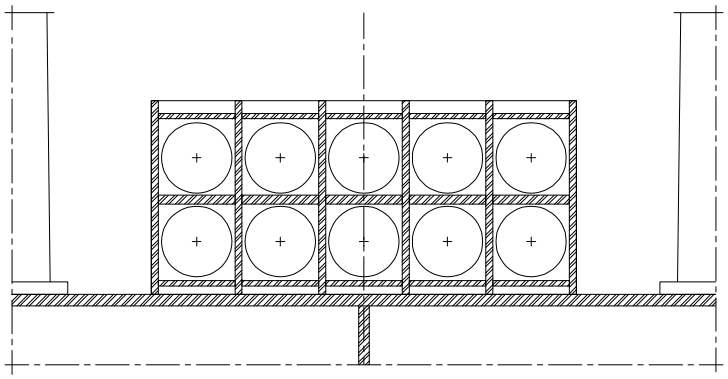

Figure 2.6: Anchorage of the strands in the top cable at each pylon top, (NPRA, 2016e)

2.4.3 Hangers

The hangers are located at 24 m intervals along the suspended span. The shortest hangers at the middle of the main spans are prone to large in-plane and out-of-plane rotations. The longest hangers closest to the pylons are susceptible to excessive vibrations. Typical hanger diameters are 70 mm and 90 mm, where the longest hangers have a diameter of 90 mm.

2.5 Pylons

The bridge consists of 4 pylons, where the southernmost and northernmost towers are fixed concrete pylons, and the two others are floating steel pylons. The floating towers have a diamond shape and are attached to the main cables at 199.5 m above MSL, see figure 2.7b. The fixed pylons both have an A-shaped frame structure, as can be seen in figure 2.7a. The two pylon legs are joined into a double cell structure 20 m below the pylon top. The southernmost pylon is attached to the main cables at 196.2 m above MSL, while the northernmost pylon is attached at 200.9 m above MSL. The northernmost tower rests at a concrete caisson, which serves as the foundation.

The concrete caisson is 61 m tall and is anchored to solid rock at an elevation of 58 m below MSL.

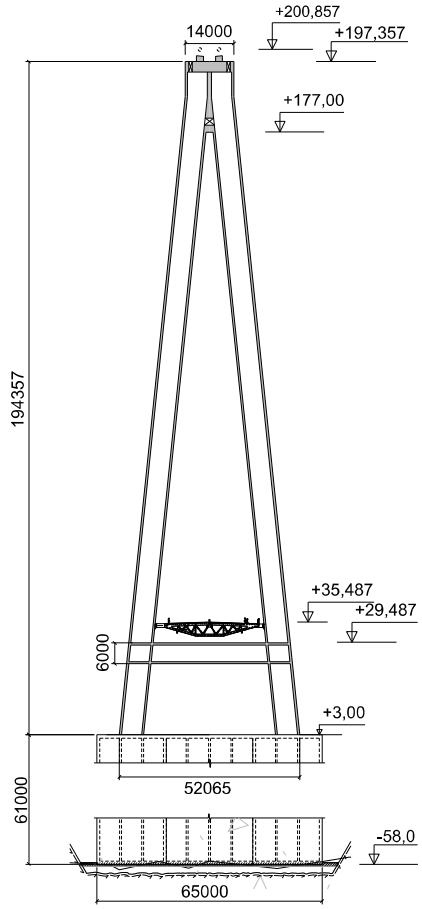

(a) The concrete pylon at the northernmost position, Flua, (NPRA, 2016f).

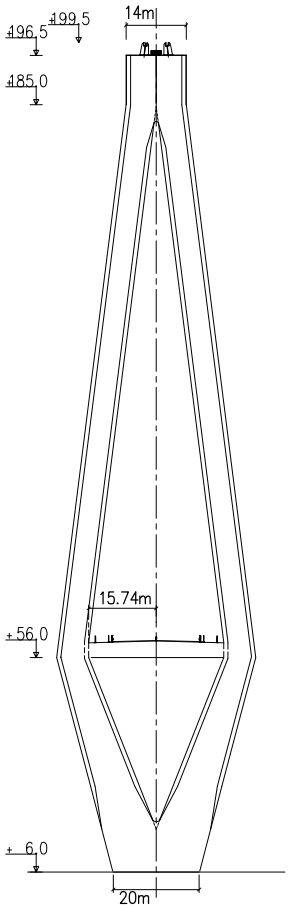

(b) The design for the floating pylons, (NPRA, 2016h).

Figure 2.7: Set up for the fixed pylon

2.5.1 Pylon saddles

The pylon saddles, see figure 2.8, support the suspension cables at the pylon tops. They are a welded system that consists of several plates that are made up of a trough, central support plate and several supporting cross ribs. The angle of the saddles where the suspended cables rest are such that they correspond to the cable alignment angle to avoid any kinks or discontinuities.

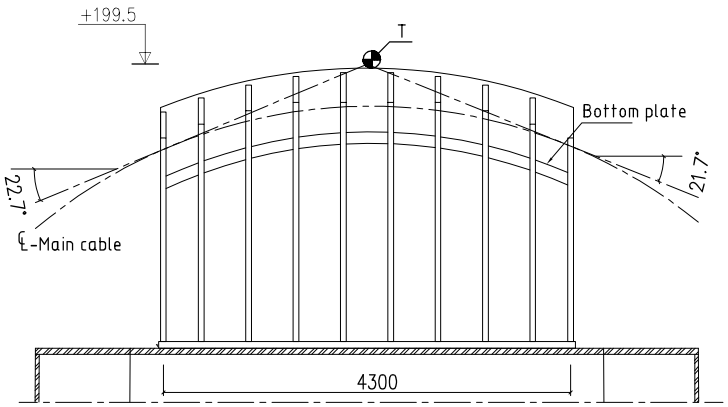

Figure 2.8: One of the pylon saddles located at one of the floating steel towers, (NPRA, 2016d)

2.6 Girder

The girder is continuous from the south pylon all the way to the shore in the north end of the side span. It can further be divided into three main spans and one side span. The three main spans have lengths of 1385 m, 1325 m and 1385 m, and the side span is 653 m long. In total this continuous span is 4748 m long, and all the four sub-spans are suspended. The girder is a closed steel-box girder as shown in figure 2.9. The cross-section of the girder varies somewhat and is bigger closer to the pylons due to the concentration of forces at these sections.

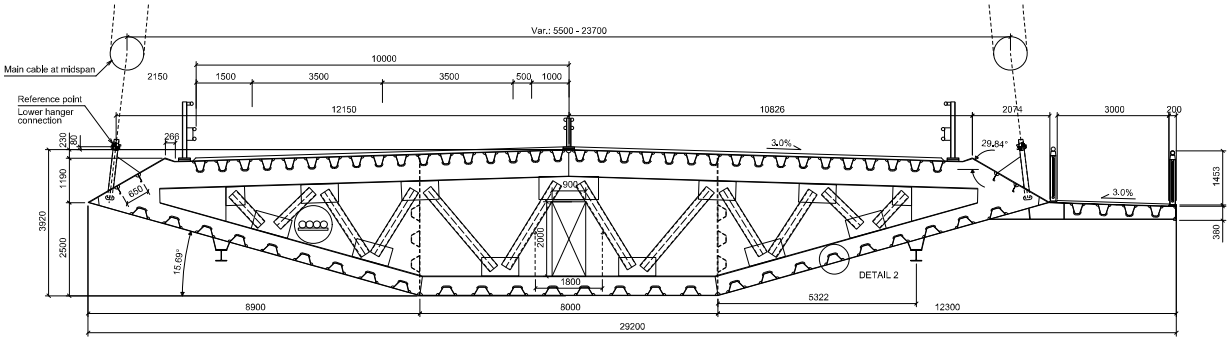

Figure 2.9: Cross-section of the girder, (NPRA, 2016c)

The cross-section is 29.2 m wide and 3.92 m tall, excluding railings. The walkway for pedestrians and cyclists is a 3 m long cantilever. The girder is connected to the southernmost tower with sliding bearings. The girder is only supported by the hangers at the northernmost tower. At the floating towers, the girder is monolithically fixed to the pylons. The support at the abutment at the north end of the bridge also consists of sliding bearings.

2.7 Anchor system

2.7.1 TLP

The anchor system for the two floating hulls is proposed to consist of a combination of suction- and gravity-type anchors. The anchorage is at water depths equal to 550 m and 450 m. The tethers are steel pipe elements which connect the floater with the seabed, (NPRA, 2016q, 1.2). The purpose of the tension legs is to create a stable foundation for the floating pylons by dragging the floaters, which the bridge is resting at, below the centre of buoyancy to create tension in the steel pipes. This approach reduces the vertical displacements at floating pylon positions substantially.

2.7.2 Splay chamber

A suggestion for the splay chamber designs is depicted in figure 2.10. The suspended cables are anchored into the abutment at the north side and anchored into a separate chamber at the south shore, (NPRA, 2016q, 1.2).

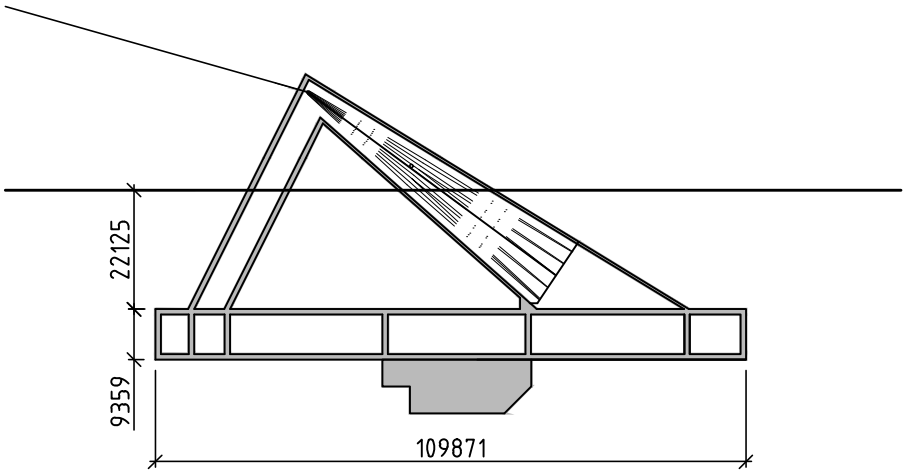

Figure 2.10: The northern splay chamber in the abutment, (NPRA, 2016m)

Chapter 3

Theory

3.1 Multimode method

Equation (3.1) is the traditional equation of motion (EOM) for a multiple degree of freedom system (MDOF): (Chopra, 2012, p.350)

$$\boldsymbol{M}\ddot{\boldsymbol{r}}(t) + \boldsymbol{C}\dot{\boldsymbol{r}}(t) + \boldsymbol{K}\boldsymbol{r}(t) = \boldsymbol{f}(t) \tag{3.1}$$

Where $\mathbf{r}(t)$, $\dot{\mathbf{r}}(t)$ and $\ddot{\mathbf{r}}(t)$ are the displacement, velocity and acceleration of the structure, respectively. $\mathbf{M}$ is the mass matrix, $\mathbf{C}$ is the damping matrix, $\mathbf{K}$ is the stiffness matrix and $\boldsymbol{f}(t)$ is the load vector.

Modal coordinates are achieved by summing up the contribution from a finite number, n, eigenvectors of the system. This finite number, n, can be less than the total number of eigenvectors, N. The displacement vector is then given by the following equation.

$$\boldsymbol{r}(t) = \sum_{n=1}^{N} \phi_n \eta_n(t) \approx \sum_{n=1}^{n} \phi_n \eta_n(t) \tag{3.2}$$

Where $\eta_n(t)$ is the generalized coordinates for mode shape n and ϕ_n is the eigenvector for mode n.

The equation of motion (EOM) can now be written as follows.

$$\tilde{\boldsymbol{M}}\ddot{\boldsymbol{\eta}}(t) + \tilde{\boldsymbol{C}}\dot{\boldsymbol{\eta}}(t) + \tilde{\boldsymbol{K}}\boldsymbol{\eta}(t) = \tilde{\boldsymbol{f}}(t) \tag{3.3}$$

where

$$\begin{aligned} &\text{Modal mass matrix :} && \widetilde{\boldsymbol{M}} = \Phi^T \boldsymbol{M} \Phi \\ &\text{Modal damping matrix :} && \widetilde{\boldsymbol{C}} = \Phi^T \boldsymbol{C} \Phi \\ &\text{Modal stiffness matrix :} && \widetilde{\boldsymbol{K}} = \Phi^T \boldsymbol{K} \Phi \\ &\text{Modal load matrix :} && \widetilde{\boldsymbol{f}} = \Phi^T \boldsymbol{f} \end{aligned} \tag{3.4}$$

By using only a small number of modes n, compared to the total number of degree of freedoms (DOF)s, N, computational efficiency is achieved. A sufficiently accurate representation of the response can be obtained if the selected n is not too small.

If the system matrices $\boldsymbol{M}$, $\boldsymbol{K}$ and $\boldsymbol{C}$ are symmetrical, the modal matrices will be diagonal, due to the orthogonality property of the eigenvectors. If all modal matrices are diagonal, no row reduction is required as the equations are uncoupled, and can be treated as n number single degree of freedom (SDOF) systems. (Chopra, 2012, Ch 9.1.1)

By taking the Fourier transform of the equation a frequency representation of equation 3.1 can be derived: (Newland, 2004, s.62)

$$\boldsymbol{a_r}(\omega) = \boldsymbol{H}(\omega)\boldsymbol{a_f}(\omega) \tag{3.5}$$

Where $\mathbf{H}(\omega)$ is defined by the following expression: (Newland, 2004, s.73)

$$\mathbf{H}(\omega) = \left[-\mathbf{M}\omega^2 + i\mathbf{C}\omega + \mathbf{K}\right]^{-1} \tag{3.6}$$

For a single degree of freedom system the following relation between the loading and the response spectrum can be derived: (Newland, 2004, s.73)

$$S_{rr}(\omega) = |H(\omega)|^2 S_{ff}(\omega) \tag{3.7}$$

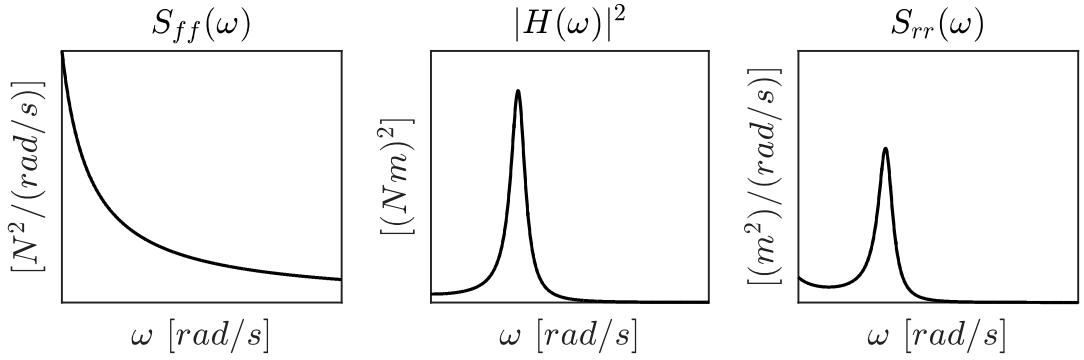

Figure 3.1: Load spectrum, transfer function and displacement spectrum for a system with only one degree of freedom

The standard deviation (STD) squared can be found by integrating the response spectrum.

$$\sigma^2 = \int_0^\infty S_{rr}(\omega) d\omega \tag{3.8}$$

The relation between the response spectrum for the displacement, velocity and the acceleration is given by the following equation

$$\omega^4 S_{rr} = \omega^2 S_{\dot{r}\dot{r}} = S_{\ddot{r}\ddot{r}} \tag{3.9}$$

3.2 Aerodynamics

3.2.1 Buffeting Analysis

Quasi-steady theory

Quasi-steady aerodynamics is an approximation to define the aerodynamic forces that a structure is subjected to. The approximation states that aerodynamic forces at any given time are only dependent on the immediate position of the considered body at a specific moment, meaning that the motion of the considered aerodynamic model can be ignored (Tamura and Kareem, 2013, Ch 4.2). In other words, ”the aerodynamic pressure or force on the bridge deck can be assumed to vary with the incoming velocity in the same manner as for steady flow (the quasi-steady assumption)” (Xu, 2013, 4.3).

Quasi-static theory implies that the loading is applied so slow that the inertial and damping effects can be ignored. By slow it is meant that the frequency of the loading is low compared to that of the structure.

Buffeting theory

The wind excitation force is in general impossible to express in an analytic form. For this reason, the wind excitation load has to be expressed in terms of its statistical properties. There are two different approaches to do this. Either to utilize the Fourier transformation when doing a response prediction in frequency domain, or to do a time domain analysis by simulating the excitation force with the estimated statistical properties (Tamura and Kareem, 2013, Ch 4.4).

The theory in the following sections are from (Strømmen, 2010, Ch 5.1).

The buffeting theory is based on the assumption that quasi-steady theory is valid for the considered flow and the structure it acts on. This assumption implies that the buffeting load may be derived using the instantaneous velocity pressure. In other words, the assumptions for Bernoulli’s equation, 3.10, holds and Bernoulli’s equation can be used to derive the forces on a bluff body because the pressure due to the wind loading is known.

$$q(t) = \frac{1}{2}\rho U(t)^2 \tag{3.10}$$

Where ρ is the density of the air and $U(t)$ is the wind velocity.

Two other basic assumptions for buffeting theory are that a linearization of the fluctuating part of the velocity does not degrade the accuracy too much and that the load coefficients can be calculated from static tests. The tests are static in the sense that the mean wind loading is considered, implying that the load coefficients are dependent on the mean wind velocity. The load coefficients are also dependent on the angle of attack.

The part of the wind load acting on a structure due to the fluctuations of the velocity of the wind flow can be denoted as buffeting wind load. The theory presented in the following sections are based on the assumption that a line-like structure is considered and that the wind field is stationary and homogeneous.

In addition, it is assumed that direction of flow is perpendicular to the span-wise x-axis of the structure. The flow component in the x-direction is thus neglected and the wind vector can be decomposed into the following components when it is also assumed that the z-position of the structure, i.e. a bridge girder, where the flow acts, is constant along the line-like structure. The total wind, $U(x,t)$, can be decomposed into the following components.

$$U(x,t) = U + u(x,t) \quad and \quad w(x,t) \tag{3.11}$$

Where U is the mean wind, $u(x,t)$ and $w(x,t)$ are the fluctuating components of the velocity vector in the along wind horizontal direction and the vertical across wind direction, respectively.

The wind loading and its decomposition

To define the wind loading the following has to be considered.

The wind velocity vector for positions along the bridge is given at the arbitrary static displacement position, $\bar{r}_y(x)$, $\bar{r}_z(x)$ and $\bar{r}_\theta(x)$, see figure 3.2.

The structure oscillates about the static, displaced position from the origin, $\bar{r}_y(x)$, $\bar{r}_z(x)$ and $\bar{r}_\theta(x)$, and are given the dynamic displacements, $r_y(x)$, $r_z(x)$ and $r_\theta(x)$, when subjected to a wind loading. When the structure is in this configuration, the instantaneous cross sectional drag, lift and moment forces are defined as the following when given in the flow axis system.

$$\begin{bmatrix} q_D(x,t) \\ q_L(x,t) \\ q_M(x,t) \end{bmatrix} = \frac{1}{2}\rho U_{rel}^2 \begin{bmatrix} D \cdot C_D(\alpha) \\ B \cdot C_L(\alpha) \\ B^2 \cdot C_M(\alpha) \end{bmatrix} \tag{3.12}$$

U_{rel} is the instantaneous relative wind velocity, α is the flow's angle of approach, B and D is the width and the height of the cross-section, respectively. $C_D(\alpha)$, $C_L(\alpha)$ and $C_M(\alpha)$ are load

coefficients. By relative wind velocity it is meant that the velocity of the exposed structure is taken into consideration.

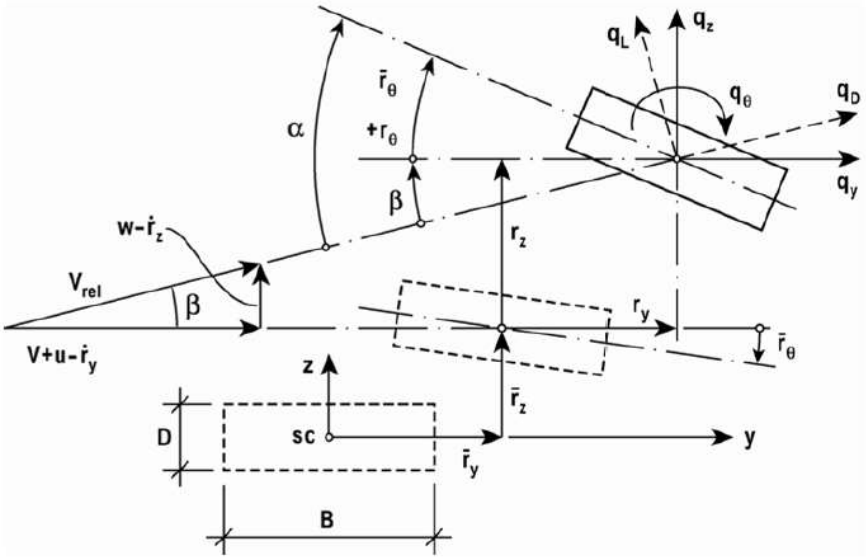

Figure 3.2: The decomposition of the response of a cross-section due to wind loading. (Strømmen, 2010, Ch 5.2, fig.5.1). Here $U = V$ and $U_{rel} = V_{rel}$.

The transformation of total wind loading, $\mathbf{q}_{tot}(x,t)$, into structural axis is done by utilizing the following relation:

$$\mathbf{q}_{tot}(x,t) = \begin{bmatrix} q_y \\ q_z \\ q_\theta \end{bmatrix} = \begin{bmatrix} cos\beta & -sin\beta & 0 \\ sin\beta & cos\beta & 0 \\ 0 & 0 & 1 \end{bmatrix} \begin{bmatrix} q_D \\ q_L \\ q_M \end{bmatrix} \tag{3.13}$$

Where β is the angle defined in figure 3.2.

The total wind loading, $\mathbf{q}_{tot}(x,t)$, can be expressed as follows below. The derivation of the expressions in 3.14 are found in (Strømmen, 2010, Ch 5.1, p. 93-95).

$$\mathbf{q}_{tot}(x,t) = \overbrace{\begin{bmatrix} \bar{q}_y \\ \bar{q}_z \\ \bar{q}_\theta \end{bmatrix}}^{\text{Static part}} + \overbrace{\begin{bmatrix} q_y \\ q_z \\ q_\theta \end{bmatrix}}^{\text{Dynamic part}} = \overbrace{\bar{\mathbf{q}}}^{\text{Static components}} + \overbrace{\mathbf{B}_q \cdot \mathbf{u}}^{\text{Buffeting force terms}} + \overbrace{\mathbf{C}_{ae} \cdot \dot{\mathbf{r}} + \mathbf{K}_{ae} \cdot \mathbf{r}}^{\text{Motion-dependent components}} \tag{3.14}$$

$$\bar{\mathbf{q}}(x,t) = \begin{bmatrix} \bar{q}_y \\ \bar{q}_z \\ \bar{q}_\theta \end{bmatrix} = \frac{1}{2}\rho U^2 B \begin{bmatrix} \bar{C}_D \frac{D}{B} \\ \bar{C}_L \\ B\bar{C}_M \end{bmatrix} = \frac{1}{2}\rho U^2 B \cdot \hat{\mathbf{b}}_q \tag{3.15}$$

$$\mathbf{B}_q(x) = \frac{\rho U B}{2} \begin{bmatrix} 2\bar{C}_D \frac{D}{B} & (C'_D - \bar{C}_L \frac{D}{B}) \\ 2\bar{C}_L \frac{D}{B} & (C'_D \frac{D}{B}) + \bar{C}_L \\ 2B\bar{C}_M & BC'_M \end{bmatrix} = \frac{\rho U B}{2} \cdot \hat{\mathbf{B}}_q(x) \tag{3.16}$$

$$\mathbf{C}_{ae}(x) = -\frac{\rho U B}{2} \begin{bmatrix} 2\bar{C}_D \frac{D}{B} & (C'_D - \bar{C}_L \frac{D}{B}) & 0 \\ 2\bar{C}_L \frac{D}{B} & (C'_D \frac{D}{B}) + \bar{C}_L & 0 \\ 2B\bar{C}_M & BC'_M & 0 \end{bmatrix} \tag{3.17}$$

$$\mathbf{K}_{ae}(x) = \frac{\rho U^2 B}{2} \begin{bmatrix} 0 & 0 & C'_D \frac{D}{B} \\ 0 & 0 & C'_L \\ 0 & 0 & BC'_M \end{bmatrix} \tag{3.18}$$

$$\mathbf{u}(x,t) = \begin{bmatrix} u & w \end{bmatrix}^T \tag{3.19}$$

$$\mathbf{r}(x,t) = \begin{bmatrix} r_y & r_z & r_\theta \end{bmatrix}^T \tag{3.20}$$

Where $\mathbf{K}_{ae}$ and $\mathbf{C}_{ae}$ are the aerodynamic damping and stiffness matrices, $\mathbf{B}_q$ and $\hat{\mathbf{B}}_q(x)$ are the buffeting dynamic force coefficient matrices and $\hat{\mathbf{b}}_q$ is the buffeting static force coefficient vector. Also, $(\bar{\ })$ denotes that the load coefficients, are evaluated at angle $\bar{\alpha}$. $(')$ denotes the slope of the load coefficient curves.

The terms, $\mathbf{C}_{ae} \cdot \dot{\mathbf{r}}$ and $\mathbf{K}_{ae} \cdot \mathbf{r}$, are motion induced forces acting on the structure due to the displacement and the velocity of the structure. In a dynamic analysis, it is common to disregard the static part of the load equation, as it can be evaluated separately.

3.2.2 Aerodynamic stiffness and damping matrices expressed by aerodynamic derivatives

The following sections are from (Strømmen, 2010, Ch 5.2).

The aerodynamic damping matrix, $\mathbf{C}_{ae}$, and aerodynamic stiffness matrix, $\mathbf{K}_{ae}$, are usually utilized in the detection of unstable motion at high wind velocities. $\mathbf{C}_{ae}$ and $\mathbf{K}_{ae}$ are defined as the following:

$$\mathbf{C}_{ae} = \begin{bmatrix} P_1 & P_5 & P_2 \\ H_5 & H_1 & H_2 \\ A_5 & A_5 & A_2 \end{bmatrix} \quad \text{and} \quad \mathbf{K}_{ae} = \begin{bmatrix} P_4 & P_6 & P_3 \\ H_6 & H_4 & H_3 \\ A_6 & A_4 & A_3 \end{bmatrix} \tag{3.21}$$

The coefficients of $\mathbf{C}_{ae}$ and $\mathbf{K}_{ae}$ in equation 3.21 are determined by wind tunnel tests of the respective cross sections.

$\mathbf{C}_{ae}$ and $\mathbf{K}_{ae}$ can be normalised with respect to $\rho B^2 \omega_i / 2$ and $\rho B^2 \omega_i^2 / 2$, where, ω_i, is the wind induced resonance frequency with respect to mode shape i. The normalisation then yields the following expressions for $\mathbf{C}_{ae}$ and $\mathbf{K}_{ae}$:

$$\mathbf{C}_{ae} = \frac{\rho B^2}{2} \cdot \omega_i^2(U) \cdot \hat{\mathbf{C}}_{\mathbf{ae}} \quad \text{and} \quad \mathbf{K}_{ae} = \frac{\rho B^2}{2} \cdot \omega_i^2(U) \cdot \hat{\mathbf{K}}_{\mathbf{ae}} \tag{3.22}$$

$\hat{\mathbf{C}}_{\mathbf{ae}}$ and $\hat{\mathbf{K}}_{\mathbf{ae}}$, see equation 3.23, contains the non-dimensional aerodynamic derivatives, P_k^* , A_k^* , H_k^* , where $k = 1\text{-}6$.

$$\hat{\mathbf{C}}_{\mathbf{ae}} = \begin{bmatrix} P_1^* & P_5^* & BP_2^* \\ H_5^* & H_1^* & BH_2^* \\ BA_5^* & BA_1^* & B^2 A_2^* \end{bmatrix} \quad \text{and} \quad \hat{\mathbf{K}}_{\mathbf{ae}} = \begin{bmatrix} P_4^* & P_6^* & BP_3^* \\ H_6^* & H_4^* & BH_3^* \\ BA_6^* & BA_4^* & B^2 A_3^* \end{bmatrix} \tag{3.23}$$

The values of $\hat{\mathbf{C}}_{\mathbf{ae}}$ and $\hat{\mathbf{K}}_{\mathbf{ae}}$ can be obtained by normalising $\mathbf{C}_{ae}$ and $\mathbf{K}_{ae}$, which are derived from buffeting theory using a frequency domain approach.

$$\begin{bmatrix} P_1^* & H_1^* & A_1^* \\ P_2^* & H_2^* & A_2^* \\ P_3^* & H_3^* & A_3^* \\ P_4^* & H_4^* & A_4^* \\ P_5^* & H_5^* & A_5^* \\ P_6^* & H_6^* & A_6^* \end{bmatrix} = \begin{bmatrix} -2\bar{C}_D \frac{D}{B} \frac{V}{B\omega_i(U)} & -(C'_L + \bar{C}_D \frac{D}{B}) \frac{U}{B\omega_i(U)} & -C'_M \frac{U}{B\omega_i(U)} \\ 0 & 0 & 0 \\ \bar{C}_D \frac{D}{B} (\frac{U}{B\omega_i(U)})^2 & C'_L (\frac{U}{B\omega_i(U)})^2 & C'_M (\frac{U}{B\omega_i(U)})^2 \\ 0 & 0 & 0 \\ (\bar{C}_L - C'_D) \frac{D}{B} \frac{U}{B\omega_i(U)} & -2\bar{C}_L \frac{U}{B\omega_i(U)} & -2\bar{C}_M \frac{U}{B\omega_i(U)} \\ 0 & 0 & 0 \end{bmatrix} \tag{3.24}$$

The quasi-static aerodynamic derivatives above can be expressed as functions of the reduced velocity, see equation 3.25.

$$\hat{U} = \frac{U}{B\omega_i(U)} \tag{3.25}$$

$\omega_i(U)$ is the resonance frequency associated with mode shape i, for a mean wind velocity equal to U. Both the eigenfrequency and the eigen mode is dependent on the mean wind velocity.

The following empirical expression for the aerodynamic forces is described in (Øiseth et al., 2012, Ch. 2.1).

$$\boldsymbol{F}_{ae}(\omega) = \frac{1}{2}\rho U^2 \left(\boldsymbol{a}_1 + \boldsymbol{a}_2 \frac{i\omega B}{U} + \boldsymbol{a}_3 \left(\frac{i\omega B}{U} \right)^2 + \sum_{l=1}^{N-3} \boldsymbol{a}_{\boldsymbol{l+3}} \frac{i\omega B/U}{i\omega B/U + d_l} \right) \tag{3.26}$$

Recalling that

$$\boldsymbol{F}_{ae}(\omega) = -\omega^2 \boldsymbol{M}_{ae} + i\omega \boldsymbol{C}_{ae} + \boldsymbol{K}_{ae} \tag{3.27}$$

Equation 3.26 can be written in the format of equation 3.27. Because the aerodynamic mass, $\boldsymbol{M}_{ae}$, is much smaller than the structural mass $\boldsymbol{M}$, aerodynamic mass is not considered. This is also the reason why the coefficient $\boldsymbol{a}_3$ does not reappear. The expressions for $\boldsymbol{K}_{ae}$ and $\boldsymbol{C}_{ae}$ are given by the following equations

$$\boldsymbol{K}_{ae} = \frac{1}{2}\rho U^2 \left(\boldsymbol{a}_1 + \sum_{l=1}^{N-3} \boldsymbol{a}_{l+3} \frac{1}{[(d_l \hat{U})^2 + 1]} \right) \tag{3.28}$$

$$\boldsymbol{C}_{ae} = \frac{1}{2}\rho U^2 \left(\boldsymbol{a}_2 + \hat{U}^2 \sum_{l=1}^{N-3} \boldsymbol{a}_{l+3} \frac{1}{[(d_l \hat{U})^2 + 1]} \right) \tag{3.29}$$

The coefficients $\boldsymbol{a}_1$, $\boldsymbol{a}_2$, $\boldsymbol{a}_4$, $\boldsymbol{a}_5$, d_1, and d_2 have been estimated for the cross section of the Hardanger bridge by wind tunnel testing at NTNU (Siedziako et al., 2017, p. 158). These are listed in table 4.2.

3.2.3 Motion induced instability

Motion induced instability is a collective term for instability phenomena that cause even a small increase in mean wind velocity to generate a large increase in dynamic response, and at the stability limit, an infinite response. The stability limit is given by a critical response frequency ω_{cr} and a critical wind speed U_{cr}. Figure 3.3 illustrates how U_{cr} acts as a vertical asymptote for the dynamic response. (Strømmen, 2010)

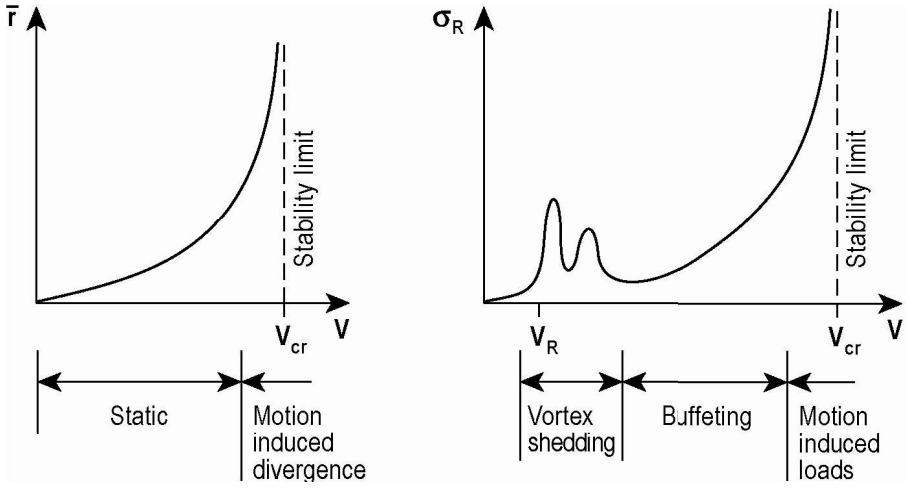

Figure 3.3: Typical response variation with mean wind velocity. (Strømmen, 2010, Ch. 6.1)

The aerodynamic stiffness and damping matrices changes with both wind velocity and frequency. To evaluate the stability of the system, the eigenvalue problem given by equation 3.30 is solved. (Simulia, 2014, Ch 6.3.6)

$$(\boldsymbol{\lambda}^2\boldsymbol{M} + \boldsymbol{\lambda}\boldsymbol{C} + \boldsymbol{K})\Phi = 0 \tag{3.30}$$

The solution to the quadratic eigenvalue problem $\boldsymbol{\lambda}$, is given by a real and a complex part as follows

$$\lambda_j = \mu_j \pm i\omega_j \tag{3.31}$$

The damping ratio for a complex eigenvalue problem is given by equation 3.32. It can be seen that the damping ratio becomes negative when the real part, μ, is positive, see equation 3.31, (Inman, 1990, Ch. 3).

$$\zeta_j = \frac{-\mu_j}{\sqrt{\mu_j^2 + \omega_j^2}} \tag{3.32}$$

The instability limit can be found by an iterative procedure, that involves confirming that the system is stable for every eigenfrequency within a range of interest for an increased mean wind velocity, until instability is reached. The iterative procedure is described in (Ge and Tanaka, 1999, Ch. 4.2), and is illustrated by a flowchart in figure 4.1.

3.3 Hydrodynamics

3.3.1 The sea surface

It is common to assume that the ocean surface elevation, η, is a stochastic wave field that can be assumed homogeneous in space and stationary in time when performing a statistically modelling of the ocean surface. The stochastic wave process is assumed to have a zero mean. For engineering purposes, it is sufficient to assume that the wave process is stationary for a limited period of 3 hours and that there are no transition periods between different sea states (Naess and Moan, 2013, 8.2.1). The sea surface can be expressed as the following when transformed from the frequency domain into the time domain using a Fourier transformation, (Kvåle et al., 2016).

$$\eta(\boldsymbol{x}_{sea}, t) = \int e^{(i\boldsymbol{\kappa}\cdot\boldsymbol{x}_{sea} - i\omega t)} dZ_\eta(\boldsymbol{\kappa}, \omega) \tag{3.33}$$

Where $\boldsymbol{\kappa} = [\kappa_x\, \kappa_y]$ is the wave number vector, $\mathbf{x}_{sea}$ is a location in space, Z_η is the spectral process related to η and ω is the frequency.

The spectral density of the sea surface between the points r and s can be found by first finding the correlation function between the respective points and then take the Fourier transformation of the correlation function.

The two-dimensional spectral density can be expressed as follows because a homogeneous stochastic wave field is considered.

$$S_{\eta_r\eta_r}(\omega,\theta) = S_{\eta_s\eta_s}(\omega,\theta) \tag{3.34}$$

Where θ denotes the wave direction. The two-dimensional spectral density is a function of wave frequency and wave direction only, because according to Airy wave theory (Kvåle et al., 2016) the wave number and the wave frequency are independent of the water depth for deep water, and they are related to each other through the following dispersion relation for deep water waves.

$$\omega^2 = g\kappa \tag{3.35}$$

In equation 3.35, g is the acceleration of gravity, and κ is the modulus of the wave number vector. The wave number vector can be expressed as the following expression when denoted in polar coordinates.

$$\boldsymbol{\kappa} = \begin{bmatrix} cos\,\theta \\ sin\,\theta \end{bmatrix} \kappa \tag{3.36}$$

Equation 3.34, when expressing the sea surface, equation 3.33, in polar coordinates, implies that the auto-spectral density of the waves can be expressed as the following, (Kvåle et al., 2016).

$$S_\eta(\omega,\theta) = S_\eta(\omega)D(\omega,\theta) \tag{3.37}$$

Where $D(\omega,\theta)$ is the directional distribution and $S_\eta(\omega)$ is the one-dimensional wave spectral density.

According to (Kvåle et al., 2016) the cross-spectral density of the water elevation can then be denoted as the following.

$$S_{\eta_r\eta_s}(\omega,\theta) = S_\eta(\omega)\int_{-\pi}^{\pi} D(\omega,\theta)\, e^{-i\frac{|\omega|\omega}{g}(\Delta x\, cos\,\theta + \Delta y\, sin\,\theta)} d\theta \tag{3.38}$$

In this thesis, $\Delta x = 1325m$ and $\Delta y = 0$. A heading angle of 90° has been selected for all analysis performed for this master thesis.

3.3.2 Empirical wave spectrums

The directional wave spectra, $S_\eta(\omega,\theta)$, in equation 3.37 are empirically determined for engineering purposes.

The one-sided Pierson-Moskowitz spectrum can be written as follows (Naess and Moan, 2013, 8.2.2):

$$S_\eta(\omega) = \frac{\alpha g^2}{\omega^5}\text{exp}(-\frac{1.25\omega_p^4}{\omega^4}) \tag{3.39}$$

Where $\alpha = 0.0081$ and is denoted as the Phillips constant and ω_p defines the peak frequency at which $S(\omega)$ is a maximum. Thus it can be seen that the Pierson-Moskowitz spectrum is a one-parameter wave spectrum dependent on the wave height, H_s, only. See figure 3.4 for an illustration of the spectre.

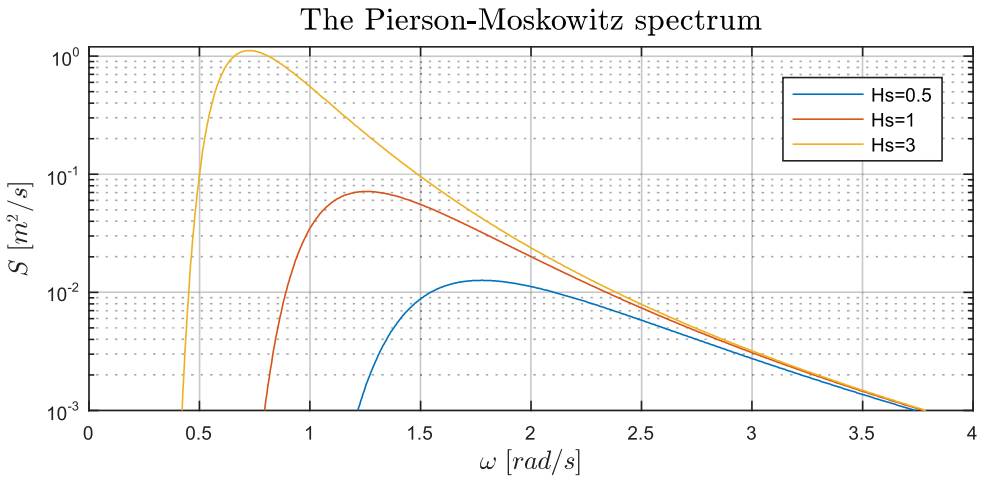

Figure 3.4: The Pierson-Moskowitz spectrum. Note that the spectrum is plotted with a log scale.

It should be noted that the Pierson-Moskowitz spectrum has a fixed peak wave period for every wave height, where the relation between the peak wave period and the wave height is given by equation 3.40, (Stansberg, 2002), and illustrated in figure 3.5.

$$T_P = \left(\frac{5}{4} \frac{(2\pi)^4}{4\alpha g^2} \right)^{1/4} \cdot H_s^{1/2} \tag{3.40}$$

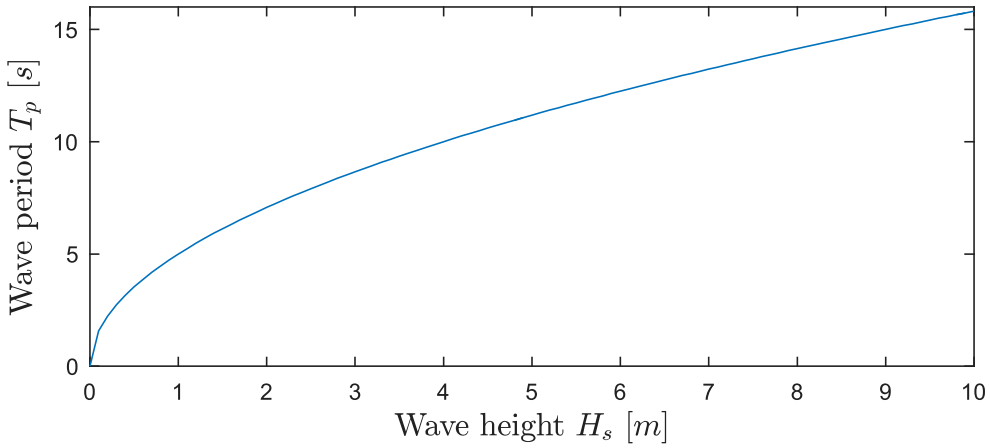

Figure 3.5: The figure shows how T_p relates to H_s for the Pierson-Moskowitz spectrum

The one-sided JONSWAP spectrum, which is a modification of the Pierson-Moskowitz spectrum, can be written as follows (Naess and Moan, 2013, 8.2.2):

$$S_\eta(\omega) = \frac{\tilde{\alpha} g^2}{\omega^5} \exp(-1.25 \frac{\omega_p^4}{\omega^4}) \cdot \gamma^{a(\omega)} \tag{3.41}$$

Where γ is a peakedness parameter and $a(\omega)$ is given as:

$$a(\omega) = \exp(-\frac{(\omega - \omega_p)^2}{2\tilde{\sigma}^2 \omega_p^2}) \tag{3.42}$$

and $\tilde{\sigma}$ is defined as:

$$\tilde{\sigma} = \begin{cases} \tilde{\sigma_a} = 0.07, & for \quad \omega \leq \omega_p \\ \tilde{\sigma_b} = 0.09, & for \quad \omega > \omega_p \end{cases} \tag{3.43}$$

The parameter $\tilde{\alpha}$ is defined as:

$$\tilde{\alpha} = 3.25 \cdot 10^-3 H_s^2 \omega_p^4 (1 - 0.287 \ln\gamma) \tag{3.44}$$

It can now be readily seen that the JONSWAP spectrum is a two parameter wave spectrum dependent on the wave height, H_s, and the peak wave frequency, ω_p. Note that increasing the value of γ generates a more narrow spectrum. An illustration of the JONSWAP spectrum can be seen in figure 3.6.

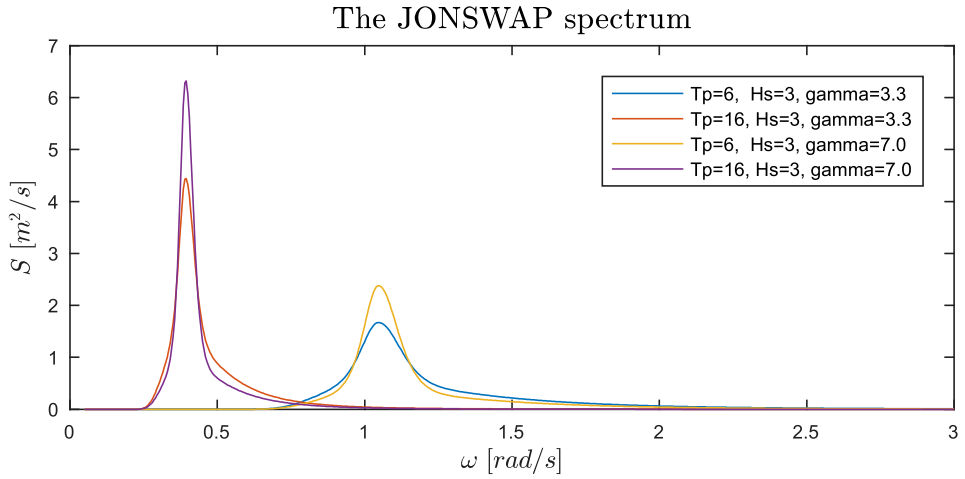

Figure 3.6: The JONSWAP-spectrum. Note that no waves of period 16 s with wave height 3 m are expected for Bjørnafjorden, but has been selected in this figure for illustration purposes.

The directional distribution function

The directional function $D(\omega, \theta)$ is frequency and directional dependent, but it is common to introduce the approximation that the frequency dependence is neglected. Thus, $D(\omega, \theta) = D(\theta)$.

The directional dependence is commonly represented by the power of a cosine function (Kvåle et al., 2016, 3.3).

$$D(\theta) = C\, cos^{2s}(\theta - \theta_0) \tag{3.45}$$

s represents the crest length of the wave, also denoted as the spreading parameter, θ_0 is the angle of the mean wave direction and θ is the angle of the wave direction within the region of validity, $-\pi/2 < \theta - \theta_0 < \pi/2$ for the wave directional function. The constant, C, ensures that $\int D(\theta)d\theta = 1$.

By varying the spreading parameter, s, the different directions the waves approaches from can be controlled. A big s implies that there is a small variation of the direction of the waves, while a small s implies that a large variation of the direction of the waves is experienced. See figure 3.7 for an illustration of the directional function with varying s.

The directional distribution function can also be written in the form $C\, cos^{n}(\theta - \theta_0)$, as done in the NPRA report, where the relation between the two forms simply is 2s=n.

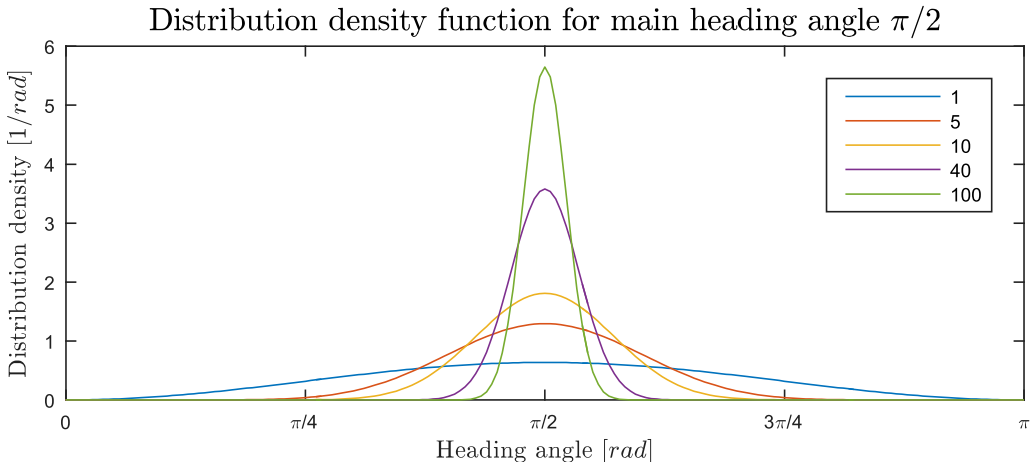

Figure 3.7: The directional spreading function plotted for different values of the spreading parameter s.

Considered wave types in this thesis

While wind waves are generated and sustained by the wind above the water surface, swell waves, are the result of distant weather systems and are no longer under the influence of the forces that created them. Swell waves usually have a low wave height, compared to the wave height of wind waves. The period of swell waves may be very long compared to typical periods for wind waves. Swell waves may be present simultaneously with locally generated waves, (Naess and Moan, 2013, Ch.8.2).

An incident wave is the first occurrence of a wave. A scattered wave is a wave which has changed its original direction after it passed through an opening or passed by a barrier in its path.

3.3.3 Hydrodynamics and hydrostatics

The hydrodynamic and -static problem can be split into two sub-problems for simplicity, (Faltinsen, 1990, Ch.3,p.39):

1. The forces and moments that occurs on the body when the structure is restrained from oscillating while regular incident waves are present. These hydrodynamic loads are called wave-excitation loads. This sub-problem is also known as the diffraction problem. Note that in this thesis the term scattering denotes the forces due to waves that are reflected by a fixed structure and diffraction denotes the sum of forces due to incident waves and scattered waves experienced by the structure. This terminology is applied in the WAMIT theory manual.

2. The forces and moments that occurs on the body when the structure is forced to have a rigid body oscillation with the same frequency as the wave excitation frequency. In this sub-problem there are no incident waves present and these hydrodynamic loads are defined as added mass, damping and restoring terms. Another terminology for these forces are radiation and restoring forces.

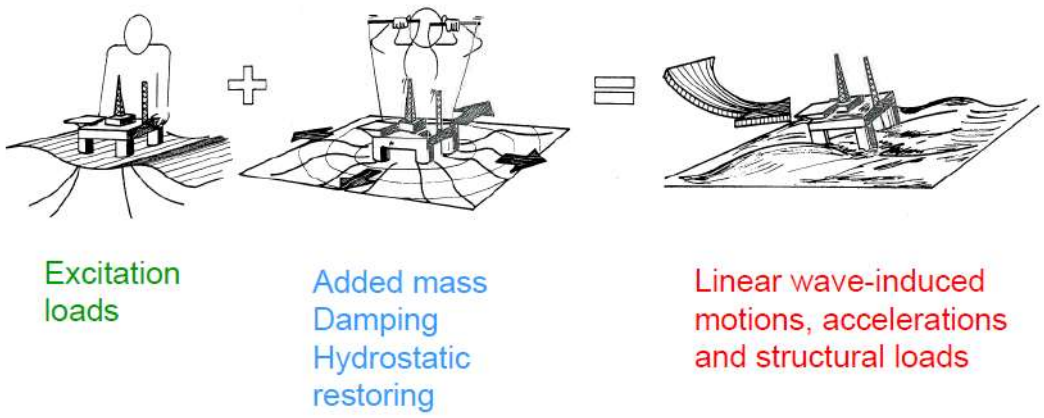

Figure 3.8: The decomposition of the hydrodynamic problem, (Faltinsen, 1990, Fig.3.1)

In figure 3.8 on the left side are the wave excitation loads acting on the submerged structure due to incident waves illustrated. In the centre of figure 3.8 are the forces acting on the submerged structure due to rigid body oscillation of the structure pictured. Together these two sub-problems add up to the total hydrodynamic load acting on the submerged structure.

3.3.4 A description of the problem by a utilization of a velocity potential

The hydrodynamic loading can be expressed by combining potential theory and Bernoulli's equation. The sea water is assumed to be incompressible and inviscid. The motion of the fluid is also assumed to be irrotational. The mentioned assumptions implies that the velocity of the fluid can be described by a velocity potential (Faltinsen, 1990, Ch.1,p.13). The velocity potential in expanded form is written as follows (Lee, 1995, Ch.1.1) .

$$\phi(x,y,z,t) = \phi^{(1)}(x,y,z,t) + \phi^{(2)}(x,y,z,t) + ... \tag{3.46}$$

Where $\phi^{(1)}(x,y,z,t)$ denotes the total first order potential and $\phi^{(2)}(x,y,z,t)$ denotes the total second order potential.

The Laplace equation in the fluid domain

A property of the velocity potential due to the incompressible flow assumption is that it satisfies the Laplace equation in the fluid domain.

$$\boldsymbol{\nabla}^2\boldsymbol{\phi} = 0 \tag{3.47}$$

Where

$$\boldsymbol{\nabla}\boldsymbol{\phi} = \frac{\partial\phi}{\partial x}\mathbf{i} + \frac{\partial\phi}{\partial y}\mathbf{j} + \frac{\partial\phi}{\partial z}\mathbf{k} \tag{3.48}$$

And $\mathbf{i}$, $\mathbf{j}$ and $\mathbf{k}$ are unit vectors in the Cartesian coordinate system, and the coordinates are given relative to a reference origin at still water level.

The boundary conditions of the velocity potential are imposed at the seabed, the body surface and at the free surface, (Roald et al., 2014, 2.2.1). The seabed condition is that the velocity potential converges to zero for an infinite water depth, z.

$$\boldsymbol{\nabla}\boldsymbol{\phi} \rightarrow 0, z \rightarrow \infty \tag{3.49}$$

The body surface condition states that the relative velocity of the boundary between the submerged body and the fluid is zero when the body is moving with a velocity, $\mathbf{U}$ and $\mathbf{n}$ is the normal vector belonging to the body.

$$\frac{\partial\boldsymbol{\phi}_{\boldsymbol{n}}}{\partial\bar{n}} = \mathbf{U}\cdot\mathbf{n} \tag{3.50}$$

There are two boundary conditions that apply to the free surface. The first is the kinematic condition, which states that a particle on the free surface has to have the same vertical velocity as the free surface itself, (Faltinsen, 1990).

$$\frac{\partial\boldsymbol{\eta}}{\partial t} + \frac{\partial\boldsymbol{\phi}}{\partial x}\frac{\partial\eta}{\partial x} + \frac{\partial\boldsymbol{\phi}}{\partial y}\frac{\partial\eta}{\partial y} + \frac{\partial\boldsymbol{\phi}}{\partial z}\frac{\partial\eta}{\partial z} - \frac{\partial\boldsymbol{\phi}}{\partial z} = 0 \quad \text{at the free surface } z = \eta \tag{3.51}$$

The second free surface condition is the dynamic condition, which states that the pressure on the fluid surface has to equal the air pressure, (Roald et al., 2014, Ch.2.2.1).

$$\frac{1}{2}\nabla\boldsymbol{\phi}\cdot\nabla\boldsymbol{\phi} + \frac{\partial\boldsymbol{\phi_n}}{\partial t} + g\eta, \quad \text{at the free surface } z = \eta \tag{3.52}$$

The last condition is the radiation condition. The radiation problem states that all waves that are present, except incident waves, have to be created by the body itself, thus, the waves have to propagate away from the body (Roald et al., 2014, Ch.2.2.1). The velocity potential is directly proportional to the right side of the equation below.

$$\boldsymbol{\phi} \propto R^{-1/2}e^{-i\kappa r} \qquad R = \sqrt{x^2+y^2} \to \infty \tag{3.53}$$

Where κ is the wave number.

The total first order velocity potential

The total first order potential for the wave-body interaction can be expressed by the sum of the real parts of the components having a circular frequency $\omega_j > 0$, (Lee, 1995, Ch.2).

$$\phi^{(1)}(x,y,z,t) = Re\sum_j \phi_j(x,y,z,)e^{i\omega_j t} \tag{3.54}$$

$\phi_j(x,y,z,)$ is the complex velocity potential, which is independent of time. The complex velocity potential is in this case related to incident waves with a frequency of ω_j and a heading angle θ_j.

The first order velocity potential can be described as a sum of the first order incident wave potential, ϕ_I, the first order scattering potential, ϕ_S, and the first order radiation potential, ϕ_R.

$$\phi^{(1)} = \phi_I + \phi_S + \phi_R = \phi_D + \phi_R \tag{3.55}$$

Where ϕ_D is the diffraction potential equal to the sum of ϕ_I and ϕ_S. The radiation potential is related to the rigid body, oscillatory motion.

The total second order velocity potential

The total second order potential for the wave-body interaction can be expressed as follows (Lee, 1995, Ch.3).

$$\phi^{(2)}(x,y,z,t) = Re\sum_i\sum_j \phi_{ij}^{+}(x,y,z,)e^{i(\omega_i+\omega_j)t} + \phi_{ij}^{-}(x,y,z,)e^{i(\omega_i-\omega_j)t} \tag{3.56}$$

Where $\phi_{ij}^{+}(x,y,z,)$ and $\phi_{ij}^{-}(x,y,z,)$ are the sum and difference potentials, respectively. j and i refers to two incident waves with wave frequencies ω_j and ω_i and heading angles θ_j and θ_i.

Analogously as with the first order velocity potential, the second order velocity potential can be written as a sum of the second order incident wave potential, $\phi_I^{\pm}$, the second order scattering potential, $\phi_S^{\pm}$, and the second order radiation potential, $\phi_R^{\pm}$.

$$\phi^{(2)} = \phi_I^{\pm} + \phi_S^{\pm} + \phi_R^{\pm} = \phi_D^{\pm} + \phi_R^{\pm} \tag{3.57}$$

3.3.5 Fundamentals of the hydrostatic and -dynamic forces and moments

In general, the nonlinear hydrodynamic and hydrostatic forces and moments (both first and second order) can be found by pressure integration, which is to integrate the pressure over the instantaneous wetted surface. It is noted that the "hat" denotes instantaneous and that the velocity potential and the body motion are functions of time (Lee, 1995, Ch.4.1.3), which is why the instantaneous submerged body, $\hat{S}_B(t)$, is a function of time. This is denoted as a direct method.

$$\mathbf{F} = \int\int_{\hat{S}_B(t)} P(\hat{\mathbf{x}})\hat{\mathbf{n}}dS \quad \mathbf{M} = \int\int_{\hat{S}_B(t)} P(\hat{\mathbf{x}})(\hat{\mathbf{x}} \times \hat{\mathbf{n}})dS \tag{3.58}$$

In the above equation is $\hat{\mathbf{x}}$ a fixed coordinate system in space which coincides with the body-fixed coordinate system $\mathbf{x}$ at rest, $\mathbf{F}$ and $\mathbf{M}$ are the hydro-static and -dynamic forces and moments, respectively, and $\mathbf{P}(\hat{\mathbf{x}})$ is the pressure given by Bernoulli's equation at $\hat{\mathbf{x}}$, see equaiton 3.59 below. $\hat{\mathbf{n}}$ is the instantaneous unit normal vector. $\boldsymbol{\alpha} = (\alpha_1, \alpha_2, \alpha_3)$ and $\boldsymbol{\xi} = (\xi_1, \xi_2, \xi_3)$ are the rotational and translational displacements of $\mathbf{x}$.

$$\mathbf{P}(\hat{\mathbf{x}}) = -\rho[\boldsymbol{\phi}_t(\hat{\mathbf{x}}) + \frac{1}{2}\boldsymbol{\nabla}\boldsymbol{\phi}(\hat{\mathbf{x}}) \cdot \boldsymbol{\nabla}\boldsymbol{\phi}(\hat{\mathbf{x}}) + g(\hat{z} + Z_0)] \tag{3.59}$$

Where Z_0 denotes the Z-coordinate of the origin of $\hat{\mathbf{x}}$ and $\boldsymbol{\phi}_t = \frac{\partial \boldsymbol{\phi}}{\partial t}$.

The relation between the instantaneous coordinate system and the coordinate system at rest and the respective normal vectors, $\hat{\mathbf{x}}$, $\mathbf{x}$, $\hat{\mathbf{n}}$ and $\mathbf{n}$, is expressed as a linear transformation given in the equations below (Lee, 1995, 4.1.2).

$$\hat{\mathbf{x}} = \boldsymbol{\xi} + T^T\mathbf{x} \tag{3.60}$$

$$\hat{\mathbf{n}} = T^T\mathbf{n} \tag{3.61}$$

T^T is the transpose of $T = T_3T_2T_1$.

$$T_1 = \begin{bmatrix} 1 & 0 & 0 \\ 0 & cos\alpha_1 & sin\alpha_1 \\ 0 & -sin\alpha_1 & cos\alpha_1 \end{bmatrix}, \qquad T_2 = \begin{bmatrix} cos\alpha_2 & 0 & sin\alpha_2 \\ 0 & 1 & 0 \\ -sin\alpha_2 & 0 & cos\alpha_2 \end{bmatrix} \tag{3.62}$$

$$T_3 = \begin{bmatrix} cos\alpha_3 & sin\alpha_3 & 0 \\ -sin\alpha_3 & cos\alpha_3 & 0 \\ 0 & 0 & 1 \end{bmatrix} \tag{3.63}$$

To express the pressure in terms of potential theory, the following need to be considered.

The pressure on the exact instantaneous wetted body surface can be expressed by a Taylor expansion with respect to the mean wetted body surface. The pressure approximated by the mean wetted surface is given as follows, see (Lee, 1995, Ch.4.1.3) for the derivation. Thus, potential theory is valid.

$$\begin{aligned} \mathbf{P}(\hat{\mathbf{x}}) = & -\rho\{g(z+Z_0) + [\boldsymbol{\phi_t}^{(1)}(\mathbf{x}) + g(\xi_3^(1) + \alpha_1^{(1)}y - \alpha_2^{(1)}x)] \\ & + [\frac{1}{2}\boldsymbol{\nabla\phi^{(1)}}(\mathbf{x}) \cdot \boldsymbol{\nabla\phi^{(1)}}(\mathbf{x}) + (\boldsymbol{\xi}^{(1)} + \boldsymbol{\alpha}^{(1)} \times \mathbf{x}) \cdot \boldsymbol{\nabla\phi_t^{(1)}}(\mathbf{x}) + g\mathbf{H}\mathbf{x} \cdot \nabla z] \\ & + [\boldsymbol{\phi_t^{(2)}}(\mathbf{x}) + g(\xi_3^{(2)} + \alpha_1^{(2)}y - \alpha_2^{(2)}x)]\} + O(\mathrm{A}^3) \end{aligned} \tag{3.64}$$

Where $\mathbf{H}$ is the second order component of T^t and A^3 is the complex wave amplitude of order 3.

$$\mathbf{H} = \begin{bmatrix} -\frac{1}{2}((\alpha_2^{(1)})^2 + (\alpha_3^{(1)})^2) & 0 & 0 \\ \alpha_1^{(1)}\alpha_2^{(1)} & -\frac{1}{2}((\alpha_1^{(1)})^2 + (\alpha_3^{(1)})^2) & 0 \\ \alpha_1^{(1)}\alpha_3^{(1)} & \alpha_2^{(1)}\alpha_3^{(1)} & -\frac{1}{2}((\alpha_1^{(1)})^2 + (\alpha_2^{(1)})^2) \end{bmatrix} \tag{3.65}$$

3.3.6 First order wave forces

The linear first order forces can be decomposed into wave excitation forces, radiation forces and restoring forces. They are denoted as follows.

Wave (Haskind) excitation forces

The wave excitation force, $F_{exc,k}$, here expressed for excitation mode k (the force's direction of rotation or translation), can be found by utilizing Haskind's relation, which is expressed as follows, (Lee, 1995, Ch.4.1.7).

$$F_{exc,k} = -i\omega\rho \int\int_{S_B} (n_k\phi_I - \frac{\partial\phi_I}{\partial n}\phi_{R,k})dS \tag{3.66}$$

n is the normal vector, $\frac{\partial}{\partial n}$ is the normal derivative, ρ is the density of the fluid, ω is the wave frequency and S_B is the wetted mean body surface.

It is common to write the excitation force in terms of force coefficients that is the transfer function for the wave excitation loads, (Roald et al., 2014). Here written for irregular seas, where the irregular sea surface is described as a sum of regular waves. $X_{k,m} = Q^{(1)}_{k,m}$ is the first order transfer function.

$$F_{exc,k} = Re(\sum_m A_m X_{k,m} e^{i\omega_m t}) \tag{3.67}$$

Where m denotes the n^{th} regular wave, $X_{m,k}$ is the force coefficient in direction k and for wave m, A_m is the complex amplitude for the n^{th} regular wave.

Wave radiation forces

The wave radiation forces are related to the added mass and damping terms for the case of no incident waves and exposure of forced harmonic rigid-body oscillations of the submerged structure in a fluid. These forced motions generate outgoing forces (waves) in the fluid, on for equilibrium to be preserved, these forces also acts on the structure. These forces can be denoted as follows (Greco, 2016).

$$F_{rad,k} = -\int_{S_B} \rho \frac{\partial \phi_R}{\partial t} dS \tag{3.68}$$

Where k is related to the direction of the force. Formally the added mass and damping terms can be written as follows, (Faltinsen, 1990, Ch.3,p.41).

$$F_{rad,k} = -A_{kj} \frac{d^2 \xi_j}{dt^2} - B_{kj} \frac{d\xi_j}{dt} \tag{3.69}$$

Where ξ is a translatory or rotational displacement, j is related to the excitation mode (direction of the motion) and A_{kj} and B_{kj} are the added mass and damping coefficients, respectively. η_j is related to the motion of the oscillating body in excitation mode j.

The coefficients, A_{kj} and B_{kj}, can be derived using potential theory and are expressed as the following according to (Greco, 2016).

$$A_{kj} = Re(\rho \int_{S_B} \phi_j n_k dS), \qquad B_{kj} = -\omega Im(\rho \int_{S_B} \phi_j n_k dS) \tag{3.70}$$

The coefficients, A_{kj} and B_{kj}, are denoted as the added-mass and damping terms, respectively.

Restoring forces

The static restoring forces related to the equation of motion for a freely floating body can be written as follows (Faltinsen, 1990, Ch.3, p.58)

$$F_{s,k} = -C_{kj}\xi_j \tag{3.71}$$

The term C_{kj} is independent of the velocity potential and may be derived using hydrostatics. Index s denotes static.

In the following is the hydrostatic coefficients derived.

The distance from the centre of buoyancy to the metacentre is given as follows (Kemp, 2001).

$$\overline{BM} = \frac{S_{ii}}{V_w} \tag{3.72}$$

Where S_{ii} is the second moment area of the water plane about the axis i and V_w is the volume of the submerged body. The distance from the centre of gravity to the metacentre is then

$$\overline{GM} = (z_B - z_G) + \overline{BM} \tag{3.73}$$

Where z_B and z_G is the the z-coordinate of the centre of buoyancy and the centre of gravity of the body. All non-zero restoring coefficients C_{kj}, for a submerged body where the water plane area S_0 is symmetric about the x-z and the x-y, plane are given by the following expressions (Faltinsen, 1990, Ch.3 p.58).

$$\begin{aligned}
C_{33} &= \rho g S_0 \\
C_{44} &= \rho g V_w (z_B - z_G) + \rho g \iint_{S_0} y^2 \, ds = \rho g V_w \overline{GM}_T \\
C_{55} &= \rho g V_w (z_B - z_G) + \rho g \iint_{S_0} x^2 \, ds = \rho g V_w \overline{GM}_L
\end{aligned} \tag{3.74}$$

If the distance from the centre of gravity to the metacenter is negative, the restoring coefficients C_{44} and C_{55} becomes negative, which indicate that the system is unstable. If the mass of the submerged body is unequal to the mass of the displaced volume, the equations must be modified as given in the WADAM user manual (DNVGL, 2014b, B1.1).

$$\begin{aligned}
C_{33} &= \rho g S_0 \\
C_{44} &= \rho g (S_{yy} + V_w z_B) - m g z_G \\
C_{55} &= \rho g (S_{xx} + V_w z_B) - m g z_G
\end{aligned} \tag{3.75}$$

The first order forces in the EOM

By superposing the first order forces of the hydrodynamic loading, the total first order hydrodynamic loading in the frequency domain, $\mathbf{F}^{(1)}_{tot}(\omega)$, can be denoted as the following, (Kvåle et al., 2016).

$$\mathbf{F}_{tot}^{(1)}(\omega) = \mathbf{F}_{exc}^{(1)}(\omega) - (-\omega^2\mathbf{M}_h(\omega) + i\omega\mathbf{C}_h(\omega) + \mathbf{K}_h)d\mathbf{Z}_r(\omega) \tag{3.76}$$

$\mathbf{F}_{exc}^{(1)}(\omega)$, is the wave excitation forces, $d\mathbf{Z}_r(\omega)$ is the spectral process of the response vector, $r(t)$, and the coefficients,A_{kj}, B_{kj} and C_{kj} of the matrices, $\mathbf{M}_h(\omega)$, $\mathbf{C}_h(\omega)$ and $\mathbf{K}_h(\omega)$, respectively, are from equations 3.70 and 3.75.

Spectrum of the first order wave excitation forces

The hydrodynamic load cross-spectral density due to wave excitation forces acting on a submerged body, between the two points r and s, can be expressed as follows, (Kvåle et al., 2016).

$$\mathbf{S}_{p_r p_s}^{(1)}(\omega) = \int_\theta \mathbf{Q}_r^{(1)}(\omega,\theta) S_{\eta_r\eta_s}(\omega,\theta) \mathbf{Q}_s^{(1)}(\omega,\theta)^H d\theta \tag{3.77}$$

Where $\mathbf{Q}_r^{(1)}(\omega,\theta)$ and $\mathbf{Q}_s^{(1)}(\omega,\theta)$ are the directional first order wave exciting transfer functions for the points r and s, respectively. H represents the Hermitian operator.

3.3.7 Second order wave forces

There is not much energy present in the ocean at low frequencies. In other words, the low frequency wave excitation based on linear theory is small and non-linear wave-structure interaction theory has to be utilized to capture the slowly-varying responses of a floating structure in the ocean (Chryssostomidis and Liu, 2011). This is known as second order slow drift forces. The other non-linear effect is called springing and operates at typically higher frequencies, (Naess and Moan, 2013, 11.3.2).

The amplitude of the first order waves are considerably bigger than the amplitude of the second order waves, but the second order waves could excite at resonant frequencies and induce considerable responses and should thus be considered (Naess and Moan, 2013, Ch.7.2.2).

The sum and difference frequencies

The sum and difference frequency forces are second order effects. The contribution from a given pair of waves is either in the range of the frequency equal to the sum or the difference of the frequencies of the waves in the pair. A wave component paired with itself gives either a contribution with a frequency equal to 0 or twice the frequency that component has. This is illustrated in 3.9.

It can be seen from figure 3.9 that the slowly varying forces, also known as second order wave drift forces or difference frequency forces, are related to the difference frequency part of the second order load spectra. The rapidly changing forces are related to the sum frequency part of of the wave loading spectrum and are referred to as springing forces or sum frequency forces.

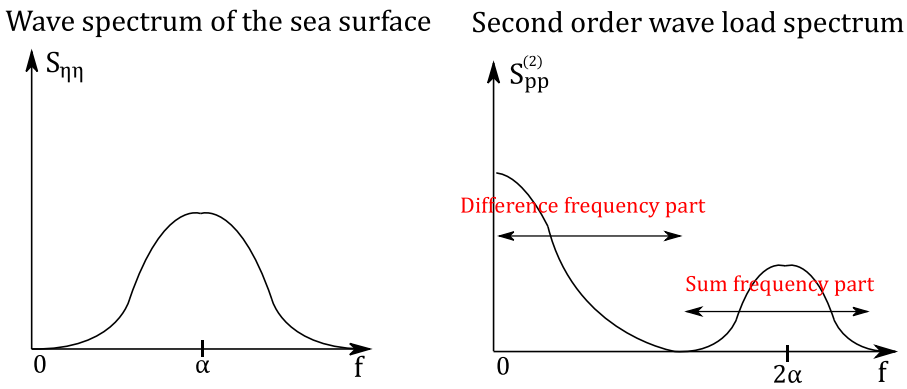

Figure 3.9: The figure shows how the sea surface is represented as a second order wave loading.

Non-linear wave forces

The non-linear second order forces and moments from the diffraction problem are defined as follows. Only the second order forces are expressed in detail here. The second order moments takes an identical form and can be found in (Lee, 1995). Note that the following expressions do not include second order forces from radiation (Roald et al., 2014).

$$\mathbf{F}_{exc}^{(2)} = \mathbf{F}_{p}^{(2)} + \mathbf{F}_{q}^{(2)} \tag{3.78}$$

$$\mathbf{M}_{exc}^{(2)} = \mathbf{M}_{p}^{(2)} + \mathbf{M}_{q}^{(2)} \tag{3.79}$$

Where $\mathbf{F}_{exc}^{(2)}$ is the second order wave excitation forces of the diffraction problem, $\mathbf{F}_{p}^{(2)}$ denotes the second order potential and $F_{q}^{(2)}$, is the quadratic interaction of the first order solution. $\mathbf{F}_{q}^{(2)}$ can be written as, (Lee, 1995, 4.1.6).

$$\begin{aligned}\mathbf{F}_{q}^{(2)} =& \frac{1}{2}\rho g \int_{wl} [\eta^{(1)} - (\xi_3^{(1)} + \alpha_1^{(1)} y - \alpha_2^{(1)} x)]^2 \sqrt{1 - n_z^2}\mathbf{n} dl \\ &- \rho \int\int_{S_B} [\frac{1}{2}\boldsymbol{\nabla}\boldsymbol{\phi}^{(1)} \cdot \boldsymbol{\nabla}\boldsymbol{\phi}^{(1)} + (\boldsymbol{\xi}^{(1)} + \boldsymbol{\alpha}^{(1)} \times \mathbf{x}) \cdot \boldsymbol{\nabla}\boldsymbol{\phi}_t^{(1)}]\mathbf{n} dS \\ &+ \boldsymbol{\alpha}^{(1)} \times F^{(1)} - \rho g A_{wp}[\alpha_1^{(1)}\alpha_3^{(1)} x_f + \alpha_2^{(1)}\alpha_3^{(1)} y_f + \frac{1}{2}((\alpha_1^{(1)})^2 + (\alpha_2^{(1)})^2) Z_0]\mathbf{k}\end{aligned} \tag{3.80}$$

Where wp is the water plane, wl is a line integral along the waterline and $\mathbf{k}$ is a unit vector.

The quadratic second order wave transfer function for the sum and difference frequencies for the second order potential read as the following when imposing Green's theorem at $\phi_S^{\pm}$ and $\phi_R^{\pm}$ and invoking Newman's approximation, (Lee, 1995, Ch.4.1.9). The second order force in the equation below is the indirect second order force as it is calculated indirectly based on the first order velocity potential.

$$F_{pk}^{(2)\pm} = -i(\omega_m \pm \omega_n)\rho[\int\int_{S_F} Q_B^{\pm}\phi_{R,k}^{\pm}dS + \frac{1}{g}\int\int_{S_F}(Q_{IB}^{\pm} + Q_{BB}^{\pm})\phi_{R,k}^{\pm}dS \tag{3.81}$$

Where p denotes potential, k represents force in the direction k and S_F denotes the inner domain of the free surface. $F_{pk}^{\pm}$ is a spectral component of the second-order potential force $F_p^{(2)}$.

$$\begin{aligned} Q_{II}^{\pm} &= -(\omega_m \pm \omega_n)^2\phi_I^{\pm} + g\frac{\partial\phi_S^{\pm}}{\partial z}, \quad z = 0 \\ Q_{IB}^{\pm} + Q_{BB}^{\pm} &= -(\omega_m \pm \omega_n)^2\phi_S^{\pm} + g\frac{\partial\phi_S^{\pm}}{\partial z}, \quad z = 0 \\ Q_B^{\pm} &= \frac{\phi_S^{\pm}}{\partial n} \end{aligned} \tag{3.82}$$

An analogous way to write equation 3.78 is to adopt the formulation in the equation for the second order velocity potential in equation 3.56.

$$\mathbf{F}_{exc}^{(2)} = Re\sum_m\sum_n \mathbf{F}_{mn}^{(2)+}\exp(i(\omega_m + \omega_n)t) + \mathbf{F}_{mn}^{(2)-}\exp(i(\omega_m - \omega_n)t) \tag{3.83}$$

Here m and k refers to two waves with frequency m and k corresponding wave heading angle m and k, respectively. $\mathbf{F}_{exc}^{(2)}$ is second order forces and contains the second order force coefficients. The exponent plus refers to sum frequencies, and the exponent minus refers to difference frequencies. It can be seen that the second order forces are comprised of second order difference forces and second order sum forces.

Another way to write 3.83 is to write it in time domain in terms of the incident wave amplitudes, A_m and A_n, and a force coefficient, $X_{mn}^{\pm} = X_{q,mn}^{\pm} + X_{p,mn}^{\pm}$, (Roald et al., 2014, 2.4).

$$\mathbf{F}_{exc}^{(2)}(t) = Re\sum_{m=1}\sum_{n=1} A_mA_nX_{mn}^{+}\exp(i(\omega_m + \omega_n)t) + A_mA_nX_{mn}^{-}\exp(i(\omega_m - \omega_n)t) \tag{3.84}$$

The force coefficient may also be denoted as the quadratic second order transfer function, $X_{mn}^{\pm} = Q_{mn}^{(2)\pm}$. It can be found by setting the incident wave amplitudes to an unit amplitude of one. The quadratic transfer function is used to obtain the second order load spectra.

Spectrum of the second order drift forces

The drift force spectrum in equation 3.85 are derived by Pinkster, (Pinkster, 1988).

$$S_{p_rp_s}^{(2)}(\mu) = 8\int_0^{\infty}\int_0^{2\pi}\int_0^{2\pi} S_{\eta_r\eta_s}(\omega+\mu,\theta_1)\, S_{\eta_r\eta_s}(\omega,\theta_2)\, |Q_{rs}^{(2)}(\omega+\mu,\omega,\theta_1,\theta_2)|^2\, d\theta_1\, d\theta_2\, d\omega \tag{3.85}$$

Where $Q_{rs}^{(2)}(\omega+\mu,\omega,\theta_1,\theta_2)$ is the second order quadratic transfer function, ω and μ are frequencies and θ_1 and θ_2 are the wave directions. The effect of summing or subtracting two frequencies is evident in the spectra in figure 3.9.

3.4 Probability theory

3.4.1 Mean and standard deviation

For a random discrete variable X, with probability p_i at the discrete value x_i, the mean value and standard deviation can be found from the following equations

$$\mu = \sum_{i=1}^{N} x_i p_i \qquad \sigma = \sqrt{\sum_{i=1}^{N} p_i (x_i - \mu)^2} \tag{3.86}$$

For a continuous probability distribution $f(x)$, an integral over the domain of the random variable X is required.

$$\mu = \int_X x f(x) dx \qquad \sigma = \sqrt{\int_X x (f(x) - \mu)^2} \tag{3.87}$$

The variance is defined as

$$\text{VAR} = \sigma^2 \tag{3.88}$$

The cumulative distribution function $F(x)$ for a continuous probability function $f(x)$ is given by the following equation (Walpole et al., 2012, 3.2)

$$F(x) = \int_{-\infty}^{x} f(t)\, dt \tag{3.89}$$

By dividing the domain x, of a continuous probability distribution $f(x)$, into different ranges, the discrete probability of the event occuring within a given range can be found from integration.

$$p(x_i < x < x_{i+1}) = \int_{x_i}^{x_{i+1}} f(x)\, dx \tag{3.90}$$

$$p(x_i < x < x_{i+1}, y_i < y < y_{i+1}) = \int_{x_i}^{x_{i+1}} \int_{y_i}^{y_{i+1}} f(x,y)\, dx\, dy$$

Chapter 4

Method

4.1 Motion induced instability

The theory about the detection of motion induced instability is outlined in section 3.2.3. As a basis for the flutter analysis, a linear elastic frequency analysis was performed in ABAQUS. The resulting modal mass and modal stiffness were extracted from the ABAQUS report, in addition to the first 150 eigenmodes of the girder and the top cable. The reason for choosing 150 eigenmodes was to ensure that several of the torsional modes were included in the analysis, as a torsional mode is expected to be critical when flutter occurs.

4.1.1 The general procedure

The algorithm deployed in MATLAB to detect motion induced instability is depicted in figure 4.1. It describes the input values and the steps that are required to be carried out to obtain the critical velocity U_{Cr} that yields flutter and the corresponding critical frequency, ω_{Cr}. What is not described in the flowchart, is the procedure about how to obtain the mode which induces fluttering and the fluttering mode shape. This is described later in section 4.1.2.

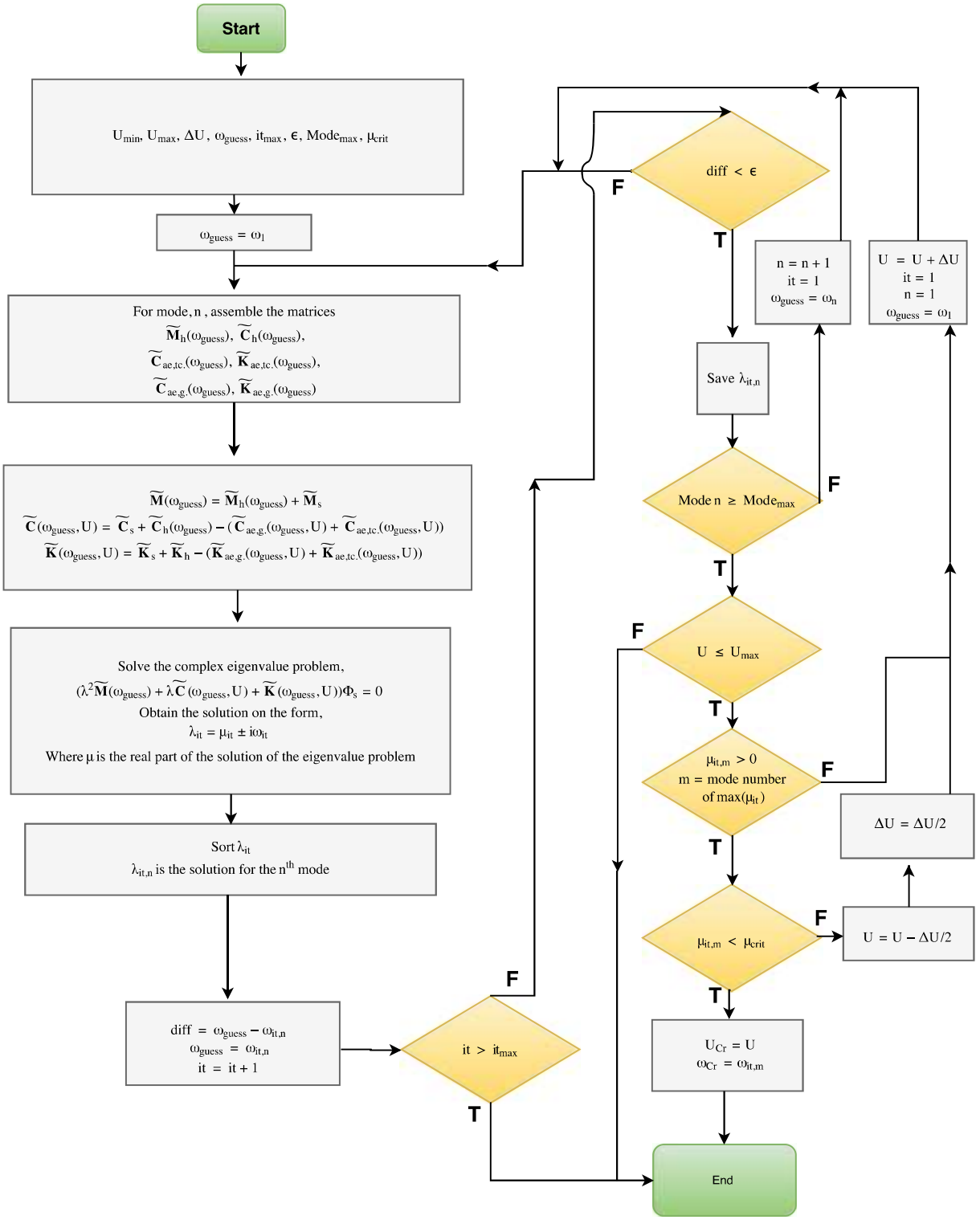

Figure 4.1: The flow chart shows how the algorithm used to find the critical velocity for motion induced instability works. The indices, tc and g, denotes that the respective properties are estimated for the top cable and the girder.

The procedure, shown in the flowchart in figure 4.1, can be described as follows. For every wind velocity, the solution of the complex eigenvalue problem, for every mode, n, is to be obtained. This is done by iteration, with a criterion of convergence $|\omega_{guess} - \omega_{it,n}| < \epsilon$, where $\omega_{it,n}$ is the imaginary part obtained from solving the complex eigenvalue problem, and ω_{guess} is the frequency used to find the frequency dependent properties of $\mathbf{M}$, $\mathbf{C}$ and $\mathbf{K}$. ω_{guess} is set to equal $\omega_{it,n}$ after each iteration until convergence has been reached.

When the real part of any mode, μ_{it} becomes larger than 0, the damping of this mode becomes negative, and flutter is induced. The required mean wind velocity for μ_{crit} to become positive, is the critical mean wind velocity. Until this velocity is reached the procedure is repeated for increasing wind velocities, with a step size equal to dU.

When the solution of the complex eigenvalue problem for any mode yields a positive real part, the step size of the wind velocity is refined to acquire the solution of the complex eigenvalue problem with an error less than μ_{crit}.

The modalized matrices, $\widetilde{\mathbf{K}}(\omega_{guess}, U)$, $\widetilde{\mathbf{C}}(\omega_{guess}, U)$ and $\widetilde{\mathbf{M}}(\omega_{guess})$, are obtained using still air eigenmodes, and adjusted for their frequency and velocity dependent properties.

The aerodynamic stiffness matrices of the top cable were estimated based on the drag coefficient and quasi-static theory. The aerodynamic stiffness matrix of the girder is established by experimental data of the Hardanger bridge, by equation 3.27. The hydrodynamic added mass and damping used in the instability analysis are calculated by interpolation of results obtained from HydroD, as the results from HydroD is given for selected frequencies only, which does not necessarily correspond to the frequency of the current iteration.

The coefficients used in both the instability analyses and the buffeting analyses are given in table 4.1 and table 4.2.

Quasi-static aerodynamic coefficients of the bridge girder from the NPRA-reports			
Quasi-static coefficients	$[-]$	Quasi-static coefficients	$[1/rad]$
C_D	0.610	$dC_D/d\alpha$	0.000
C_L	-0.030	$dC_L/d\alpha$	1.800
C_M	-0.028	$dC_M/d\alpha$	0.650
Quasi-static aerodynamic coefficients of the top cables from the NPRA-reports			
Quasi-static coefficients	$[-]$	Quasi-static coefficients	$[1/rad]$
C_D	0.800	$dC_D/d\alpha$	0.000
C_L	0.000	$dC_L/d\alpha$	0.000
C_M	0.000	$dC_M/d\alpha$	0.000
Quasi-static aerodynamic coefficients of the pylons from the NPRA-reports			
Quasi-static coefficients	$[-]$	Quasi-static coefficients	$[1/rad]$
C_D	1.600	$dC_D/d\alpha$	0.000
C_L	0.000	$dC_L/d\alpha$	0.000
C_M	0.000	$dC_M/d\alpha$	0.000

Table 4.1: The table shows the quasi-static ADs from the NPRA-reports, (NPRA, 2016a, 3.2) and (NPRA, 2016r, 6.1). α is the angle of attack and is given in radians.

	Free vibration			Forced oscillation		
$\boldsymbol{a}_1$	0	0	-0.1432	0.0056	-0.0076	-0.0243
	0	0	2.4000	-0.0592	0.0284	3.3494
	0	0	0.7400	-0.0090	0.0025	1.0562
$\boldsymbol{a}_2$	1.1706	0.6010	0.4145	-0.3760	-0.1482	-0.1678
	-8.1415	2.1530	0.2121	0.7468	-0.9188	0.7209
	1.8010	-1.3929	0.3496	-0.0825	-0.7223	0.1220
$\boldsymbol{a}_4$	0.2573	-0.1416	0.0461	-0.0205	0.0017	-0.0342
	-1.1213	0.0631	-0.3090	-0.0155	0.0204	-0.0137
	-0.1448	-0.2701	-0.0030	0.0012	-0.0187	-0.0464
$\boldsymbol{a}_5$	-7.2733	-1.9074	-1.8798	0.0954	-0.0913	0.0998
	40.5199	-17.4432	1.7870	0.0859	-2.0255	-1.0318
	-5.3886	4.5938	-1.8816	0.0703	-0.1367	-0.4566
d_1			0.4375			0.1000
d_2			3.6164			0.7920

Table 4.2: The table shows the empirical parameters used in equation 3.28, found by by wind tunnel testing of the cross section of the Hardanger bridge. Coefficients are obtained from (Siedziako et al., 2017, p. 158).

The empirical aerodynamic derivatives are determined from wind tunnel tests of the cross section of the Hardanger bridge, as more accurate data was unavailable, and the cross section shape of the Hardanger bridge is quite similar to the suggested cross section of the Bjørnafjorden bridge.

As coefficients from the NPRA-reports are given for a left-handed coordinate system, and the expressions for the aerodynamic stiffness and damping by a right-hand system, some transformation between axis systems had to be performed to keep all input in the same format.

The sorting algorithm

The aerodynamic stiffness and damping matrices are dependent on the wind velocity, consequently, the eigenfrequencies of the system vary with the wind velocity. As the aerodynamic damping and stiffness increase, some of the modes pass each other in terms of the value of the eigenfrequency. This causes the modes to switch mode numbers with each other. Because the iterative procedure in MATLAB stores the eigenfrequency solutions from the complex eigenvalue problem in a matrix according to the current mode number, eigenfrequencies at different mean wind velocities for a specific mode is no longer stored in a single row, but fragmented over several rows. To easily identify which mode that eventually obtained a positive real value, and to efficiently reduce the number of modes required to induce flutter, a sorting algorithm was developed.

No single criterion was found that could detect every lost intersection point for the plot of the eigenfrequency, without creating any incorrect intersection points in the plot. Even with quite small steps there exist points where it is very hard to determine the correct path of the eigenfrequency plot. Nonetheless, a combination of several criteria proved to be sufficient to assess the eigenmodes that induce flutter. See figure 4.2 for an illustration of the criteria used.

1. The first and most simple criterion was to look for a big leap in the real value.
2. The second criterion was whether there would be a significantly smaller change in the derivative if two adjacent lines crossed than if they continued on their original path.

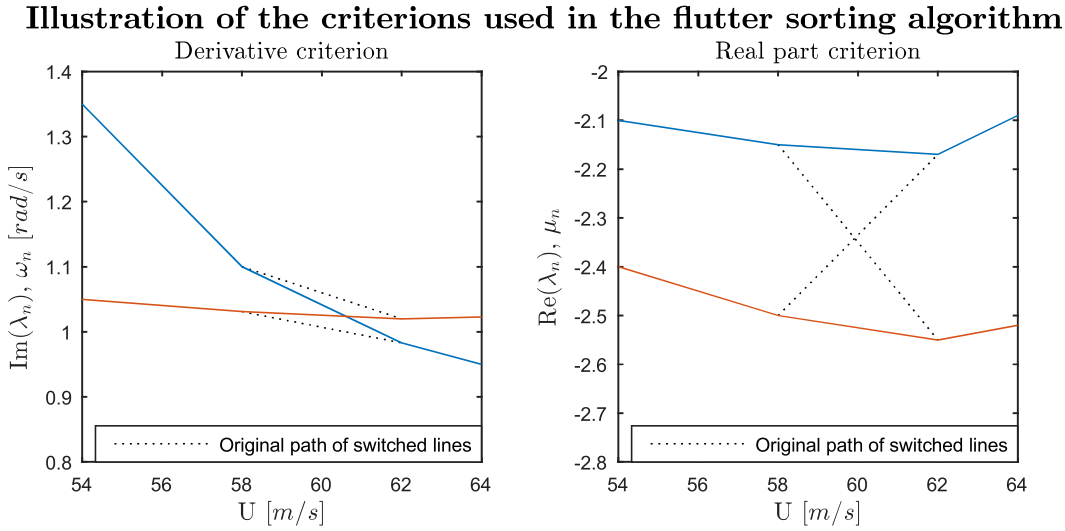

Figure 4.2: The figure shows how parts of the sorting algorithm developed for obtaining the critical mode work. The dotted lines implies switched lines.

Even when including and combining both criteria, the code never performed perfectly for all the available data sets without having very small velocity increments. To optimize the efficiency and usability of the code two additional requirements were added. These were the option of forcing lines to cross or never to cross, at a given coordinate and which was manually selected after a visual examination of the plot.

4.1.2 How to obtain and verify the fluttering mode shape

For a fluttering problem it can be desirable to obtain the fluttering mode shape. This can be done through a weighting scheme of the modes included in the flutter analysis. The described procedure is developed with input from the advisor of this thesis, Associate Professor Ole Øiseth.

The critical eigenvector is related to the critical eigenfrequency and the solution of the complex eigenvalue problem. The critical eigenvector acts as a weighting scheme of how much each mode should be weighted when obtaining the fluttering mode shape. Equation 4.1 illustrates how the fluttering mode shape is obtained by weighting all the modes involved in the flutter analysis.

$$\phi_{Flutter} = \Phi_{Modes}\phi_{Cr} \tag{4.1}$$

Where $\phi_{Flutter}$ is the fluttering mode, Φ_{Modes} is a matrix containing all the still air eigenmodes included in the analysis and ϕ_{Cr} is the critical eigenmode obtained from solving the complex eigenvalue problem.

In reality, the fluttering mode shape needs to be animated because the position of the inflection points and the maximum values can change with time. In this thesis, only the real part of the complex eigenvector was used, and a simplified illustration of one of the instances of the fluttering mode shape was obtained.

4.2 Wind, wave and motion induced loads

This section and the following sections explain the assumptions made in the buffeting analysis and also explains what equations and processes that were involved in the buffeting analysis. A summary of the method itself is first presented, and the assumptions are then elaborated.

4.2.1 The buffeting method, including both wave and wind loading

The general procedure used in the buffeting analysis carried out in MATLAB is briefly explained in figure 4.3. Note that this is not a flowchart of the script, but rather an explanation of the equations and processes that are involved in the buffeting analysis performed.

The following is an explanation of the different processes in figure 4.3.

The indexing and notation in figure 4.3 are as follows. s denotes structural, $tc.$ denotes top cables, $g.$ denotes the bridge girder, $p.$ denotes the pontoons, $t.$ denotes the towers and $k = 1, 2$ denotes the numbering of the pontoons.

1. The eigenvectors and the eigenfrequencies, which are obtained from ABAQUS when accounting for the static effects of the increasing wind, are imported into the MATLAB script. This implies that the eigenfrequencies and eigenvectors changes with the wind velocity. Infinite added mass and damping was used for all frequencies in the ABAQUS analysis.
2. The modalized mass matrix, $\widetilde{\mathbf{M}}_s$ and the eigenfrequencies ω_n is used to obtain the generalized stiffness and damping matrix, $\widetilde{\mathbf{K}}_s$ and $\widetilde{\mathbf{C}}_s$. The damping ratio is set to 0.5 % for all modes, according to equation 4.4.
3. The hydrodynamic added mass, damping and restoring forces, $\mathbf{M}_k$, $\mathbf{C}_k$ and $\mathbf{K}_k$ are imported from result files from HydroD.
4. $\mathbf{M}_k$, $\mathbf{C}_k$ and $\mathbf{K}_k$ are modalized for each pontoon.
5. The modalized hydrodynamic matrices including both of the pontoons are assembled.
6. The aerodynamic stiffness and damping matrices, $\mathbf{K}_{ae}$ and $\mathbf{C}_{ae}$, are assembled by using the empirical Hardanger coefficients from table 4.2 and equation 3.28.
7. $\mathbf{K}_{ae}$ and $\mathbf{C}_{ae}$ are modalized. Also, as the aerodynamic derivatives are defined per unit length, the $\mathbf{K}_{ae}$ and $\mathbf{C}_{ae}$ need to be integrated over the length of the respective structural parts.
8. The linear and quadratic transfer functions for the wave excitation forces are imported from result files from HydroD.
9. The cross spectral wave spectra, $S_{\eta_r \eta_s}$ are calculated by the use of equation 3.38. Where either JONSWAP or Pierson-Moskowitz, in equation 3.41 or equation 3.39, is used to calculate the one-dimensional wave spectral density, S_η.
10. The first and second order environmental wave load spectra are calculated in Cartesian coordinates. The matrices are $[6 \times 6]$.

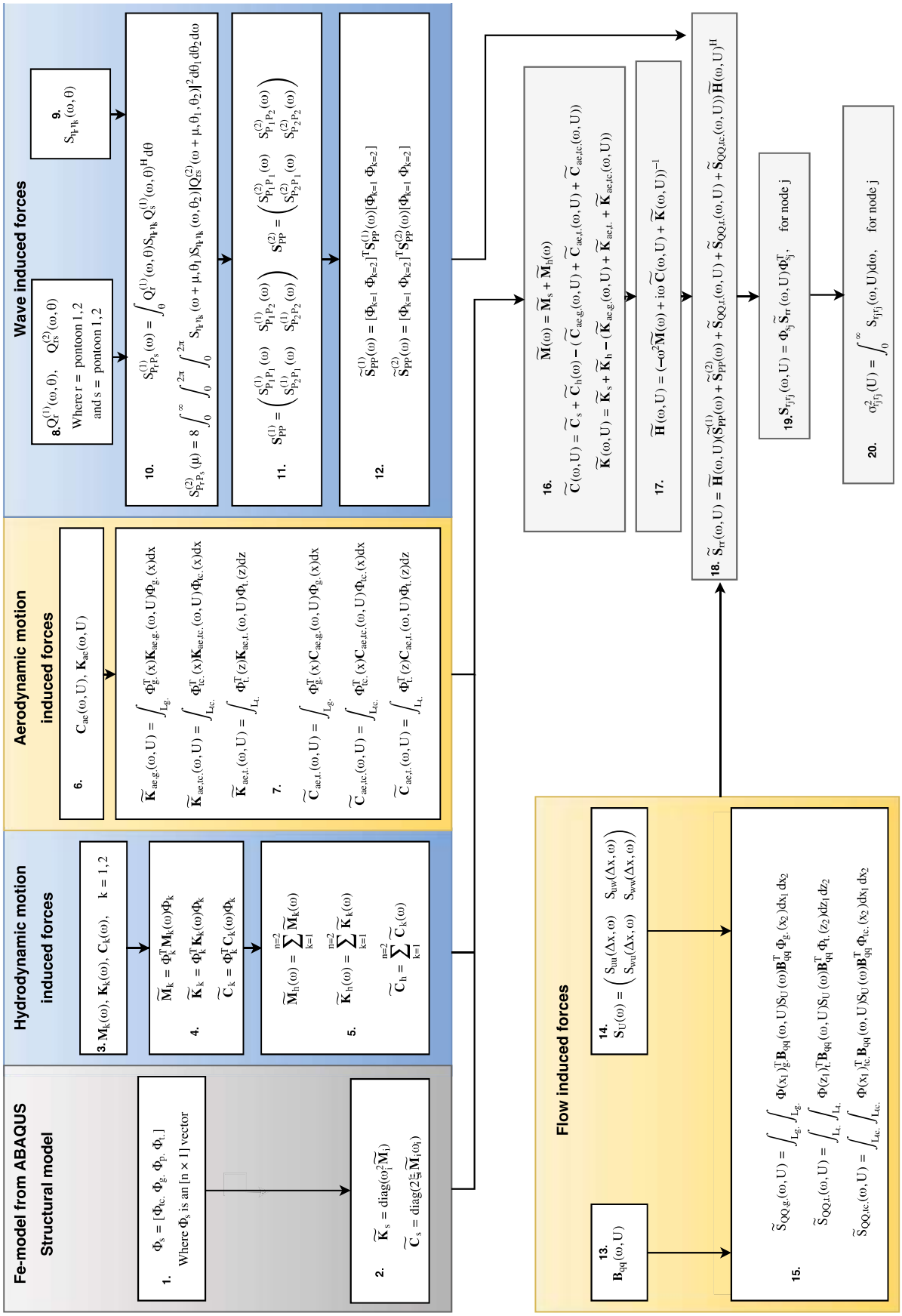

Figure 4.3: The buffeting method used in MATLAB.

11. The first and second order environmental wave load spectra are assembled into global load matrices comprising both pontoons. The matrix is $[12 \times 12]$.
12. The modalized environmental wave load spectra, $\widetilde{\mathbf{S}}_{pp}^{(1)}(\omega)$ and $\widetilde{\mathbf{S}}_{pp}^{(2)}(\omega)$ are calculated.
13. The quasi-static buffeting load matrices due to wind are assembled by the use of equation 3.16 and quasi-static coefficients from table 4.1.
14. The cross spectral densities for the wind field is established by the use of equation 4.3.
15. The buffeting wind force spectra are modalized and the correlation between the points on the different structural parts is accounted for by integrating twice over the length of each of the different structural parts.
16. All the modal contributions from the environmental loading and the structural properties are added together to obtain the modal system matrices, $\widetilde{\mathbf{M}}(\omega)$, $\widetilde{\mathbf{C}}(\omega, U)$ and $\widetilde{\mathbf{K}}(\omega, U)$.
17. The modal transfer function of the complete system is obtained.
18. The modal response spectra are obtained.
19. The response spectra at each node, j, can be obtained by transforming the response back into the Cartesian coordinate-system.
20. The standard deviation at each node, j, is obtained by integration of the response spectra over all frequencies at each node, j.

4.2.2 Assumptions and basis for the analysis

The power law wind profile

The wind speed at a given height h is determined according to equation 4.2, which gives wind profile based on a power law. h denotes the height over the ground surface, which for this thesis is height over the MSL. The constant α_{power} can be determined based on a known relation between the wind speed at two different heights. The procedure to determine the power law wind profile exponent is described in (Hsu et al., 1994, p. 757).

$$U(h) = U(h_{ref})\left(\frac{h}{h_{ref}}\right)^{\alpha_{power}} \qquad \alpha_{power} = \frac{ln(U_2/U_1)}{ln(h_2/h_1)} \tag{4.2}$$

In this master thesis, a reference height of $h_{ref} = 45$ m have been used. $\alpha_{power} = 0.12$ has been used throughout this master thesis. In the NPRA-report, (NPRA, 2017), which the authors of this thesis gained access to at a late stadium, a value of $\alpha_{power} = 0.127$ at a reference height of 10 m is recommended for Bjørnafjorden.

The distribution of the wind loading over the bridge

The wind loading acting on the bridge in ABAQUS is applied to the girder, floating pylons and the top cables as shown in figure 4.4.

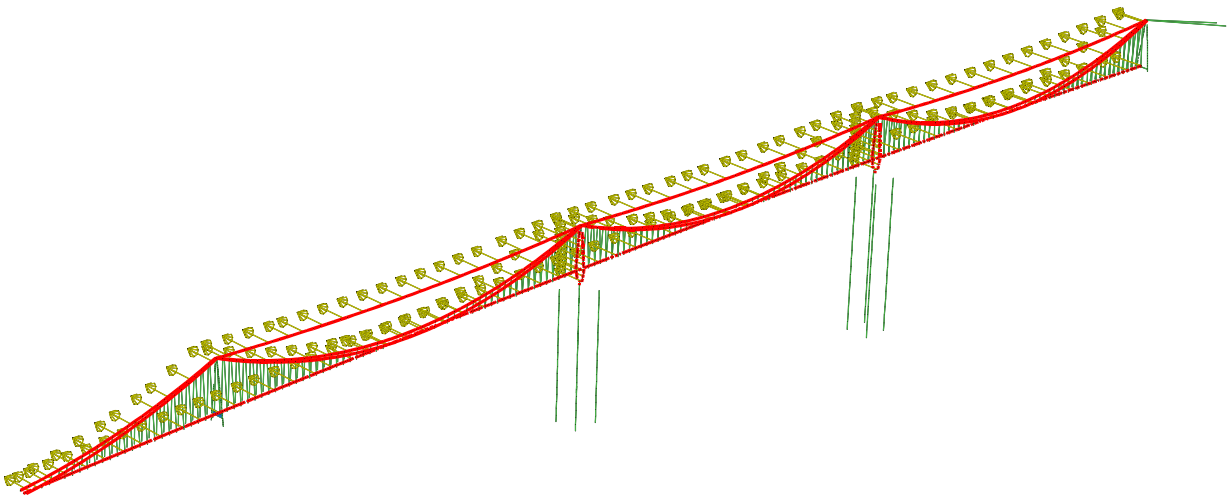

Figure 4.4: Area subjected to wind loading in the buffeting analysis.

A distribution of the wind load over the height of the tower can be seen in figure 4.5. It shows how the wind velocity increases over the pylon height, how the width of the pylon cross-section changes with the height and finally how the corresponding loading is distributed over the pylon height. Due to the change in the pylon cross-section and the increasing wind velocity with increasing height, the wind loading is more or less constant.

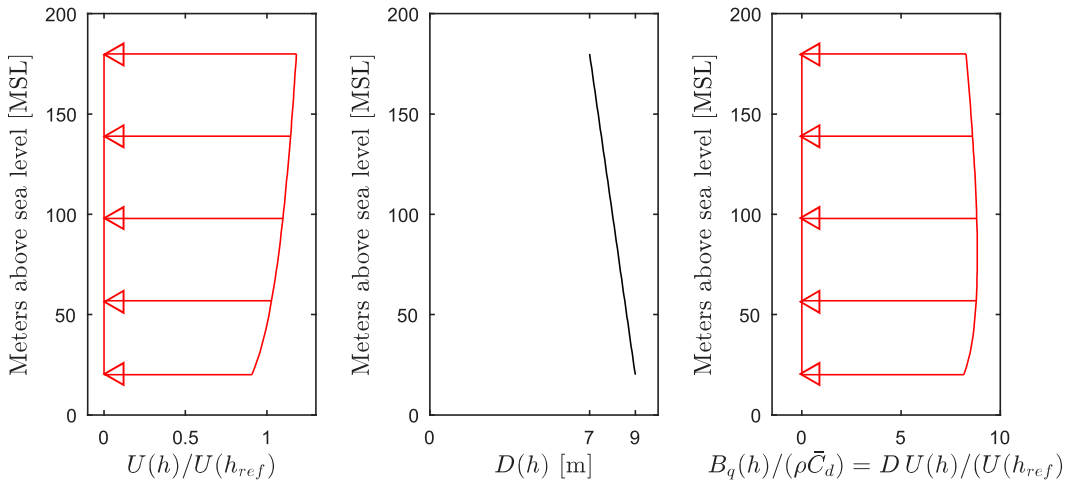

Figure 4.5: Wind load distribution over the height of the tower based on quasi-static theory, where $h_{ref} = 45$ m.

The wind spectra

The cross spectral densities of the wind field used in the buffeting analysis are from (Øiseth et al., 2012, Ch.3.2) and can be seen in equation 4.3. $\kappa = 0.0031$.

$$
\begin{aligned}
S_{uu}^{+}(\omega) &= \frac{40.58Uz\kappa}{(1+9.74\omega z/U)^{5/3}} exp(-1.4\frac{\Delta x\omega}{U}) \\
S_{ww}^{+}(\omega) &= \frac{0.82Uz\kappa}{(1+0.79\omega z/U)^{5/3}} exp(-\frac{\Delta x\omega}{U}) \\
S_{uw}^{+}(\omega) &= \frac{2.23Vz\kappa}{(1+1.67\omega z/U)^{7/3}} exp(-\frac{\Delta x\omega}{U})
\end{aligned}
\tag{4.3}
$$

Also a comparison of the spectral densities of the wind spectrum between the spectra in equation 4.3 and the wind spectra from the NPRA-reports can be seen in figure 4.3.

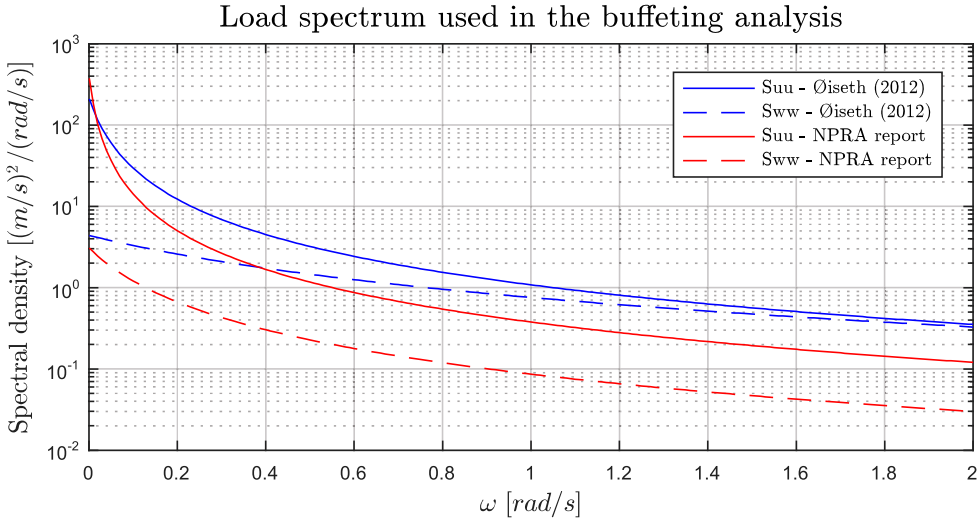

Figure 4.6: Spectrum of the turbulence components of the wind velocity.

Modification of the eigenmodes in ABAQUS with respect to the increasing wind velocity

Representing the mass and stiffness matrices in modalized coordinates can be compared to representing a signal by a Fourier series. Any curve can be imitated if enough shapes are included, but fewer shapes are required if there is an effective variation of shapes. Similarly, any motion of the bridge can be represented by adding the contributions of the different mode shapes, if enough modes are included. If the mode shapes are found without taking all properties of the bridge into account, a higher number of modes might be required to imitate the correct motion. Mode shapes are desired as shape functions, as they are guaranteed to be independent due to the orthogonality of modes (Chopra, 2012, Ch.10.4).

For this reason, an accuracy of mode shapes are desired, but not required for good results. For the buffeting analysis in this thesis, only the change of eigenmodes due to drag forces from static wind loading is taken into account in ABAQUS, and not the frequency dependent properties, as this would increase in calculation time of a factor at least equal to the number of modes included. The imperfections in mode shapes should be irrelevant as long as a sufficient number of modes is included. The frequency dependent properties, such as aerodynamic damping and stiffness, and the difference in hydrodynamic added mass compared to that of the infinite period, were added at a later stadium in the buffeting analysis.

Structural damping

Structural damping was first estimated for a frequency range of interest as Rayleigh damping. Because the same damping ratio is not achieved for every frequency by the use of Rayleigh damping, it was decided to use mode equivalent damping, which applies a constant damping ratio to every mode. An outline of how to apply Rayleigh damping if desired can be found in the appendix.

The entries of the mode equivalent damping matrix, which is diagonal, can be found from by the following equation.

$$\widetilde{C}_{nn} = 2\zeta\omega_n\widetilde{M}_{nn} \tag{4.4}$$

Where $\widetilde{M}_{nn}$ defines the diagonal entry position, n, of the modal mass matrix $\widetilde{\boldsymbol{M}}$, ω_n is the eigenfrequency of mode number n and ζ is the damping ratio.

Number of modes included in the analyses and the frequency range

To argue for the selected methods used in the buffeting analysis, figure 4.7, 4.8 and 4.9 provide some of the initial results achieved in this thesis. Even though the results are estimated for the bridge considered in this thesis, the results are provided in this part only for illustration purposes.

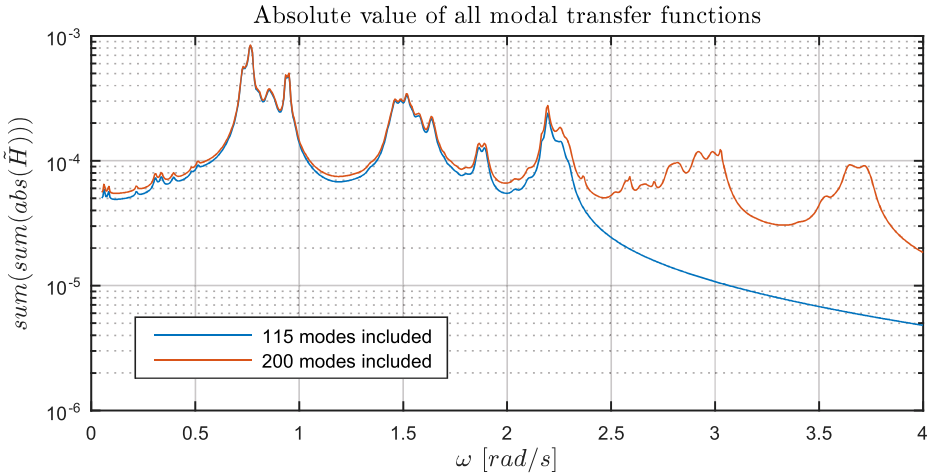

Figure 4.7: The modal transfer functions calculated by including 115 and 200 modes in the analysis.

As shown in figure 4.7 and 4.8, deviation between the results achieved when including 115 and 200 modes, is small until the eigenfrequency of mode 115, which for the considered case is 2.3 rad/s. As the response declines for increasing frequencies, no significant contribution to the STD is missed when including only 115 modes. An exception is for torsional response which peaks after 2.3 rad/s.

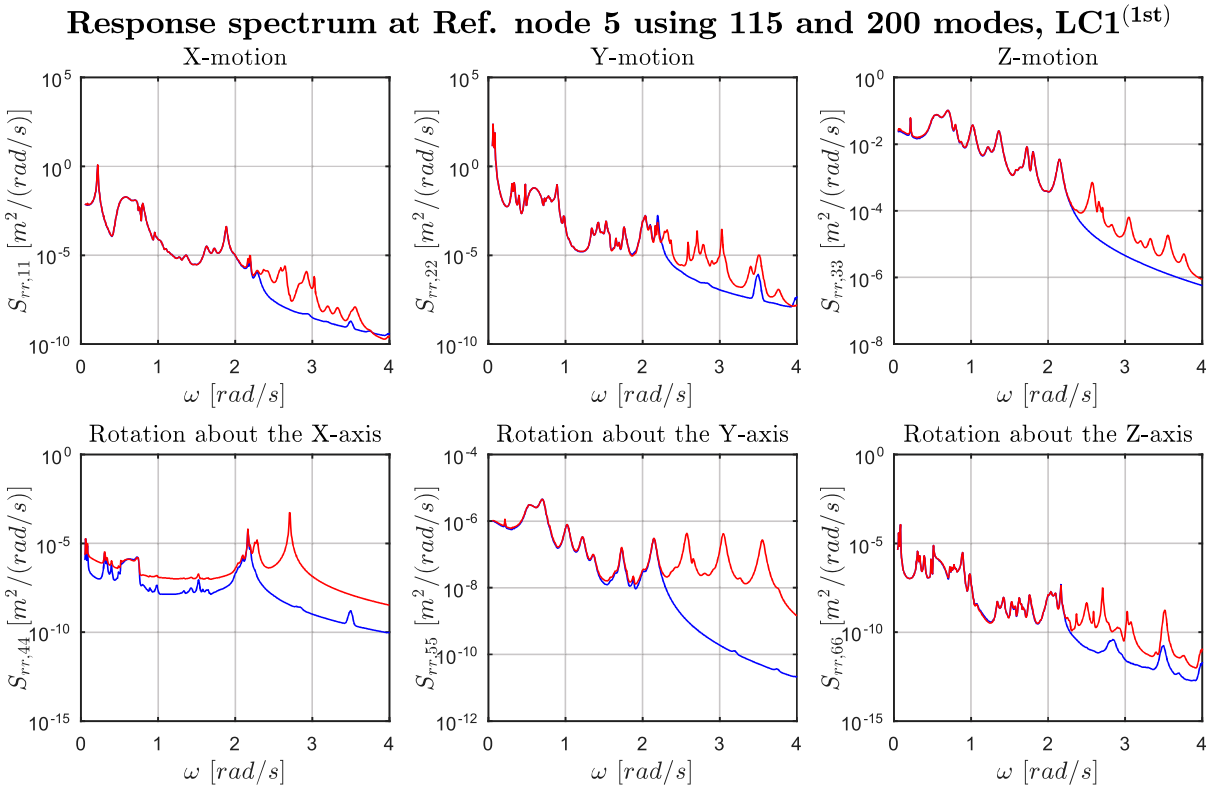

Figure 4.8: The response spectra of the girder at Ref. node 5 of all the six degree of freedoms. 115 and 200 modes are included in the analyses. The position of Ref. node 5 can be found in figure 5.3.

Considering that response in the lateral and vertical direction is the main focus of this thesis, it was judged to be sufficient to include 115 modes in the buffeting analysis, because this drastically reduces the calculation time and only affect the response of high frequencies. From figure 4.8 it can be seen that the spectral density of vertical and lateral motion of higher frequencies is insignificant to the STD, which is proportional to the are under the response spectrum.

It is recommended to use a fine resolution for the first part of the frequency axis in the buffeting analysis because it is easy to miss the exact peaks of the first horizontal modes, as these are quite spike-like and contributes significantly to the STD.

	Frequency range $[rad/s]$
Frequency axis	[0.001:0.001:0.25, 0.255:0.005:2.5]

Table 4.3: The resolution and the range of the frequency axis used in the buffeting analysis for the response spectrum calculation.

MATLAB specific simplifications to reduce calculation time

A complete buffeting analysis with 115 modes, six wave periods, 17 wave heights and 1000 frequencies require approximately 12 hours on a regular laptop. Because MATLAB does not allow the user to save matrices above 2GB without compressing them, and to not run out of memory while storing the large matrices included in the calculations, the analysis was performed for four wind speeds at the time. Variables were stored throughout the analysis, and could be imported if an analysis crashed halfway through.

The modal wave load spectra, calculated using modes dependent on static wind loading

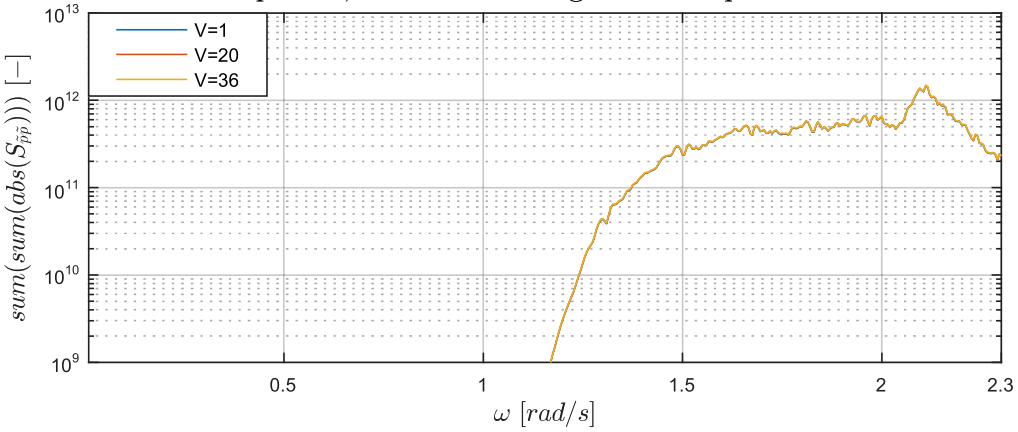

Figure 4.9: The purpose of this figure is to show that the modal wave loading is independent of the mean wind velocity, as the modes of the COB does not change much due to the static wind loading applied. The wave loading was calculated for $Hs = 3$ m and $T_p = 6$.

Figure 4.9 which shows the sum of all modal contributions to the modal wave loading, illustrates that change of the mean wind velocity U is of no importance when representing the wave loading, even though the modes shapes are dependent on the static wind loading. Hence the wave loading did not have to be updated for every mean wind velocity, but only for every wave height and wave period. As calculation time is quite large for second order wave loading, this update to the code was very advantageous.

Wave spectra included in the analyses

The Pierson–Moskowitz spectrum is a one-parameter wave spectrum, with a fixed relation between the wave period and wave height. For a wave height of 3 m, unrealistically large wave periods are achieved for the Bjørnafjorden area, as shown in figure 4.10.

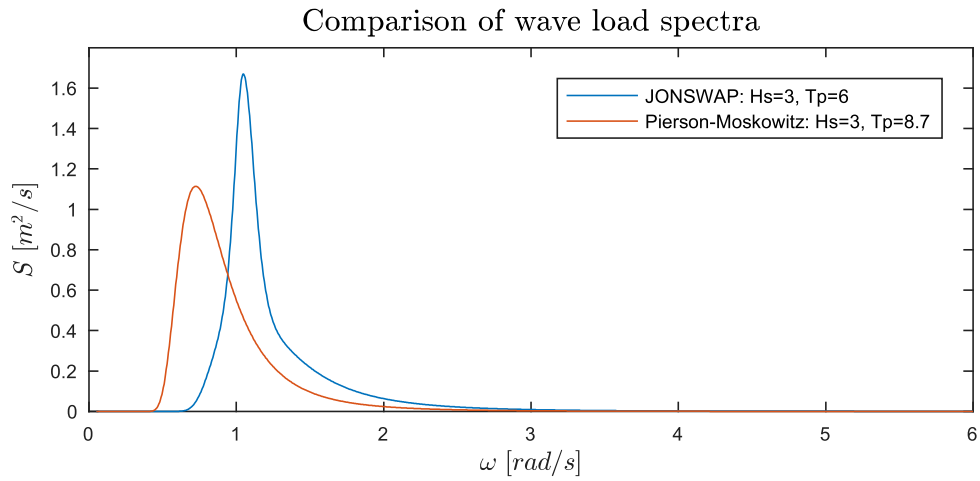

Figure 4.10: Comparison of the JONSWAP wave spectrum and the PM–Moskowitz wave spectrum.

Also, swell waves cannot be represented well by a Pierson–Moskowitz spectrum, because a long wave period can only be achieved by a corresponding high wave height. Figure 4.11 compares three JONSWAP spectra to the equivalent Pierson–Moskowitz spectra given by the wave period and the relation shown in figure 3.5 and equation 3.40.

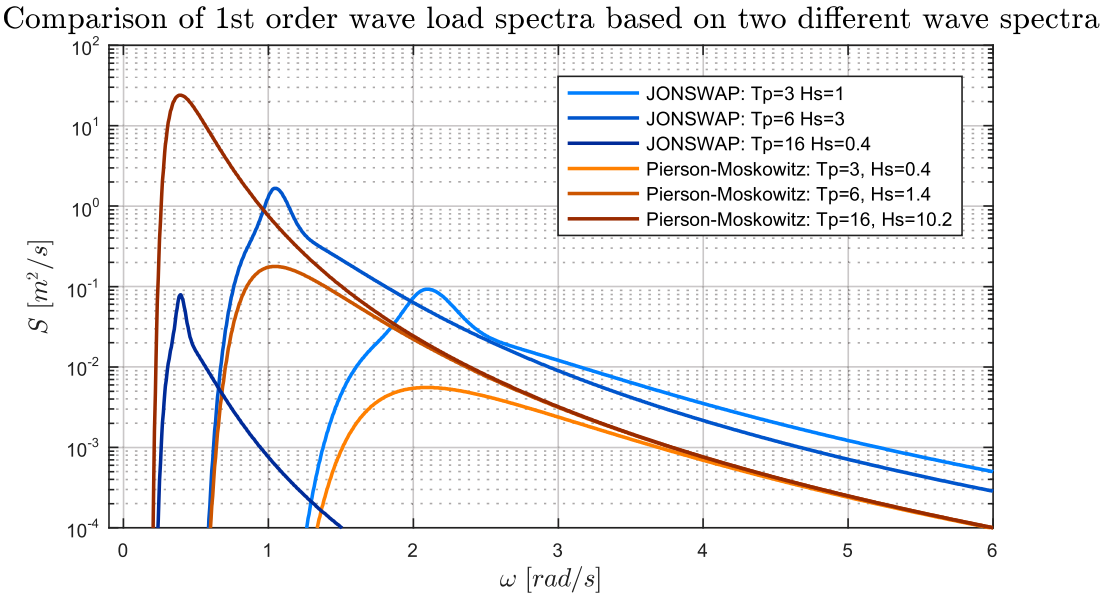

Figure 4.11: Comparison of the first order wave load spectra calculated based on the JONSWAP wave spectrum and the Pierson–Moskowitz wave spectrum.

For the reasons stated above, the JONSWAP-spectrum has been used in the buffeting analyses.

4.3 Curve fitting of probabilistic models to environmental scatter data

This section explains how the different probability density functions for the environmental scatter data are obtained. The fitting of all curves has been done in MATLAB using the statistical toolbox cftool. The method for fitting each curve has been the non-linear sum of least squares method, presented in section 4.3.1. All the PDFs have been compared to each other with their respective R^2-value and χ^2-value to assess the best PDF, according to procedures described in section 4.3.2 and 4.3.3.

4.3.1 Non-linear least sum of squares

The non-linear least sum of squares is a method where a data set is fitted to a non-linear model that tries to capture the distribution of the data set.

Consider a data set with m points, $(x_1, y_1), ..., (x_m, y_m)$ and a model $y = f(x, \beta_1, \beta_2, ..., \beta_n)$, where $m \geq n$. The best fit of the curve (model) is found by minimizing the sum of squares by adjusting the, n, β-parameters by iteration, (Wolfram, 2017).

$$SSE = \sum_{i=1}^{m} r_i^2, \qquad \text{Where } r_i = y_i - f(x, \beta_1, \beta_2, ..., \beta_n) \tag{4.5}$$

Where r_i = are the residuals between the measurements and the curve (model), which is to be fitted.

4.3.2 The coefficient of determination, R-squared

R^2 is often referred to as the coefficient of determination and is a measure of the proportion of the variance captured by a fitted probability model to a pool of measurement data. It can be expressed as follows, (Walpole et al., 2012, 11.5).

$$R^2 = 1 - \frac{SSE}{SST} \tag{4.6}$$

Where SSE is the error sum of squares and SST is the total sum of squares.

$$SST = \sum_{i=1}^{n} (y_i - \bar{y})^2 \tag{4.7}$$

Here y_i is a measured quantity and $\bar{y}$ is the mean of the measured quantities.

$R^2 = 1$ indicates a perfect fit, while R^2 close to 0 indicates a very poor fit. For a probability function, the points with largest probability, will have the largest effect on the R^2 value. Thus,

the selection of a model for a given data set should not solely be based on the R^2-value, but also include another test, e.g., a chi-squared goodness of the fit test.

4.3.3 The chi-squared goodness of fit test

A chi-squared goodness of fit test is used to test if sample data fits a distribution from a certain population. The chi-squared goodness of fit test tests whether the difference between the suggested model and the observed results are statistically unlikely to occur or not. Usually, a significance level of 5 % is selected as the limit, which means that the chi-squared goodness of fit test is rejected if the probability of the observed deviation is less than 5 %.

To calculate the χ^2-value numerically the following formula can be used, (Statistics Solutions, 2017).

$$\chi^2 = \sum_{i=1}^{n} \frac{(O_i - E_i)^2}{E_i} \tag{4.8}$$

Where O_i and E_i is the number of observed and expected occurrences within a given category. The number of degrees of freedom, $\nu = n - 1$, are defined by the number of categories, n. Tabulated p-values can be found for combinations of χ^2 and ν. For a hypothesis to be ruled false, the p-value must be less than 0.05.

4.3.4 The two-parameter Weibull distribution

The two-parameter Weibull distribution's density function can be written as follows for the continuous random variable X, (Walpole et al., 2012, 6.10).

$$f(x;\alpha,\beta) = \begin{cases} \alpha\beta x^{\beta-1} e^{-\alpha x^{\beta}}, & x < 0 \\ 0, & \text{elsewhere} \end{cases} \tag{4.9}$$

Where $\alpha > 0$ and $\beta > 0$.

4.3.5 The two-parameter lognormal distribution

The two-parameter lognormal distribution's density function can be written as follows for the normal distributed random variable $Y = \ln(X)$, (Walpole et al., 2012, 6.9).

$$f(x;\mu,\sigma) = \begin{cases} \frac{1}{\sqrt{2\pi}\sigma x} e^{-\frac{1}{2\sigma^2}[ln(x)-\mu]^2}, & x \geq 0 \\ 0, & x > 0 \end{cases} \tag{4.10}$$

Where σ and μ is the standard deviation and the mean, respectively, of the variable Y.

4.3.6 The Lonowe-model

The Lonowe-model is a combination of a lognormal-model and a Weibull-model. For a given wave data set it could be that for moderate values of H_s a lognormal-distribution is suitable in this range, but for the higher values in the cumulative sample distribution, a Weibull-distribution would be more appropriate. When this is the case, a Lonowe-model could be the suitable choice to represent the distribution, (Haver, 1980).

$$f_{H_s}(h) = \begin{cases} \frac{1}{\sqrt{2\pi}\sigma_{LHM}h} \cdot exp\left[-\frac{1}{2}\left(-\frac{ln(h)-\mu_{LHM}}{\sigma_{LHM}}\right)^2\right], & h \leq h_0 \\ \frac{\alpha_{HM}}{\beta_{HM}}\left(\frac{h}{\beta_{HM}}\right)^{\alpha_{HM}-1} \cdot exp\left[\left(-\frac{h}{\beta_{HM}}\right)^{\alpha_{HM}}\right], & h > h_0 \end{cases} \tag{4.11}$$

Where σ_{LHM}, μ_{LHM}, α_{HM} and β_{HM} are all parameters to be obtained from a regression-analysis.

$$f_{T_p|H_s}(t|h) = \frac{1}{\sqrt{2\pi}\sigma_{LCT}t} \cdot exp\left[-\frac{1}{2}\left(\frac{ln(t)-\mu_{LTC}}{\sigma_{LTC}}\right)^2\right] \tag{4.12}$$

where

$$\mu_{LCT} = c_1 + c_2 h^{c3} \qquad \sigma^2_{LTC} = d_1 + d_2 \cdot exp(d_3 h) \tag{4.13}$$

4.4 Assessing the short-term and long-term extremes

The short and long-term extremes can be evaluated by creating a probabilistic model containing three load generating sources, wave height, wave period and wind velocity. The largest response that occurs e.g. once every 100th year, due to an environmental load combination can be obtained by applying statistics.

4.4.1 Environmental contour surface method

The environmental contour surface method is based on the Inverse First order Reliability Method, IFORM. The IFORM is the inverse of the First Order Reliability Method, FORM. Both methods are explained here for the sake of completeness, even though only the IFORM framework is applied in this thesis.

A sea state is governed by the following three parameters, H_s, T_p and U. A combination of these parameters gives a specific sea state, whereas some combinations are more common than others. For instance, the environmental contour surface method can be used to obtain the combinations that for any given year has the probability of 1 % to occur. These combinations are often referred

to as the 100 year extremes. The combinations do not necessarily yield an extreme response, but the combinations are extreme in the sense of their statistical probability to occur.

A contour surface can be achieved by transforming a joint probability distribution into a standard Gaussian nonphysical space, the U-space, consisting of three independent standard Gaussian variables, using the Rosenblatt transformation, (Li et al., 2015) and (Haver, 2008). The contour surface in this thesis corresponds to a probability level equal to that of a parameter that has an annual exceedance probability equal to 1 %. The probability of exceedance in an arbitrary d-hour sea state is the annual exceedance probability divided by the number of d-hour sea states included within the considered frame of time, (Haver, 2008). The contour surface is estimated by setting the limit state function, as defined in structural reliability analysis, equal to zero. See equation 4.14 for the limit state function.

$$g(X_d, H_s, T_p, U; x_{crit}) = x_{crit} - X_d(H_s, T_p, U) \tag{4.14}$$

The d denotes the length of a given sea state given in hours, X_d is a maximum response value within, in this thesis, a d-hour sea state. $g(X_d, H_s, T_p, U; x_{crit})$ is the limit state function and fails for negative values. $g(X_d, H_s, T_p, U; x_{crit}) = 0$ defines the failure boundary and x_{crit} is a critical value that makes the system fail if exceeded, e.g. a standard deviation or a displacement.

A way to transform the parameters between the physical space and the U-space is to utilize a Rosenblatt transformation, see equation 4.15. The design point can be found in an iterative process, where points in the U-space are estimated for a number of x_{crit} values. The probability distribution is known for every parameter involved to calculate x_{crit}. The point which is closest to the origin in the U-space has the highest probability of occurring, this is the design point. This procedure is also known as the First Order Reliability Method.

$$\begin{aligned} F_U(u) &= \Phi(u_1) \\ F_{H_s|U}(h|u) &= \Phi(u_2) \\ F_{T_p|U,H_s}(t|u,h) &= \Phi(u_3) \end{aligned} \tag{4.15}$$

Here Φ represents the standard Gaussian distribution function and u_1, u_2 and u_3 represents points in the U-space. Within the FORM framework, the following simplification of the failure surface in the U-space is defined.

$$\hat{p}_f(x_{crit}) = \Phi(-\beta) \tag{4.16}$$

Where $\hat{p}_f(x_{crit})$ is the probability related to a design point, and β is the distance from the point in the U-space to the origin.

Within the Inverse First Order Reliability Method framework, an opposite approach is used. Since the probability of exceedance is known and constant, a sphere with radius, β, in the U-space can be obtained. The radius of the sphere is given by, $\beta = \sqrt{u_1^2 + u_2^2 + u_3^2}$. β, also known as the reliability index, denotes a constant probability in the standard Gaussian space. The points,

(u_1, u_2, u_3), can be transformed into the physical space by the use of 4.15. This is illustrated in 4.12.

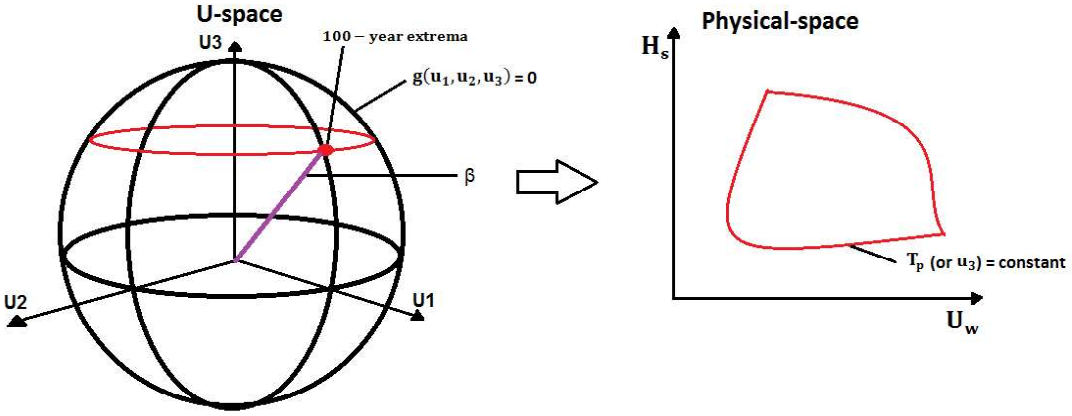

Figure 4.12: Illustration of the failure sphere in the U-space transformed into the failure contour line in the physical space for a constant u_3-coordinate.

All points on the sphere in the U-space have the same probability of occurring, but only one of them are the design point which yields a critical e.g. displacement in the physical space. Thus, the task is to find which of these points on the surface in the U-space that yield a critical value in the physical space. The back-calculation of a point, (u_1, u_2, u_3), on the sphere yields a X_d-value in the physical space. The worst of all the calculated X_d-values is defined to be x_{crit}.

In this thesis, the physical space corresponds to a contour plot of the three parameters, wave height, wave period and wind velocity plotted against each other, all found by solving equation 4.15. The corresponding STD for each combination of H_s, T_p and U is also calculated for all combinations. x_{crit} is defined to be the largest horizontal displacement based on the estimated environmental load combinations.

All short-term extremes

The following equation for the short-term extreme response can be derived from equation 4.26 presented later, by considering only one sea state with duration, T_p, equal to 1 hour.

$$F_{\hat{X}}(H_s, T_p, \xi) = \exp(-T_{short}\frac{\sigma_{\dot{X}}(H_s, T_p)}{2\pi\sigma_X(H_s, T_p)}\exp(-\frac{\xi^2}{2\sigma_X(H_s, T_p)^2})) \tag{4.17}$$

By considering the short-term response for an extreme load case, a simplified estimation of the long-term response can be obtained.

4.4.2 Empirical joint probability distributions

The joint distribution of U, H_s and T_p is given by the following definition (Li et al., 2015).

$$f_{U,H_s,T_p}(u,h,t) = f_U(u) \cdot f_{H_s|U}(h|u) \cdot f_{T_p|U,H_s}(t|u,h) \tag{4.18}$$

$f_U(u)$ represents the marginal distribution of U, $f_{H_s|U}(h|u)$ is the conditional distribution of H_s given U and $f_{T_p|U,H_s}(t|u,h)$ is the conditional distribution of T_p given H_s and U.

$$f_U(u) = \frac{\alpha_U}{\beta_U}(\frac{u}{\beta_U})^{\alpha_U - 1} \cdot \exp[-(\frac{u}{\beta_U})^{\alpha_U}] \tag{4.19}$$

$$f_{H_s|U}(h|u) = \frac{\alpha_{HC}}{\beta_{HC}}(\frac{h}{\beta_{HC}})^{\alpha_{HC} - 1} \cdot \exp[-(\frac{h}{\beta_{HC}})^{\alpha_{HC}}] \tag{4.20}$$

$$\begin{aligned} \alpha_{HC} &= a_1 + a_2 \cdot u^{a_3} \\ \beta_{HC} &= b_1 + b_2 \cdot u^{b_3} \end{aligned}$$

$$f_{T_p|U,H_s}(t|u,h) = \frac{1}{\sqrt{2\pi\sigma_{\ln(T_P)}t}} \cdot \exp[-\frac{1}{2}(\frac{\ln(t) - \mu_{ln(T_p)}}{\sigma_{\ln(T_P)}})^2] \tag{4.21}$$

$$\mu_{\ln(T_p)} = \ln(\frac{\mu_{T_p}}{\sqrt{1+\nu_{T_p}^2}}), \quad \sigma^2_{\ln(T_p)} = \ln(\nu^2_{T_p} + 1), \quad \nu_{T_p} = \frac{\sigma_{T_p}}{\mu_{T_p}} \tag{4.22}$$

$$\begin{aligned} \mu_{T_p} &= \bar{t}(h) \cdot [1 + \theta(\frac{u - \bar{u}(h)}{\bar{u}(h)})^{\gamma}] \\ \bar{t}(h) &= e_1 + e_2 \cdot h^{e_3} \\ \bar{u}(h) &= f_1 + f_2 \cdot h^{f_3} \end{aligned} \tag{4.23}$$

$$\nu_{T_p}(h) = k_1 + k_2 \cdot \exp(hk_3) \tag{4.24}$$

All the coefficients α_U, β_U, θ, γ, a_i, b_i, e_i,f_i and k_i, when $i = 1, 2, 3$, are empirical coefficients obtained from curve fitting measurement data from a given site.

The empirical coefficients from (Li et al., 2015) and (Johannessen et al., 2002) read as follows.

Parameter, (Li et al., 2015)	[−]	Parameter, (Johannessen et al., 2002)	[−]
a_1	2.136	a_1	2
a_2	0.013	a_2	0.135
a_3	1.709	a_3	1
b_1	1.816	b_1	1.8
b_2	0.024	b_2	0.1
b_3	1.787	b_3	1.322
e_1	8.0	e_1	4.883
e_2	1.938	e_2	2.68
e_3	0.486	e_3	0.0
f_1	2.5	f_1	1.764
f_2	3.001	f_2	3.426
f_3	0.745	f_3	0.78
k_1	-0.001	k_1	-0.0017
k_2	0.316	k_2	0.259
k_3	-0.145	k_3	-0.113
α_U	2.029	α_U	1.708
β_U	9.409	β_U	8.426
θ	-0.255	θ	-0.19
γ	1.0	γ	1.0

Table 4.4: Empirical parameters used in equation 4.18. from (Li et al., 2015) and (Johannessen et al., 2002)

4.4.3 Long-term extreme value

A more accurate long-term estimation, than from short-term extreme load cases, can be found using equation 4.26, which is referred to as the long-term extreme method throughout the thesis.

Long-term extreme method

This method utilizes equation 4.25 and integrates over all wind velocities, wave periods and wave heights. This means that all possible combinations of the standard deviations have to be calculated from a buffeting analysis. The displacement with a 100 year return period can then be obtained from equation, 4.25.

The CDF, $F_{\hat{X}}(\xi)$, of the extreme value $\hat{X} = \hat{X}(T)$, or the most extreme response over a long-term period, T, can be written as follows, (Naess and Moan, 2013, 12.4.3).

$$F_{\hat{X}}(\xi) = \exp(-T \int_h \int_t \frac{\sigma_{\dot{X}}(h,t)}{2\pi\sigma_X(h,t)} \exp(-\frac{\xi^2}{2\sigma_X(h,t)^2} f_{H_s,t_p}(h,t) dh\, dt) \tag{4.25}$$

Where σ_X and $\sigma_{\dot{X}}$ is the standard deviation and the derivative of the standard deviation, respectively, of the extreme value $\hat{X}$. ξ is a global extreme response value that occurs with a probability $P(\xi) = 1 - F_{\hat{X}}(\xi)$ within the period T.

If the PDF varies with respect to the wind, equation 4.25 has to be expanded into a triple integral and can be denoted as follows:

$$F_{\hat{X}}(\xi) = \exp(-T \int_u \int_h \int_t \frac{\sigma_{\dot{X}}(u,h,t)}{2\pi\sigma_X(u,h,t)} \exp(-\frac{\xi^2}{2\sigma_X(u,h,t)^2} f_{U_s,H_s,T_p}(u,h,t)) dh\, dt\, du) \tag{4.26}$$

Chapter 5

Finite element modelling in ABAQUS

In the following sections is the modelling of the bridge in the finite element program, ABAQUS, presented. ABAQUS is part of a software suite that is used for computer-aided engineering and finite element analysis.

The purpose of modelling in ABAQUS is to perform a frequency analysis of the bridge concept to obtain the eigenmodes and structural properties of the bridge. These properties will then be exported to MATLAB for further analyses. The only difference between the bridge concept comprising the steel hull alternative and the concrete hull alternative is the number of tethers and the pontoon properties. Thus, only a general description of one model is given in this thesis.

Models in ABAQUS can be created with the help of input files. Input files are text files built up by keywords. Keywords are commands in ABAQUS, which add a property to the model if the correct syntax is applied in relation with the keyword.

5.1 MATLAB

MATLAB is a multi-paradigm numerical computing environment.

MATLAB is used in this context to generate input files to ABAQUS, and ABAQUS analysis can also be executed through MATLAB. The advantage of this modification is that it enables swift changes to be made to an ABAQUS model because an entirely new input file is generated in an instant after each change of the model. Also, MATLAB enables several analyses to be executed in succession. This gives the possibility of running iterative analyses, where each model is updated automatically based on previous analyses.

By involving MATLAB, it is possible to decompose the composition of the model into several parts. Several scripts create small parts of the model itself, and a main script assembles it all together. This feature also enables for a parametrization of the bridge.

5.2 The ABAQUS model

5.2.1 Model parametrization

It should be noted, that due to the asymmetric geometry and boundary conditions of the bridge, some properties were hard to parametrize. To account for these asymmetries, properties as tower heights, span lengths and the amount of sag, are entered as vectors. This means that adding an extra span will require an additional entry in many input parameters. The assembly algorithm also requires a side span in the northern end. Thus, it is not possible to model the bridge without a northern side span without altering the assembly algorithm. The model is also parametrized in the sense that it is possible to change the materials, structural properties, which pontoon alternative to use, the number of hangers, and all dimensions of the structural parts. It is also possible to remove some parts of the model, as to inflict damage to the bridge.

The tower design is a key element that changes rapidly. Thus, the input files of the towers are generated separately. This allows the user to completely change the geometry of the towers, or the procedure used to model them.

5.2.2 Geometry

The following right-hand coordinate system, seen in figure 5.1, has been used in the ABAQUS and HydroD modelling.

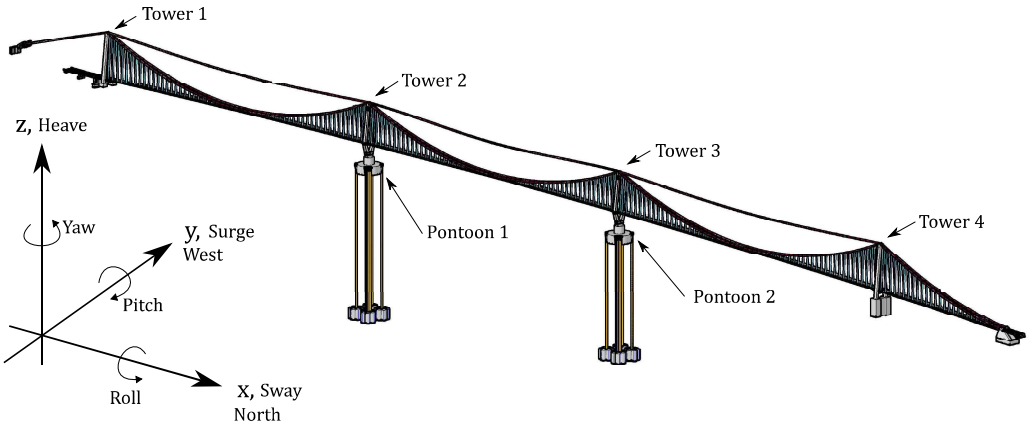

Figure 5.1: The axis system of the bridge, with origo at the south end of the bridge. For angular reference, $\theta = 0$ is in the north direction, and $\theta = 90$ is in the east direction. (NPRA, 2016i)

The geometry is generated with node lists printed to text files by the use of MATLAB. Each node represents a coordinate, (x, y, z). The elements that make up the bridge are also printed to text files by the use of MATLAB. These text files make up part of the main input file, which generates the complete ABAQUS model.

The shape of the bridge girder is modelled as a second order polynomial with the coordinate of the girder at mid-span (the middle of the central span, see figure 5.3) and at the two fixed towers as input.

The geometrical values, which served as input to the ABAQUS model for the bridge alternative with the concrete hull, are presented in table B.3 in the appendix.

As for the material properties, a section data sheet in Excel was used. All sections, materials and so forth were listed in an Excel document. MATLAB could retrieve the material data for each section of this document. This reduced the probability for errors and made it easy to change or add new element properties. The element properties can be found in table B.1 in the appendix.

5.2.3 Elements

The bridge is made up of several kinds of wire elements and point elements. All who are presented here.

B31 and B32 elements

B31 and B32 elements are first and second order 3D beam elements. Where first and second order refers to the order of interpolation, i.e. the linear or quadratic shape function. B31 and B32 belong to the class of Timoshenko beam elements and allow for transverse shear deformation.

In the case of consistent mass representation, the B32 elements represent the rotary inertia better than the B31 elements. The mass representation in the girder plays a vital part in the eigenfrequency analysis. For this reason, if consistent mass representation is used, B32 elements are the natural choice of elements to use to represent the bridge girder. Also, B31 elements can only account for a moment constant over the element, while B32 are able to represent a linear varying moment over the element, which gives increased continuity and accuracy when representing the moment in the girder. Reason for sometimes to choose B31 over B32 is simply to reduce the computational power needed to execute an analysis.

The B31 elements can handle compression, but as desired, only tension forces were present in the cables and the hangers.

User defined element

The user defined elements have been applied to the model to account for the structural properties of the pontoons and, also, to account for the environmental effects of the wave loading. The input data of the pontoons to the user elements have been retrieved from another finite element software suite, called Sesam.

The mass properties of the pontoon are added to the centre of gravity, while the added mass and added damping are applied to the centre of buoyancy. The added mass can be applied to a user defined element, while the damping properties must be added to spring elements linked to the

ground. The waterplane stiffness is added at the centre of the waterplane area. In hindsight, the authors of this thesis would recommend applying all properties to the same reference point. Which point is chosen does not make a difference as long as the same reference point is used in both HydroD and ABAQUS. A natural selection could be the centre point of the water plane.

User defined elements were also used to represent the aerodynamic damping and stiffness matrix in a complex frequency analysis.

Mass lumping

Initially, the mass was represented by a consistent mass representation. This representation was later changed to a lumped mass formulation to be able to represent the rotary inertia of the bridge girder accurately. The lumped masses were added as separate mass elements. The average length of girder elements is used to lump mass since the length of these elements varies with less than one percent.

Because it is desirable that the bridge can recreate high order modes sufficiently accurate, the amount of girder elements can easily be adjusted to suit the needs of the user.

When changing from a consistent mass representation to a lumped mass representation, it was observed that at least two elements between each hanger should be used for the lumped mass representation to give the same deflected shape under static loading. The eigenfrequencies and mode shapes of the first horizontal and vertical modes appeared to be unaffected by the change in mass representation.

5.2.4 Boundary conditions and constraints

The boundary conditions and the interaction between structural parts have been given as to replicate the real behaviour of the bridge. How the different coupling between structural parts and how the boundary conditions have been given for the model can be seen in figure 5.4.

The kinematic coupling option has been used when connecting different structural parts in the ABAQUS model, with one exception. The multi point constraint option was used to connect the girder and the fourth tower. The tower only constrains movement in the lateral direction. By comparing the mode shape obtained for torsional motion with results from the report (NPRA, 2016g), irregularities were observed for torsional motion. Switching the coupling options solved this problem. Other couplings in the model did constrain only the DOFs assigned, and did not have to be changed.

Where the pylons of the towers meet and act as a monolithic column, the centre line of the two pylons are connected to the monolithic part with a kinematic coupling. Note also that the centre line of the crossbeam and the girder does not intersect. With the exception of tower four, these are connected with a kinematic coupling. Figure 5.2 shows how the tower constraints have been modelled. Kinematic coupling is indicated by a red ring and a pink link. The red ring indicates the master node, and the pink line represents the connections to the slave nodes.

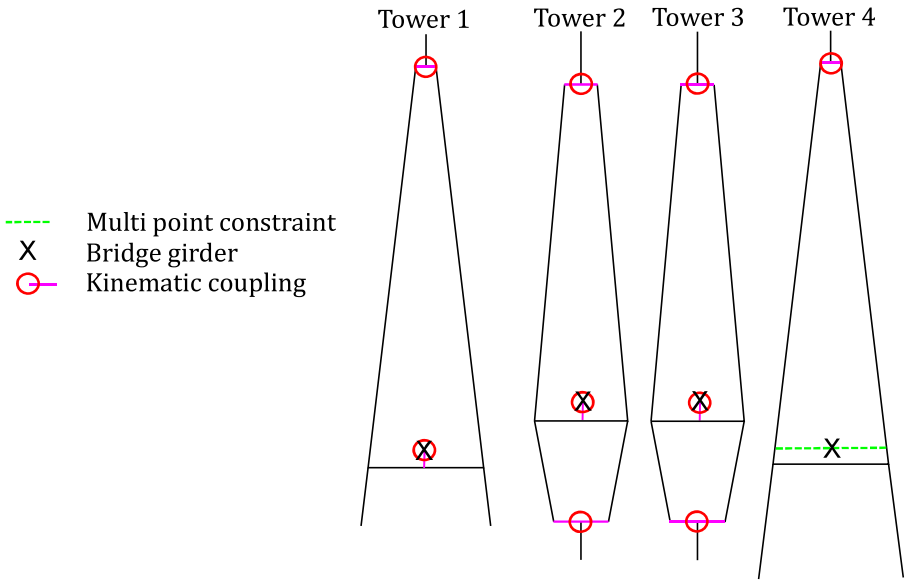

Figure 5.2: The figure depicts how the constraints and couplings of the four towers have been modelled in ABAQUS and how the girder is connected to the towers. The top cables and the pontoons are omitted from this figure.

Figure 5.3 shows the labelling of important nodes that are referred to later in this thesis and that have been given particular attention with respect to the study of the results.

5.2.5 Temperature loading and particular challenges of the modelling

A particular challenge that arises when the model is loaded with gravity loading is to keep the initial geometry of the bridge because the initial geometry is created for an unloaded state. The loading alters the geometry, which has to be restored to its original state. In this thesis, a temperature loading is applied to the cables in the structure, to reverse the elongation of the elements that occurs due to the gravity loading.

As mentioned, the bridge has several asymmetrical aspects. The asymmetries increase the complexity of the procedure required to retrieve the initial geometry. Some of the asymmetries are the different tower heights, different span lengths, a different number of hangers at each span, and a different amount of sag for each main cable and top cable, all of them which have been considered in this thesis.

The top cable and the added side span required a lot of attention with respect to the asymmetry. All top cable spans have a sag of less than 23 m and spans of more than 1300 m. This span sag ratio makes the sag very sensitive to movements of the towers in the longitudinal direction.

It was challenging to obtain force equilibrium in the longitudinal direction due to the top cable. Longer spans and less sag give higher cable forces. In addition, for a span between two towers with a different height, the angle of the cable end is not opposite equal at both sides of the tower attachment point, and nor at the opposite tower.

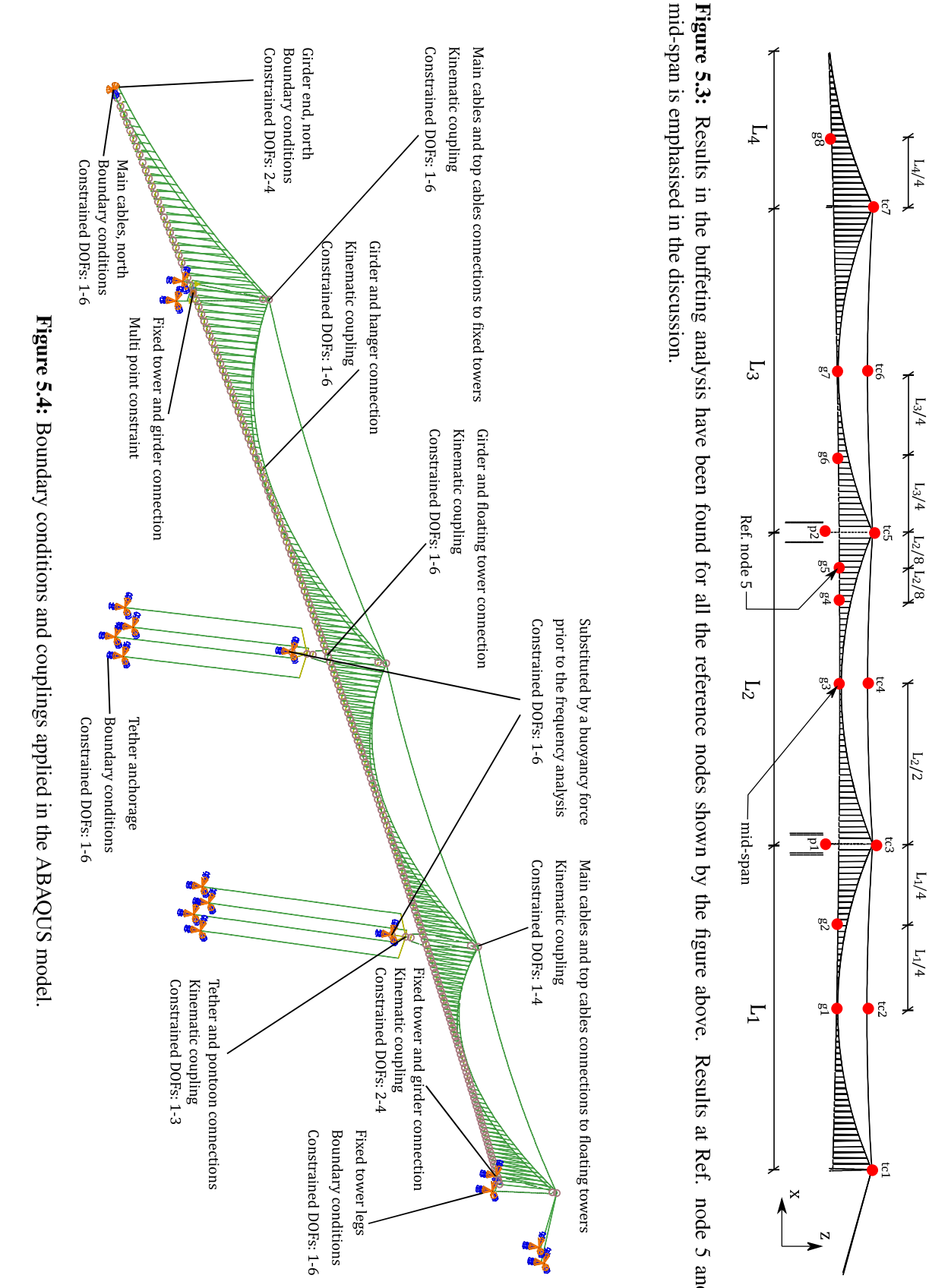

Figure 5.3: Results in the buffeting analysis have been found for all the reference nodes shown by the figure above. Results at Ref. node 5 and at mid-span is emphasised in the discussion.

Figure 5.4: Boundary conditions and couplings applied in the ABAQUS model.

An algorithm was developed to optimize the sag and prestressing force of the cables. To minimize the number of iterations required, the optimization was divided into several steps, and the half step method was applied to ensure an efficient convergence. The top cable was optimized isolated in a separate model since the sag of all three spans was given, and the towers could be modelled as rigid supports. This is illustrated in figure 5.5.

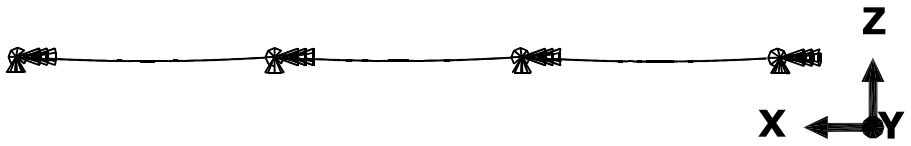

Figure 5.5: The figure illustrates how the top cable was isolated and then exposed to temperature loading to adjust the geometry.

By adding boundary conditions to the top of the two fixed towers, the prestressing of the main cables and the side cable at the south end of the bridge was optimized without being affected by the behaviour of the side span. The main span prestressing force was adjusted using the deflection of the girder as an iteration criteria. The tension in the side cables, at the south end of the bridge, was simultaneously adjusted to minimize the reaction force at the temporary boundary conditions at the top of the southern fixed tower.

Finally, after applying all the temperature loads obtained at this point, the sag of the side span was optimized with an interior loop, which optimized the temperature loading for the given sag. The criterion for the temperature loading was to minimize deflection at the midpoint of the side span. The criterion for the exterior loop was to minimize longitudinal movement of the north tower. No temporary boundary conditions were used for the final optimization.

Because temperature loading is added to the nodes, and the hangers are attached to the main cables, and consist of a single element, they also experience a temperature loading. The procedure could be developed further to ensure that this temperature load has the correct magnitude. Higher accuracy might be possible to obtain with a more advanced optimization procedure.

Temperature loading for the tethers could be found by hand calculation, as the temperature coefficient, the area and the final tension force of the tethers were known from the NPRA-reports.

5.2.6 Steps and loading of the model

The steps required to complete a frequency analysis are listed below.

1. Step 0: The model is loaded with an initial temperature loading to prevent the analysis from crashing.
2. Step 1: The model is loaded with gravity loads. This makes the bridge deviate from the initial geometry.
3. Step 2: The temperature loading is applied to revert the geometry of the bridge to its initial state. Also, temperature load was applied to the tethers, to get the correct tether force.

4. Step 3: In the previous steps, temporary boundary conditions have been placed at the location of the pontoons, to fix their position and rotation. In this step, these temporary boundary conditions were removed and replaced by a corresponding buoyancy force. The buoyancy force could be automatically updated based on the previous analysis if desired, which was very useful during the development of the model. The automatic update procedure was turned off at a later stage to avoid an update in reaction force that could affect results, for instance when evaluating the effect of damage to top cables or tethers.
5. Step 4: In step 4 is the frequency analysis performed. Desired output, such as eigenmodes, eigenfrequencies and modal masses can be extracted from the result file. Note that damping is not taken into account in a regular frequency analysis. This thesis has taken damping into account after the frequency analysis by mode equivalent damping.
6. Step 5: In step 5 a complex frequency analysis was performed. Even though this step was fully developed, it was not implemented to obtain any of the results presented in this thesis.

5.3 Model verification and comparison

This section attempts to verify the ABAQUS model by comparing deflections and forces to target values, and by comparing results to those obtained by the finite element models from RM Bridge and ORCAFLEX, of the same bridge concept, presented by NPRA-reports. The following tests have been performed.

- Comparing eigenfrequencies with and without added mass, to the eigenfrequencies from the NPRA-reports. A presentation and comparison of the eigenfrequencies and eigenmodes are presented in the results. See table 7.1, 7.2 and 7.3 and figure 7.4.
- The tension of the cables is compared with values achieved by the consultants for the same components.
- The geometry was confirmed by looking at the vertical displacement at the middle of the main spans, the side span and the top cable.
- The buoyancy force required to keep the bridge in position after adding the gravity loading was compared to the values given in the NPRA-report.
- To confirm the horizontal stiffness of the bridge, a stiffness test presented in (NPRA, 2016t) was reproduced. By plotting the displacement of the girder, for a point load of 10 MN at mid-span, which is at the middle of the central main span, the results are compared with those from the report.

5.3.1 Model verification

A verification of the effects of the temperature loading was made. In table 5.1, 5.2 and 5.3 can the deviation of the geometry of the model from the initial geometry after applying gravity, buoyancy and temperature loading be seen. The larges deviation is observed for the top cable over the central main span. Because the sag of the top cables is very small, a large change of the sag is experienced for small movements of the tower tops. The deviation is judged to be acceptable

considering that the non-symmetrical appearance makes the reverting of the geometry to its initial state quite challenging. r1, r2 and r3 describes the displacement in the x, y and z-direction.

Vertical displacement of the midspan of the different bridge mainspans and the sidespan	
	Displacement [m]
r3 at span 1	0.2547
r3 at span 2	0.2768
r3 at span 3	0.2020
r3 at the side span	-0.0035

Table 5.1: The table shows how much the midpoints at each girder span deviates from the original geometry after a correction with a temperature loading has been applied.

Vertical displacement of the midspan of the top cable spans	
	Displacement [m]
r3 at Top Cable 1	0.271
r3 at Top Cable 2	-0.731
r3 at Top Cable 3	0.273

Table 5.2: The table shows how much the midpoints at each top cable span deviates from the original geometry after a correction with a temperature loading has been applied.

Longitudinal displacement of the tower tops	
	Displacement [m]
r1 at Tower top 1	0.0014
r1 at Tower top 2	0.1165
r1 at Tower top 3	-0.1043
r1 at Tower top 4	0.0018

Table 5.3: The table shows how much the top of each pylon deviates from the original geometry after a correction with a temperature loading has been applied.

5.3.2 Model comparison

Some comparisons of the ABAQUS model with the models from ORCAFLEX and RM Bridge from the NPRA-reports have been made. The first comparison can be seen in figure 5.6. It depicts the displacement along the bridge girder when a horizontal point load of 10 MN is applied at midspan. The three curves match each other very well.

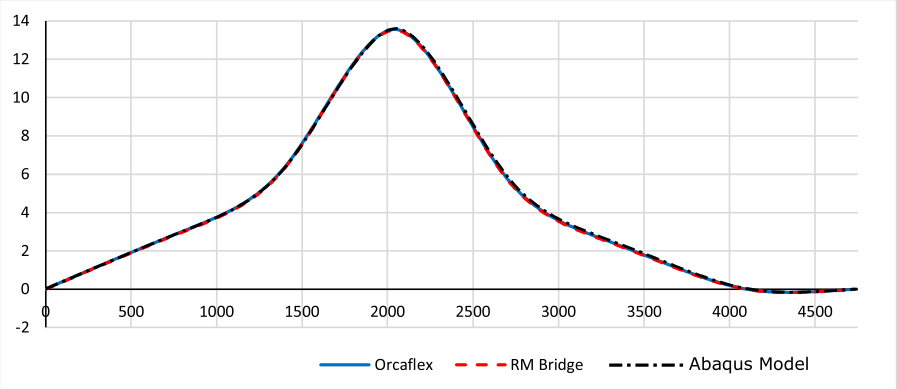

Figure 5.6: The figure compares the horizontal deflection in meters of 3 different FEM models of the same bridge exposed to a lateral point load at the mid-point of the girder.

As the bridge has been modelled after measures given in the NPRA-reports, it is natural to also compare the tension forces in the main cables, the top cables and the buoyancy forces. This comparison can be seen in table 5.4, 5.5 and 5.6. It can be seen that the deviations are small and satisfactory.

Main cable section force			
	Abaqus [MN]	Report [MN]	Deviation [%]
Span 1	143.87	138.8	3.65
Span 2	145.58	138.8	4.88
Span 3	143.83	138.8	3.62

Table 5.4: The table shows a comparison of the main cable forces in the ABAQUS model and the RM Bridge model from the NPRA-report.

Top cable section force			
	Abaqus [MN]	Report [MN]	Deviation [%]
Span 1	66.99	66	1.50
Span 2	63.97	66	-3.07
Span 3	66.95	66	1.44

Table 5.5: The table shows a comparison of the top cable forces in the ABAQUS model and the RM Bridge model from the NPRA-report.

Buoyancy Force			
	Abaqus [MN]	Report [MN]	Deviation [%]
Pontoon 1	1622.5	1724	-5.89
Pontoon 2	1621.3	1724	-5.96

Table 5.6: The table shows a comparison of the buoyancy forces in the ABAQUS model and the RM Bridge model from the NPRA-report.

Chapter 6

Modelling in HydroD and GeniE

In the following sections, the use of the stability analysis tool HydroD and the FEM program GeniE is explained. The modelling of the concrete and steel hull in this thesis is also described. Moreover, the results from the modelling in HydroD and GeniE are presented and compared with the results in the NPRA-reports.

6.1 HydroD and GeniE

HydroD and GeniE are integral parts of the Sesam system developed by DNVGL. GeniE is a FEM software, which is used to create FEM models to be utilized in a finite element analysis (FEA). It is used for both static and dynamic analysis (DNVGL, 2015). HydroD is an interactive application in the Sesam system used for computation of wave loads and motion response, hydrostatics and stability for ships and offshore structures. WADAM and WASIM, which are also a part of the Sesam system, calculates the wave loads and motion. WADAM uses Morison's equation and first and second order 3D potential theory for the wave load calculations (DNVGL, 2014a, Ch 1.1). In addition, the Haskind relation has been used to assess the wave excitation forces. The wave excitation forces have been expressed as transfer functions in terms of force coefficients. An indirect calculation method has been used to estimate the second order wave excitation forces.

The purpose of HydroD and GeniE is to capture the hydrodynamic and static properties of the reinforced concrete pontoon and the steel pontoon. The focus will mainly be on the concrete pontoon for the further analyses, but the steel pontoon is also modelled and compared with the concrete pontoon. The properties of the pontoons, represented by the added mass and damping matrices, the mass inertia matrix, the hydrostatic stiffness matrix and the first and second order wave transfer functions, are exported to Abaqus and MATLAB for post-processing. GeniE models the geometry and meshes the models, while HydroD performs an analysis of the models using the subprocessor, WADAM.

6.2 Pontoon modelling

After some trial and error it was decided to introduce several simplifications to ease the pontoon modelling. Because added mass, added damping and wave excitation forces are only dependent on the exterior geometry, the interior walls of the pontoon was neglected. This simplification reduced calculation time drastically, as fewer elements were used. When obtaining the mass inertia properties, the density of the pontoon was scaled to match the target weight of the pontoon, including the ballast, hence the ballast was assumed to have the exact same movement as the structural parts of the pontoon at all times. The mass and centre of gravity was selected according to target values, when estimating the hydrostatic water plane stiffness.

The hydrodynamic properties are dependent on the submerged body, i.e. the position of the water line. The draft, centre of buoyancy and centre of gravity are provided in NPRA-reports.

6.2.1 Concrete hull modelling

Several models of the concrete hull have been developed in HydroD and GeniE. Only the final model is presented here. An explanation of each model of the concrete hull can be found in the appendix, C.1.

One fourth of the concrete hull is modelled and mirrored about the XZ- and the YZ-plane as the pontoon is double symmetric.

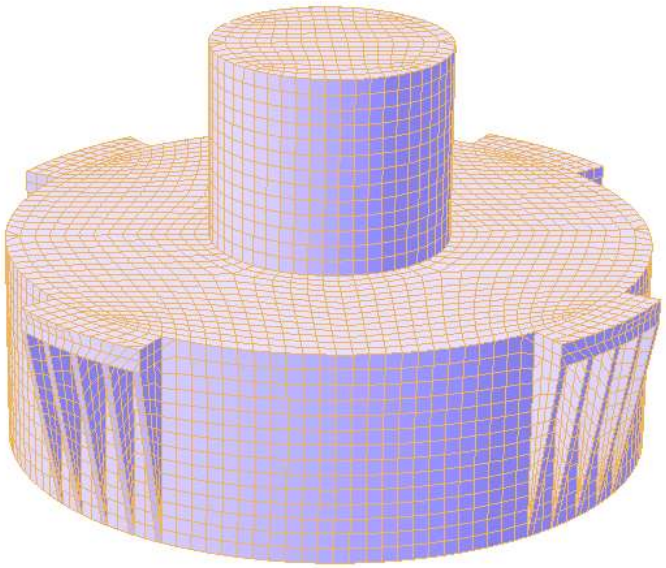

Figure 6.1: The final GeniE FEM-model of the concrete pontoon, mirrored about the XZ- and the YZ-plane.

The final double-symmetric model of the pontoon used can be seen in figure 6.1.

As only one forth of both the steel and the concrete hull were modelled, the corresponding wave excitation forces had to be mirrored according to figure 6.2 when used in the buffeting analysis in

MATLAB.

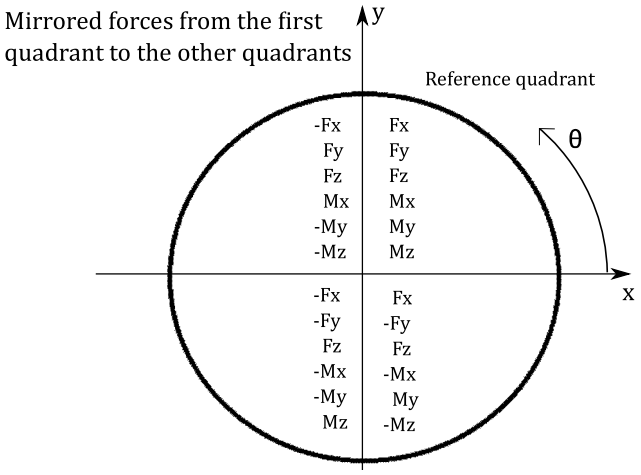

Figure 6.2: The excitation forces have been mirrored as follows due to symmetry. Only the first quadrant were computed in HydroD.

6.2.2 Sea surface modelling

To take into account the second order forces the sea surface, figure 6.3, has to be modelled in GeniE and extracted to HydroD for analysis. The diameter of the free surface needs to be 5-10 times larger than the largest diameter of the pontoon. The sea surface modelled in this thesis has a diameter of 500m. The mesh has to be finer closer to the pontoon. It is important that the mesh for the pontoon and the sea surface matches, as well as no triangular elements can be used for the modelling of the sea surface. Also, the sea surface has to be circular (DNVGL, 2014a).

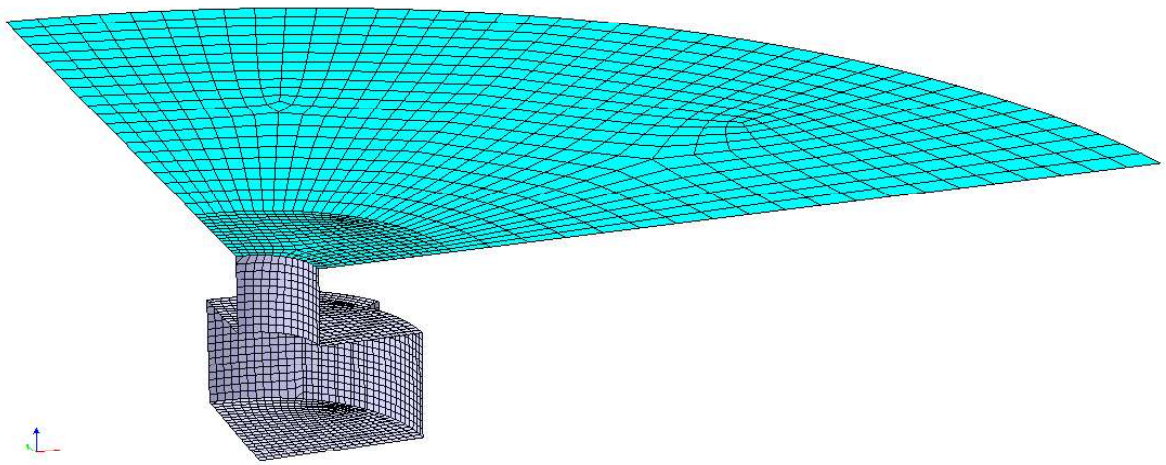

Figure 6.3: One quarter of the modelled sea surface in HydroD used with the concrete hull.

To ease the mesh fitting of the sea surface and pontoon, the 6 m tall freeboard of the pontoon were removed, as everything above sea level is cut away automatically in HydroD anyway. This resulted in a concrete pontoon that was 47.5 m tall, the same as the draft.

6.2.3 Steel hull modelling

The same reasoning was made for the steel pontoon, figure 6.4, as for the concrete pontoon. Only one fourth of the model was accurately modelled with a mesh size of approximately 2 m $\times$ 2 m. Everything on the pontoon above the water level was cut away, as those parts are not needed. The compartments were neglected as no information about the distribution of the ballast in the different tanks are provided. Added mass, added damping and wave excitation forces, extracted from HydroD, are as mentioned purely dependent on the user-defined waterline and geometry of the model. A sea surface, similar to the concrete pontoon's sea surface, with a diameter of 500 m, was also modelled for the steel pontoon.

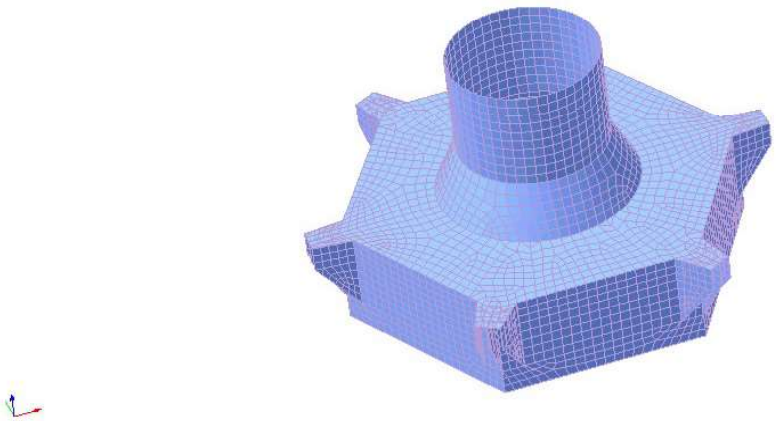

Figure 6.4: Double symmetric configuration of the steel pontoon.

6.3 Model verification

A validation of the analysis results from HydroD, for both the concrete and the steel hull alternative, was made by carrying out a comparison between the obtained results and the values found in the NPRA-reports. The centre of gravity and the centre of buoyancy are listed in the appendix in table B.3, and was found to correspond well with data given in the NPRA-reports. Because the stiffness provided by the tethers and the superstructure is accounted for by the modelling of these elements in ABAQUS, the only additional stiffness that should be added for the pontoon is the hydrodynamic water plane stiffness. A different approach is believed to be employed in the assessment of the hydrodynamic water plane stiffness in the NPRA-reports, hence the values from AQWA and HydroD could not be compared as the assumptions were not explicitly stated.

6.3.1 Mesh size validation of the concrete hull

The concrete alternative was analysed for several different mesh sizes, see figure 6.5. Mesh size 1 denotes a mesh size of approximately 1 m $\times$ 1 m. As the analyses could be very time consuming, especially the second order analyses, it was desirable to use as few elements as possible.

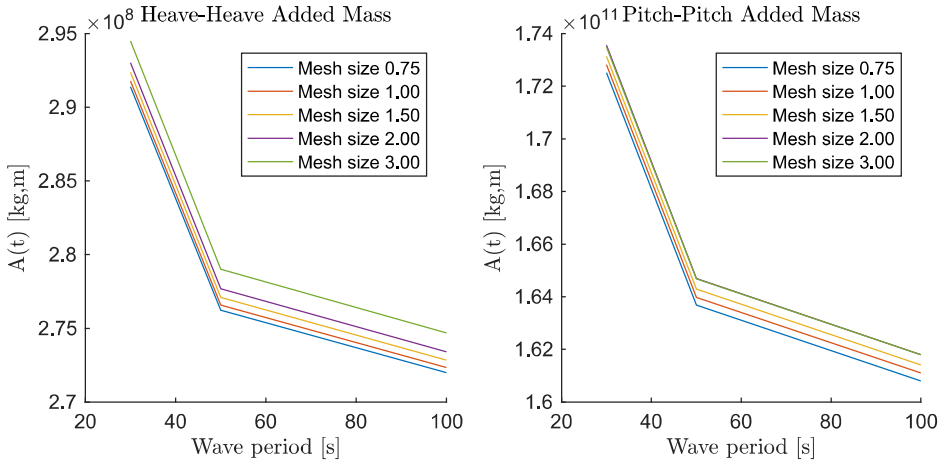

Figure 6.5: The added mass heave and pitch values for the final pontoon option are plotted for 5 different mesh sizes at 3 different periods.

The mesh size has affected the verification results, but the effects are rather small. This can be seen in figure 6.5, note that the axes are scaled up and could yield an interpretation of big differences between the mesh sizes, which is not the case. For added mass in heave, the difference in the values for the mesh sizes 1 and 3 are ranging between 1% and 2%. The trend is that the HydroD results converge towards a lower bound for smaller mesh sizes. It was then judged based on figure 6.5 that a mesh size of 2 was sufficient for the modelling. This choice of mesh size compared to a mesh size of 0.75 drastically reduced the calculation time needed to perform an analysis.

6.3.2 Verification of the first order dynamic properties

A comparison of the results from HydroD for both the steel and the concrete hull have been compared to the results from AQWA, provided by the report (NPRA, 2016s). The added mass, the added damping and the QTF for both the first and second order wave excitation forces had been compared. Results are calculated with the centre of the water plane area as a reference point. The data from the NPRA-reports were only given graphically. The results obtained from HydroD are plotted on top of these graphs by the use of MATLAB to make a comparison.

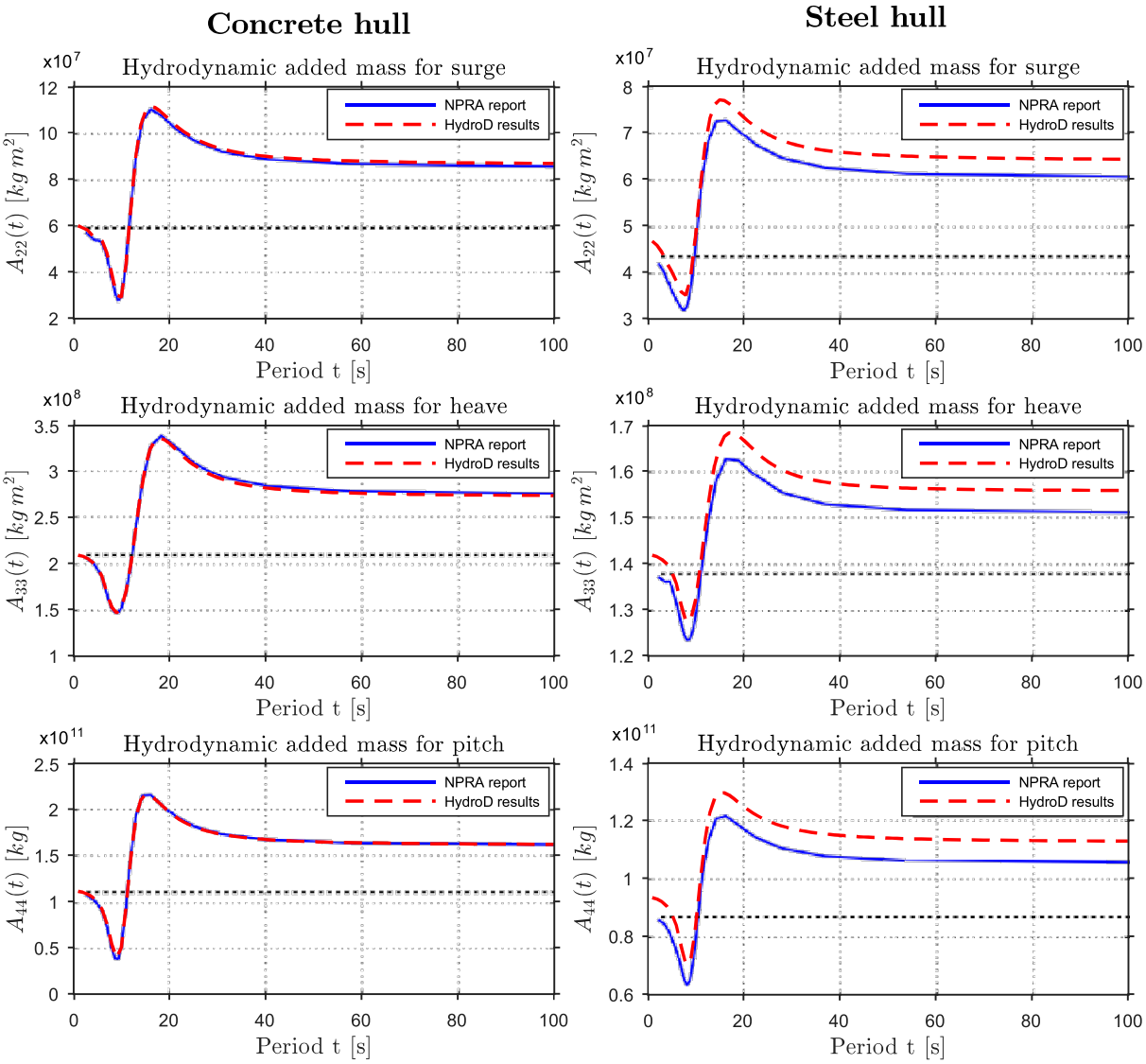

Figure 6.6: Comparison of some of the entries in the added mass matrix modelled in HydroD and in AQWA.

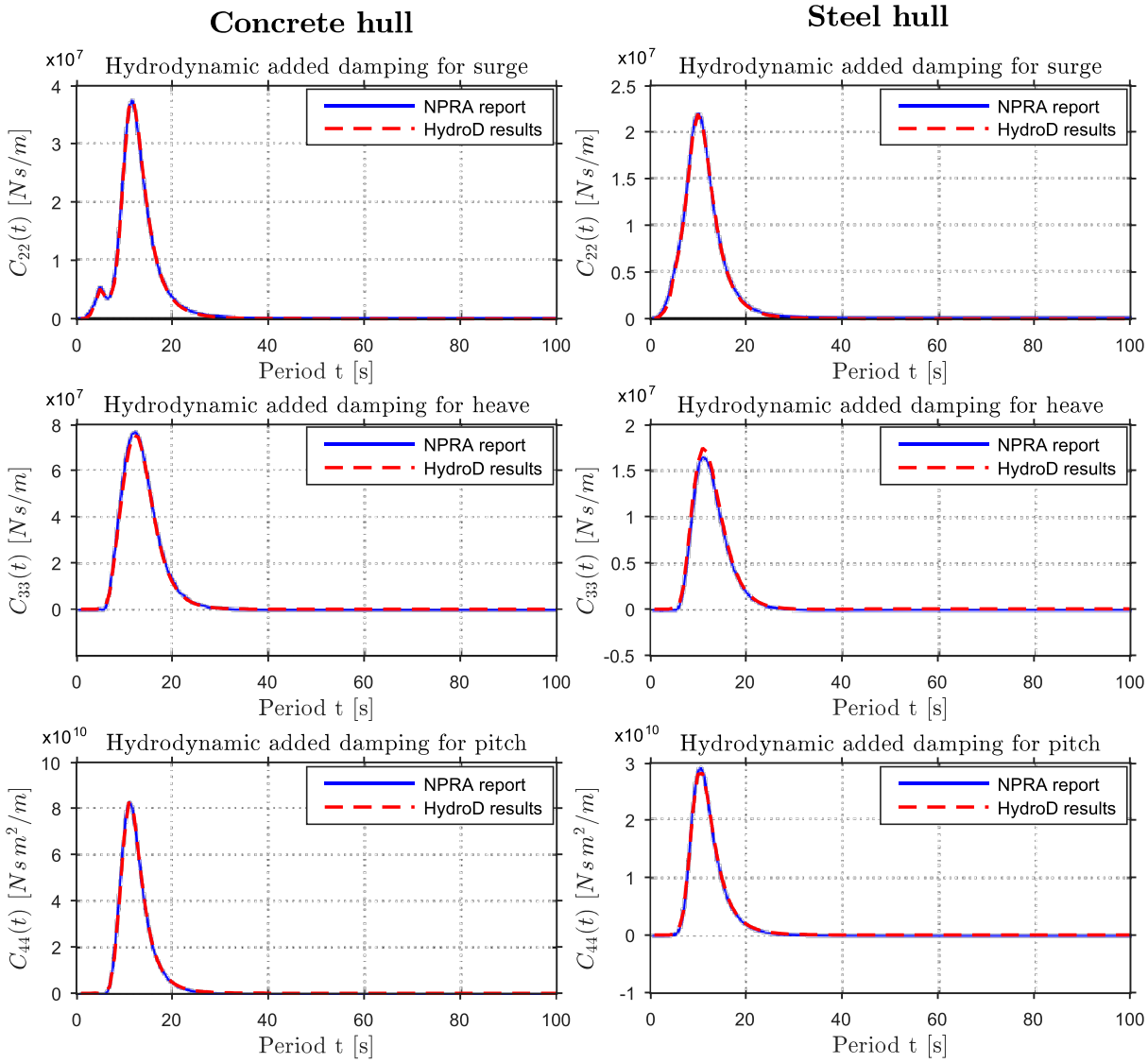

Figure 6.7: Comparison of some of the entries in the added damping matrix modelled in HydroD and in AQWA.

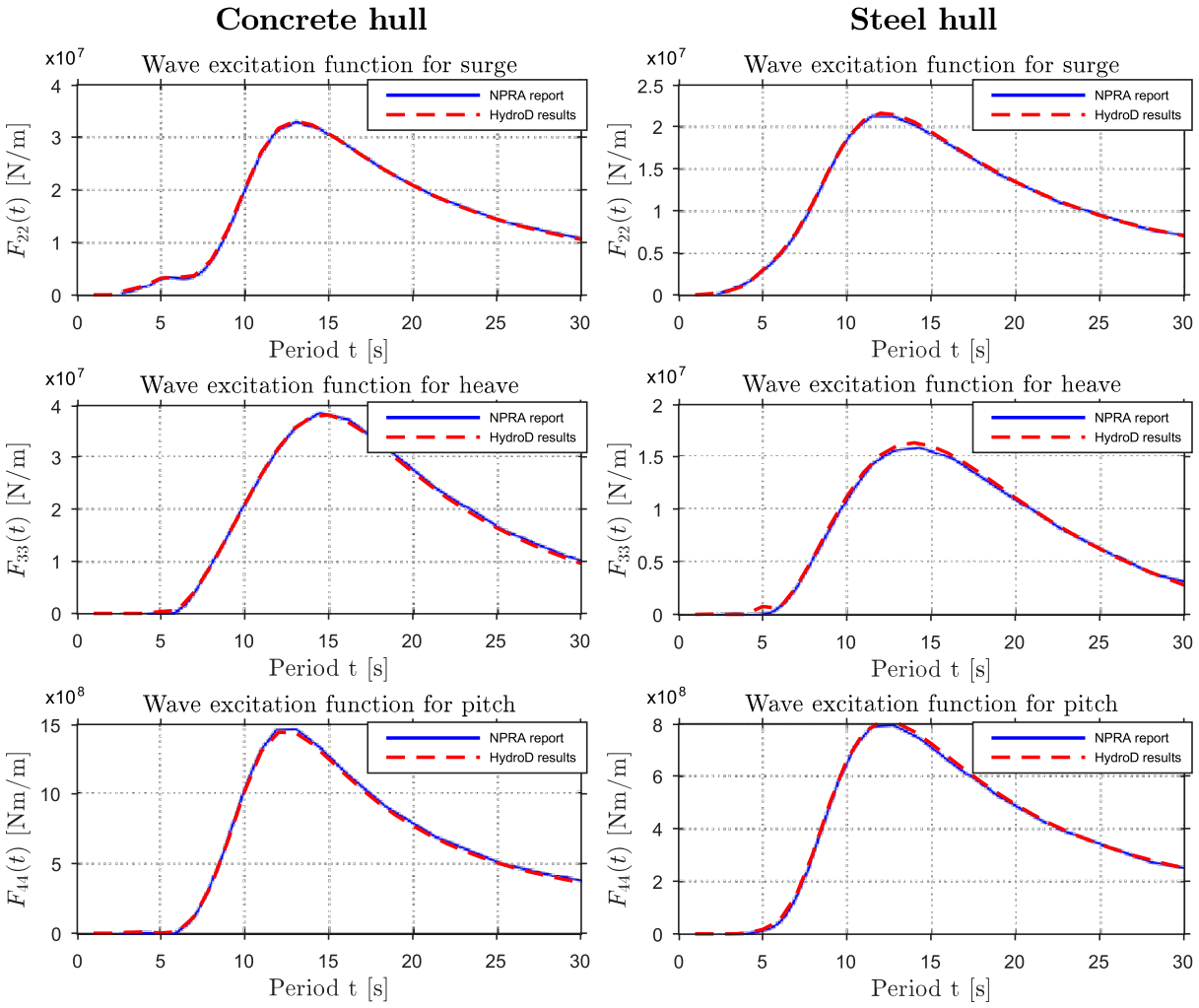

Figure 6.8: Comparison of the transfer function for the first order wave excitation forces modelled in HydroD and in AQWA.

The results in figure 6.6, 6.7 and 6.8 shows that the results from HydroD corresponds well with the results of the report (NPRA, 2016s). The only discrepancy is the added mass terms of the steel pontoon, which differs at most 5% from the NPRA-results. The error is believed to be caused by small differences in the geometry, as similar discrepancies were experienced for the concrete hull before improving the accuracy of the geometry of the tether porches. The tether porches of the steel hull were however very difficult to model exact, and it was decided that the results were accurate enough for the purpose of the model.

It should also be mentioned that the yaw parameter, which is not presented in this thesis, is off by 20% compared to the results in NPRA-reports, most likely because the yaw parameter is very sensitive to the modelling of water flow around the tether porches. Because the sharp edges introduced by the tether porches in both the steel and the concrete hull could create irrotational flow, which is a violation of one of the assumptions in Bernoulli's equation, it could cause problems for the calculations in WADAM, which is based on linear potential theory. For a concrete hull

modelled without tether porches, the yaw parameter becomes virtually equal to zero, as expected for a cylinder shaped object.

6.3.3 Verification of the second order dynamic properties

The quadratic transfer functions obtained from second order analysis in HydroD (this thesis) and AQWA (NPRA-report) are presented in figure 6.9 and 6.10. The pattern of the QTFs is similar for frequencies below 0.2 Hz. For the QTF from HydroD rapid changes can be seen at higher frequencies. As these peaks have magnitudes larger than those obtained in the report (NPRA, 2016s), it is suspected that these rapid changes of the QTF are numerical noise. Especially the QTF plots of the amplitude, shown in the appendix in figure C.2, have very distinct peaks at the end of the frequency range.

It is suspected that the numerical noise is caused by a too rough mesh size, as the wavelengths of higher frequencies can be very short. The wavelengths can be calculated in HydroD, i.e. the highest wave frequency, 2 rad/s, has a corresponding wavelength of 15.4 m. The effects of a finer mesh size have not been checked due to the fact that a second order analysis is very time consuming. Another possible explanation for the difference in the QTFs is that the consultants might have used a smoothing function. It could also be that a direct calculation method was used to calculate the QTF in AQWA, while an indirect calculation method was utilized in HydroD. By direct calculation method of the second order forces it is meant pressure integration over the instantaneous wetted surface of the body, (Lewandowski, 2004,, Ch.5.9.1,p.327). The QTF for the both the amplitude and the steel hull alternative are given in the appendix C.2.

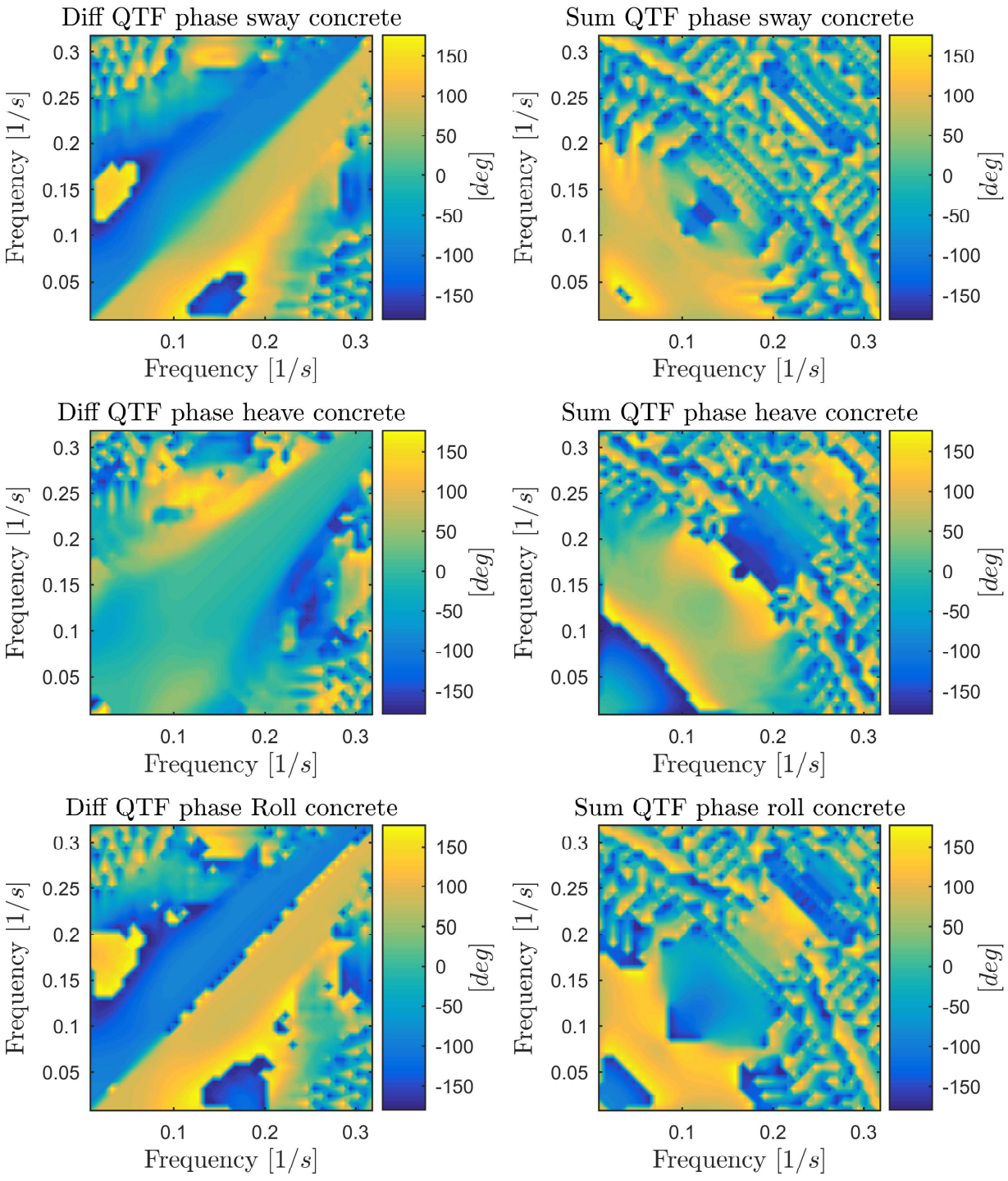

Figure 6.9: The QTF from HydroD for phase angles for the concrete hull. Wave direction 90 degrees.

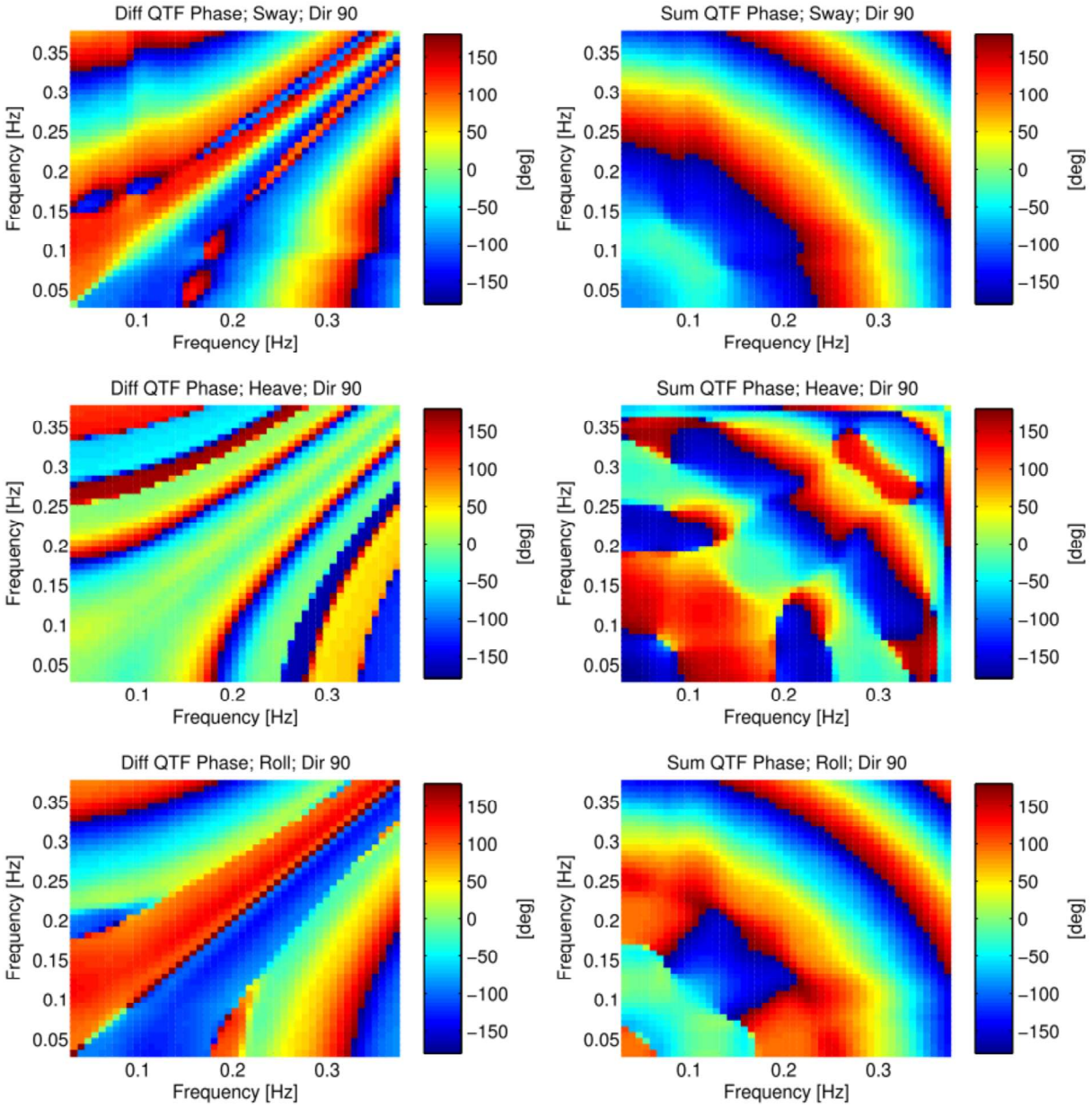

Figure 6.10: The QTF from AQWA for phase angles for the concrete hull from the consultants. Wave direction 90 degrees.

As the noise in the QTF was expected to give unreasonably large second order forces, a smoothing function has been applied to the QTF calculated in HydroD and the resulting QTF is presented in figure 6.11. The effect on the load spectrum is discussed later in section 7.3.5. The smoothing of the peaks can be seen to be as intended. Note that the range of the colour bars are different between the smoothed and non-smoothed QTFs.

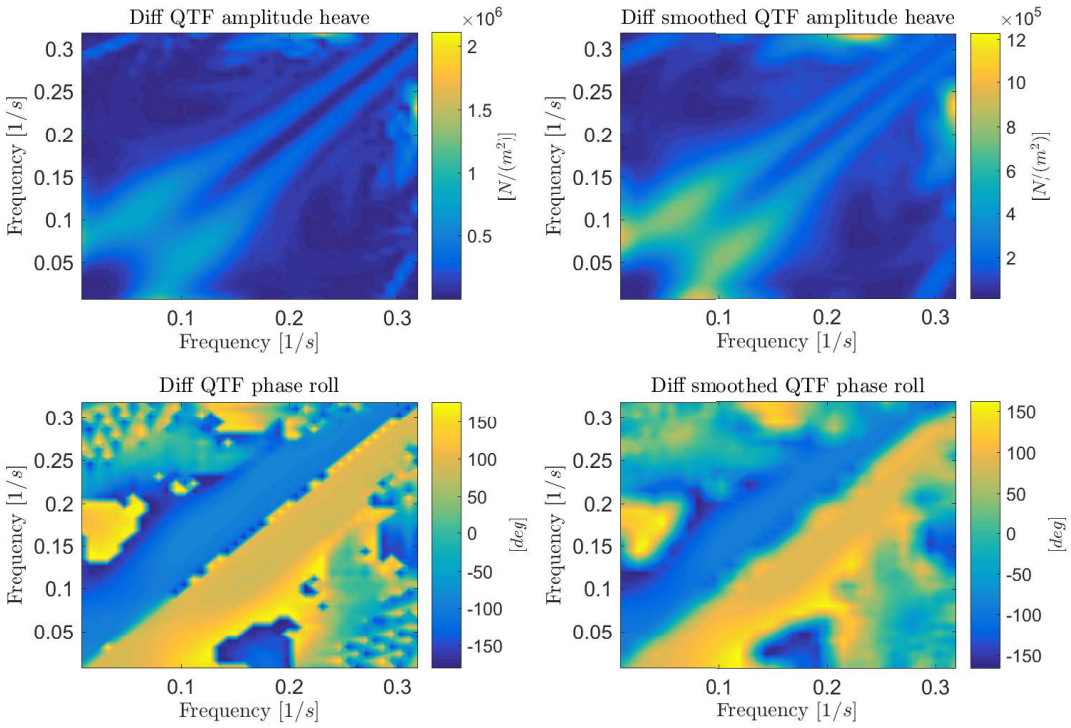

Figure 6.11: A comparison of the QTF that is smoothed versus the QTF that is not smoothed. Note the difference in the range of the colour bar in the QTF for the amplitude between the smoothed and non-smoothed QTF.

6.3.4 Discussion about the input parameters to the HydroD analysis

Frequency range

The floating towers are anchored at depths at 550 m and 450 m. An average anchorage depth of 500 m is used to model the sea state surrounding the pontoon in HydroD, because the sea state is virtually unaffected by the difference due to the significant water depth. The wave frequencies and heading angles have been distributed as presented in table 6.1. Note that the heading angles have been calculated between 0-90 degrees and mirrored to obtain heading angles in the range from 0 to 360 degrees.

Hydrodynamic parameters	Frequency range [rad/s]	Heading angles [degrees]
Added mass, added damping	[0.05:0.001:0.08; 0.085:0.005:0.38; 0.39:0.01:0.98; 1:0.1:6]	Independent
1st order wave excitation forces	[0.05:0.001:0.08; 0.085:0.005:0.38; 0.39:0.01:0.98; 1:0.1:6]	[0:5:360]
2nd order wave excitation forces	[0.05:0.05:2]	[0:30:360]

Table 6.1: The frequency ranges and headings angles inputed into HydroD to assess the hydrodynamic parameters.

The reason for the finer resolution at lower frequencies is that it is desirable to capture all the eigenfrequencies of the lowest modes. The range of resolution is set such that it captures the lowest eigenfrequencies with a solid margin. The upper bound is set to include all the modes from ABAQUS. From ABAQUS it is exported 300 modes, whereas mode 300 has an eigenfrequency of 5.57 rad/s. The 6 rad/s limit should then capture the effects of all these modes. The evaluation of the hydrodynamic parameters at frequencies above and below the natural frequencies extracted from ABAQUS is due to the fact that an interpolation procedure is utilized in the buffeting analysis in MATLAB. At a later stage, it was decided only to use 115 modes in the overall analysis, as was discussed in section 4.2.2.

The frequency range for the second order wave excitation forces is set to be as small as possible due to the extremely time consuming second order analysis. The step size should, at worst, not be bigger than the first natural period of the bridge, (Naess and Moan, 2013, p. 260). 0.05 rad/s was selected to achieve a sufficient accuracy and a feasable calculation time. The range is defined to be such that it captures the JONSWAP spectra for the wind generated waves, $T_p = 6$ s, and the swell generated waves, $T_p = 16$ s, see figure 3.6.

With the results for 0, 30, 60 and 90 degrees, the effect of the directional wave distribution could be taken into account by cubic interpolation.

In order to include the second order wave forces, the second order transfer function had to be imported from the WADAM analysis. The second order WADAM analysis is a very time consuming analysis, and can last for weeks if a bad selection of input parameters is made. A MATLAB script was developed to reduce the run time for an analysis in HydroD, as it was discovered that WADAM uses more than 50 % of the calculation time to find results that are not required for the buffeting analysis in this thesis. This is further outlined in the appendix in section C.3.

Chapter 7

Results and Discussion

7.1 The bridge behaviour - eigenfrequencies and eigenmodes

The following section presents the obtained structural properties of the bridge in terms of eigenfrequencies and eigenmodes. The eigenfrequencies are also compared to the models of the same bridge in the NPRA-reports.

	ABAQUS	**ORCAFLEX**		**RM Bridge**	
	Period $[s]$	Period $[s]$	%	Period $[s]$	%
Mode 1	80.2	82.0	-2.2	79.8	0.5
Mode 2	59.3	61.4	-3.5	59.8	-0.8
Mode 3	23.2	25.7	-10.8	25.5	-9.9
Mode 4	20.3	19.9	2.0	20.6	-1.5
Mode 5	18.4	18.2	1.1	18.7	-1.6
Mode 6	15.4	15.4	0.0	15.8	-2.6
Mode 7	12.7	12.4	2.4	12.2	3.9
Mode 8	12.5	11.6	7.2	11.3	9.6
Mode 9	11.9	9.5	20.2	10.0	16.0
Mode 10	11.6	9.4	19.0	9.9	14.7

Table 7.1: The eigenfrequencies of the ABAQUS-model without hydrodynamic properties compared to the RM Bridge model and the ORCAFLEX model of the bridge without hydrodynamic properties from the NPRA-reports. The deviation of the ABAQUS model compared to the models from the NPRA-reports are given in the columns marked with %.

	ABAQUS and **HydroD**	**ORCAFLEX** and **AQWA**	
	Period $[s]$	Period $[s]$	%
Mode 1	101.4	102.7	-1.3
Mode 2	75.7	77.7	-2.6
Mode 3	29.0	32.0	-9.4
Mode 4	20.4	19.9	2.5
Mode 5	18.7	18.3	2.1
Mode 6	15.8	15.8	0.0
Mode 7	13.1	12.7	3.1
Mode 8	12.6	11.7	7.1
Mode 9	12.3	9.6	22.0
Mode 10	11.7	9.6	17.9

Table 7.2: The eigenfrequencies of the ABAQUS-model with hydrodynamic properties of the concrete hull from HydroD compared to the ORCAFLEX model of the bridge with hydrodynamic properties from the NPRA-reports.

In table 7.1 are the eigenfrequencies of the bridge alternative with the concrete hull compared to models in RM Bridge and ORCAFLEX of the same bridge concept from the NPRA-reports. No hydrodynamic or aerodynamic effects are included. The first six modes have fairly similar

eigenfrequencies, but some variation can be observed, in particular for mode 3, which is the 1st vertical mode. The mode shape for mode 3, achieved in this thesis and shown in figure 7.2, is identical to that given by the report NPRA (2016g), even though some variation is observed for the eigenfrequency. Mode 1 and 2, which are the most important contributors to the lateral response, have almost the exact same frequency for all alternatives. After mode 6, mode shapes do not occur in the same order for the model in this thesis, and the ORCAFLEX model. They have, however, been compared according to their mode number. As modes are not presented for all models in the NPRA-reports, the discrepancy might be larger than suggested by the tables above. Nonetheless, some variation between the results of this model and the models presented in the NPRA-reports are expected, as different assumptions for the geometry most likely are made and a different software is used for the calculations.

In table 7.2 are the bridge alternative with the concrete hull modelled in ABAQUS with hydrodynamic properties from HydroD compared to the ORCAFLEX model, when hydrodynamic properties from AQWA are included. As expected, the eigenperiods increase quite a lot when the hydrodynamic properties are included. The trend of the deviation between the ABAQUS and ORCAFLEX model is more or less the same as for the structural model without hydrodynamic properties. Note that by including the added mass and added damping due to the motion of the bridge, the first natural period is increased by roughly 20 s. This implies that the hydrodynamic properties are very important for the bridge behaviour, and can not be ignored. This becomes particularly apparent when keeping in mind that the loading is frequency dependent.

In table 7.3 are the eigenfrequencies of the bridge with the steel hulls compared to the same model made in ORCAFLEX found in the NPRA-reports. The calculations have included hydrodynamic properties.

	ABAQUS and **HydroD**	**ORCAFLEX** and **AQWA**	
	Period $[s]$	Period $[s]$	%
Mode 1	92.1	90.6	1.6
Mode 2	66.0	65.7	0.5
Mode 3	24.8	26.5	-6.9
Mode 4	20.3	19.8	2.5
Mode 5	18.5	18.2	1.6
Mode 6	15.8	15.6	1.3
Mode 7	12.7	12.5	1.6
Mode 8	11.8	11.7	0.8
Mode 9	11.4	9.6	15.8
Mode 10	10.7	9.6	10.3

Table 7.3: The eigenfrequencies of the ABAQUS-model with hydrodynamic properties of the steel hull from HydroD compared to the ORCAFLEX model of the bridge with hydrodynamic properties from the NPRA-reports. The deviation of the model from the NPRA-reports are given in the column marked with %.

Even though both the mode shapes and the mode numbers only match for the lower modes, similar mode shapes can be observed for similar frequencies. This becomes evident when modes of higher frequencies are compared. Also note the difference between the first eigenperiods for the the two different bridge alternatives, 92.1 s and 101.4 s. This implies that some eigenfrequencies are quite sensitive to the pontoon and tether design.

The mode shapes of the bridge for the first 136 modes are presented in section D.2 in the appendix, but a selection of these are showed in figure 7.4. As the thesis developed, different properties have been added to the structural model in ABAQUS. The modes shapes of four of these alternatives are compared in figure 7.4. Alternative D was not fully developed at the start of the buffeting analyses, and, thus, it has not been used due to the purpose of being consistent to be able to compare results. Implementing this in the buffeting analyses is left for further work.

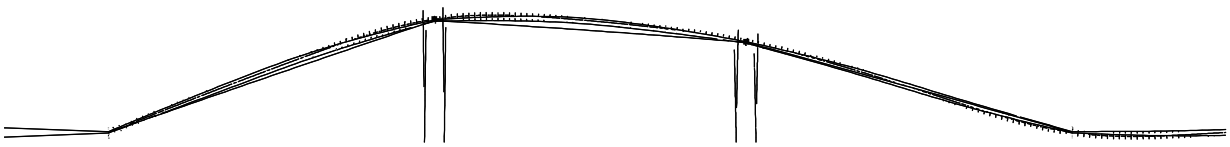

Figure 7.1: First horizontal mode shape from the ABAQUS model viewed from above.

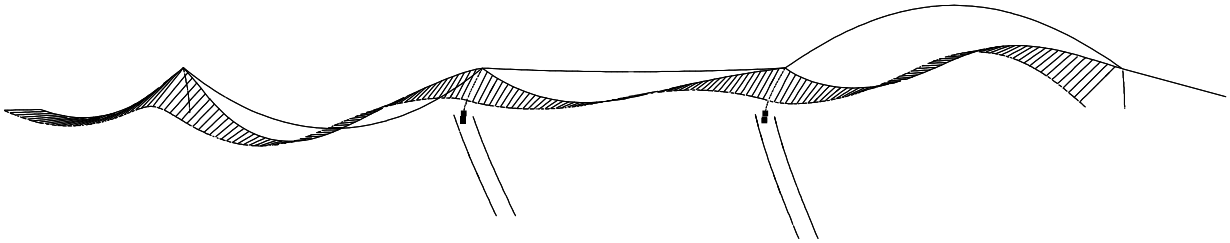

Figure 7.2: First vertical mode shape from the ABAQUS model viewed from the side.

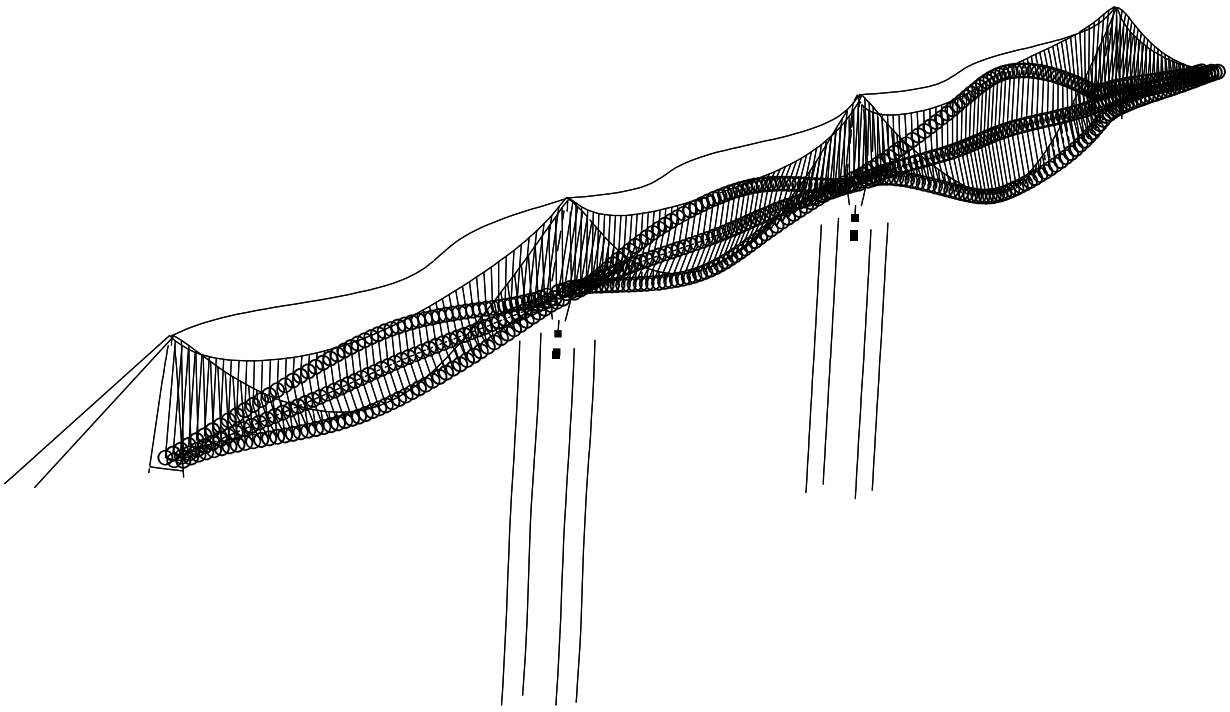

Figure 7.3: The first pure torsional mode shape from the ABAQUS model. The circles mark the connection points between hangers and the girder.

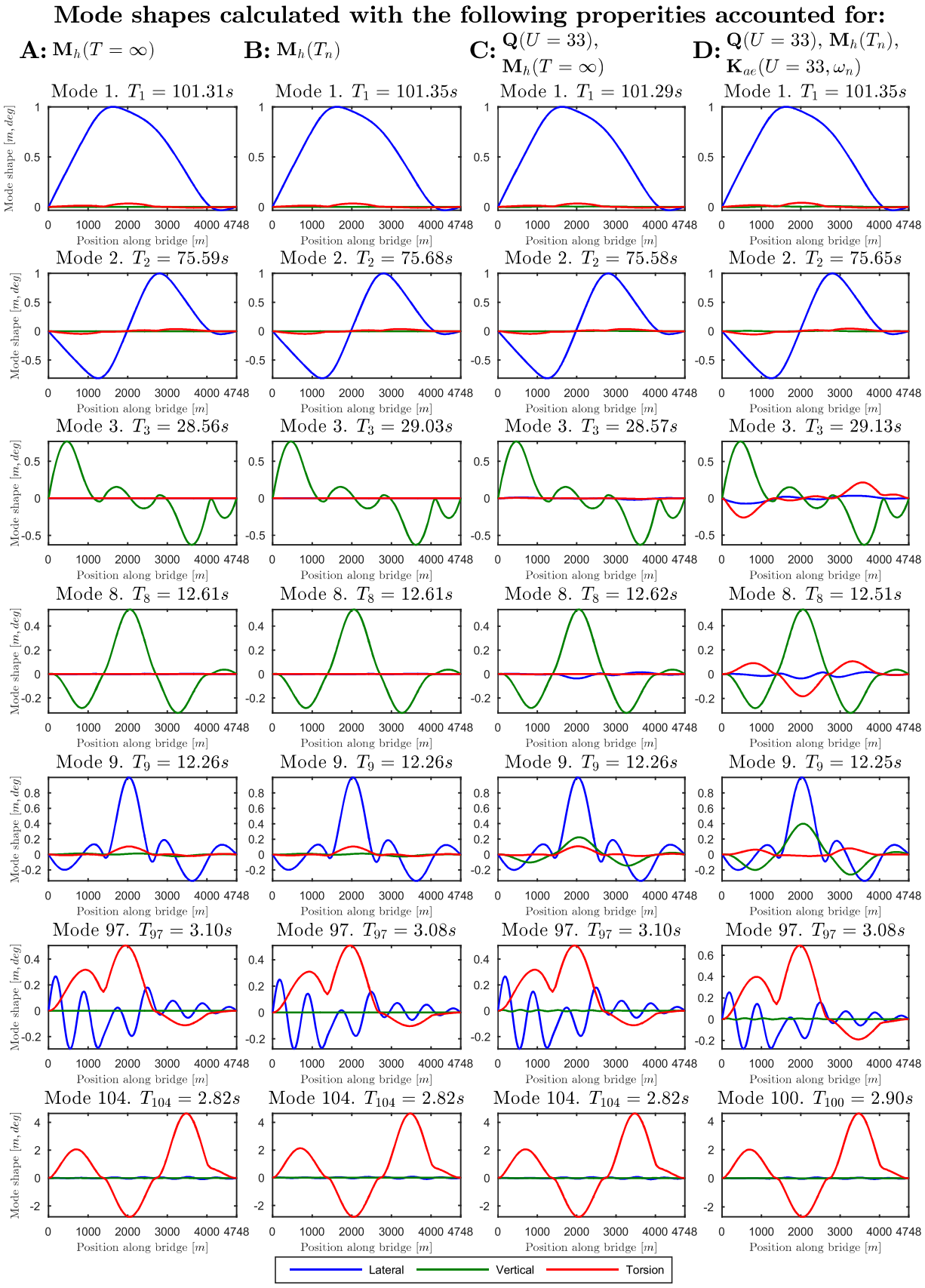

Figure 7.4: Mode shapes for procedures A, B, C and D. Caption continues on the next page.

Figure 7.4: Illustration of how taking into account the correct added mass, $\mathbf{M}_h$, static wind loading on the bridge, $\mathbf{Q}$, and aerodynamic stiffness, $\mathbf{K}_{ae}$, affects the obtained mode shapes of the girder. Note that alternative C has been used for the buffeting analysis, as the procedure to obtain the results for alternative D was not fully developed at the time, and it is more computationally expensive. Procedure B and D can easily be changed to include the correct aerodynamic and hydrodynamic damping as well, by performing a complex frequency analysis.

In figure 7.4 it should be noted that the mode shapes are asymmetrical and that they are plotted for the bridge girder only. This is due to the asymmetries of the bridge. It can be seen that the four different alternatives do not deviate much from each other. The two first modes are horizontal, the third mode is vertical and the first mode of pure torsional motion only, is either mode 100 or mode 104, dependent on the procedure used. Note that using the correct added mass appears to have a larger effect on the mode shape and the eigenperiod than adding the static wind loading. By correct added mass it is meant using the added mass which corresponds to the respective frequency considered and not the infinite added mass. Accounting for aerodynamic stiffness proves to have the largest impact on the eigenmodes. As shown in figure 7.4, torsional mode 104 changes eigenperiod with almost 3 percent and becomes mode number 100.

In summary, the eigenfrequencies of the ABAQUS model look reasonable and correspond well with the models from the NPRA reports, both for the steel hull and the concrete hull alternative. The largest discrepancies are experienced for the vertical modes. The hydrodynamic properties of the pontoons change the eigenfrequencies quite a lot, and these effects cannot be ignored in the modelling. Using infinite added mass in the ABAQUS analysis does, however, generate sufficiently accurate mode shapes.

7.2 Flutter analysis

In this section are the results of the flutter analyses presented. The flutter analyses have been performed for the bridge alternative with the concrete pontoons. It has been investigated if the critical mode and the critical velocity that induces instability is affected by the number of modes included in the flutter analyses. It has also been studied if the results are dependent on the type of aerodynamic derivatives (AD) used to establish $\mathbf{K}_{ae}$ and $\mathbf{C}_{ae}$ to be used in the complex eigenvalue problem. Lastly, the fluttering mode shape has been assessed.

In the table 7.4 are the primary results from the flutter analyses presented.

The instability analyses have been carried out by including the aerodynamic damping and stiffness contributions from the motion induced forces. The effect of accounting for the aerodynamic damping and stiffness, along the bridge girder and the top cable, has been studied. It can be seen from table 7.4 that the inclusion of the top cable in the instability analyses is virtually insignificant. There is only a slight increase of the critical mean wind velocity when the top cable has been included in the analysis.

	Critical velocity U_{cr} $[m/s]$		**Critical frequency** ω_{cr} $[rad/s]$		**Critical mode number**	
Number of modes included in the analysis	150 modes	5 modes	150 modes	5 modes	150 modes	5 modes
Empirical AD - With top cable	85.09	96.40	1.71	1.23	104	104
Empirical AD - Without top cable	85.08	96.34	1.71	1.23	104	104
Number of modes included in the analysis	150 modes	6 modes	150 modes	6 modes	150 modes	6 modes
Quasi-static AD - With top cable	61.84	74.01	2.00	1.92	97	97
Quasi-static AD - Without top cable	61.77	73.54	2.00	1.93	97	97

Table 7.4: The table shows the critical velocities and the critical frequencies that induce instability. Empirical ADs based on the Hardanger bridge cross section have been used, and ADs derived from quasi-static theory have been used. The analyses have been using a different amount of still air modes, and they have been carried out with and without the inclusion of the effects of wind loading on the top cable. Without top cable should however not be interpreted as if the top cable was removed from the structural model.

A quasi-static approach was used to add the effect of the top cable. Since the top cable has a circular cross section, all coefficients are zero except the drag coefficient. This ensures that regardless of the movement of the top cable, the added damping contribution will be positive. From equation 3.23 and equation 3.2.2, it can be seen that including only the drag coefficient yields a negative $\hat{\mathbf{C}}_{ae}$ and thus a positive damping contribution to all nodes along the top cable. This explains why the critical velocity goes up when the top cable is included in the analysis.

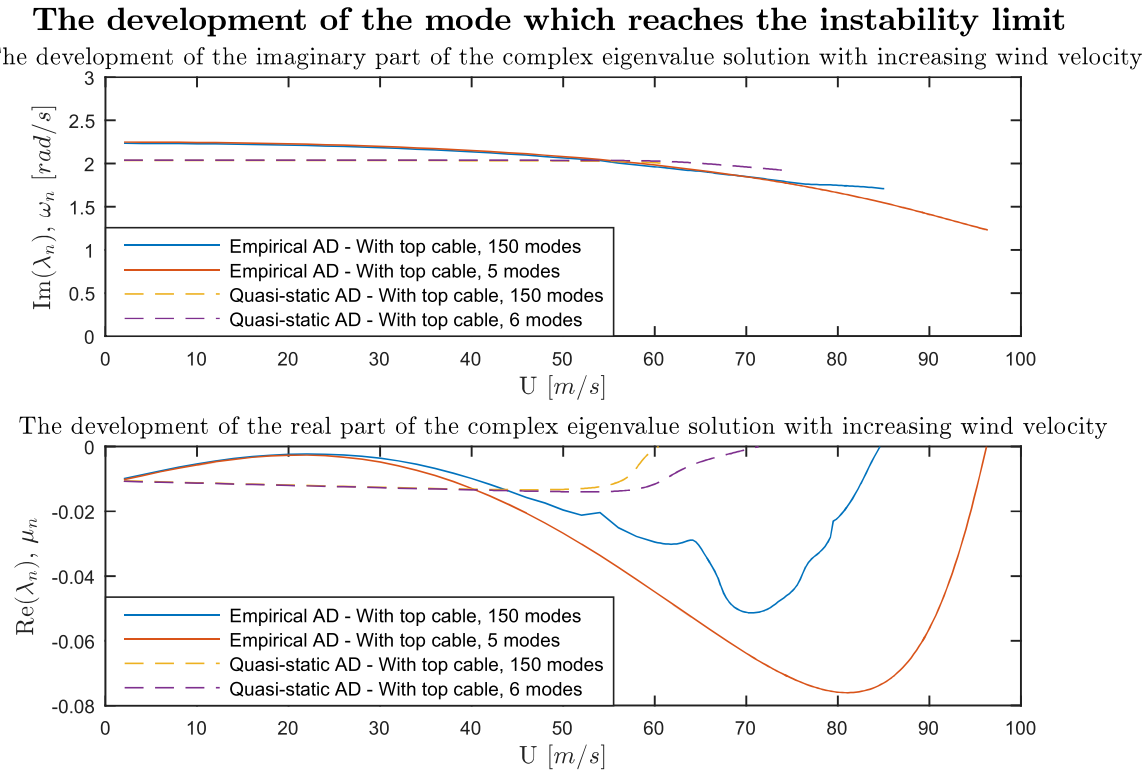

Figure 7.5: Critical eigenvalue solution for different ADs and different number of modes.

Moreover, the two different methods, empirical ADs and quasi-static ADs, used to establish the $\mathbf{K}_{ae}$ and the $\mathbf{C}_{ae}$ yield significantly different results. It is believed that the quasi-static ADs yield an estimate that is highly uncertain due to several reasons. Quasi-static coefficients established for relatively low mean wind velocities are very inaccurate for high mean wind velocities. In addition, the emperical ADs are based on wind tunnel testing for a similar cross section, while the quasi-static coefficients are determined numerically. Thus, the results from the method comprising the empirical AD have been emphasised and further elaborated.

It has also been found that the critical wind velocity that induces instability increases with less than 15 % when only a few carefully selected still air mode shapes are used in the fluttering analysis. This demonstrates the significant contributions these modes have for flutter to occur. Also, the critical mode which induces instability is not affected by the number of modes included in the analysis as long as the critical mode is one of the modes that are included in the analysis.

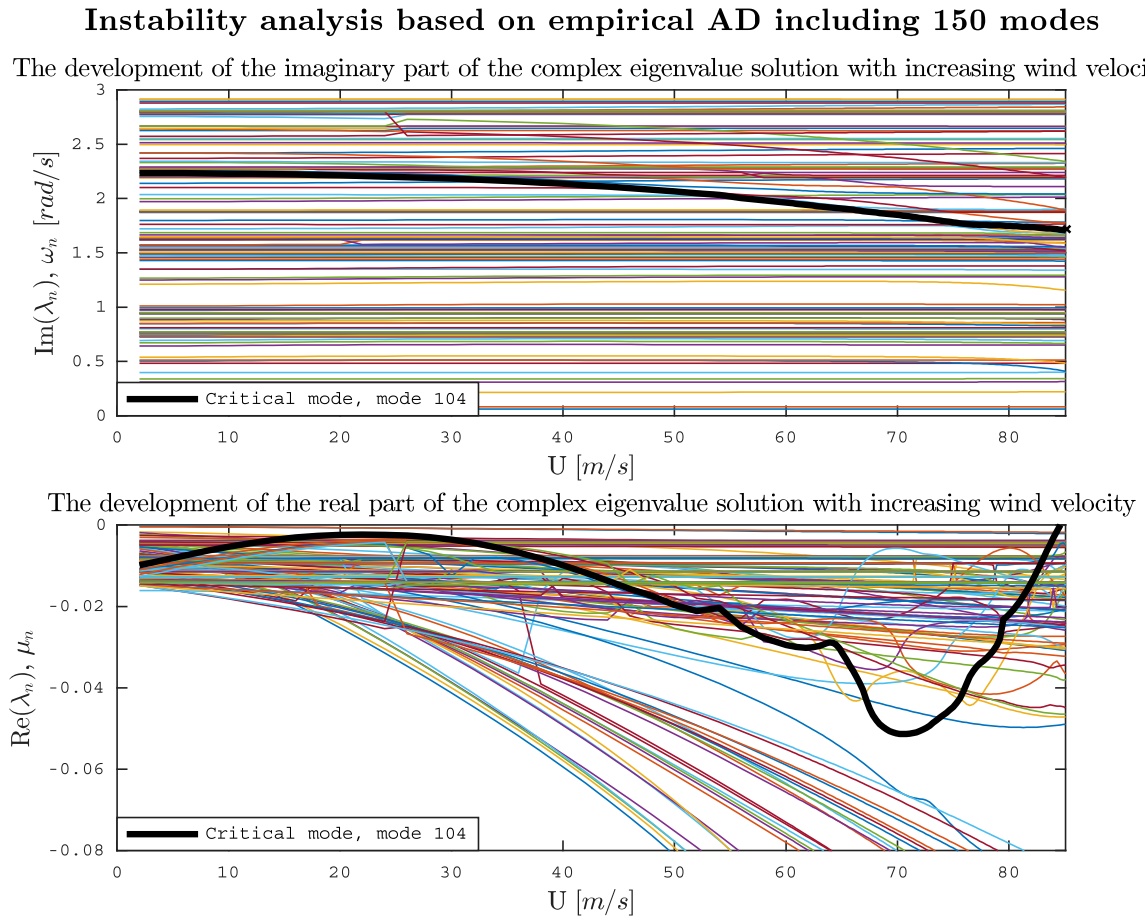

Figure 7.6: The figure shows how the values of the eigenmodes in the complex eigenvalue problem changes as a function of the wind velocity. Each line represents a mode and the analysis included 150 modes.

It was expected that the critical mode for the analyses comprising empirical AD was found to be the first pure torsional mode, mode 104. The mode shape used for the analysis can be seen in table 7.4 in column A. However, results based on the quasi-static AD yield a different critical mode,

mode 97, which is a mode that is a combination of vertical and torsional motion. This could be due to the questionable procedure of using quasi-static coefficients.

In figure 7.5 can the development of the critical modes' complex eigenvalue solutions be seen. The shape-wise similarity between the cases of 150 and 6 modes included in the analyses makes the results seems plausible. It also adds trustworthiness to the sorting algorithm used to obtain the critical modes. The curve of the real part, based on the sorting algorithm using 150 modes, shows some discontinuity in the derivative. This behaviour is believed to be caused by the sorting algorithm occasionally switching lines one velocity step too early or too late. This should however not affect which mode that is found to be the critical mode.

In figure 7.6 and figure 7.7 can the sorted eigenmodes be seen as the complex eigenvalue solution develops, with increasing wind velocity for the case of 150 modes included and the case of 6 modes included in the analysis. The black, emphasised line is the critical mode. Note how the eigenfrequency of the critical mode changes as it crosses other eigenmodes. This implies that the mode number also changes. It can be seen that at the critical mean wind velocity, the real part of the critical mode has gone to zero.

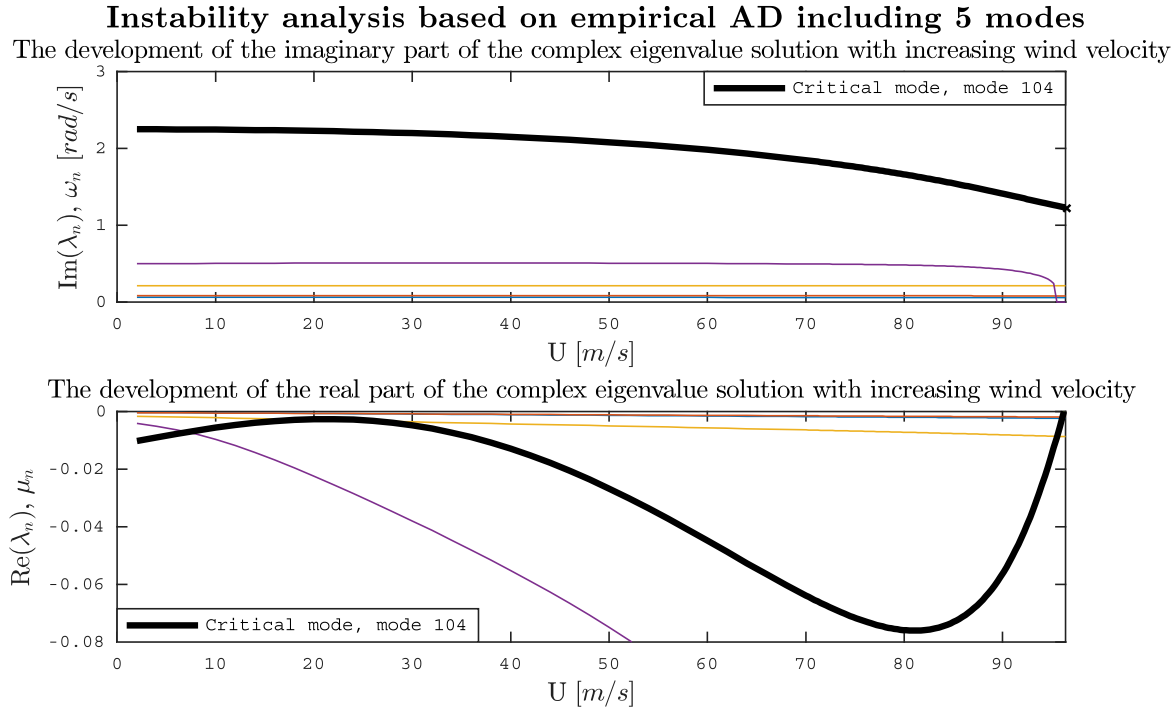

Figure 7.7: The figure shows how the values of the eigenmodes in the complex eigenvalue problem changes as a function of the wind velocity. Each line represents a mode and the analysis included 5 modes.

In figure 7.7 it should be noted that just prior to the fluttering instability limit is reached, the imaginary part of the complex eigenvalue solution of mode 8 drops to zero. This is the second vertical mode. This implies that the instability limit for static divergence is obtained prior to the fluttering instability when only including five modes in the instability analysis. Static divergence was however not found to occur prior to fluttering, based on the analysis including 150 modes. Hence, this irregularity will not be emphasised.

The fluttering mode was obtained from the real part of the complex critical eigenvector. A complex mode shape does not have a fixed inflection point, and the maximum can occur at different locations with time, unlike mode shapes found from an undamped eigenfrequency problem. For a correct representation of the fluttering mode, it has to be animated, hence plotting the flutter mode from the real part, only, is a simplification to be able to represent it in this thesis.

In figure 7.8 can the fluttering mode shapes compared to the first torsional mode be seen. The fluttering mode shape obtained from the analysis comprising the empirical AD and including only five modes shows strong similarities to the 2nd vertical mode, and to the torsional mode. This is expected as the torsional mode was the mode to reach the instability limit, and the second vertical mode is shape-wise similar to the first torsional mode.

The fluttering mode shape obtained from the analysis comprising the empirical AD and including 150 modes does not resemble the first torsional mode, or the mode shape found using five still air modes. Some difference is expected when a different amount of still air mode shapes are used in the flutter analysis. The significant difference observed in figure 7.8 might also be caused by a representation at two different instances of the motion, or by an error in the solution algorithm.

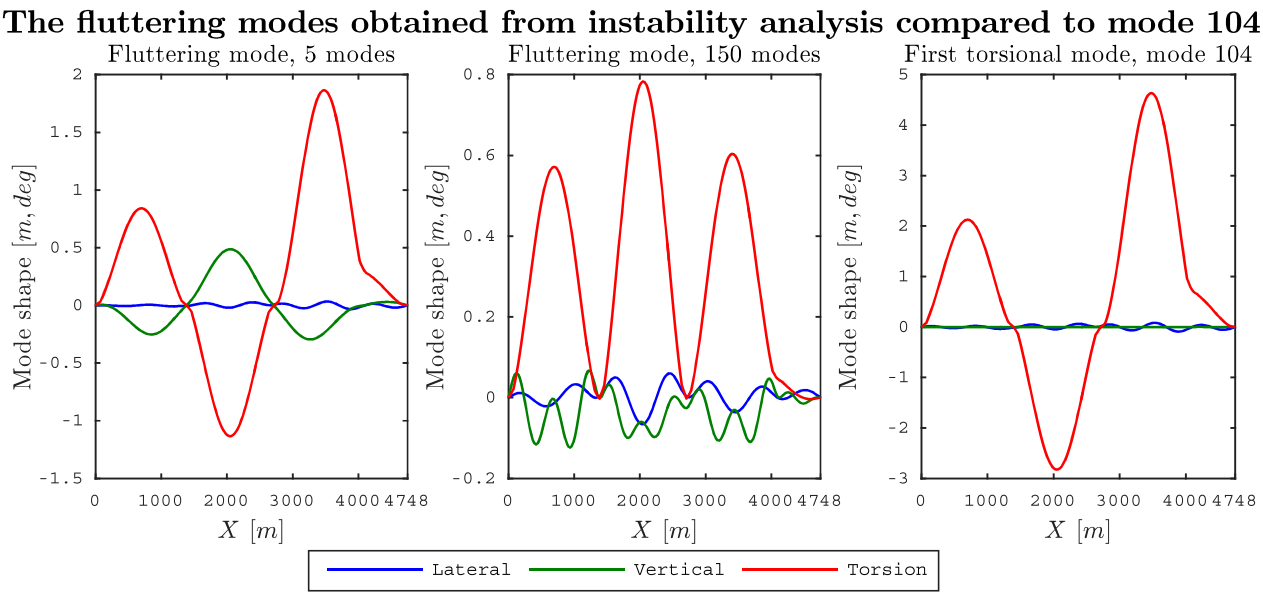

Figure 7.8: The figure shows the fluttering mode shapes compared to the first torsional mode. The fluttering mode shapes are obtained from analyses using 150 modes and five modes, empirical ADs and including both the top cable and the girder in the instability analyses. Left: Fluttering mode shape including five modes in the flutter analysis. Middle: Fluttering mode shape including 150 modes in the flutter analysis. Right: First pure torsional mode shape, mode 104.

The critical eigenvector, i.e. the weighting vector, for the fluttering mode shape from the analysis including five modes is given in table 7.5. It can be seen that mode 8 and mode 104, are weighted the most. Also note that the contribution from the horizontal modes is virtually zero, as expected.

For the case of 150 modes, no mode is weighted more than 0.12 by the real part, and significant changes to the mode shape can be seen even after the contribution from mode 104 has been

added, which is number 17 in terms of the largest real value. Because many still air modes have significant contributions to the fluttering mode shape, the numbers and weights are listed in table D.1 in the appendix.

Mode number	**Critical eigenvector** ϕ_{Cr} $[-]$
Mode 1 (1st horizontal mode)	0.0005
Mode 2 (2nd horizontal mode)	-0.0004
Mode 3 (1st vertical mode)	0.0099
Mode 8 (2nd vertical mode)	0.9032
Mode 104 (1st torsional mode)	0.4023

Table 7.5: The table shows which eigenmodes the critical eigenvector weights to obtain the fluttering mode from a flutter analysis including 5 modes.

In summary, the effect of the top cable on the critical instability velocity is insignificant. The empirical derived aerodynamic derivatives yield a more plausible critical velocity compared to the aerodynamic derivatives derived from quasi-static theory. The first torsional mode and the second vertical mode seems to be critical to induce flutter. A flutter velocity of 85.09 m/s is obtained when including 150 modes and the damping contributions from the top cable. The fluttering mode shape obtained from an analysis including only five modes seems plausible.

7.3 A buffeting analysis of the bridge with the concrete hull

As pointed out earlier, the response of the bridge with concrete hulls will be emphasised. The analyses are carried out for all reference nodes marked in figure 5.3, but only the result at some of the reference nodes are presented in this thesis. Ref. node 5 is particularly important because few modes have inflection point at this location, especially compared to the node at mid-span. This conclusion is based on an initial parameter study, shown in figure D.10 in the appendix.

As mentioned in section 4.2.2, only the first 115 modes were included in the following buffeting analyses, as the results for the vertical and the lateral motion are expected to be well represented within this range.

The environmental data used to represent the loading are obtained from (NPRA, 2016n) are listed in table 7.6.

It should be pointed out, according to (NPRA, 2016n), that swell waves should be combined with wind waves and a wind velocity, all corresponding to the 100 year condition. To more easily assess the effects of swell waves on the bridge, swell waves and wind waves have been studied separately, where figure 7.39 is the only exception.

	Environmental loading, 100 year condition	
	Wind waves	**Swell waves**
Origin	West	West
Wind velocity, $U\ [m/s]$	33	33
Significant wave height, $H_s\ [m]$	3	0.4
Peak wave period, $T_p\ [s]$	6	16
Wave crest length, $s\ [-]$	5	40
JONSWAP-parameter, $\gamma\ [-]$	3.3	7.0

Table 7.6: The table shows the environmental loading conditions with a 100 year return period. The values are from (NPRA, 2016n). Note that the wave crest length for swell in this thesis is twice the value of the wave crest length in (NPRA, 2016n) because of different definitions of the spreading function have been used.

The notation and abbreviations in table 7.7 have been used as explanations in titles and legends in the figures.

Abbreviation	Explanation
U=0	Wind velocity equal to 0 m/s
U=15	Wind velocity equal to 15 m/s
U=33	Wind velocity equal to 33 m/s
Wind waves	$H_s = 3$ m, $T_p = 6$ s, wind generated waves
Swell waves	$H_s = 0.4$ m, $T_p = 16$ s, swell generated waves
JS	The JONSWAP spectrum is used to generate the waves
PM	The Pierson–Moskowitz spectrum is used to generate the waves
1st order waves	First order wave forces are included
2nd order waves	Second order wave forces are included
no waves	No wave forces are included
$LC1^{(1st)}$	Load case 1, this includes a wind velocity equal to 33 m/s and only first order wave forces, where $H_s = 3$ m and $T_p = 6$ s
$LC1^{(1st+2nd)}$	Load case 1, this includes a wind velocity equal to 33 m/s and first and second order wave forces, where $H_s = 3$ m and $T_p = 6$ s

Table 7.7: The table shows abbreviations used in the legends in the different figures. Load combinations for wind waves and swell waves were suggested in the report (NPRA, 2016n).

7.3.1 Load spectra

For the 1st order wave loading, it can be seen that the wave loading for different load types and wave spectra peaks according to the corresponding wave period. 16 s (0.39 rad/s) for swell waves, 6 s (1.05 rad/s) for wind waves defined by the JONSWAP spectrum and 8.7 s (0.72 rad/s) for wind waves defined by the Pierson–Moskowitz spectrum, as shown in figure 4.10. The position of the peaks is of importance for the magnitude of the response. 1st order swell waves induce a higher response of the structure compared to wind waves, even though 1st order wind waves have a bigger spectral peak value, because swell waves have a longer period, and excites different modes. This can be seen by comparing results in figure 7.11 and 7.14.

It should also be noted that the second order swell waves are insignificant compared to the other environmental load cases. The load spectra for second order wind waves peaks at 2.15 rad/s,

and have higher spectral densities than wind loading and first order wave loading, for frequencies larger than approximately 1.8 rad/s. A thorough discussion of the effect of second order forces can be found in section 7.3.5.

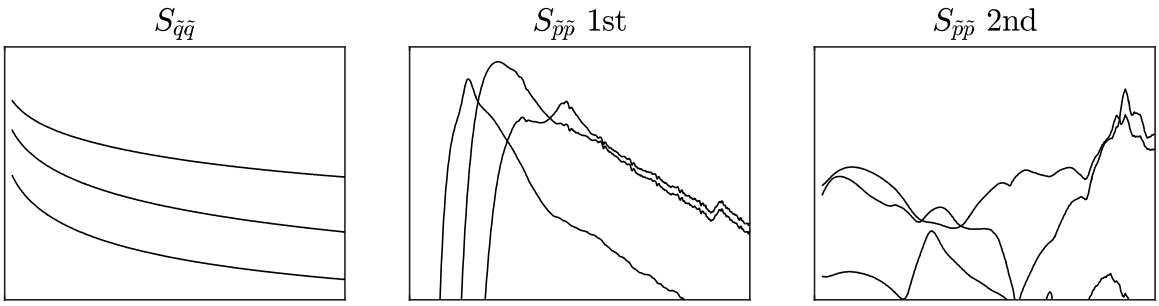

Figure 7.9: This figure is a visual legend of figure 7.10. The behaviour of each loading type, i.e. wind load, first order wave load and second order wave load can be seen. The purpose of this figure is to ease the tracing of each line in figure 7.10.

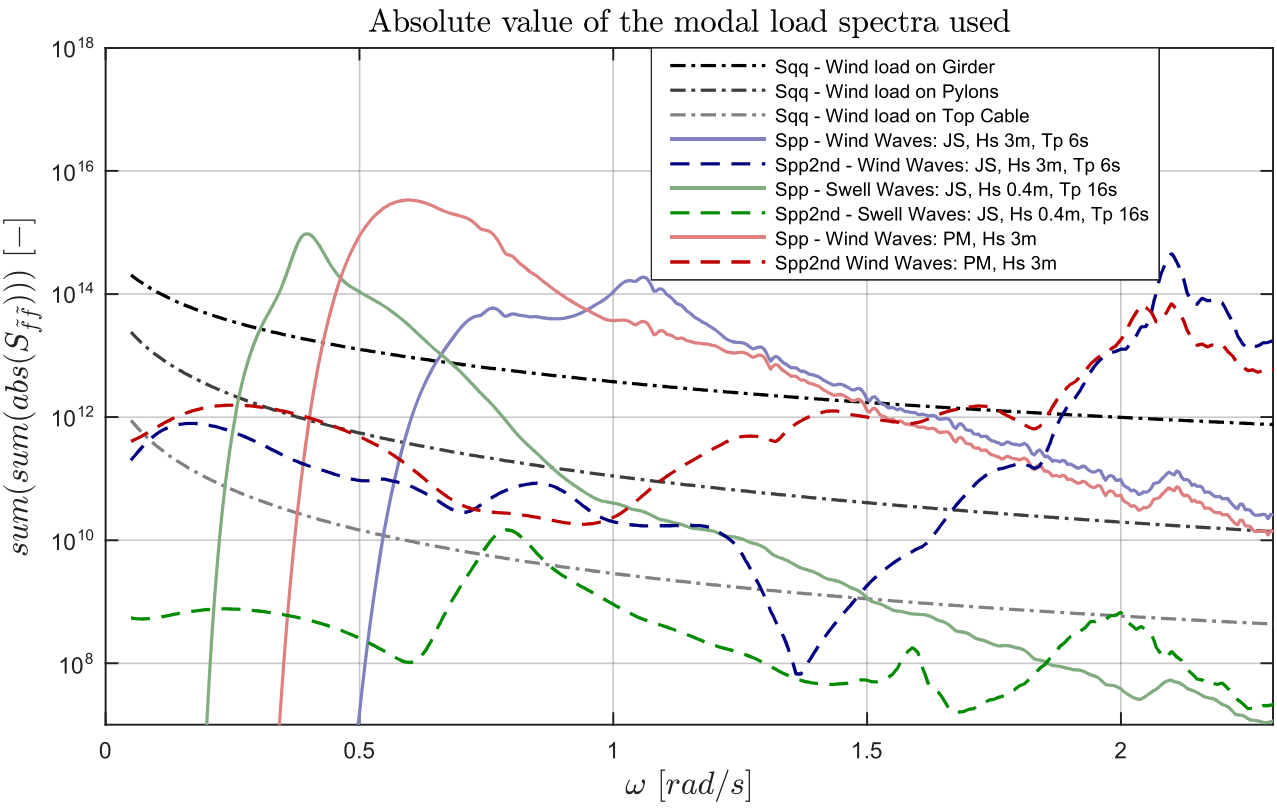

Figure 7.10: The figure shows the absolute values of the modal load spectra. The wind load is derived from a mean wind velocity, $U = 33$ m/s.

7.3.2 Spectral response for various locations throughout the bridge

Figure 7.11 shows the response spectrum at Ref. node 5, for both the lateral and vertical direction, when exposed to both wind and wind waves, and the separate load cases. The total response is shown by a black line, which is dotted when the line is hidden behind other curves. Figure D.7 in the appendix, compares the total response of the vertical and horizontal response spectrum in a large illustration, if more accurate curves are required. Not surprisingly, on the girder, the lateral response is dominating, which can be seen by comparing the spectral densities of the total response in the lateral and vertical direction. This is because the first horizontal modes occur with lower eigenfrequencies compared to the first vertical modes, and the wind loading shown in figure 7.10 is larger for the lower frequencies. It is also because the spectral density for the fluctuating wind component, shown in figure 4.6, is larger for the fluctuating part in the horizontal direction compared to the vertical direction. It is evident from the response spectrum in figure 7.11 that the first horizontal modes dominate the response.

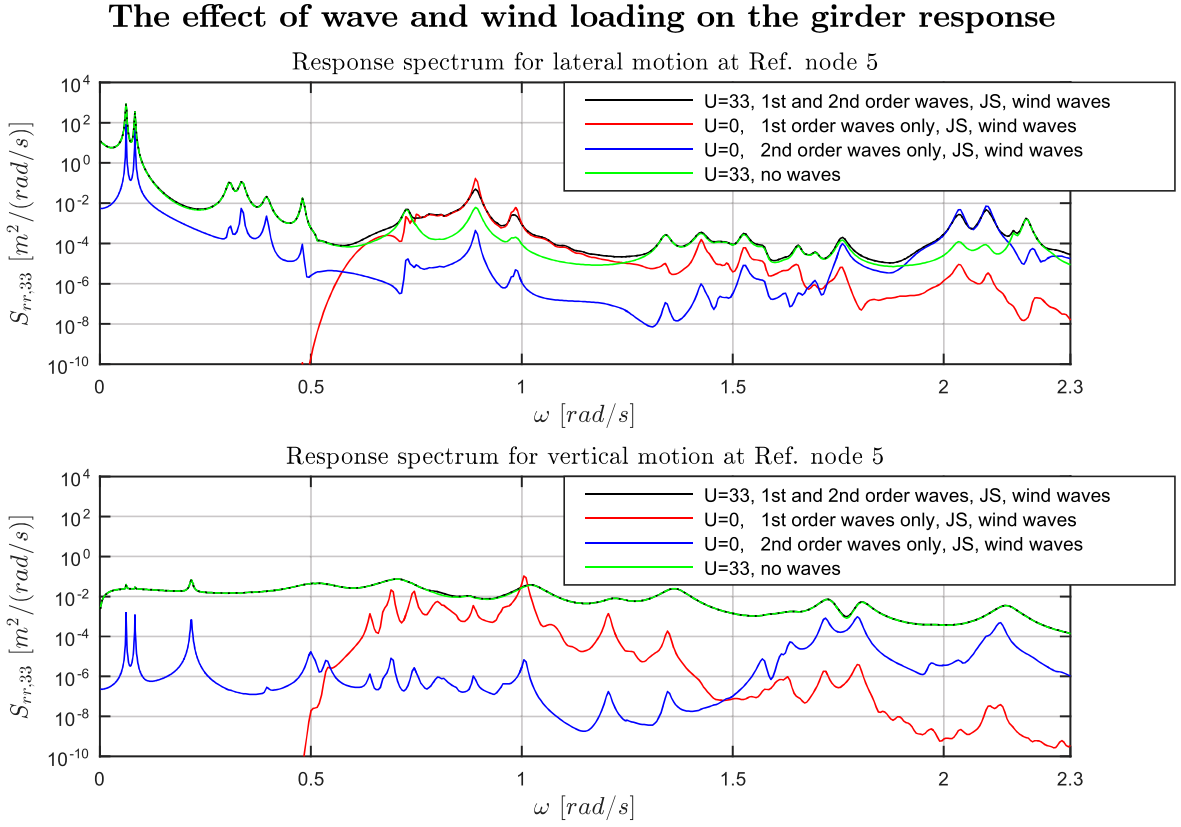

Figure 7.11: The response spectrum for the lateral and vertical direction at Ref. node 5 for the girder plotted for various load cases. The bridge alternative with the concrete pontoon is considered.

An interesting observation is that the vertical response spectrum peaks for frequencies in the range of the wave loading, but it is proved to be caused by the wind loading, which can be seen in figure 7.11. However, at the pontoon, the wave loading dominates the response within this frequency range, which can be seen in figure 7.12. It seems reasonable that the wave loading controls the

vertical response at the pontoon, while the wind loading controls the response at the girder, if considering the locations the loads are applied.

The effect of the wind loading and the first and the second order wave loading for lateral motion at pontoon 1 can be seen clearly in figure 7.12. The behaviour of the total response, the black line, is as follows. It follows the response spectrum for the wind loading for the lower frequencies, then, the total response follows the response spectrum of the first order wave loading between 0.6 and 1.2 rad/s, and, finally, the total response follows the response spectrum of second order wave loading at higher frequencies.

As the area under the response spectrum equals the variance of the response and keeping in mind that figure 7.12 is plotted with a log axis; it can be observed that both the lateral and the vertical motion is dominated by the wind loading.

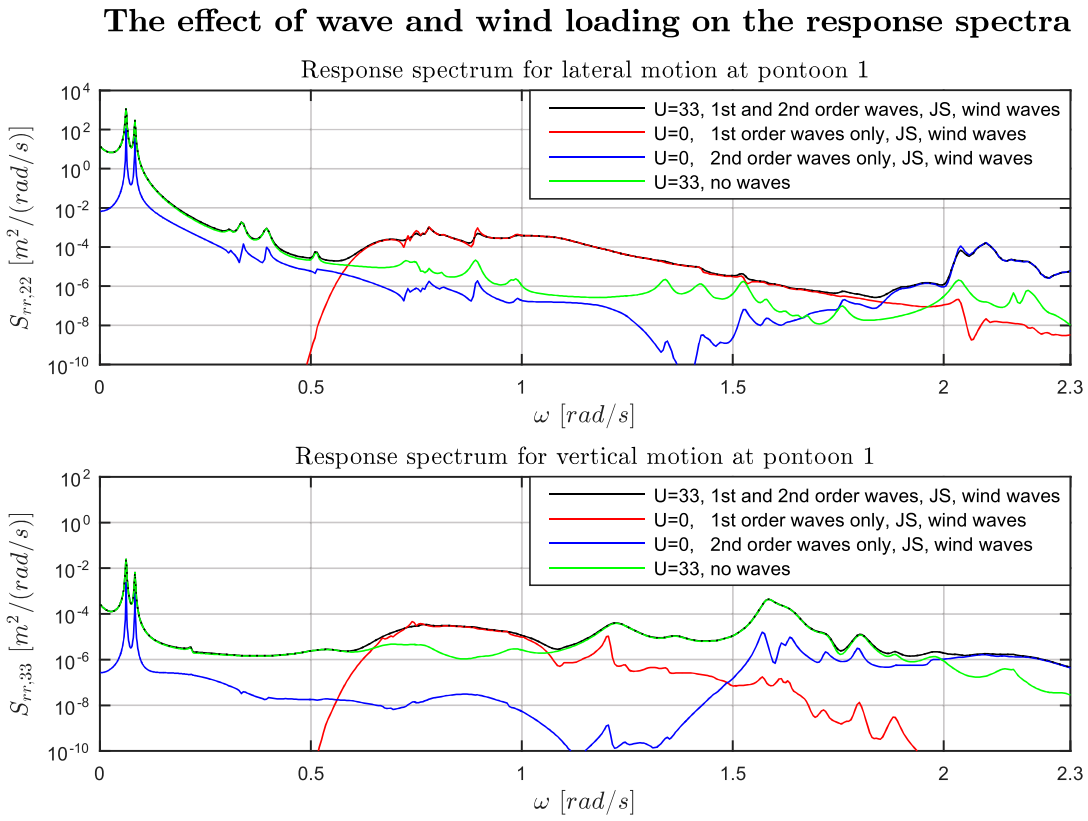

Figure 7.12: The response spectrum for the lateral and vertical direction at pontoon 1 for the bridge with the concrete pontoon alternative plotted for various load cases. Note that dotted lines are used when the curve for the total response is hidden behind other curves.

7.3.3 The standard deviation

The following section focuses on the resulting standard deviation along the girder of the bridge with the concrete pontoon alternative. The effects of swell waves on the STD are studied in section 7.6.3. Because the expected wave height is correlated with the mean wind velocity, as

shown in figure 7.36, unlikely combinations of a large wave height, and low mean wind velocities have not been included in this thesis.

	Lateral motion			**Vertical motion**		
Environmental loading included in the analysis	mid-span $[m]$	hull 1 $[m]$	hull 2 $[m]$	mid-span $[m]$	hull 1 $[m]$	hull 2 $[m]$
Only 1st order waves	0.0225	0.0135	0.0134	0.0029	0.0029	0.0021
Only 1st and 2nd order waves	0.3722	0.4432	0.4189	0.0077	0.0024	0.0028
Only wind, U=33	2.0620	2.3040	2.0812	0.3129	0.0123	0.0117
U=33, and 1st order waves	2.0620	2.3040	2.0813	0.3145	0.0126	0.0119
U=33 + 1st and 2nd order waves	2.0691	2.3143	2.3143	0.3145	0.0127	0.0120

Table 7.8: The table shows how the STD at mid-span and at the pontoons is affected by the different load cases.

The standard deviation in figure 7.13 depicts the STD along the bridge girder, when exposed to both wind and wind waves, and the separate load cases, for vertical and lateral motion. It can be seen that for high wind velocities the first order wave loading has virtually no contribution to the total STD.

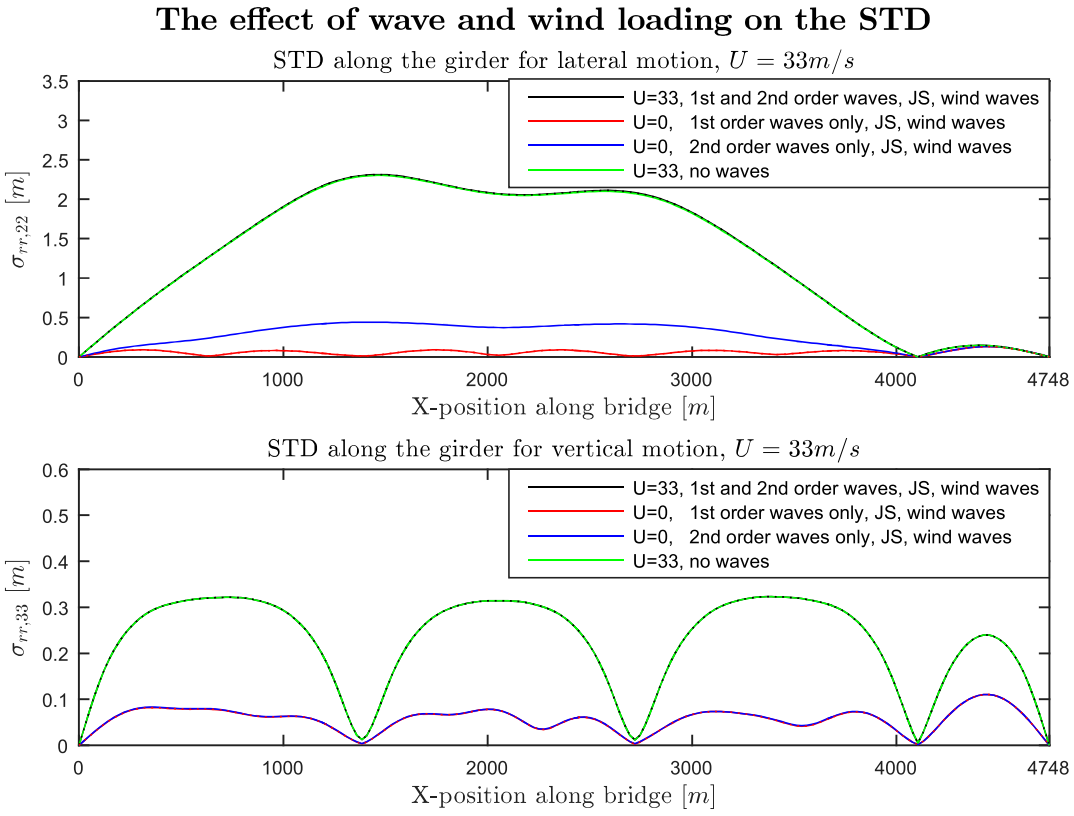

Figure 7.13: The maximum STD along the girder is 2.313 m for lateral motion and 0.323 m for vertical motion. Note that dotted lines are used when curves are hidden behind each other.

If the standard deviation in figure 7.13 is compared to the mode shapes presented in figure 7.4,

it can be seen that the sum of the first two mode shapes dominates the standard deviation in the horizontal direction. It can also be seen that different modes are excited by the wind and the first order wave loading in the lateral and vertical direction, as the shape of the standard deviation along the girder differs.

As expected, the standard deviation in the lateral direction is significantly larger than the standard deviation in the vertical direction. Keeping in mind that waves carry more energy in the vertical direction, and the wind carries more energy in the horizontal direction, it should not be surprising that the relative difference in the STD, caused by wind loading and wind waves, is smaller for the motion in the vertical direction compared to the horizontal direction. This is shown in figure 7.13. For this reason, if wind loading is already present, the STD for vertical motion along the bridge increases by 4 % when adding loading from wind waves, while no significant change of the STD can be seen for lateral motion. This is shown in table 7.8.

In figure 7.13 it can be seen that the largest STD in the lateral direction is at pontoon 1. This can also be seen in table 7.8. The STD for the vertical motion shown by the same table and figure is different. The STD for the vertical motion tends to reach maximum values at the middle of the four spans that the bridge consists of. This is because the structural and geometric stiffness from the tethers is larger in the vertical direction than in the lateral direction. Hence the towers can only experience large displacements in the lateral direction. The different shapes of the standard deviation along the girder for the wave and the wind loading suggest that different modes are excited by the two types of environmental loading.

The STD in table 7.8 could give an impression that second order forces are more important than they are, as the STD due to the wave loading increases by a very large factor when second order forces are included. This is however mainly because the difference frequency forces excite the first and second horizontal mode, which causes the STD to increase. The contribution from the difference frequency second order forces to the response spectrum is however very small when a realistic wind loading is added. First order forces have however an apparent effect on the response spectrum in the frequency range of the wave loading, even though the STD does not change much, as seen in figure 7.12 and in table 7.8.

It should be noted that the vertical displacement of the pontoons is very small, between 1.2 cm and 1.3 cm. The reason for this is unknown, but tether forces, buoyancy forces and tether stiffness have been confirmed. It is suspected that the pontoons may not participate as much as they should in the vertical mode shapes. This has not been studied in detail. However, in the eigenfrequency table, table 7.1, it can be seen that the vertical modes are those that matches the eigenfrequencies from the NPRA-reports the least. This indicates that the vertical modes may not have been modelled properly.

7.3.4 Assesment of the wave spectra and parameters used in the buffeting analysis

Recall that the parameter γ used in the JONSWAP spectrum affects the frequency range of the applied wave loading, as shown in figure 3.6. Selecting a large spreading parameter, s, will, however, induce wave loading approaching from a single direction. Figure 7.14 shows how the

response and the standard deviation for swell waves vary with the variation of these parameters. With a period of 16 s, swell waves can excite mode 4 to 7, which are horizontal modes. As expected, the standard deviation and response in this range increases with increasing values of γ and s. This is expected because it means that both of the pontoons will experience a larger load within a smaller frequency range, applied more simultaneously and to a larger degree perpendicular to the bridge. Note that the variation of the response spectrum and the STD, for the same variation of γ and s, might be different if the response is evaluated at a different DOF.

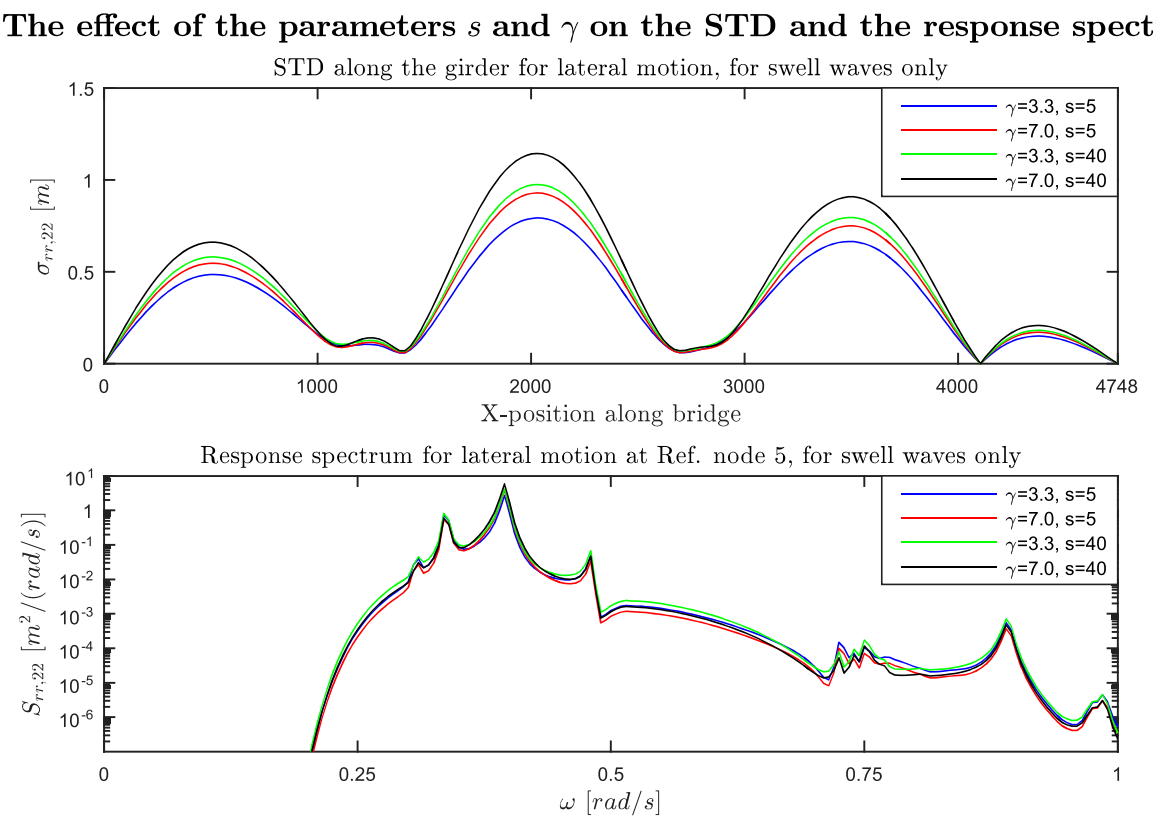

Figure 7.14: The effect of the parameter γ and s is evaluated by examining the standard deviation and the response spectrum. The response spectrum goes towards zero outside the range presented by the figure.

The response spectrum is in general dominated by the mean wind loading. However, it can be shown a different trend with the variation of mean wind velocity and wave height when considering a fixed frequency. Figure 7.15 shows that for a frequency of 0.75 rad/s, the vertical response at mid-span declines with increasing mean wind velocities before the response starts increasing again at a mean wind velocity of 12 m/s. This might be because aerodynamic damping decreases the response until the wind load is significant enough to cause an increase in the response. Peaks of the response spectrum are not expected to move in terms of frequency as the wave period is kept constant and the eigenfrequencies do not change much when only static wind loading is taken into account. This is shown in figure 7.4 and can be seen by comparing eigenfrequencies from procedure A and C.

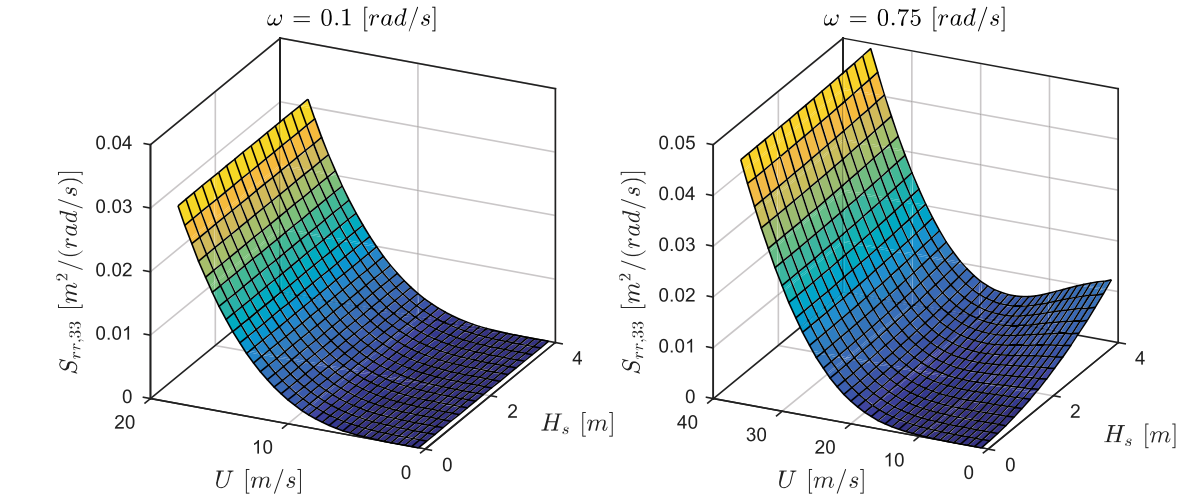

Figure 7.15: The figure shows a comparison of the response spectra for two different frequencies. Vertical motion, with a variation of the wind speed and wave height using the JONSWAP spectrum with $T_p = 6$ s, when only first order wave loading is considered.

Figure 7.16 shows how the standard deviation of the mid-span changes with different mean wind velocities and wave heights, for lateral motion. The STD is calculated using either a JONSWAP or a Pierson–Moskowitz spectrum. Remember that the Pierson–Moskowitz spectrum is a one-variable spectrum and that the period for a given wave height can be found from equation 3.40.

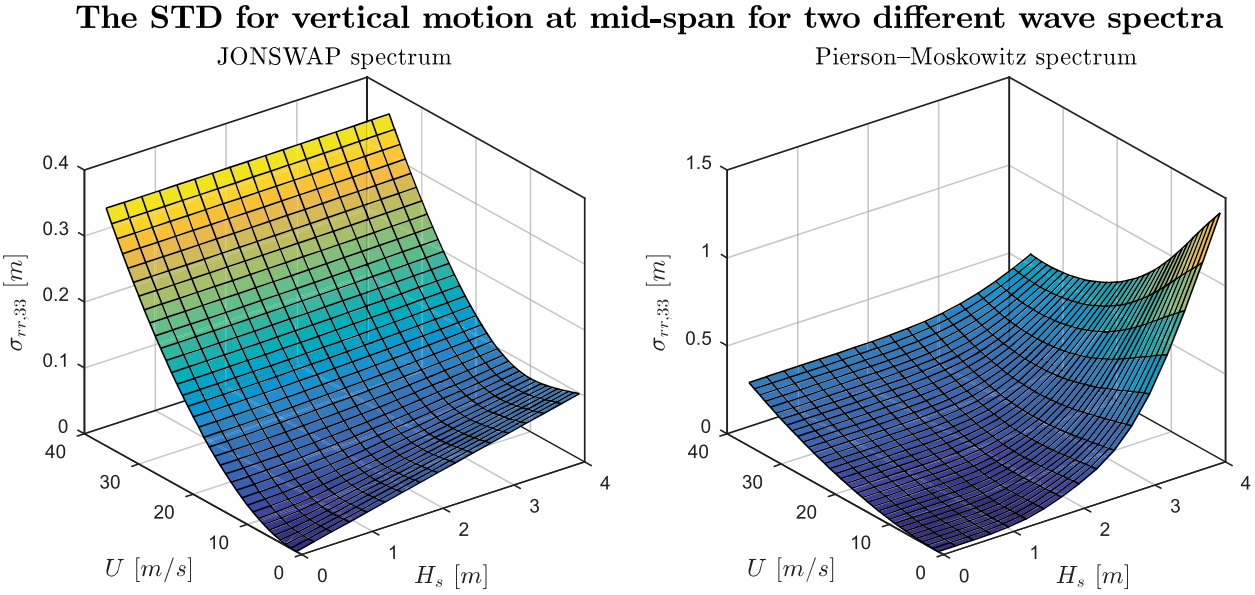

Figure 7.16: The figure shows the variation of the STD with for different mean wind velocity and wave height for the JONSWAP spectrum using wave period $T_p = 6$ s, and for the Pierson–Moskowitz spectrum.

Figure 7.17 shows a surface plot and a contour plot of the difference between the STD achieved by the two wave spectra.

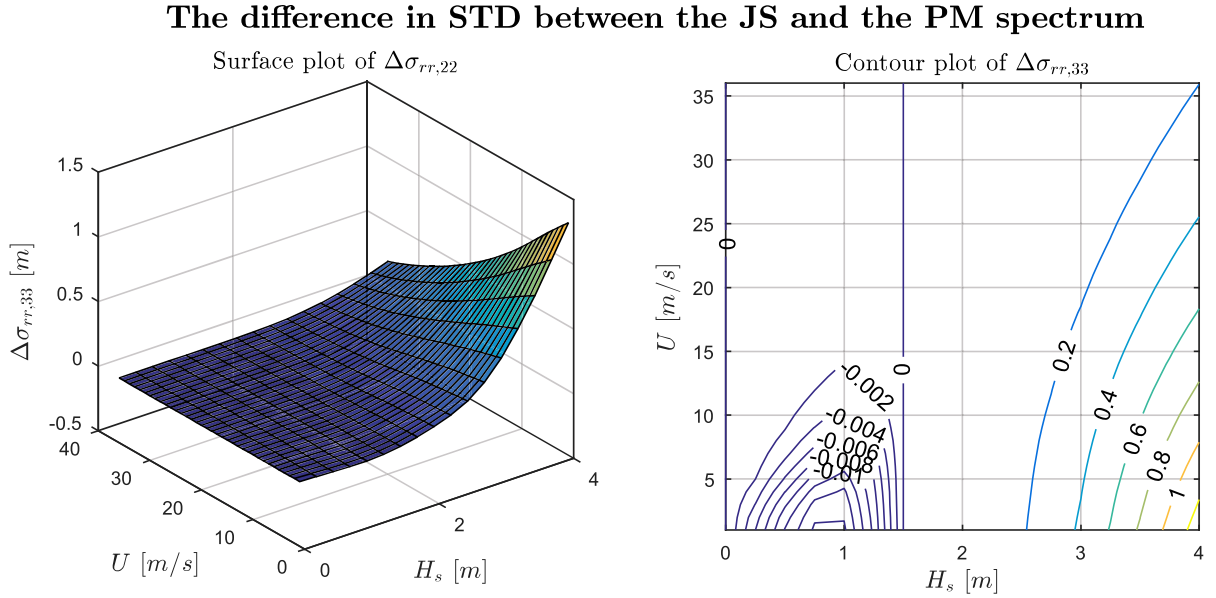

Figure 7.17: The figure shows the difference in the STD, $\Delta\sigma$, between calculations based on the JONSWAP spectrum and the Pierson–Moskowitz spectrum. The JONSWAP spectrum is based on $T_p = 6$ s.

When comparing the STD, a period of 6 s is chosen for the JONSWAP spectrum. A wave height of 1.44 m in the Pierson–Moskowitz spectrum corresponds to a period of 6 s, which from the contour plot in figure 7.17 looks to be approximately where the two spectra yield the same STD.

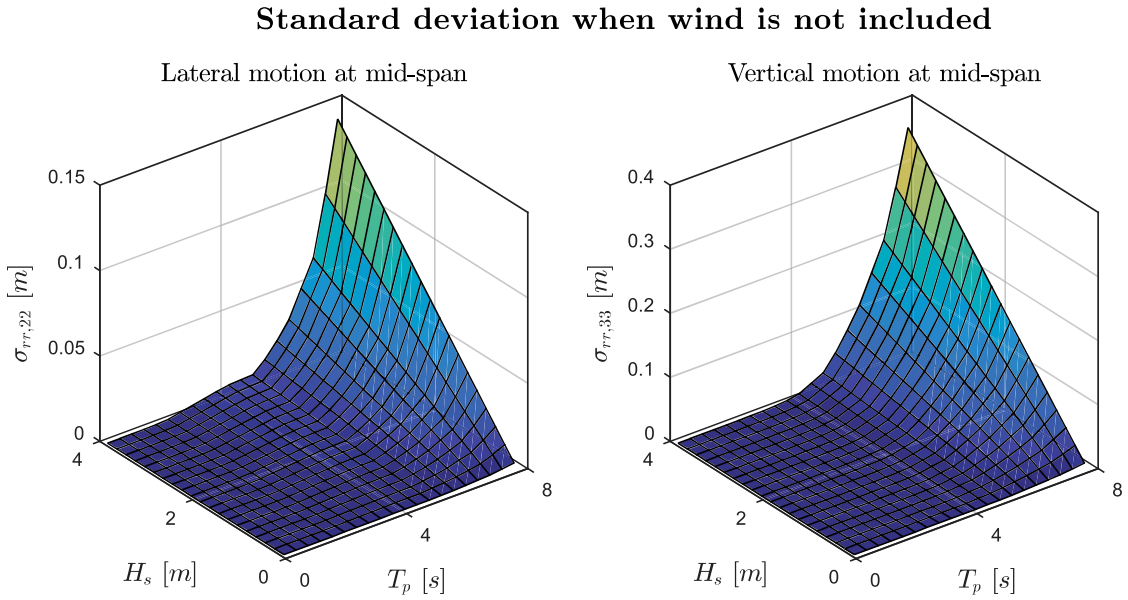

Figure 7.18: The figure shows the variation of the standard deviation as a function of the wave height and wave period for wind waves including first and second order forces. No wind load is included.

By keeping the period constant for the JONSWAP spectrum, it is expected that the Pierson–Moskowitz provides a smaller standard deviation for small wave heights, and a higher standard deviation for large wave heights, as figure 7.17 shows. The statement that the response increases with an increasing wave period is based on figure 7.18. Due to inaccuracies caused by this fixed relation of wave height and wave period by the Pierson–Moskowitz spectrum, it will not be used in any further analyses.

The effect, wave height and wave period have on the STD, is shown in figure 7.18. Note that the wave period appears to be of greater importance to the STD than the wave height, though both have a distinct contribution to the STD. Also, note the rapid growth of the STD for wave periods larger than 6 s, as this gives an indication that large STD can be achieved due to swell waves.

7.3.5 The effect of including the second order wave forces

The effect of the second order wave loading, for the critical load combination of wind waves, can be seen in figure 7.19. As wind loading dominates the response for lower frequencies, the second order difference frequency forces appear to have no impact on the response for this frequency range. As shown in figure 7.10, the load spectrum for first order wind waves peaks in the range 0.5 rad/s and 1.5 rad/s, while the second order loading primarily has its largest amplitude outside this range. This explains why no effect from second order loading can be spotted within this range. However, for high frequencies, a change in the response due to second order forces can be observed. This range is not important for the STD of vertical and lateral motion, but might be of importance if moment or shear forces are studied, as higher modes can have a large curvature even if the maximum displacements are small.

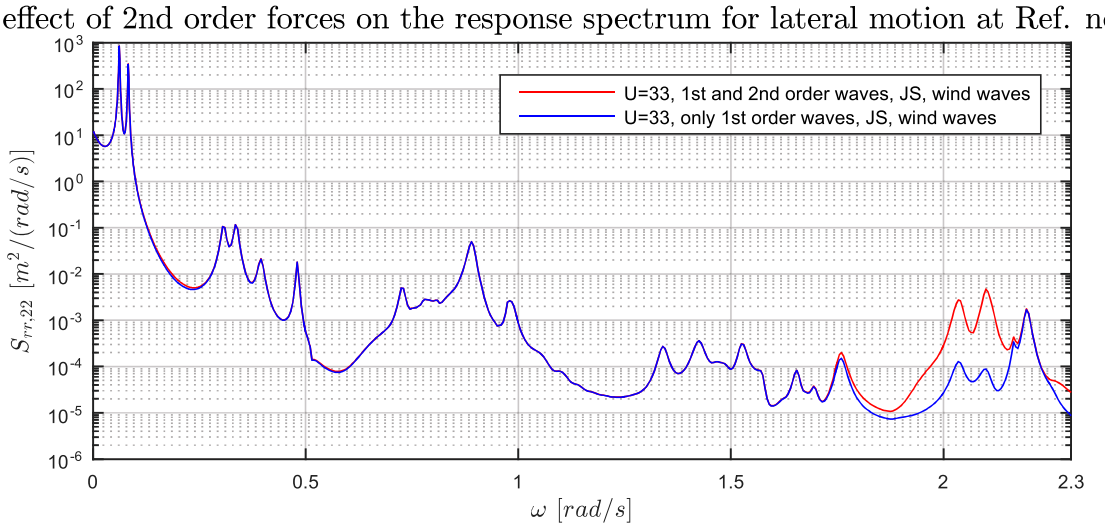

Figure 7.19: The figure shows the the effect of including the second order wave forces. The considered bridge alternative has concrete pontoons.

As mentioned in section 6.3.3, the QTF displayed some noise-like behaviour for higher frequencies. Thus, a smoothing of the QTF was performed. The corresponding modal environmental

second order wave loading and the response spectrum for the node at mid-span can be seen in figure 7.20.

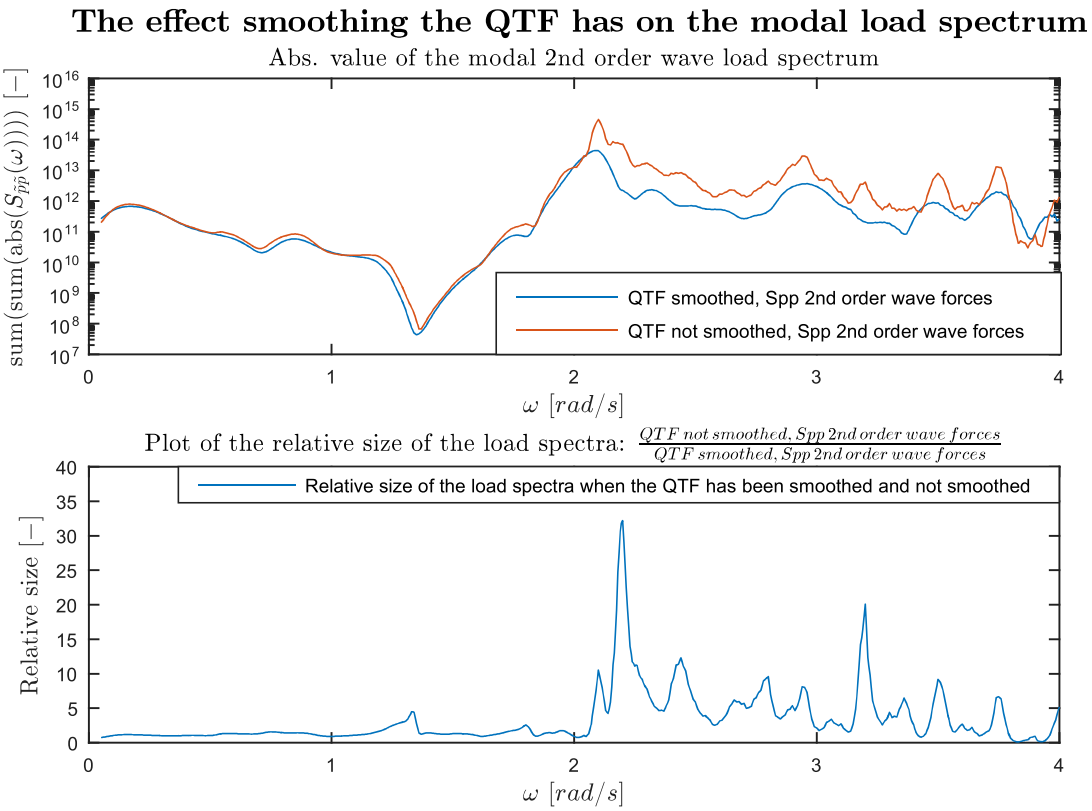

Figure 7.20: This figure shows the modal wave load spectrum due to second order wave forces calculated based on the smoothed and non-smoothed QTF. It also shows the relative difference between the the modal load spectra based on a smoothed and non-smoothed QTF.

The modal environmental second order wave load spectrum in figure 7.20 shows the desired decrease of spectral densities for higher frequencies by a factor between 1 and 35. While smoothing the modal loading directly would only flatten out peaks, smoothing the QTF reduces the modal loading for higher frequencies, while the modal loading for lower frequencies appears unaffected. As this procedure was developed at a late stage in the thesis it has not been implemented for any of the following calculations.

Based on the results achieved, smoothing of the QTF is an easy way to reduce the effect of numerical noise of the modal loading. However, the authors of this thesis would recommend confirming that numerical noise for higher frequencies is caused by a rough mesh size and that smoothing of the QTF will provide similar results as decreasing the mesh size, before implementing the method.

7.4 Buffeting results obtained for the steel hull alternative

In this section, the results from the buffeting analysis of the bridge with the steel hulls are presented and compared to results obtained for the bridge with the concrete hulls.

7.4.1 A comparison of the wave loading spectra

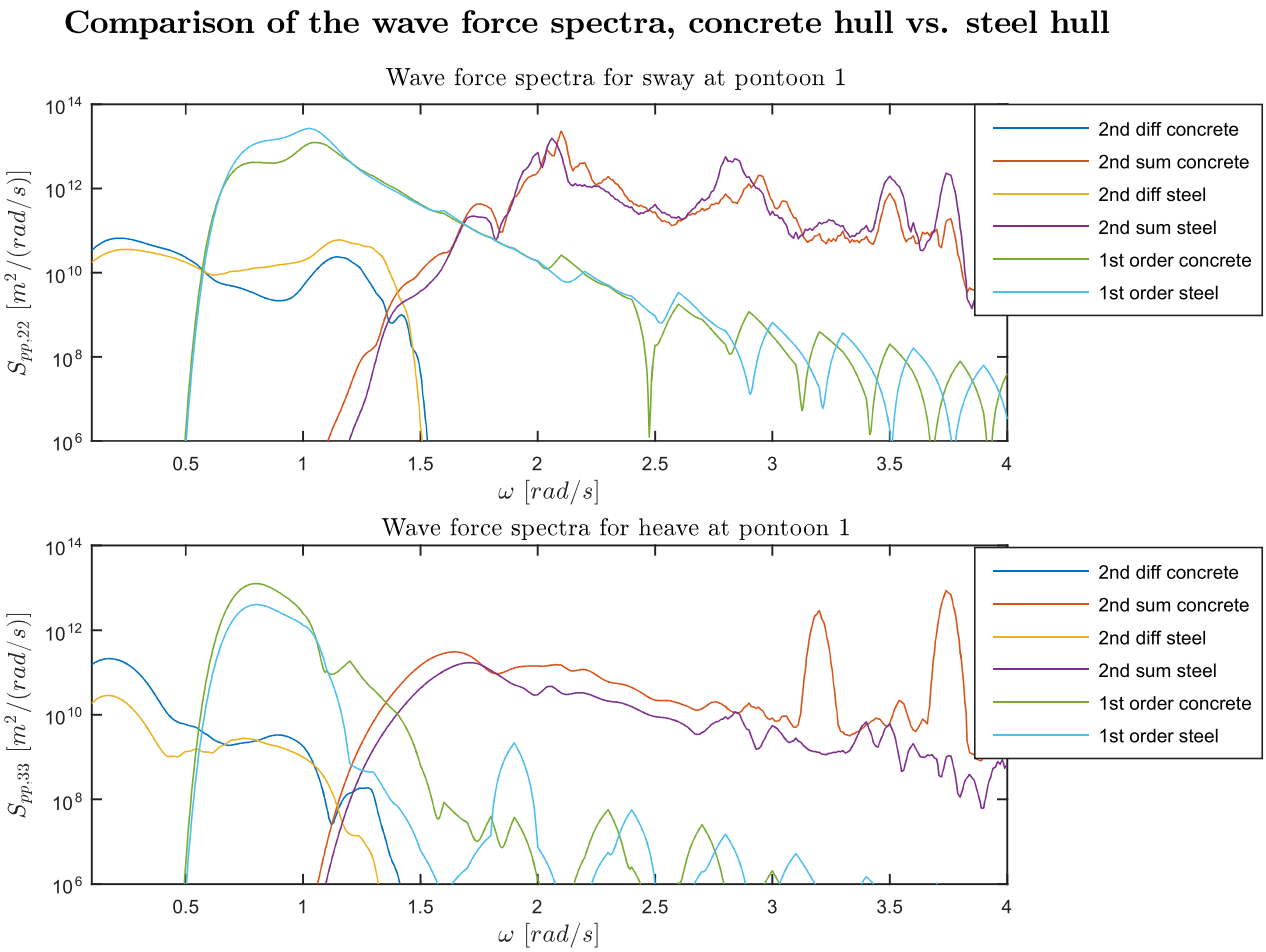

Figure 7.21: Comparison of the first and second order S_{pp} of the concrete pontoon alternative and the steel pontoon alternative.

Before comparing the response of the bridge for the two alternative pontoon designs, the steel hull and the concrete hull, the change of loading due to the change of geometry is studied.

For first order wave loading, figure 7.21 shows that the largest loading in heave is experienced by the concrete pontoon, and the largest loading in sway is experienced by the steel pontoon. As the wave exciting forces is a function of the geometry of the pontoon, and the steel pontoon is smaller than the concrete pontoon, the wave excitation forces presented in figure 6.8, is generally larger for the concrete hull design. This is also the case for heave at a period of 6 s. However, for surge

and a wave period of 6 s, the steel hull have larger self exciting forces. This discovery explains the observed behaviour for the current load condition.

The two distinct peaks for heave motion of the concrete hull alternative in figure 7.21 is probably due to the nature of the QTF of the concrete hull. It can be seen from the QTF in the appendix, in figure C.2, that the QTF for heave motion has two extreme peaks at the corresponding sum frequencies. This is not the case for the steel hull alternative. The nature of these peaks are hard to justify and might be the result of a numerical error from the analysis in HydroD due to the selected mesh size of the pontoon and the sea surface.

The oscillating behaviour of the first order wave forces in the load spectrum, for higher frequencies, could also be a mesh-related problem. As the magnitude of the load spectrum for the first order wave forces is quite small for higher frequencies, the oscillations are not expected to affect the extreme response.

7.4.2 A comparison of the response spectra

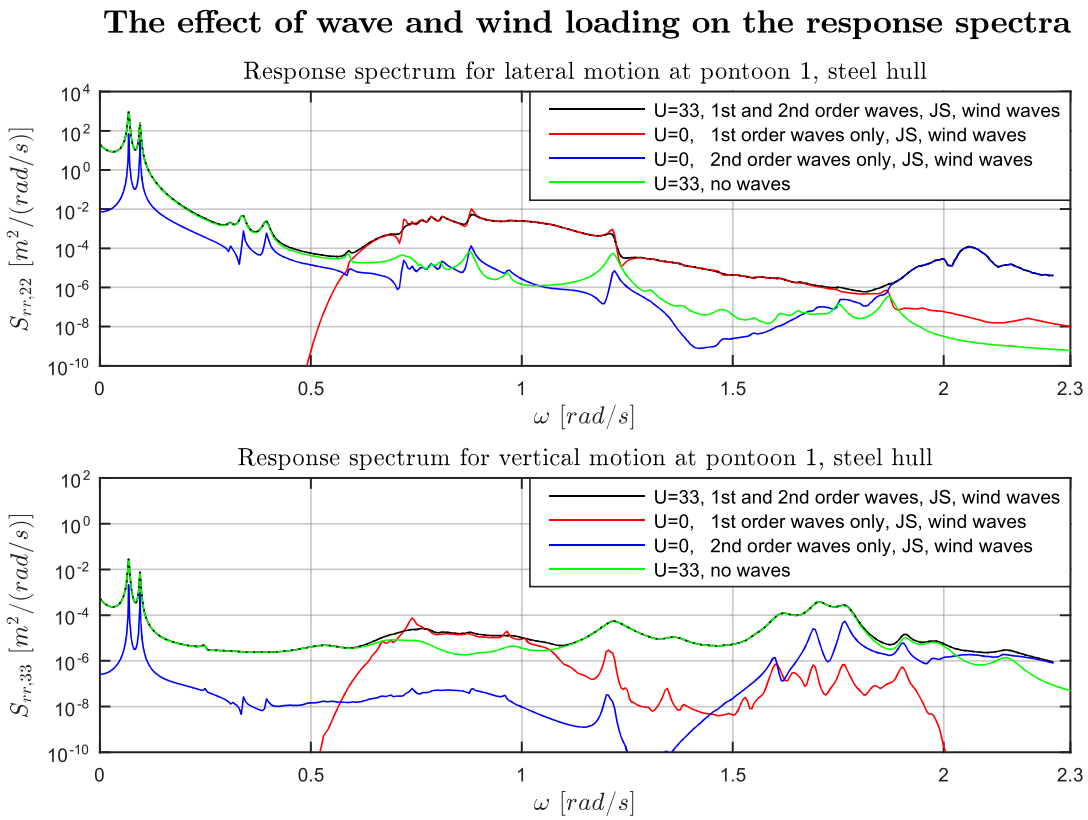

Figure 7.22: The response spectrum for the lateral and vertical direction at pontoon 1 for the bridge alternative with the steel pontoon plotted for various load cases.

Figure 7.22 shows the response spectra at pontoon 1 for the bridge with the steel pontoon. As observed for the concrete hull earlier, in figure 7.12, the response spectra due to the second order

wave forces peaks at the first eigenfrequencies of the structure, but is insignificant for the extreme response due to the large excitation from wind loading at the same frequencies. The first order wave loading contributes mainly in a range of 0.6 rad/s and 1.2 rad/s, but the contribution to the STD is rendered insignificant due to the larger spectral density values at the lower frequencies of the wind loading.

For both the vertical and the lateral direction, second order forces peak at the frequencies of the first two horizontal modes, where the wind loading is very dominant. Smaller peaks due to second order loading can be seen in the high-frequency range. Similar results was found for the concrete hull in figure 7.12.

Figure 7.23 shows a comparison of the response spectra of the two bridge alternatives. In the frequency range of the first order wave loading, figure 7.23 shows that the response spectrum of the bridge alternative with the steel hull is largest, which corresponds well with the load spectra from figure 7.21. High frequency response is however insignificant for the STD for lateral motion. The response due to the first two modes occurs at slightly different frequencies, which is expected as the eigenfrequencies for the two hull alternatives are different. The eigenfrequencies of the steel pontoon are larger because the reduction of mass is greater than the reduction of the stiffness for the hull alternative. The mass of the steel pontoon is almost half of the mass of the concrete pontoon, while the number of tethers only is reduced from 16 to 12. Because wind loading declines for increasing frequencies, the peaks of the first two modes are smaller for the steel pontoon. The peaks are however wider, causing the STD for the steel hull alternative to be larger than that the STD for the pontoon, which can be seen in table 7.9.

Hull alternative	**Lateral motion**		**Vertical motion**	
	$max(S_{rr,22})$	$\sigma_{rr,22}$	$max(S_{rr,33})$	$\sigma_{rr,33}$
Concrete	8.476E02	2.1099	7.485E-02	0.1790
Steel	7.408E02	2.2552	7.573E-02	0.1788

Table 7.9: Comparison of the short-term extreme response values for lateral displacement at mid-span, calculated by eq. 4.17.

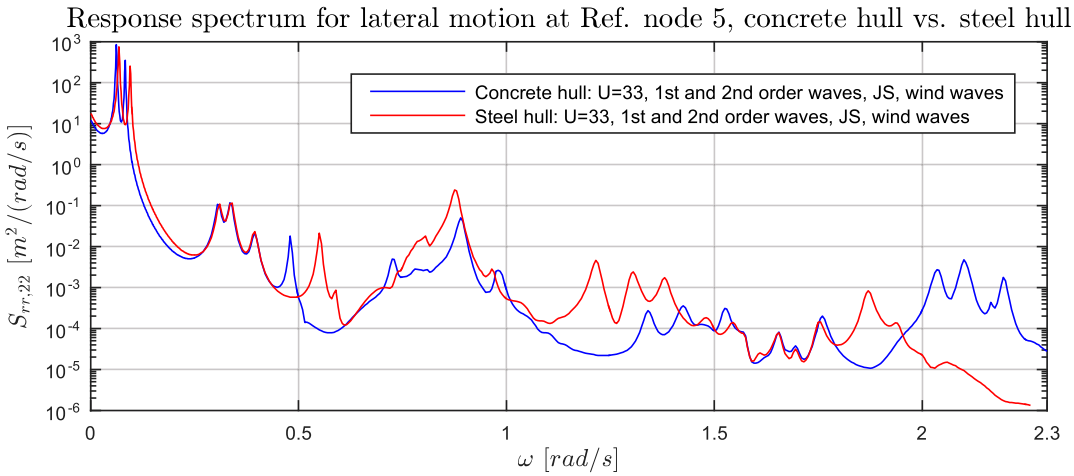

Figure 7.23: The response spectrum at Ref. node 5 of the concrete pontoon versus the steel pontoon.

As shown in figure D.8 in the appendix and table 7.9, the response in the vertical direction at the girder is completely dominated by wind loading. Figure D.9 in the appendix, compares the response spectrum of the vertical direction of the two hulls. Except for the change in eigenfrequency for some of the peaks in the response spectra, no significant difference can be seen for the two hulls. This suggest that the choice of hull mainly affect the lateral motion at the pontoons. As discussed in section 7.3.3, the STD for vertical motion at the pontoons were found to be unreasonably small. A different result for the importance of hull selection, for the vertical response at the pontoons and along the girder, might by obtained by a model with a greater displacement of the pontoons due to vertical modes.

In summary, the concrete pontoon has the smallest standard deviation of the two alternatives, for lateral motion. Although subtle differences are measured, the pontoon design could be critical with respect to controlling the eigenfrequencies of the bridge. It can be seen from table 7.2 and table 7.3 that the lower eigenfrequencies are quite different. Increasing or decreasing the eigenfrequencies of vertical modes could be done by simply adjusting the mass or geometry of the pontoons. The following step would then to be to adjust the eigenfrequencies of important modes by changing the pontoon design such that they do not match the frequency of e.g. the critical wave loading. With this reasoning, the pontoon design cannot be concluded to be insignificant for the bridge design. Based on the results achieved in this thesis, it is not possible to renounce any of the two hull alternatives.

7.5 A parameter study - damaged tethers and top cable

A parameter study has been performed to see the effects of damaged tethers and top cable. In principle different elements have been removed, i.e. top cable at a certain span or a given number of tethers. All analyses have been performed for wind waves with a wave height of 3 m and a wave period of 6 s, without including the effect of second order wave forces. The mean wind velocity was set to $U = 33$ m/s. 150 modes were used in the analysis, to properly include the effect of torsion.

7.5.1 Damaged tethers

The tethers provide geometric stiffness in the surge and sway direction. The stiffness against roll and pitch motion is mainly structural stiffness provided by the distance between tethers and the total area of the tethers. In the heave direction is the total area of the tethers the main contributor to the stiffness. Most of the stiffness against motion in the yaw direction is expected to come from the girder, and not from the tethers.

The effect of damage to the pontoon tethers have been investigated and can be seen in figure 7.24. The figure shows how the standard deviation of the motion in the two pontoons is affected by an increasing number of damaged tethers. The change in the STD is given in percentage. All damage occurs within a single group of tethers on pontoon one.

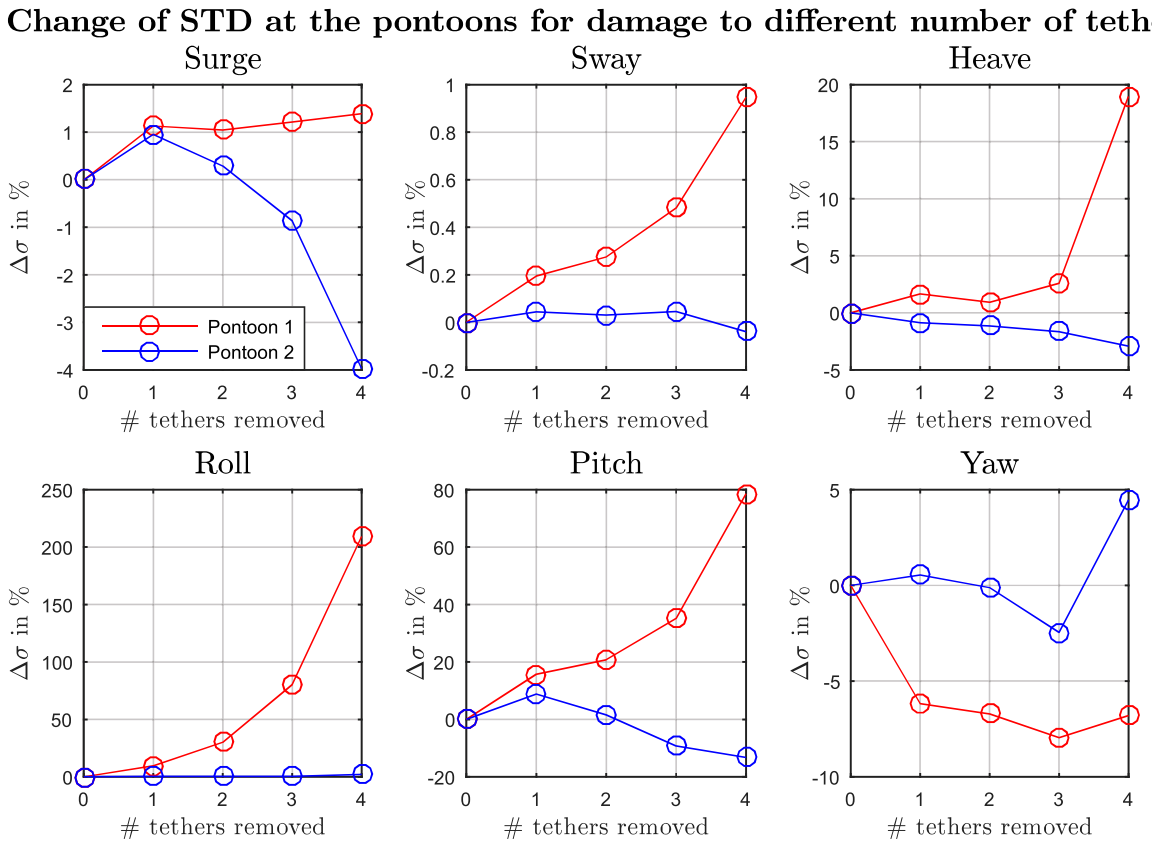

Figure 7.24: Plot of the change of the STD, $\Delta\sigma$, given in percent at the two pontoons for an increasing number of damaged tethers. All damaged tethers are at pontoon 1, below Tower 2. The standard deviations are listed in the appendix in table D.4.

For pontoon 1, where the damage to the tethers occurs, the standard deviation increases, with the number of damaged cables, for motion in all directions except for yaw, which can be seen from the red lines in figure 7.24. The standard deviation of pontoon 2, the blue line, varies without a clear trend for every motion.

	Undamaged	**1 tether damaged**		**2 tethers damaged**		**3 tethers damaged**		**4 tethers damaged**	
	ω_n	ω_n	%	ω_n	%	ω_n	%	ω_n	%
Mode 1	6.211E-02	6.207E-02	-0.057	6.207E-02	-0.065	6.204E-02	-0.102	6.196E-02	-0.244
Mode 2	8.319E-02	8.316E-02	-0.037	8.314E-02	-0.068	8.308E-02	-0.139	8.290E-02	-0.351
Mode 3	2.200E-01	2.197E-01	-0.105	2.194E-01	-0.241	2.188E-01	-0.509	2.179E-01	-0.955
Mode 4	3.076E-01	3.075E-01	-0.023	3.075E-01	-0.016	3.075E-01	-0.033	3.075E-01	-0.036
Mode 5	3.374E-01	3.372E-01	-0.059	3.370E-01	-0.113	3.367E-01	-0.219	3.357E-01	-0.525
Mode 6	3.972E-01	3.971E-01	-0.030	3.968E-01	-0.101	3.961E-01	-0.274	3.949E-01	-0.574
Mode 7	4.809E-01	4.814E-01	0.100	4.820E-01	0.227	4.783E-01	-0.534	4.873E-01	1.337
Mode 8	4.973E-01	4.972E-01	-0.022	4.969E-01	-0.095	4.959E-01	-0.286	4.924E-01	-0.991
Mode 9	5.123E-01	5.123E-01	0.004	5.125E-01	0.043	5.071E-01	-1.009	5.178E-01	1.070
Mode 10	5.371E-01	5.367E-01	-0.074	5.363E-01	-0.155	5.281E-01	-1.676	5.326E-01	-0.836

Table 7.10: Eigenfrequencies calculated from models where the tethers are damaged.

From table 7.10, it can be seen that the eigenfrequencies decrease with an increasing number of damaged tethers. As the stiffness of the structure is reduced by removing tethers, it is sensible that the eigenfrequencies decrease, and the corresponding eigenperiods increase, with an increasing number of damaged tethers.

Only small changes to the mode shapes of the bridge were observed due to damaged tethers. Of the first mode shapes, only mode 7 is presented in this thesis, as it experiences the most significant change. The eigenfrequency is fluctuating with increasing number of damaged tethers, and for the case of 4 damaged tethers, the vertical motion around pontoon 1 increases significantly, which could be explained by the asymmetric stiffness provided by the tethers.

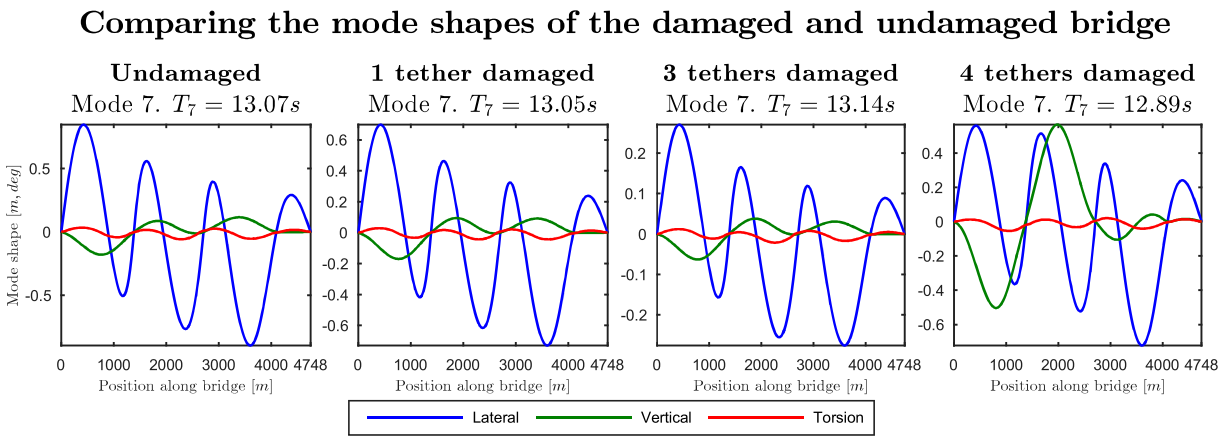

Figure 7.25: The effect damage to the tethers have on the 7th mode.

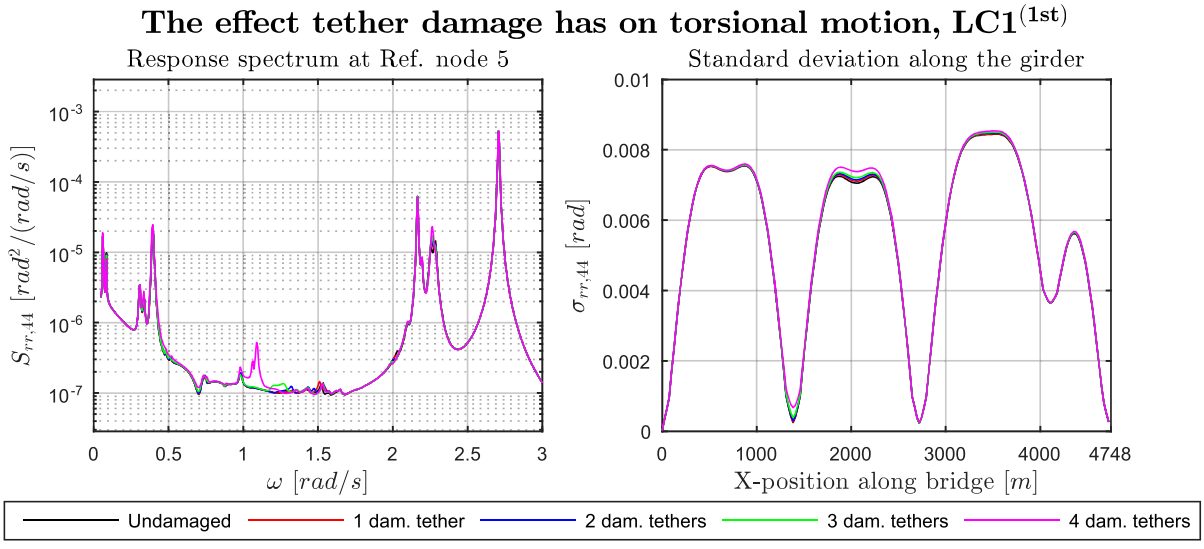

Figure 7.26: The effect damage to top cables or tethers has on torsional motion.

For torsional motion at Ref. node 5, figure 7.26 shows that even the removal of all four tethers at one of the porches does not affect the torsional response significantly. At around a frequency of

1 rad/s, a small new peak can be spotted in the torsional response spectrum. However, the little magnitude of the peak suggests that it is not of importance.

7.5.2 Damaged top cable

Due to the little sag of the top cable, the longitudinal stiffness provided by the top cable is larger than the geometric stiffness provided by the main cables, despite the significantly smaller cross section of the top cable. If the total stiffness, in the longitudinal direction at top of the pylons, is reduced, the main cables will tighten and loosen more easily, which will lift and lower the bridge girder. For this reason, damage to one of the top cables is expected to mainly influence the vertical modes.

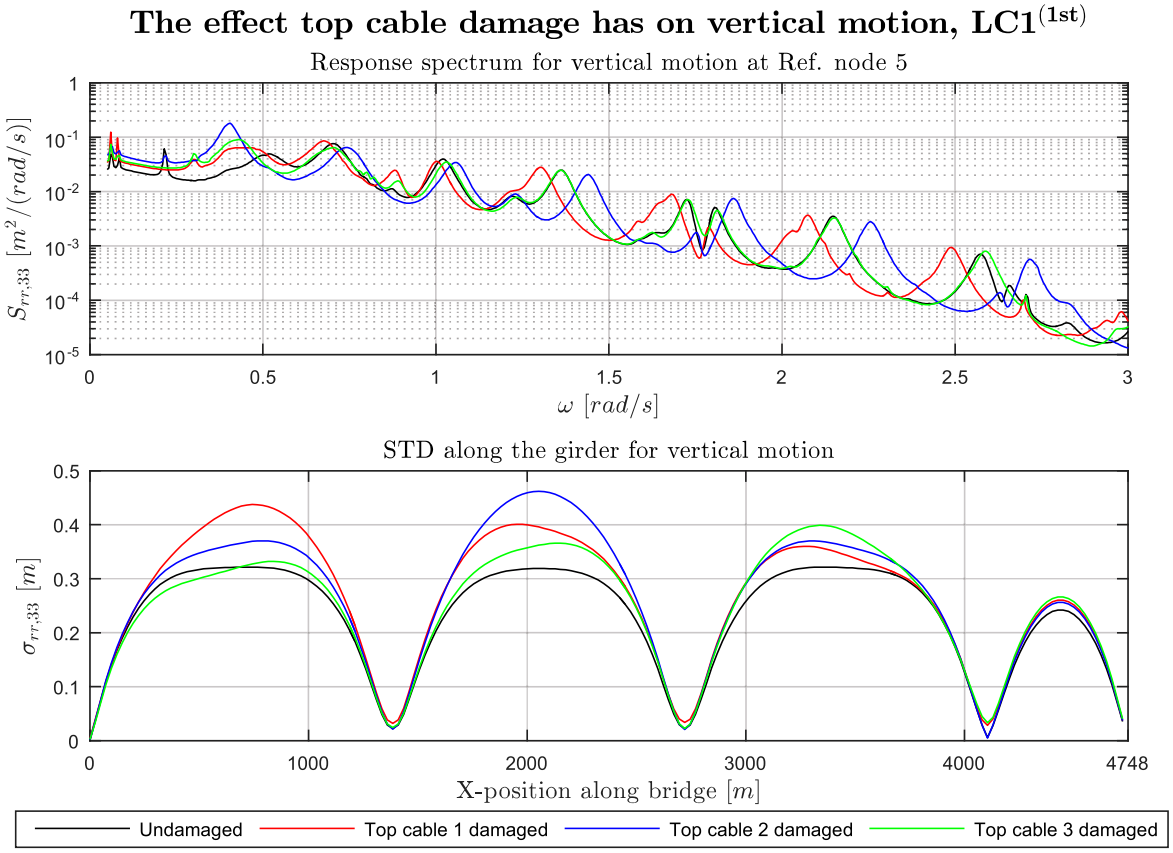

Figure 7.27: Change of the STD and the response spectrum due to damaged top cables for the vertical motion.

By studying the response spectrum for vertical motion in figure 7.27, it can easily be seen that the peaks occur for different values of ω, for damage to different top cable spans. This is due to the change of eigenfrequencies as a result of the change of stiffness in the system. Mode shapes are plotted in figure 7.29, but because some modes change mode number, the comparison is made according to the mode shape and not the mode number. By evaluating the change in mode shape and eigenperiod, it can be seen that the vertical modes experience the largest change, as expected.

Figure 7.27 also shows that the STD for vertical motion increases for almost every point along the girder, when one of the top cable spans are removed. Although results are not included in this thesis, a brief study showed that the altered eigenfrequency of the first and second vertical mode does not increase the response due to swell waves significantly.

Figure 7.28 shows how the standard deviation, for the movement of the top of each tower, changes when removing the top cable for different main spans.

It can be seen that the standard deviation increases as the stiffness of the structure is reduced. Keep in mind that because the values are given as change in percent, nodes with a very small STD might experience a very big relative change. This happens for vertical motion of tower 4, which is fixed to the ground. All STDs are listed in the appendix in table D.4. The percentage change is calculated with respect to the STD of the undamaged bridge.

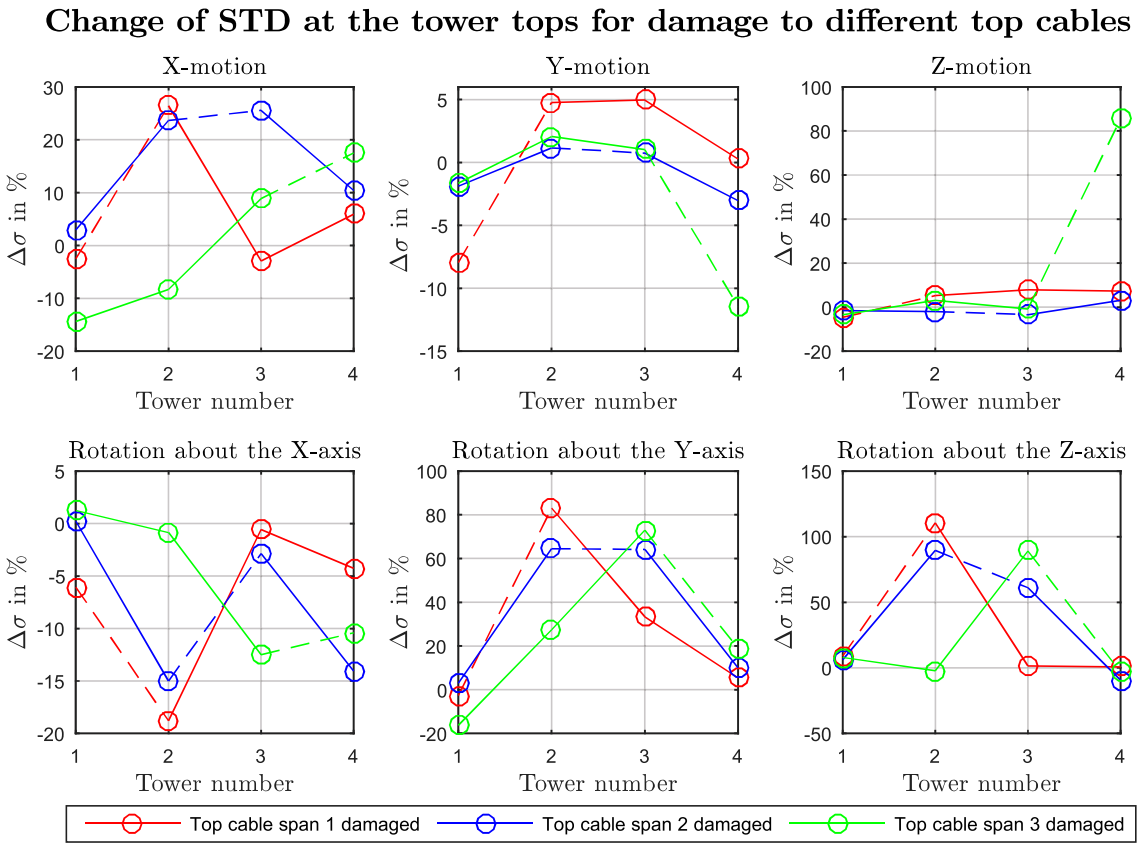

Figure 7.28: Plot of the change of the STD, $\Delta\sigma$, given in percent when removing the top cable at the three main spans. Dotted lines indicate the damaged span (where the top cable is removed). Only the STD at the location of the towers is included in this plot. The lines only indicate which points that belong together.

Figure 7.28 also shows that for motion in the longitudinal direction, referred to as Y-motion in the figure, the STD only increases significantly for the floating tower which is connected to the damaged top cable span. This can be explained by increased excitation of the second vertical mode, at the span of the damaged top cable, seen by comparing modes in the last row of figure 7.29.

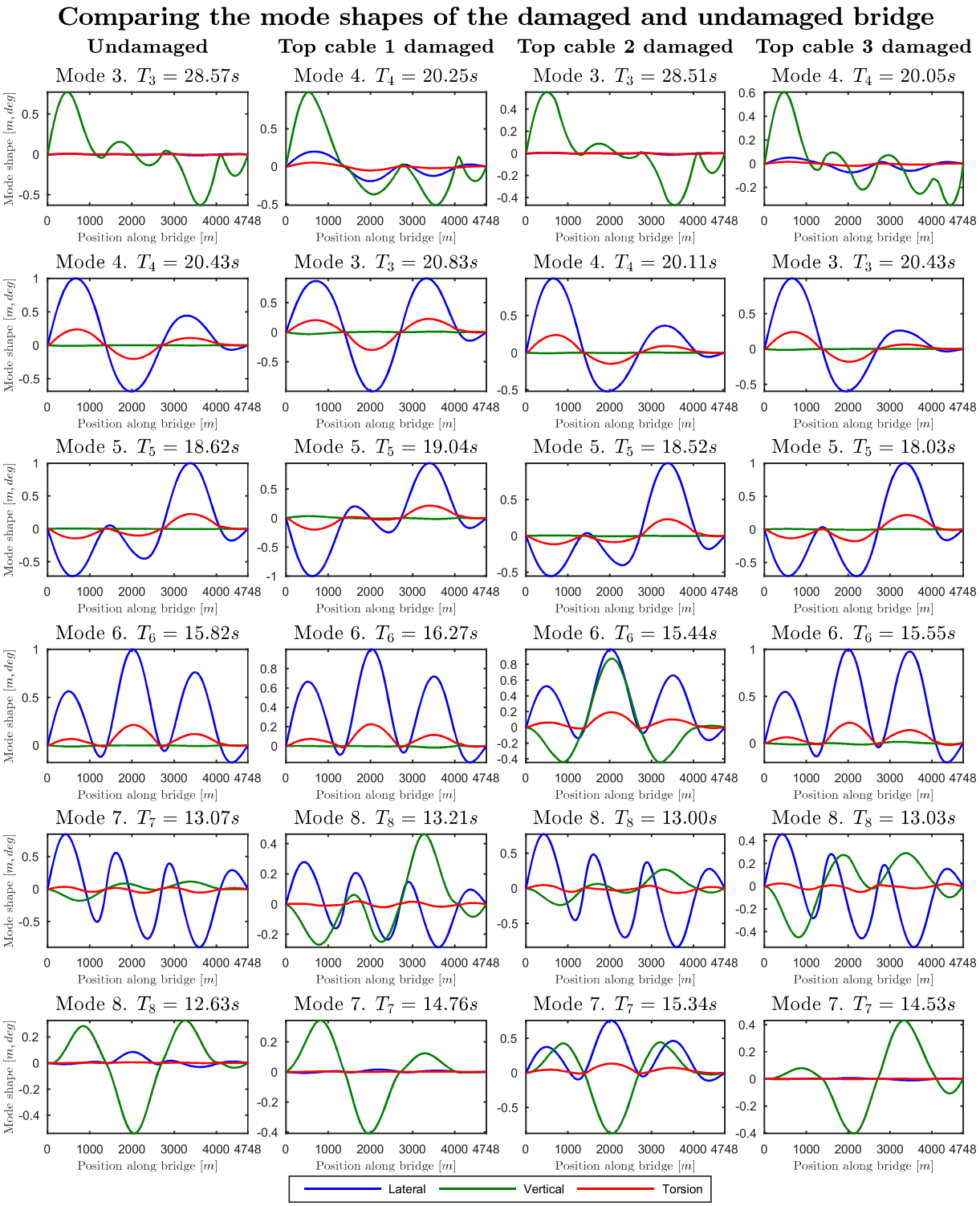

Figure 7.29: Mode shapes for damage to the different top cable spans. To easily compare mode shapes, modes are not necessarily plotted according to mode numbers, as some of them interchange positions. Relative change of eigenfrequency 1 to 9 can be found in the appendix in table D.2.

The STD at the top of the floating towers are shown in figure 7.28 to increase for lateral motion

when any of the top cables are damaged. Increased excitation of the first and second horizontal mode have caused the increase of the STD. A small decrease in the eigenfrequency of these modes is expected to have caused a larger excitation of the bridge because the wind load has greater spectral densities for the lower frequencies. This can be seen in table D.2 and figure D.6 in the appendix.

It can be seen that damage to a top cable in either span 1 or span 3 induces the greatest changes in the STD for torsional motion. The removal of the top cable in span 2 actually reduces the STD along the second and third span. It becomes evident that unsymmetrical changes to the bridge are not favourable.

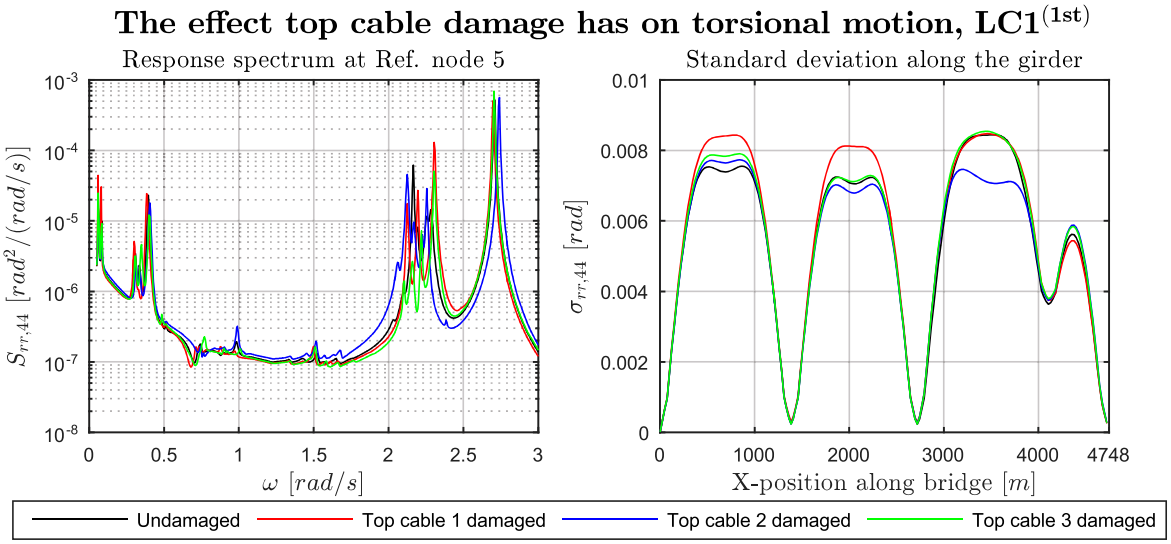

Figure 7.30: The effect damage to top cables or tethers has on torsional motion.

From the parameter study, tether damage has been found to cause relatively small changes to the bridge behaviour. For damage to the top cables, a more significant change in the bridge behaviour can be observed, especially for the vertical modes. Increased asymmetry of the bridge, as for the case of a damaged top cable over span 1 or 3, is found to be more critical than damage to the top cable over span 2. Response due to swell waves was also studied, but was found to generate similar results as found for wind waves, hence the results have not been included in this thesis.

7.6 Extreme value distribution

In this section, the extreme response of the bridge is assessed.

Initially, due to lack of access to environmental data, scaled North Sea PDFs were used for the initial extreme value analyses. Note that the scaled PDFs from the North Sea area do not differentiate between swell sea and wind sea components. Due to the uncertainties that followed the use of scaled North Sea PDFs, access to a NPRA-report, (NPRA, 2017), was requested and

granted. This report contains environmental scatter data for the rate of occurrence for different wave heights and wave periods for Bjørnafjorden.

The scatter data for wave and wind are partly based on real measurements and are partly based on computer simulations, but is treated as real measurement data in the following section. Based on the environmental conditions given by the scatter data, PDFs for the Bjørnafjorden area has been estimated. Scatter data was provided independently of mean wind velocity, and only the correlated mean wind velocity, given a specific range of wave heights, was provided. In order to determine the coefficients of a PDF also dependent on the mean wind velocity, scatter data of a lot of different mean wind velocities are required. To perform a long-term analysis with PDFs that were also dependent on the mean wind velocity, the scaled PFDs by (Li et al., 2015) and (Johannessen et al., 2002) were used. Correlated mean wind velocity is shown in figure 7.31.

As only the report by (Li et al., 2015) provides both $f_{H_s,T_p}(h,t)$ and $f_{U,H_s,T_p}(u,h,t)$, results are compared to results based on (Haver, 2008) and (Johannessen et al., 2002) according to the type of analysis performed.

The STDs used to estimate the long-term response is calculated for wind waves and swell waves with values for the spreading parameter s and the parameter γ for the JONSWAP spectrum according to values listed in table 7.6. Second order wave forces have not been included, because the effect is negligible compared to that of wind loading. In addition, when the wind loading is not included, the extreme response is desired to be a response in the frequency domain of the 1st order wave loading.

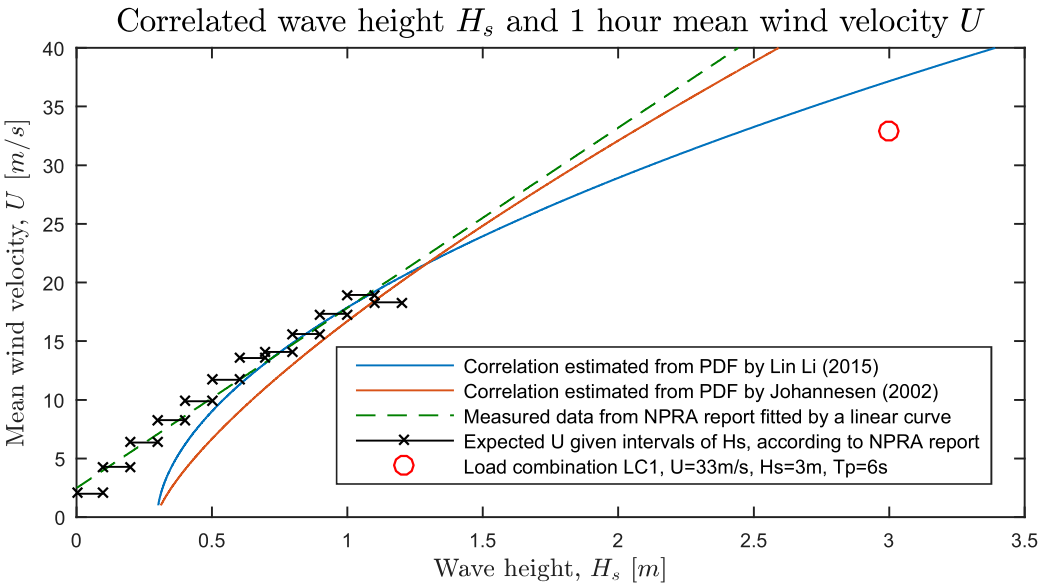

Figure 7.31: The correlated mean wind from (NPRA, 2017, Tab.8) and from estimations.

From figure 7.31, it is clear that the correlation between mean wind velocity and wave height derived from (Li et al., 2015) fits better with the results from (NPRA, 2017, Tab.8) and the extreme load combination listed in table 7.7, than the correlation derived from (Johannessen et al., 2002).

7.6.1 Estimating the PDFs for Bjørnafjorden

Figure 7.32 shows the curve-fitting of the environmental data from Bjørnafjorden, used to obtain the PDF of the wave height and the wave period. Since the built-in tool in MATLAB used for the curve fitting finds the optimal curve by minimizing the sum of squares, it must be used with caution when fitting a probability function to be used in an extreme value analysis. This is because the large values of long-term analysis with a correspondingly low probability are the most important values, but their contributions to the sum of squares are most likely very small. This can be solved by applying a weighting function. A weight that provides good results is $1/p$, where p is the probability of the point evaluated. Note that some of the coefficients cannot be negative.

To evaluate the goodness of fit for the values, it is recommended to perform the chi-squared test, control the size of the R^2-value in addition to a visual control. Different visual controls are important to be able to spot the positive and negative properties of the fit.

Results from the chi-squared test can be found in the appendix in table D.5 and D.6. The amount of sample points used to obtain the scatter data had to be assumed, as the data, in reality, was estimated numerically. The PDF, $f_{H_s}(h)$, for swell waves passes the chi-squared test, while the PDF for wind waves only passes the test for a small range around the mean wave height.

In (Haver, 1980, p. 46) it is stated that proposed models often are not accepted by a chi-squared goodness of fit test, but because significantly better models are difficult to obtain in this case, it can be justified to keep the suggested models. However, based on results shown in figure 7.32, the authors of this thesis would recommend to develop the model further. Unfortunately, there was not enough time to improve the fit of the PDF, and the suggested weighting scheme has not been fully implemented.

Figure 7.32 shows the curve fitting of the measurement data to obtain the empirical PDFs.

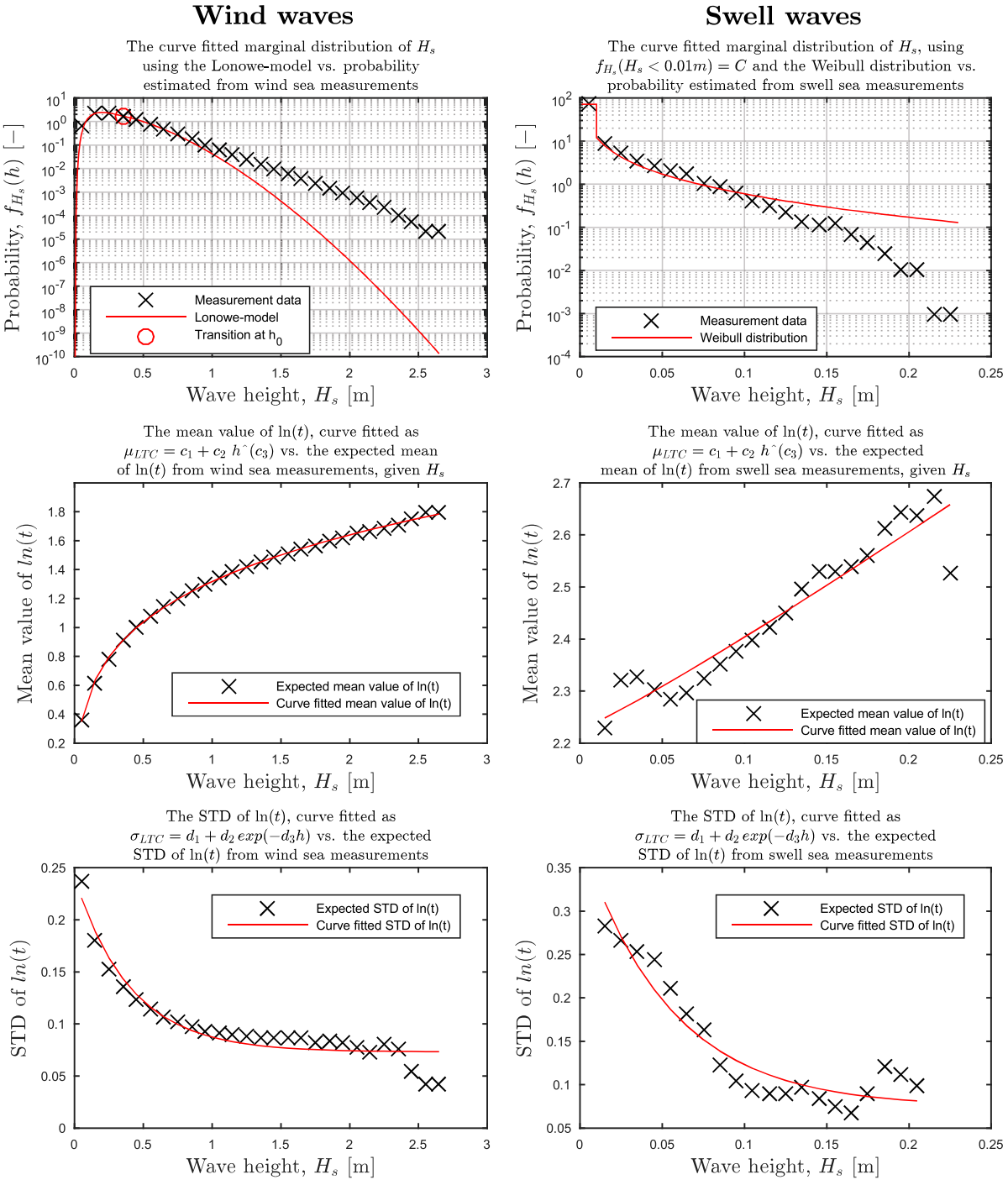

Figure 7.32: The curve fitting performed above was required to obtain the PDF $f_{H_s,T_p}(h,t)$ for wind waves and swell waves.

Note that the log plot of the curve fitting of $f_{H_s}(h)$ reveals that extreme values are not estimated correctly for both the swell and wind waves. This result will most likely result in a probability distribution function that underestimates the wind waves in Bjørnafjorden and overestimates the effect of swell waves. This is pointed out in section 7.6.4.

The curve fitting coefficients used to establish $f_{H_s,T_p}(h,t)$ can be found in table 7.11 and 7.12.

	μ_{LTC}, **eq. 4.13**			σ^2_{LTC}, **eq. 4.13**		
	c_1	c_2	c_3	d_1	d_2	d_3
Coef. estimated for Bjørnafjorden, wind waves	-0.7982	2.116	0.2045	0.07311	0.1673	2.4624
Coef. estimated for Bjørnafjorden, swell waves	2.226	2.217	1.096	0.07427	0.3119	18.56
Coef. source: (Haver, 2008)	1.134	0.892	0.225	0.005	0.120	0.455
Coef. source: (Li et al., 2015)	1.886	0.365	0.312	0.001	0.105	0.246

Table 7.11: The coefficients used in the probability distribution of $f_{T_p|H_s}(t|h)$. See equation 4.12.

	Lognormal, eq. 4.11 $h \leq h_0$		**Weibull, eq. 4.11** $h > h_0$		**Limit of validity**
	σ_{LHM}	μ_{LHM}	α_{LHM}	β_{LHM}	h_0
Coef. estimated for Bjørnafjorden, wind waves	0.662	-1.174	1.610	0.355	0.350
Coef. source: (Haver, 2008)	0.573	0.893	1.550	2.908	3.803
Coef. source: (Li et al., 2015)	0.506	0.871	1.443	2.547	5.0

	Constant probability $h \leq h_0$	**Weibull, eq. 4.9** $h > h_0$		**Discontinuity point**
		α	β	h_0
Coef. estimated for Bjørnafjorden, swell waves	71.960	6.521	0.385	0.01

Table 7.12: The coefficients used in the probability distribution of the wave height, $f_{H_s}(h)$.

The PDFs by (Li et al., 2015) and (Johannessen et al., 2002) have been empirically designed for the North Sea area, where the sea state is much more extreme than in the Bjørnafjord area. To be able to use the empirical PDFs for the North Sea area, they had to be scaled down.

Scaling was done by comparing the extreme values with a 100 year return period found by the contour plot method with the 100 year extremes given in (NPRA, 2016n, B.1). The scaling parameter, κ, of the wave height axis was selected such that a wave height of 3 m would be achieved for the 100 year extreme load combination. The scaling parameter of the period axis was set to, $\sqrt{\kappa}$, as recommended by one of the advisor for this thesis, PhD Candidate Yuwang Xu. An extreme load combination of $H_s = 3$ m, $T_p = 6$ s and $U = 33$ m/s with a 100 year return period has been applied throughout this thesis. The contour plot based on coefficients from (Li et al., 2015) in figure 7.36 corresponds well with this load combination when $\kappa = 5.4$. As the PDFs by (Johannessen et al., 2002) and (Haver, 2008) also are given for the North Sea, the same scaling factor of $\kappa = 5.4$ was applied. This assumption proved to be unreasonable, which will be discussed later section 7.6.2. The scaling factors were also applied to the probability so that the total probability of the entire area of definition still summed up to one.

The scatter data from the report (NPRA, 2017) was fitted to the PDF of the wave height and the wave period outlined in (Haver, 2008). As this probability distribution function is based on 11 different coefficients, different properties of the PDF is fitted separately.

The swell waves are present less than 40 % of the time, and the scatter data only provide the rate of occurrence. Based on this, it was found that having a discontinuous probability function, with

the first part equal to a constant, was well suited to obtain the correct probability for swell not to occur while obtaining a best possible fit of the measurement data.

Comparison of scatter data for wind generated waves and the estimated PDF

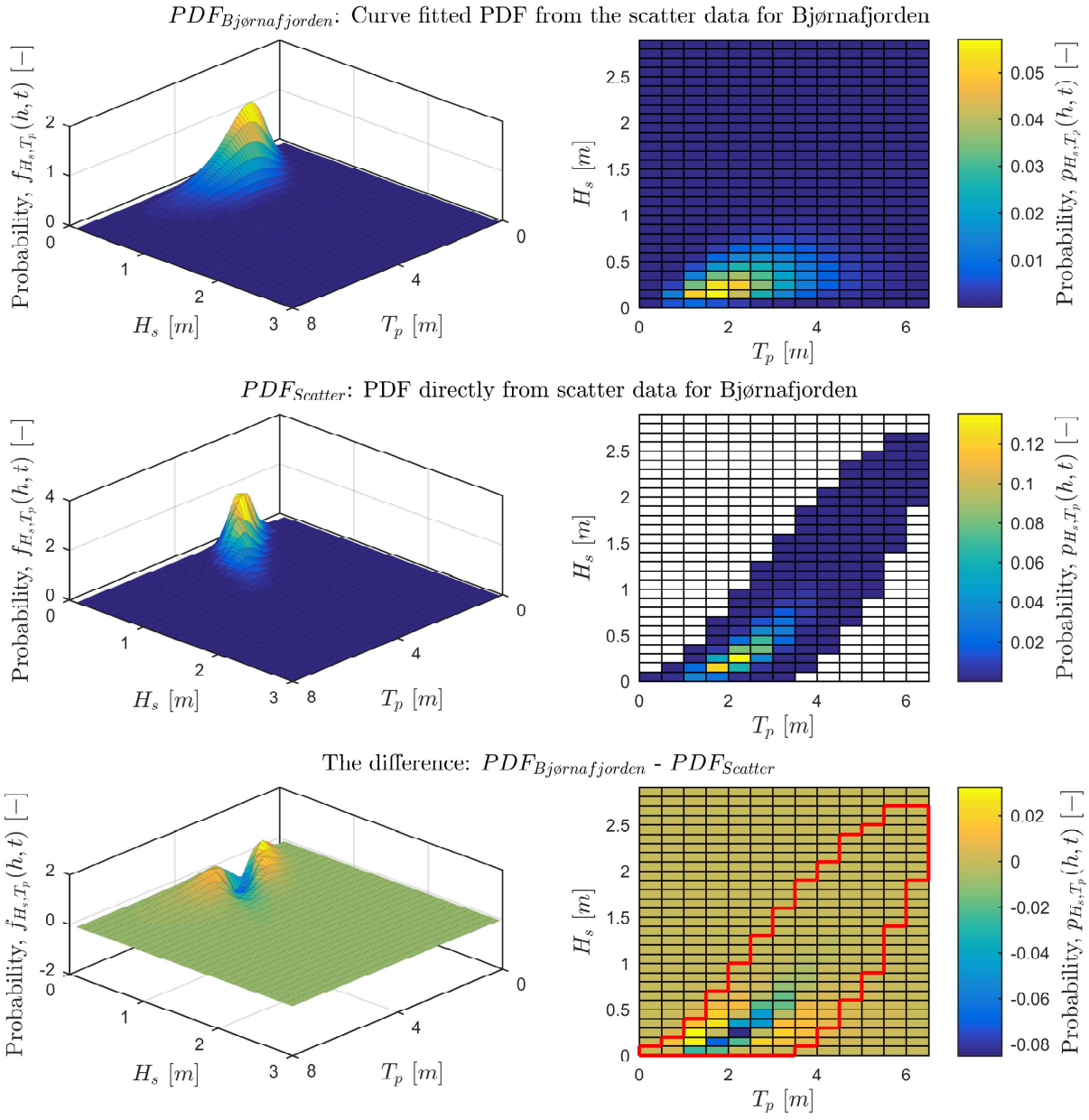

Figure 7.33: Comparison of an empirical PDF and probabilities given by scatter data for wind waves. Note that the surface plot on the left is a continuous probability and the scatter plots in the right column are a discrete probability. As the scatter data is given as a discrete probability, while the fit of the PDF for Bjørnafjorden is estimated by a continuous PDF, conversion has been performed according to equation 3.90 and interpolation of the estimated continuous probability at the mean value of the scatter data. The red line in the scatter plot outline of the area where scatter data has been provided. Outside this area, the scatter data is assumed to equal zero. Note also that the colour bar given on the right is not valid for the surface plot, and the colours on the surface plot vary only with the z-axis, to better show the dominant parts of the PDF.

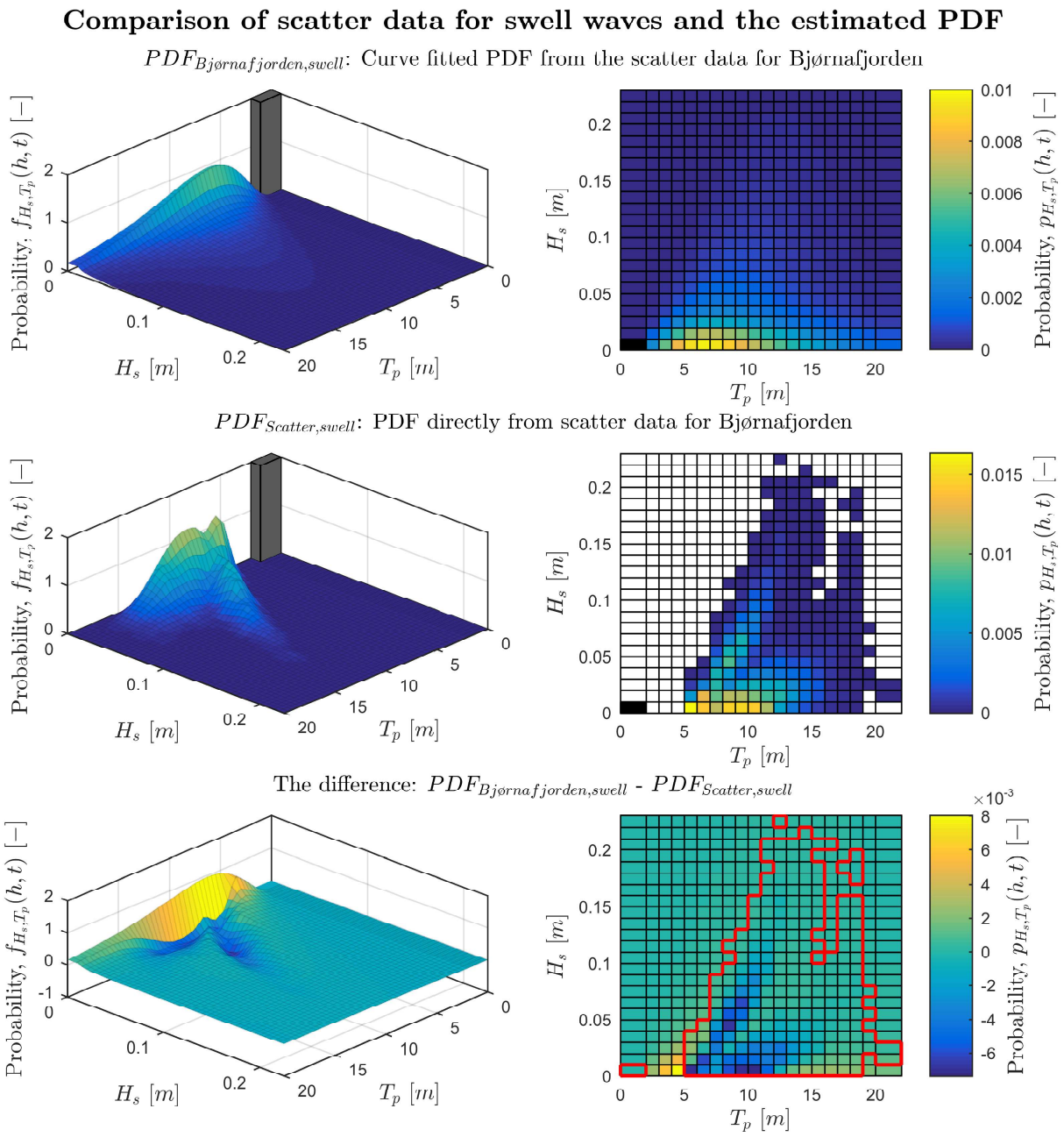

Figure 7.34: Comparison of an empirical PDF and probabilities given by scatter data for swell waves. See figure caption of figure 7.33 for the general figure description. Also, this figure has a grey box in the surface plot, marked as a black square in the scatter plot, representing the probability of having no swell waves. 60 % of the time swell waves are within this range. Hence the grey box is not scaled correctly, to ease the visual presentation of other data. The first and the last column of the scatter plots are for periods less than 2 s and longer than 20 s.

From the plot of the curve fitting in figure 7.32 and from the residuals, the measurement data for wind waves seems to follow a more clear trend than the measurement data for swell waves. The indication that there are more uncertainties related to the occurrence of swell waves are

reasonable, as this is also stated by the report (NPRA, 2017).

Figure 7.34 shows that the PDF, which represents swell waves in Bjørnafjorden, fits quite well, and properly takes the constant probability of wave height less than 0.01 m and wave period 2 s into account. The probability of large wave heights does, however, appear to be overestimated, as pointed out.

7.6.2 The environmental contour surface

The contour lines in 7.35 shows the load combinations with a 100 year return period, considering wave loading only. The contour plot for Bjørnafjorden is compared to results obtained by scaled PDFs from (Li et al., 2015) and (Haver, 2008). Estimations based on scatter data from Bjørnafjorden corresponds well with estimations based on (Li et al., 2015) for large wave periods, but does not have the same distinct peak for the maximum wave height. A smaller deviation might have been experienced if the marginal distribution of H_s did not underestimate the probability of large wave heights, as shown in figure 7.32 and 7.33.

The contour plot in figure 7.35 estimated by the PDF developed for Bjørnafjorden from figure 7.33, seems reasonable, as the shape and position of the peak in the developed PDF corresponds well to the estimated contour line.

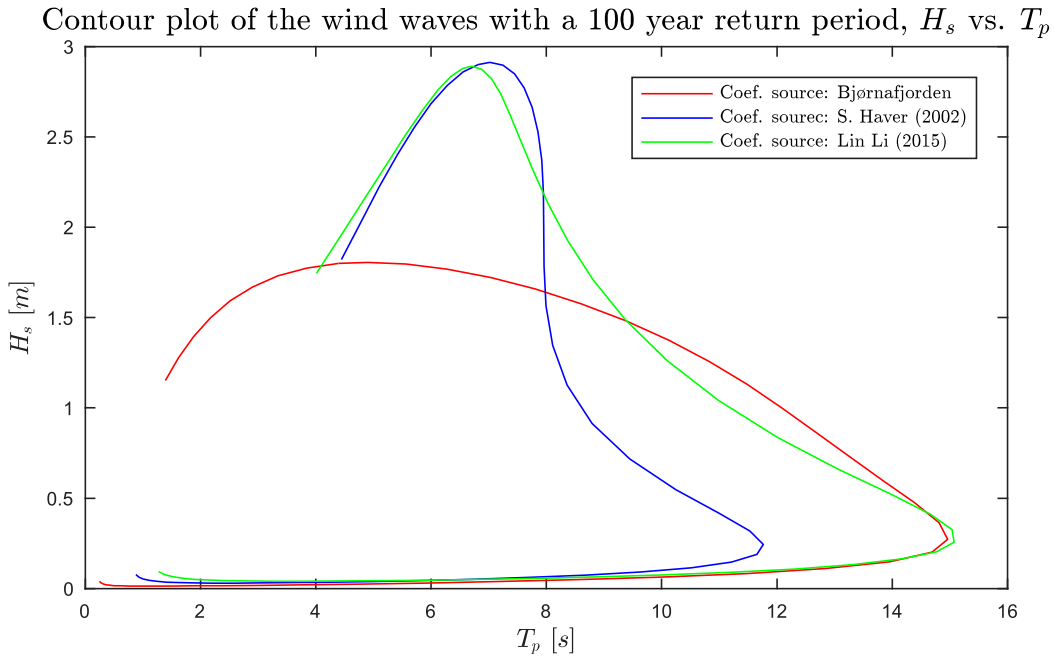

Figure 7.35: The figure shows the contour line calculated using the PDF obtained by curve fitting scatter data of wave periods and wave heights measurements from Bjørnafjorden versus the contour lines obtained from scaled PDFs for the North Sea area.

A contour plot of the swell waves has not been made, due to the nature of the obtained PDF from the curve-fitted data.

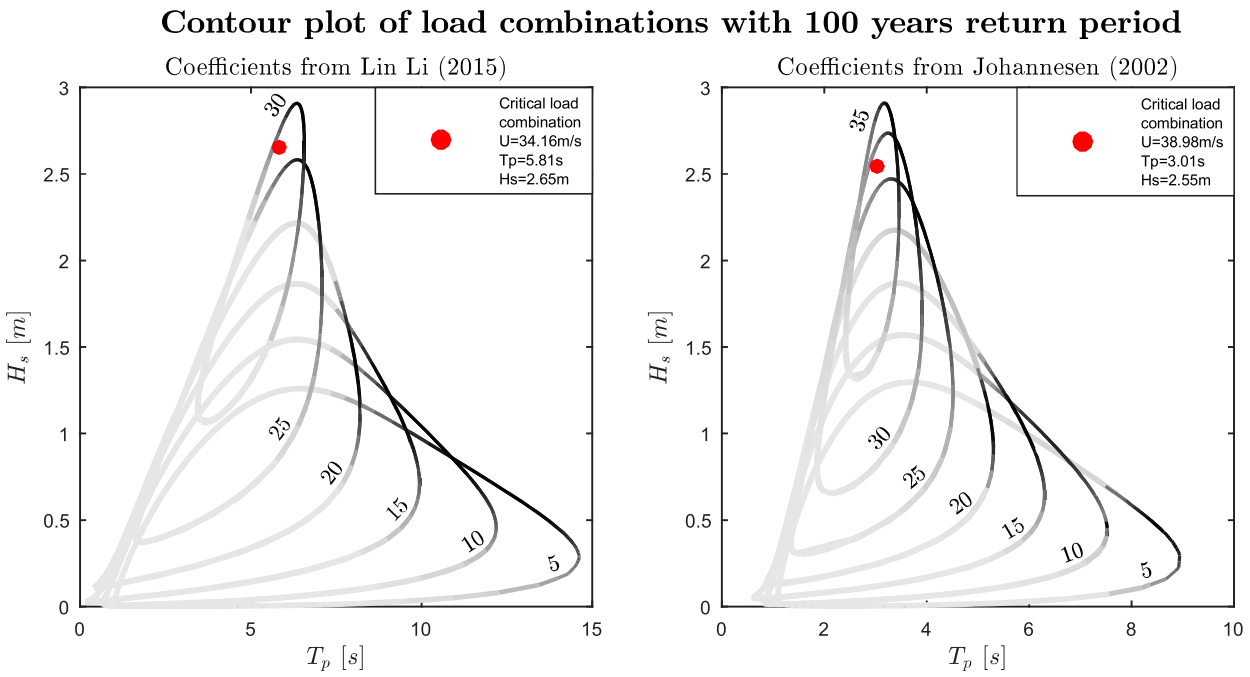

Figure 7.36: The extreme load combinations with a 100 year return period are shown by the contour plot. Labels along contour lines indicate the mean wind velocity, U. The standard deviation is calculated at mid-span. The colour of the contour plot indicates if the standard deviation is big or small compared to the other extreme values with a 100 year return period. Black indicates high standard deviation compared to other values on the same line, and light grey indicates a small standard deviation. Variation of standard deviation within a line or difference between STD for different mean wind velocity can be seen from table 7.13.

In figure 7.36 can the contour lines of the scaled PDFs be seen. In hindsight, it is noted that the scaling of the PDF from (Johannessen et al., 2002) is not good when considering that the critical STD is calculated based on a wave height and wave period that cannot occur according to (DNV GL AS, 2014, 3.4.6). It is stated that due to a maximum possible wave steepness, the breaking wave height for a deep water wave is roughly 2 m for a wave period equal to 3 s. Thus a wave period of 3.01 s with a corresponding wave height of 2.55 m cannot occur. This implies that the scaling factors that were applied to the PDF from (Li et al., 2015) are not applicable to the PDF from (Johannessen et al., 2002).

Mean wind velocity U $[m/s]$	**PDF from (Li et al., 2015)**		**PDF from (Johannessen et al., 2002)**	
	$min(\sigma_{100}(U))$	$max(\sigma_{100}(U))$	$min(\sigma_{100}(U))$	$max(\sigma_{100}(U))$
5	0.0434	0.4154	0.0434	0.0948
10	0.2082	0.4283	0.2082	0.2092
15	0.4726	0.5790	0.4726	0.4729
20	0.8262	0.8572	0.8262	0.8262
25	1.2504	1.2513	1.2504	1.2504
30	1.7415	1.7422	1.7415	1.7415
35			2.2869	2.2869

Table 7.13: Maximum and minimum standard deviation for the different mean wind velocities given in the contour plot in figure 7.36. The STDs are calculated at mid-span.

The contour plots in figure 7.36 shows that the variation of extreme wave loading decreases when the mean wind velocity increases. From the variation of STD shown by the colour of the contour lines, the combination of a big wave height and long wave period proves to generate a larger standard deviation, than achieved by the maximum wave height or the maximum wave period for the given mean wind velocity. Similar results are observed using different reference nodes.

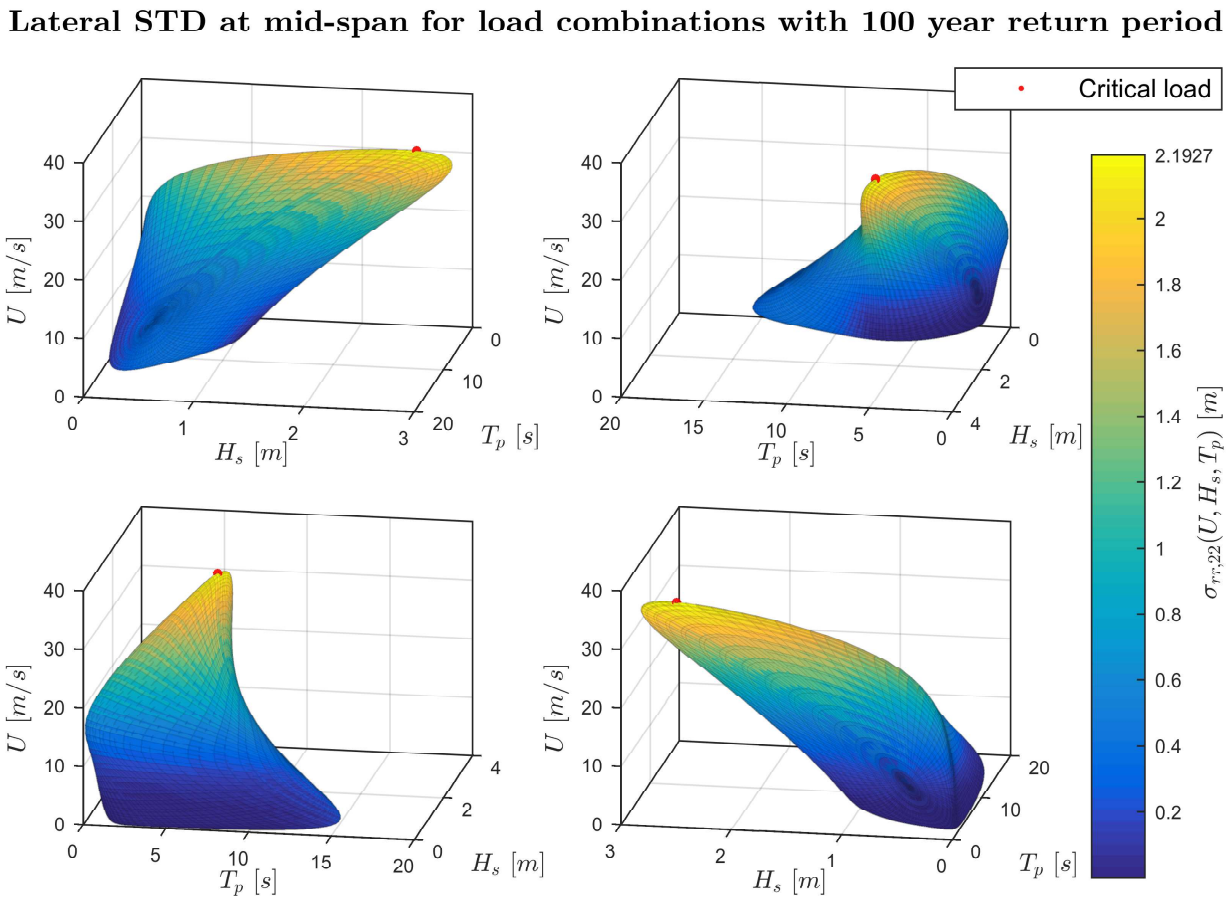

Figure 7.37: The figure shows the STD for extreme value combinations with a 100 year return period in a surface plot. All four figures show the same plot but from four different angles. Note that the colour of the surface plot varies with the STD and not only with the given mean wind speed. It is just that the mean wind speed generates most of the STD, for mean wind velocities above approximately 10 m/s. Parameters for the PDF are taken from (Li et al., 2015, p. 8).

From the surface plot in figure 7.37 and table 7.13, it becomes obvious that the STD at mid-span is dominated by the wind response. The colour of the surface plot appears to mainly vary with the mean wind velocity. For high velocities, a large number of decimals is required in the table to be able to observe the effect of changing the wave loading.

7.6.3 All short-term extremes

This section comprises the results of equation 4.17. The probability limit for short-term extremes is 50 % to obtain the mean value, as suggested by (Haver, 2007, Sec. 7.5.3). The probability limit combined with the low probability of the load condition enables a long-term response to be estimated by a short-term extreme.

The CDF for short-term extreme responses can be found from the procedure in section 4.4.1. By considering all the load cases with a 100 year return period found by the contour plot method in figure 7.36, an estimate for the long-term response can be obtained by finding the short-term load condition that yields the largest response.

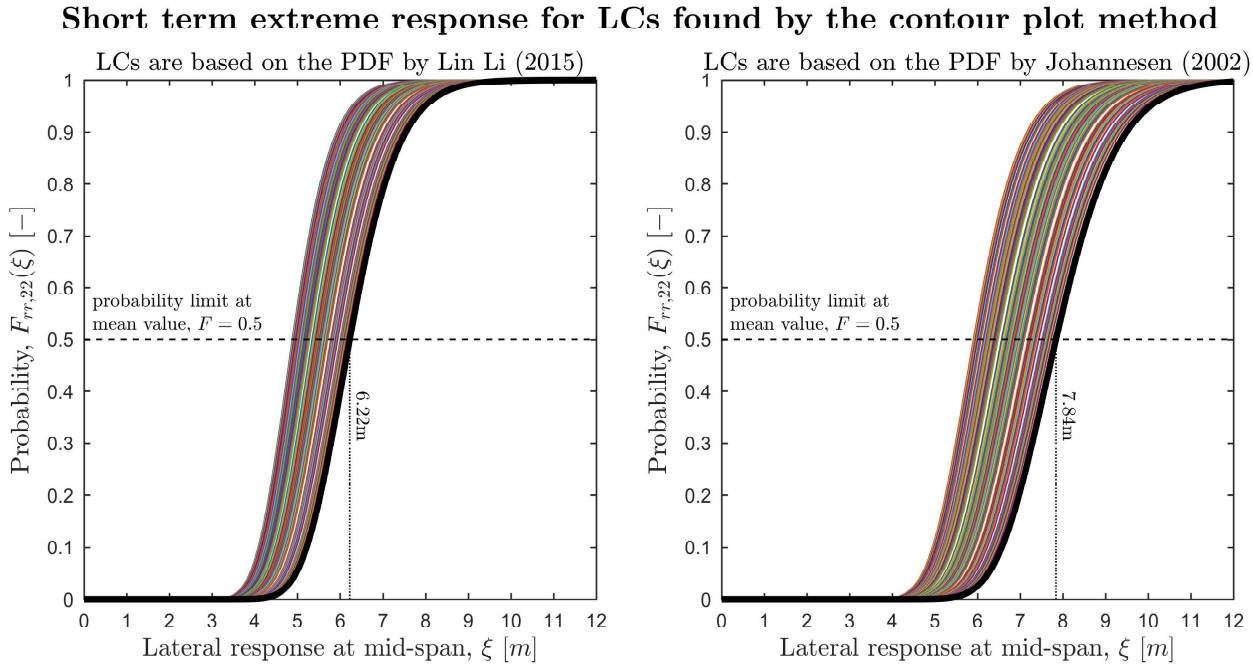

Figure 7.38: The figure shows a plot of the CDFs of the short-term responses for the load combinations found from the contour plot method. (Top 5% of the load combinations are plotted with respect to the lateral response.) The extreme response is found to be 6.22 m based on the PDF by (Li et al., 2015) and 7.84 m based on the PDF by (Johannessen et al., 2002). Note that the load combinations used include both wind and wave loading.

In the result sections from the buffeting analyses, it is shown that the wind loading is, in general, determining the size of the STD. As higher wind speeds are obtained by the contour plot method by using the PDF by (Johannessen et al., 2002) compared to the PDF by (Li et al., 2015), it should not be surprising that the largest response is found by the PDF by (Johannessen et al., 2002).

The NPRA report, (NPRA, 2017, p. 17), suggests an extreme load combination that combines wind waves, swell waves and mean wind velocity with a 100 year return period. Figure 7.39 shows the effect the inclusion of swell waves has on the total response.

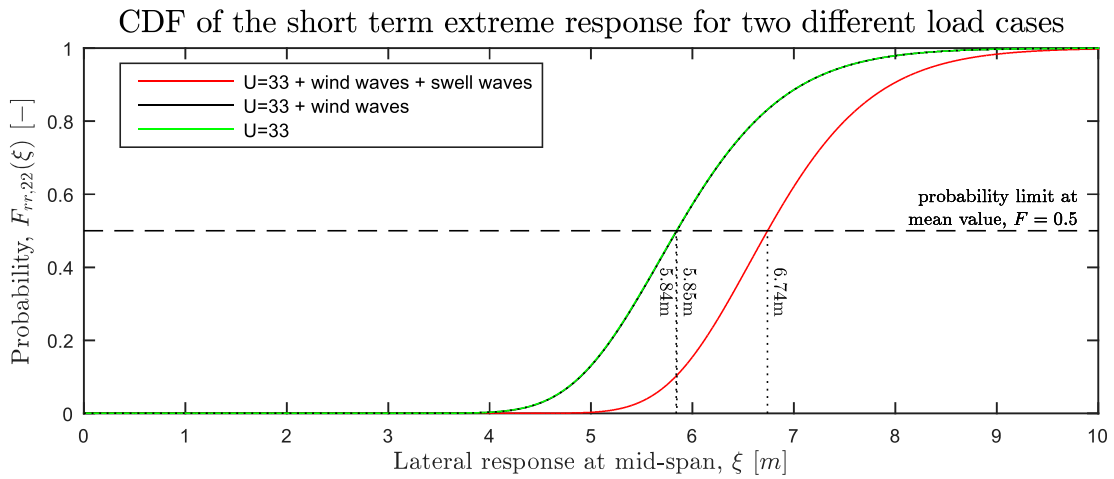

Figure 7.39: The short-term extreme response CDF calculated for two load cases from the NPRA-reports, and the load case of $U = 33$m/s as reference. The properties of wind waves and swell waves are found in table 7.7.

Adding swell waves to the problem, seen in figure 7.39, increases the response by roughly 15 %. It can thus be concluded that neglecting the effect of swell waves could severely underestimate the response of the structure.

In table 7.14 is a comparison of the results from the short-term analyses based on equation 4.17. It is as expected that the response based on the PDF from (Li et al., 2015) is similar to the response of the NPRA-load case without swell waves, because the PDF from (Li et al., 2015) is scaled to match that particular NPRA load case. The PDF from (Johannessen et al., 2002) has a bad scaling and is thus expected to yield different results.

Short-term extreme response for lateral displacement at mid-span Eq. 4.17	
Load condition	Response $[m]$
From contour plot method with coef. source (Johannessen et al., 2002)	7.84
From contour plot method with coef. source (Li et al., 2015)	6.22
For reference: U=33	5.84
NPRA load suggestion: U=33 + wind waves	5.85
NPRA load suggestion: U=33 + wind waves + swell waves	6.74

Table 7.14: Comparison of the short-term extreme response values for lateral displacement at mid-span, calculated by eq. 4.17.

In table 7.14 can the insignificant contribution of the wind waves to the extreme lateral response at mid-span be seen. The response increases from 5.84 m to 5.85 m when adding wind waves loading to the wind loading. This confirms the assumptions made when studying the response spectra and the STD from the buffeting analyses, that the wind waves contributes little to the extreme lateral displacement of the bridge.

In figure 7.40 is the lateral STD, the lateral static deflection and the lateral extreme short-term response shown based on the load combination from the NPRA-reports, $U = 33$ m/s, $H_s = 3$ m,

$T_p = 6$ s. It can be seen that the static deflection due to wind generates the largest displacement in the lateral direction. Maximum expected displacement is found by combining the static wind response and the estimated short-term response. It can be seen that the static deflection along the girder in the vertical direction due to wind is virtually zero, as expected. For the lateral direction, the static deflection is largest at mid-span, while the STD peaks at the first floating tower. This is because of the second horizontal mode shape, which has a significant contribution to the STD, have no movement at mid-span. When wind loading is applied perpendicular to the length of the bridge, maximum displacement is however expected at mid-span.

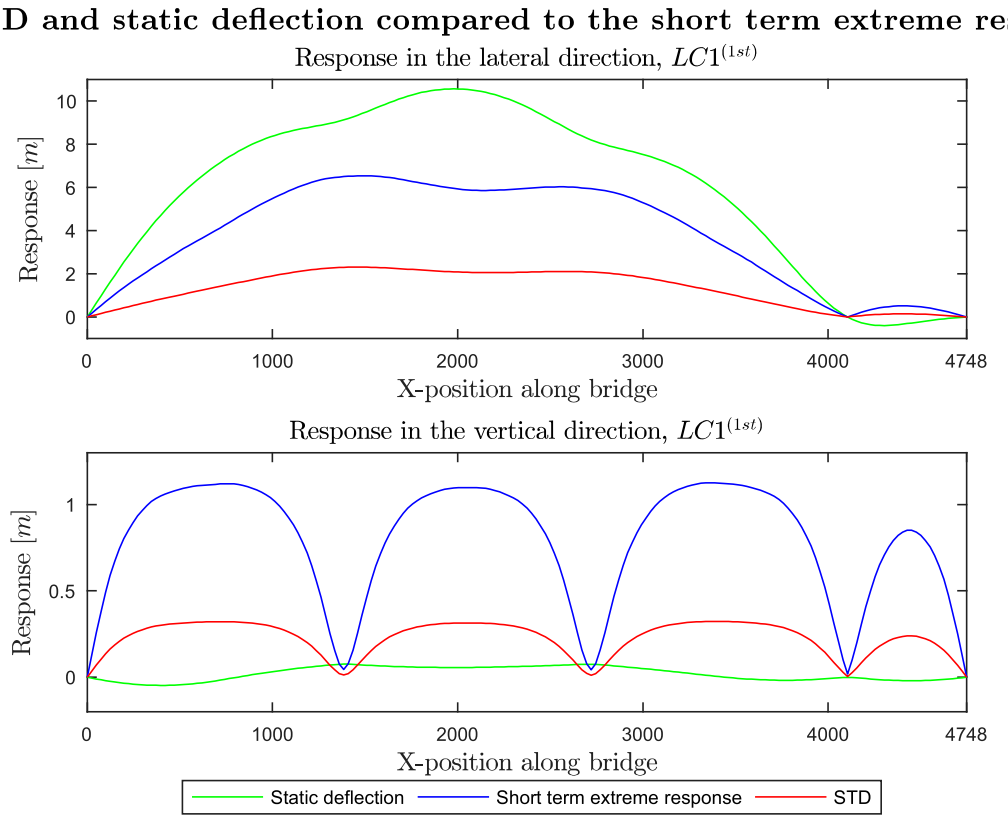

Figure 7.40: The figure shows the load combination from the NPRA-reports, $U = 33$ m/s, $H_s = 3$ m, $T_p = 6$ s. The static deflection is due to wind loading only. The lateral short-term response calculated by equation 4.17. The static deflection is measured from the equilibrium position. Maximum static deflection is 10.57 m.

7.6.4 The long-term extreme

This section presents the results of long-term response analyses of the lateral response, based on equation 4.25 and 4.26, due to environmental loading with a 100 year return period.

In the articles by (Li et al., 2015) and (Haver, 2008) it is pointed out that $f_{H_s,T_p}(h,t)$ are estimated based on the occurrence of both wind and swell waves. The estimations for swell and wind waves for Bjørnafjorden are, however, done by two separate PDFs.

To differentiate the significant contributions from wind waves and swell waves from each other the integral limits of equation 4.25 have been set to $T_p = [0, 8]$ and $H_s = [0, 4]$ for wind waves, as the period and wave height is believed to be well within these limits. Similarly, a limit of $Tp = [0, 20]$ and $Hs = [0, 0.4]$ was set for swell waves. This simplification is possible because swell occurs with long wave periods and small wave heights, while wind waves have significantly larger wave heights and shorter periods. Preferably the integration would be over the entire domain of the probability density function, but because both the s-parameter and the γ parameter is different for the two wave types, it was decided to separate the results into two different load cases, as they can occur simultaneously.

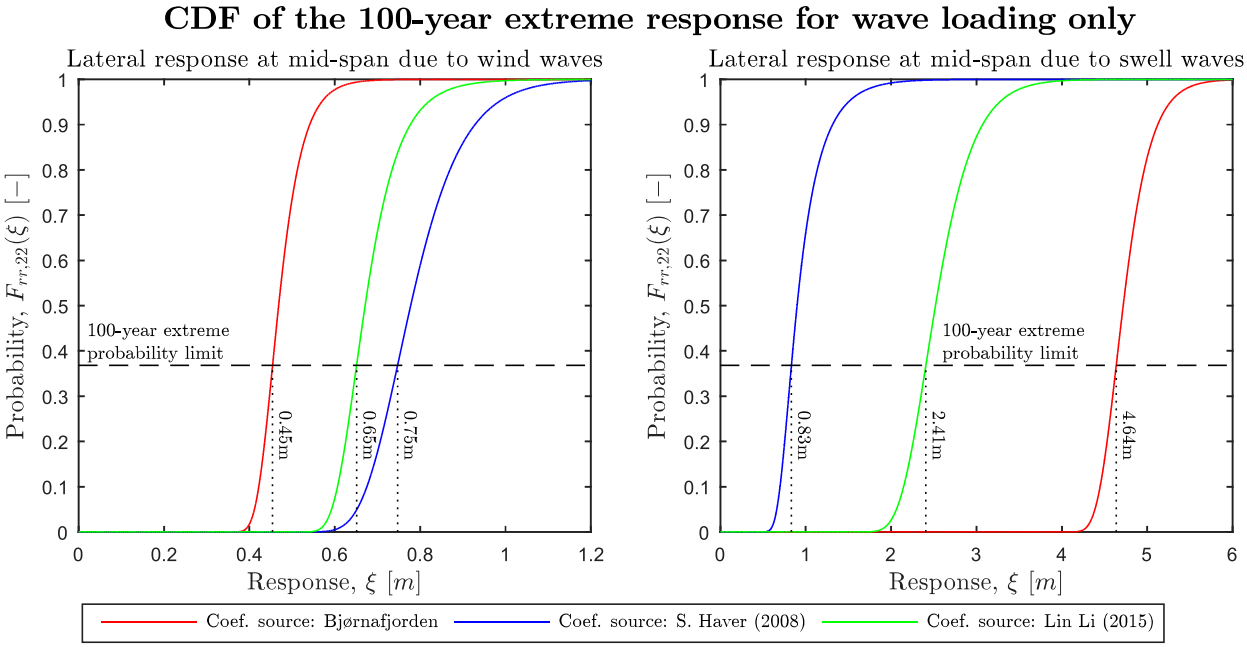

Figure 7.41: Cumulative probability function for the long-term extreme response at mid-span using three different probability distribution functions. Note that the response is calculated for wind waves and swell waves only, no wind loading has been considered. Second order wave forces are not included.

Figure 7.41 shows that swell waves generates a significant larger result than wind waves. The swell response from the PDF for Bjørnafjorden might be overestimated, as the marginal distribution of H_s appears to be overestimated, as shown in figure 7.32.

It is assumed that the swell waves are not properly represented in the scaled North Sea PDFs. Thus, a comparison of the results obtained using the PDF from Bjørnafjorden yields, not surprisingly, swell wave response results that differ substantially from each other. See table 7.15 and figure 7.41. The extreme response calculation based on scatter data from Bjørnafjorden support results found for the short-term extremes, that considering swell waves is important. The results using the PDF from Bjørnafjorden are considered the most reliable swell wave estimation, as the PDFs by both (Haver, 2008) and (Li et al., 2015) are not established solely to represent swell waves.

Long-term lateral extreme response at mid-span for wave loading only, eq. 4.25		
PDF source	Wind waves	Swell waves
	Response $[m]$	Response $[m]$
Bjørnafjorden	0.75	4.64
(Haver, 2008)	0.65	0.83
(Li et al., 2015)	0.45	2.41

Table 7.15: The table shows the long-term extreme response at mid-span based on equation 4.25. The response is calculated for three different PDFs.

It should be mentioned that an extreme response based on the scaled PDF of (Li et al., 2015), calculated using the gamma and spreading parameter for wind waves for the entire range $H_s = [0, 4]$ and $T_p = [0, 20]$, generates a slightly smaller response than the response found for swell waves in figure 7.41. Hence, changing the integration limits to take swell properly into account generated a more conservative response.

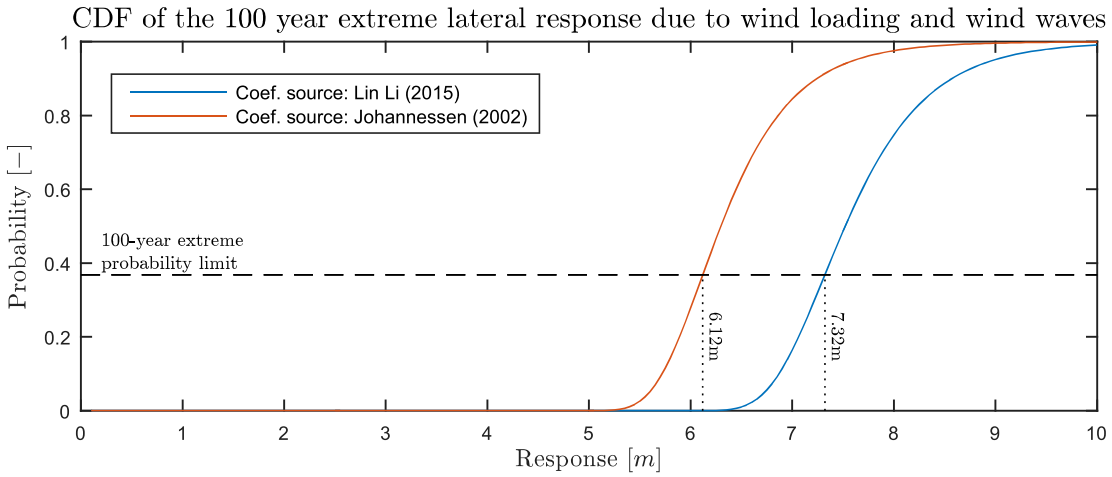

Figure 7.42: CDF of the lateral response at mid-span with a 100 year return period. The considered loading is wind waves and wind. Equation 4.26 has been used.

7.6.5 Comparison of the short-term extreme and the long-term extreme

It is expected that the long-term response based on the long-term method is larger than the extreme short-term response. However, this is only the case for the response based on the PDF by (Li et al., 2015). This can be seen in table 7.16. Integration limits for equation 4.26, which the long-term analysis is based on, is supposed to exceed the 100 year probability limit with a good margin. Earlier estimates of the STDs from the buffeting analyses were however only found for mean wind velocities up to 40 m/s, as mean wind velocities above 33 m/s were unexpected. After recalculating the STD for a range up to 60 m/s, only an insignificant change in the extreme response was observed, and the short-term extreme response still greatly exceeded the response found from the long-term method. The solution algorithm was also confirmed by a separately

developed script. As the scaled PDF of (Johannessen et al., 2002) provides bad results either way, no further effort was put into explaining this irregularity.

Lateral extreme response at mid-span		
	Long-term extreme response, eq.4.26	**Short-term extreme response, eq. 4.17**
PDF source	Response $[m]$	Response $[m]$
(Johannessen et al., 2002)	6.12	7.84
(Li et al., 2015)	7.32	6.22

Table 7.16: A comparison of the lateral short-term extreme response and the lateral long-term extreme response at mid-spa based on two different PDFsn.

The large variability of the results in table 7.16 stresses the importance of representing the environmental loading with a proper probability density function. The scaled PDF from (Johannessen et al., 2002) presents unreliable results, as some of the load combinations were found to be impossible, physically speaking. It also provides a less accurate fit of the correlated wave height and mean wind velocity than the PDF of (Li et al., 2015). For this reason, the long-term extreme calculated based on the PDF from (Li et al., 2015) of 7.32 m is considered as the long-term extreme response.

The significant difference between the responses found by the short-term method and the long-term method suggest that the critical displacement might be underestimated severely if only the short-term method is applied. Comparing results from the two methods did, however, prove to be a good way to verify the magnitude of the expected extreme response.

The importance of developing a PDF that provides a good representation of the environmental conditions of the Bjørnafjorden area should not be underestimated, as the long-term response is directly dependent on the PDF.

Chapter 8

Conclusion

The main topics of this thesis have been to establish a parametrized model of the bridge with two different floater alternatives by the aid of ABAQUS and HydroD, perform a modal buffeting analysis including both wave and wind loading, perform an instability analysis to obtain the critical flutter velocity and, finally, carry out an extreme value analysis to assess the largest horizontal displacement with a 100 year return period. The following conclusions have been made.

Models of the the bridge alternative with concrete hulls and also the bridge alternative with steel hulls match the eigenfrequencies, added mass, added damping and self excited forces of two independent FE-models developed in RM Bridge and ORCAFLEX, to quite some extent. Including the added mass proved to be of great importance as the first eigenperiod of the concrete hull alternative changed from 80.2 s to 101.4 s.

Only subtle differences can be seen for the load and response spectrum comprising the two hull alternatives, but the pontoon design could be critical with respect to controlling the eigenfrequencies of the bridge. Based on results achieved in this thesis, it is however not possible to renounce any of the two hull alternatives.

From the buffeting analyses it is found that the STD in the lateral direction is several times bigger compared to the STD in the vertical direction. At mid-span, the STD was found to be 0.315 m for the vertical direction and 2.069 m for the lateral direction, when exposed to the critical wind and wave loading. However, either of these values could be critical for the bridge design.

If wind loading is already present, the STD for vertical motion along the bridge increases by 4 % when adding loading from wind waves, while no significant change of the STD can be seen for the lateral motion.

By investigating the response spectra, it can be judged that the second order wave forces should be included if the response at higher frequencies is of importance. To avoid numerical noise in the higher frequency range, a fine mesh of the model is suggested, or smoothing of the QTF. When studying the maximum displacement, second order forces was found to be of no importance.

From the parameter study, tether damage has been found to cause relatively small changes to the bridge behaviour. Damage of the top cables yields a more significant change in the bridge behaviour, especially for vertical modes. Increased asymmetry to the bridge, as for the case of a damaged top cable over span 1 or 3, is found to be more critical than damage to the top cable over span 2, as the eigenfrequencies of some of the vertical modes change with more than 20%.

A critical velocity of 85.09 m/s is found when using ADs empirically derived and a critical velocity of 61.84 m/s is found when using ADs derived from quasi-static theory. Including more modes in the instability analysis makes the critical velocity converge to a lower bound. The second vertical mode, and the first pure torsional mode, mode 8 and mode 104, have been found to be the most important modes for the flutter analysis. Quasi-static derived ADs have been found to be highly unreliable for a flutter analysis.

The most indisputable finding from the extreme value analyses is the importance of using the correct PDF to represent the environmental data. Slight changes in the PDFs affect the response directly. Nonetheless, scaled PDFs developed for different geographical locations could produce satisfying results when scaled properly and when good judgement is exercised. A comparison of the PDF estimated from measurement data for Bjørnafjorden to down scaled PDFs representing conditions in the North Sea yielded that the down scaled PDF developed by (Li et al., 2015) demonstrated a realistic behaviour of both the correlated mean wind velocity, and the wave properties expected for the Bjørnafjorden area.

For long-term estimation based on integration over the PDF and by short-term extremes for critical load combinations, swell waves and wind loading was found to be most important for the maximum displacement at mid span. The static deflection was found to be 10.57 m, while the maximum dynamic displacement was found to be 7.32m. The contribution from the wind waves to the extreme lateral response at mid-span was found to be of little importance.

Chapter 9

Further work

Suggestions for further development of the bridge concept and research are listed below.

1. It is in particular recommended to develop realistic probability distribution functions that represent swell waves and joint occurrence of wind and wind waves in the Bjørnafjorden area.
2. Obtain aerodynamic derivatives from wind tunnel testing of the actual cross-section of the bridge.
3. Use the complex eigenmodes, obtained from ABAQUS, in a modal buffeting analysis to include the effect of damping on the eigenmodes.
4. Improve the temperature optimization algorithm to achieve smaller imperfections in the geometry for a larger range along the bridge.
5. Investigate if the second order wave forces have an effect on the moments and the shear forces in the bridge girder, as second order forces has been found to mainly affect the high frequency response of the bridge.
6. Investigate whether numerical noise in the 1st and 2nd order transfers function is caused by to large mesh size, and if smoothing the QTF is an efficient way to achieve the same accuracy that can be obtained by increasing the mesh size.
7. Perform time domain analyses of the bridge.
8. As the critical wind velocity in reality is approaching from north-west and not west, a procedure to account for skew wind loading on the bridge girder should be developed.

Bibliography

Chopra, A. K., 2012. Dynamics of Structures, Theory and Applications to Earthquake Engineering, 4th Edition. Prentice Hall, Boston.

Chryssostomidis, C., Liu, Y., February 2011. 2.019 design of ocean systems.

Cook, R. D., 2002. Concepts and application of finite element analysis, 4th Edition. John Wiley —& Sons, Inc., Wisconsin.

DNV GL AS, 2014. Environmental conditions and environmental loads (DNV-RP-C205).

DNVGL, 2014a. Hydrod, wave load —& stability analysis of fixed and floating structures. HydroD User Manual.

DNVGL, 2014b. Wadam, wave analysis by diffraction and morison theory. WADAM User Manual.

DNVGL, 2015. Genie, vol 1 - concept design and analysis of offshore structures. GeniE User Manual.

Faltinsen, O., 1990. Sea Loads on Ships and Offshore Structures, 1st Edition. Cambridge University Press, New York.

Ge, Y. J., Tanaka, H., 1999. Aerodynamic flutter analysis of cable-supported bridges by multi-mode and full-mode approaches. Journal of Wind Engineering and Industrial Aerodynamics 86, 123–153.

Greco, M., September 2016. Lecture notes in the course TMR4215 Sea Loads, week 36.

Haver, S., 1980. Analysis of uncertainties related to the stochastic modelling of ocean waves. Ph.D. thesis, Norwegian Institute of Technology.

Haver, S., 2007. Prediction of characteristics response for design purposes.

Haver, S., 2008. Environmental contour lines: A method for estimating long term extremes by a short term analysis. Transactions - Society of Naval Architects and Marine Engineers 67.

Hsu, S. A., A., E., Meindl, Gilhousen, D. B., 1994. Determining the power-law wind-profile exponent under near-neutral stability conditions at sea. Journal of Applied Meteorology 33(6), 757–765.

Inman, D. J., 1990. A tutorial on complex eigenvalues.

Johannessen, K., Meling, T., Haver, S., 2002. Joint distribution for wind and waves in the northern north sea. International Journal of Offshore and Polar Engineering 12(1), 19–21.

Kemp, J., 2001. Ship stability notes & examples, 3rd Edition. Butterworth-Heinemann, Oxford.

Kvåle, K. A., Sibjrnson, R., Øiseth., O., 2016. Modelling the stochastic dynamic behaviour of a pontoon bridge: A case study. Marine Structures, Elsevier 165, 123–135.

Lee, C.-H., 1995. Wamit theory manual. WAMIT Theory Manual.

Lewandowski, E. M., 2004,. Dynamics of Marine Craft, Maneuvering and Seakeeping, 1st Edition. World Scientific Publishing Company, Singapore.

Li, L., Gao, Z., Moan, T., 2015. Joint distribution of environmental condition at five european offshore sites for design of combined wind and wave energy devices. Journal of Offshore Mechanics and Arctic Engineering 137.

Naess, A., Moan, T., 2013. Stochastic dynamics of marine structures, 1st Edition. Cambridge University Press.

Newland, D. E., 2004. An Introduction to Random Vibrations, Spectral and Wavelet Analysis, 3rd Edition. Dover Publications, Mineola, New York.

NPRA, 2016a. Aerodynamic coefficients for the bjørnafjorden tlp (SBT-PGR-TN-212-003-B).

NPRA, 2016b. Bjørnafjorden suspension bridge - k2 concrete hull design (SBT-PGR-RE-211-018).

NPRA, 2016c. Bjørnafjorden suspension bridge, k1 and k2 bridge girder, general arrangement (SBT-PGR-DR-211-401).

NPRA, 2016d. Bjørnafjorden suspension bridge, k1 and k2 cable structures, pylon saddles axis 5 and 6 (SBT-PGR-DR-211-506).

NPRA, 2016e. Bjørnafjorden suspension bridge, k1 and k2 cable structures, top cable and top cable anchorage (SBT-PGR-DR-211-504).

NPRA, 2016f. Bjørnafjorden suspension bridge, k1 and k2 concrete pylon axis 7, general arrangement (SBT-PGR-DR-211-203).

NPRA, 2016g. Bjørnafjorden suspension bridge, k1 and k2 south approach bridge, general arrangement (SBT-PGR-DR-211-003).

NPRA, 2016h. Bjørnafjorden suspension bridge, k1 and k2 steel towers axis 5 and 6, general arrangement (SBT-PGR-DR-211-301).

NPRA, 2016i. Bjørnafjorden suspension bridge, k2 3d model of susp. bridge with concrete hull (SBT-PGR-DR-290-002).

NPRA, 2016j. Bjørnafjorden suspension bridge, k2 concrete floater alternative, general arrangement (SBT-PGR-DR-211-001).

NPRA, 2016k. Bjørnafjorden suspension bridge, k2 concrete floater, main dimensions (SBT-PGR-DR-211-701).

NPRA, 2016l. Bjørnafjorden suspension bridge, k2 steel floater alternative, main dimensions (SBT-PGR-DR-211-601).

NPRA, 2016m. Concrete floater alternative, bjørnafjorden suspension bridge, overview drawing (K1001).

NPRA, 2016n. Desgin basis (SBT-PGR-BA-211-001-0).

NPRA, 11 2016o. Fjordkryssing - Bjørnafjorden. Available at: http://www.vegvesen.no/Europaveg/e39stordos/fjordkryssing-bjornafjorden, Accessed 09-06-17.

NPRA, 2016p. K1 & k2 cable system design (SBT-PGR-RE-211-013-0).

NPRA, 2016q. K1 & k2 design summary (SBT-PGR-RE-211-011).

NPRA, 2016r. K1 & k2 environmental load analysis (SBT-PGR-RE-211-004-0).

NPRA, 2016s. K1 & k2 hydrodynamic analysis (SBT-PGR-RE-213-001-0).

NPRA, 2016t. K1 & k2 rm bridge structural analysis model report. part 1: Model description (SBT-PGR-RE-211-001-0).

NPRA, 08 2016u. The E39 Coastal Highway Route. Available at: http://www.vegvesen.no/vegprosjekter/ferjefriE39/English, Accessed 07-03-17.

NPRA, 2017. Design basis metocean (SBJ-01-C3-SVV-01-BA-001).

Øiseth, O., Rönnquist, A., Sigbjörnsson, R., 2012. Finite element formulation of the self-excited forces for time-domain assessment of wind-induced dynamic response and flutter stability limit of cable-supported bridges. Finite Elements in Analysis and Design 50, 173–183.

Pinkster, J. A., 1988. The influence of directional spreading of waves on mooring forces. Offshore Technology Conference.

Roald, L., Jonkman, J., Robertson, A., 2014. The effect of second-order hydrodynamics on a floating offshore wind turbine (NREL/TP-5000-61452).

Siedziako, B., Øiseth, O., Rönnquist, A., 2017. An enhanced forced vibration rig for wind tunnel testing of bridge deck section models in arbitrary motion. Journal of Wind Engineering and Industrial Aerodynamics 164, 152–163.

Simulia, 2014. Abaqus analysis user's guide.

Stansberg, D. C. T., 2002. Final report and recommendations to the 23rd ittc. In: The Specialist Committee on Waves. 23rd International Towing Tank Conference.

Statens vegvesen, 05 2017. Ferjefri E39 strekningskart - alle kryssingar. Available at: https://www.flickr.com/photos/96309692@N06/21592393715/in/album-72157648236066771/ , Accessed 13-05-17.

Statistics Solutions, 02 2017. Chi-Square Test of Independence. Available at: http://www.statisticssolutions.com/non-parametric-analysis-chi-square/, Accessed 31-05-17.

Strømmen, E., 2010. Theory of bridge aerodynamics, 2nd Edition. Springer Science —& Business Media.

Tamura, Y., Kareem, A., 2013. Advanced Structural Wind Engineering, 1st Edition. Springer, New York.

Walpole, R. E., Myers, R. H., Myers, S. L., Ye, K., 2012. Probability & Statistics for Engineers and Scientists, ninth Edition. Pearson, Boston.

Wolfram, 02 2017. Nonlinear Least Squares Fitting. Available at: http://mathworld.wolfram.com/NonlinearLeastSquaresFitting.html, Accessed 20-05-17.

Xu, Y.-L., 2013. Wind Effects on Cable-Supported Bridges, 1st Edition. WILEY, Singapore.

Appendix A

Supplementary theory

A.1 Rayleigh damping

Rayleigh damping can be used to establish the damping matrix for a couplex MDOF system, because it is in general very difficult to obtain the full damping matrix. Rayleigh proportional damping is a combination of mass and stiffness proportional damping, and is frequency dependent. Equations for Rayleigh proportional damping, and for the coefficients required can be found in (Cook, 2002, Ch. 11.5).

$$\boldsymbol{C} = \alpha \boldsymbol{M} + \beta \boldsymbol{K} \tag{A.1}$$

The expressions for the coefficients α and β are derived based on a frequency range of interest, $[\omega_1, \omega_2]$. The selected damping ratio will be obtained at the limits of the interval, while the response outside the range of interest experience a higher damping ratio. On the contrary, the damping ratio is underestimated inside the range of interest.

The terms for α and β is given by the following expressions.

$$\alpha = \frac{2\omega_1\omega_2(\xi_2\omega_1 - \xi_1\omega_2)}{\omega_1^2 - \omega_2^2} \qquad \beta = \frac{2(\xi_1\omega_1 - \xi_2\omega_2)}{\omega_1^2 - \omega_2^2} \tag{A.2}$$

Rayleigh damping was initially used for the fluttering analysis, but was later substituted by mode equivalent damping. The values for α and β derived above was calculated for a desired damping ratio of 0.5% for both the highest and lowest frequency of interest. The eigenfrequencies of mode 3, which is the first vertical mode, and mode 150 was used as the limit for the frequencies of interest for the initial flutter analysis. This ensured that the vertical mode was not damped out. It

also limits the underestimation of the damping within the range of interest. Damping ratio as a function of frequency is given in the figure below.

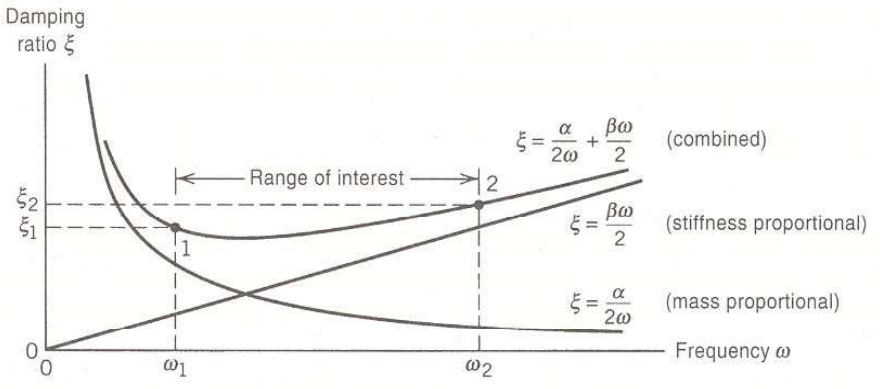

Figure A.1: An illustration of how the Rayleigh proportional damping works.

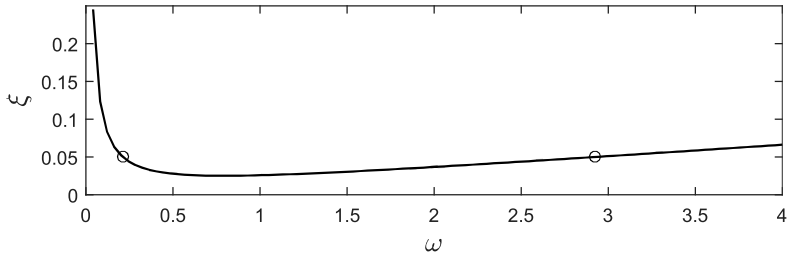

Figure A.2: Damping ratio for different values of omega, when the range of interest is based on mode 3 and mode 150. $\alpha = 0.019779$ and $\beta = 0.031870$

Appendix B

Modelling details in ABAQUS

B.1 Element propertied used in the ABAQUS model.

	Span 1	Span 2	Span 3	Side Span	Unit	Source
Span Lengths	1385	1325	1385	653	[m]	SBT-PGR-DR-211-002
Y-Position at first tower	2.75	2.75	2.75	2.75	[m] (meters away from centerline)	SBT-PGR-DR-211-505
Y-Position at midspan	12.4	12.4	12.4	7.9233	[m] (meters away from centerline)	SBT-PGR-DR-211-402
Y-Sag	9.65	9.65	9.65	3.098	[m]	
Z-Sag	146.9	133.28	146.9	26.1	[m]	RM Bridge analysis part 1 sec. 2.2.1
Number of Hangers	57	55	57	27		
Temperature load	318.49	339.21	319.87	408.77	C°	Estimated from itteration
Top Cable						
Z-Sag	23	21.05	23	-	[m]	RM bridge analysis part 1 sec. 2.2.2
Temperature load	401.63	401.78	402	-	C°	Estimated from itteration
Towers	**Tower 1**	**Tower 2**	**Tower 3**	**Tower 4**		
Tower Height	196.17	199.5	199.5	200.857	[m] (meters above sealevel)	SBT-PGR-DR-211-002
Girder	**Tower1**	**Midspan**	**Tower 4**			
Girder Z-values (At centroid)	30	59.75	33.45	-	[m] (meters above sealevel)	SBT-PGR-DR-211-003
	y-direction	**z-direction**				
Connector size	12.4	1.4			[m] (Girder centroid to hanger)	
Side Cables	**Temp**					
Temperature load	487.43				C°	Estimated from itteration
	x	**y**	**z**			
Position Side Cable South	-443	-20	73.644		[m] (global coordinate)	SBT-PGR-DR-211-101
Position Side Cable North	4748	12.4	13.27		[m] (global coordinate)	SBT-PGR-DR-211-002
Concrete Pontoon				**Pontoon 1 and 2**		
Ballast				22810	tonn	RM bridge analysis part 1 sec. 2.5.1
Meters above sealevel where tension legs are attached				-20	[m] (meters above sealevel)	SBT-PGR-DR-211-701
Width				84.2	[m]	SBT-PGR-DR-211-701
Center of bouyancy				-31.46	[m] (meters above sealevel)	RM bridge analysis part 1 sec. 2.2.7
Center of mass				-26.83	[m] (meters above sealevel)	RM bridge analysis part 1 sec. 2.2.7
Tethers			**Tower 2**	**Tower 3**		
SeaDepthAtTower			550	450	[m]	SBT-PGR-DR-211-002
Fixed Towers			**Tower 1**	**Tower 4**		
Distance between the center line of the pylon legs when the legs meet			4	4	[m] (meters away from centerline)	SBT-PGR-DR-211-(202/203)
Base of tower y-position			24.443	26.029	[m] (meters away from centerline)	SBT-PGR-DR-211-(202/203)
Base of tower z-position			15	3	[m] (meters above sealevel)	SBT-PGR-DR-211-(202/203)
Length of tower top which is acting as a single beam			13	13	[m] meters below the top	SBT-PGR-DR-211-(202/203)
Height of fixed towers			196.17	200.857	[m] (meters above sealevel)	SBT-PGR-DR-211-002
Position of crosser beams			23.034	26.487	[m] (meters above sealevel)	SBT-PGR-DR-211-(202/203)
Floating Towers			**Tower** 2	**Tower 3**		
Height of fixed towers			199.5	199.5	[m] (meters above sealevel)	
Distance between the center line of the pylon legs when the legs meet			12	12	[m] (meters between centerlines)	
Distance between the center line of the pylon legs when the legs meet			20	20	[m] (meters between centerlines)	
Distance between the center line at the position of the crosser			34	34	[m] (meters between centerlines)	
Position above sealevel for the crosser			56.845	56.845	[m] (meters above sealevel)	
Position where the pylon is acting as a single colum			180	180	[m] (meters above sealevel)	
Position where the pylon splits into two columns			20	20	[m] (meters above sealevel)	
Tower base z-level			6	6	[m] (meters above sealevel)	

Table B.3: Input table. Note that sources for the listed values can be found in the NPRA-reports. The specific reports are listed in the rightmost column.

Element properties used in the ABAQUS model

	$Area$	I_{11}	I_{12}	I_{22}	$J(I_T)$	Density	Elastic Modulus	Shear Modulus	Thermal Expansion
	$[m^2]$	$[m^4]$	$[m^4]$	$[m^4]$	$[m^4]$	$[kg/m^3]$	$[N/m^2]$	$[N/m^2]$	$[-]$
Main Cable	2.2930E-01	6.6628E-03	0	6.6628E-03	1.3260E-02	8.6760E+03	2.00E+11	7.6923E+10	1.0E-05
Side Span Cable	2.2930E-01	6.6628E-03	0	6.6628E-03	1.3260E-02	8.6760E+03	2.00E+11	7.6923E+10	1.0E-05
Side Cable	2.2930E-01	6.6628E-03	0	6.6628E-03	1.3260E-02	8.6760E+03	2.00E+11	7.6923E+10	1.0E-05
Top Cable	8.2190E-02	1.1060E-03	0	1.1060E-03	2.2120E-03	7.8491E+03	2.00E+11	7.6923E+10	1.0E-05
Hangers	3.0420E-03	1.6710E-06	0	1.6710E-06	3.3420E-06	8.3510E+03	1.60E+11	6.1538E+10	2.0E-05
Girder at pylon axis	9.0100E-01	4.7490E+01	0	1.8830E+00	3.4960E+00	0*	2.10E+11	8.0769E+10	1.0E-05
Girder at bridge span	9.0100E-01	4.7490E+01	0	1.8830E+00	3.4960E+00	0*	2.10E+11	8.0769E+10	1.0E-05
Tension Legs	5.1532E-01	9.0000E-09	0	9.0000E-09	1.8600E-08	8.3510E+03	2.10E+11	8.0769E+10	1.0E-05
Tension Legs	2.5766E-01	9.0000E-09	0	9.0000E-09	1.8600E-08	8.3510E+03	2.10E+11	8.0769E+10	1.0E-05
Fixed towers									
Single column at tower top	2.3600E+01	1.9000E+02	0	5.8000E+02	4.6600E+02	2.5000E+03	3.60E+10	1.2538E+10	2.0E+05
Crossbeam	5.0000E+01	1.4100E+02	0	5.0000E+01	5.0000E+01	2.5000E+03	3.60E+10	1.2538E+10	2.0E+05
Column bottom	1.8800E+01	1.4100E+02	0	2.5100E+02	2.8900E+02	2.5000E+03	3.60E+10	1.2538E+10	2.0E+05
Column top	1.5600E+01	1.0800E+02	0	1.1600E+02	1.7900E+02	2.5000E+03	3.60E+10	1.2538E+10	2.0E+05
Floating towers									
Single column top	3.1540E+00	3.3723E+01	0	3.3723E+01	1.0000E+01	8.6760E+03	2.10E+11	6.1000E+10	1.0E-05
Single column bottom min	4.1180E+00	1.8922E+02	0	6.1508E+01	1.0000E+01	8.6760E+03	2.10E+11	6.1000E+10	1.0E-05
Single column bottom max	4.4060E+00	2.4626E+02	0	5.9087E+01	1.0000E+01	8.6760E+03	2.10E+11	6.1000E+10	1.0E-05
Column below crosser min	1.8160E+00	23.106	0	1.5674E+01	1.0000E+01	8.6760E+03	2.10E+11	6.1000E+10	1.0E-05
Column below crosser max	3.3540E+00	8.2330E+01	0	2.8520E+01	1.0000E+01	8.6760E+03	2.10E+11	6.1000E+10	1.0E-05
Column above crosser min	1.5510E+00	1.1514E+01	0	1.1241E+01	1.0000E+01	8.6760E+03	2.10E+11	6.1000E+10	1.0E-05
Column above crosser max	1.5770E+00	1.1514E+01	0	1.5158E+01	1.0000E+01	8.6760E+03	2.10E+11	6.1000E+10	1.0E-05
Crossbeam	1.0000E+01	1.0000E+00	0	1.0000E+01	1.0000E+01	8.6760E+03	2.00E+11	6.1000E+10	1.0E-05

Table B.1: Element properties applied to the ABAQUS model. *The mass properties of the girder are added separately. Components with unknown area and moment of inertia is set equal to 10

Mass properties applied to the girder

	Mass $[kg/m]$	Ratary inertia m_θ $[kg\,m^2/m]$
Girder at bridge span	14 099	387 582
Girder at pylon axis	17 678	523 653

Table B.2: The basis for applying the lumped mass elements along the girder.

Appendix C

Modelling details in HydroD and GeniE

C.1 Concrete hull models

A collection of the various models of the concrete pontoon can be seen in figure C.1

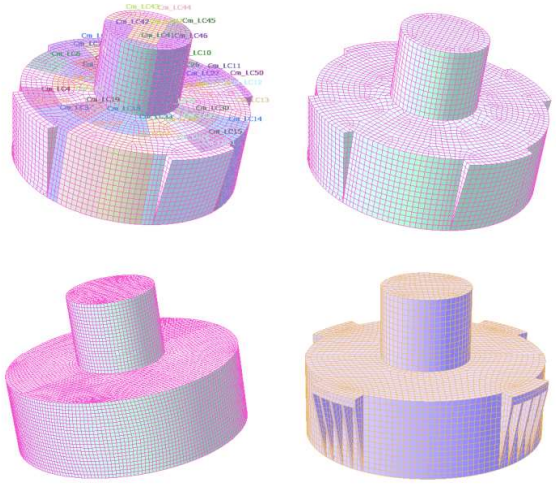

Figure C.1: Different GeniE FEM-models of the concrete pontoon used in the analysis. Top left: Tether porches are modelled as triangles, inner walls included and also compartment loading is included. Top right: Tether porches are modelled as triangles, compartments are neglected. Bottom left: Inner walls, compartments and tether porches are neglected. Bottom right: The inner walls and compartments are neglected.

In the following the five different models that were developed is described and it is also explained why they were discarded or used in the final analysis.

1. The pontoon is modelled as two cylinders with the tether-attachments modelled as 4 solid 3D-triangles. The density of all the parts is correct, except from the density of the triangles, which are scaled to obtain a total ballast-free pontoon weight of 86 000 tons. 50 compartments have been modelled inside the pontoon to account for the dynamics of the ballast.

   To include the ballast in the different compartments within the pontoon a structural model with one separate load case for each compartment had to be created in GeniE and exported to HydroD as a FEM-file. For this reason, it was not possible to exploit the symmetry and only model one fourth of the model to save computational power. A hydrodynamic analysis in HydroD yielded results which differed substantially from the results presented in the reports provided by NPRA. In the NPRA-reports, it seems that the dynamic effects of the ballast have been neglected in the preliminary study. If either all the tanks were half full or a few tanks were completely full it would render two completely different results. It was then decided to remove the dynamic effects of the ballast as no information about how the ballast is distributed in the 50 tanks is given and it was also desirable to compare the results from HydroD with the results reported in the NPRA-reports.

2. The pontoon is modelled as two cylinders with the tether porches modelled as 4 solid 3D-triangles. The density of all parts is correct except from the density of the triangles, which are scaled to obtain a total ballast-free pontoon weight of 86 000 tons. The inner walls are modelled in accordance with the technical drawings.

   The ballast was neglected and the compartment definitions were removed in the original model. The added mass and damping from the analysis results matched with the results from the NPRA-reports fairly good. The problem was that the analysis results overestimated the values for the pitch, surge, sway and yaw a little bit. It was decided to remove the tether porches to see the effects of it in the added mass and damping matrix.

3. The pontoon is modelled as two cylinders with the tether porches neglected. The whole cylinder density is scaled to equal the ballast-free pontoon weight of 86 000 tons.

   Option 3 was modelled to see the effects of neglecting the tether attachments, and if the results of this action would be as expected. All entries in the added damping and mass matrices were highly affected by the neglection and reduced. It was decided to model the geometry of the tether attachments carefully.

4. The pontoon is modelled as exact as possible with respect to geometry and weight. The density is correct in all parts of the pontoon, except from the tether porches, which had to be scaled a little bit to obtain a target weight of 86 000 tons.

   The results from the analysis matched the results from the NPRA-reports better than earlier. But at this stage the time required to run an analysis started to become a problem. The computational effort of running a simple analysis in WADAM for several frequency ranges through HydroD is extremely expensive with respect to time. It was decided to only model one fourth of the model and increase the number of elements per unit area. This was not

possible at an earlier stage because compartments had been defined and the old model had just been modified at each stage. Removing the compartments and the inner walls and also reducing the model size made the analysis more accurate and a little bit faster as the total number of elements in the new model was fewer than the initial total number of elements in the old model.

5. Only 1 fourth of the pontoon is modelled and then mirrored about the XZ- and the YZ-plane as the pontoon is double symmetric. The inner walls are removed. The density is scaled to match the target weight of the pontoon. The tether attachments are carefully modelled.

C.2 Quadratic transfer functions

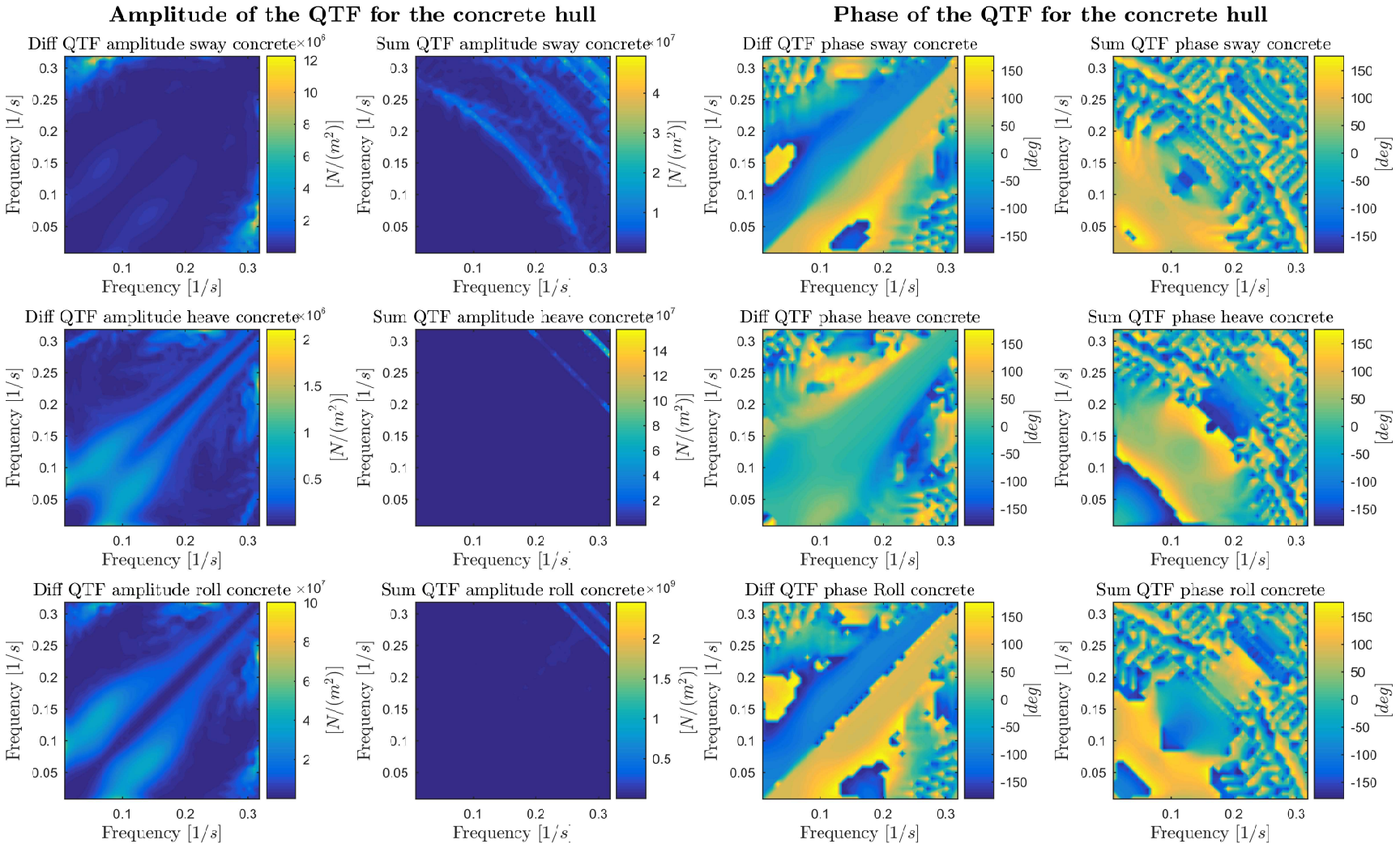

Figure C.2: The quadratic transfer functions of the concrete hull.

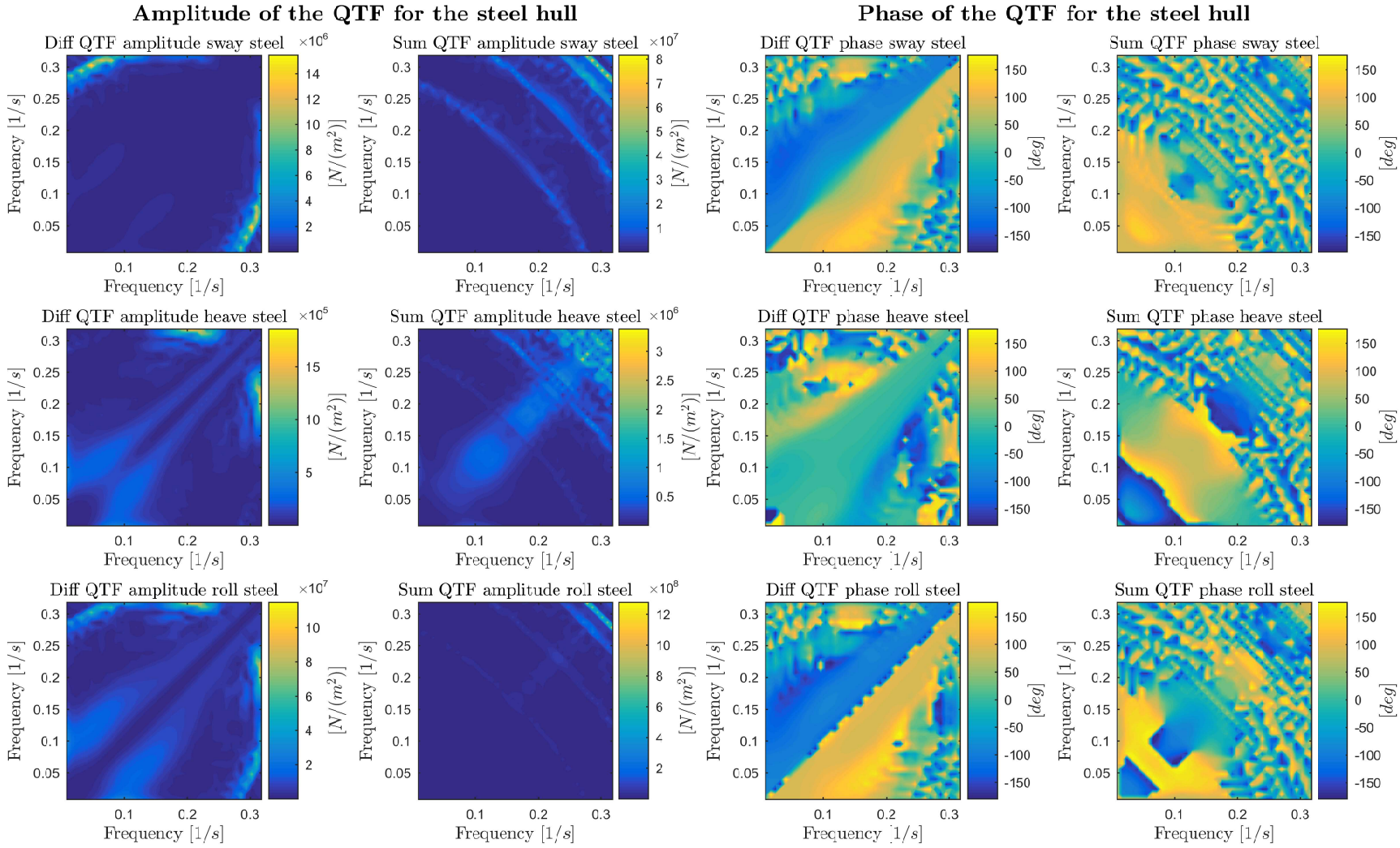

Figure C.3: The quadratic transfer functions of the steel hull.

C.3 A method developed for an efficient 2nd order HydroD analysis

.

When monitoring the progress of 2nd order jobs in HydroD, it was observed that HydroD runs three programs in in batch mode, *FORCE*, *WADAM* and *POTEN*. In addition it was discovered that all results required to extract the second order frequency dependent loading has been generated once calculations in *FORCE* has completed. By making a MATLAB script that read the .LIS result file to see if all required output had been generated, the HydroD job could be terminated after only 13 hours. Completing the full HydroD job required 36 hours, hence calculation time was cut by 64 %. The extracted results from the completed and the terminated analysis were completely identical. The difference was only that the terminated analysis lacked the the redundant results, which are created as the WADAM analysis continues. For this observation to be useful an automatic procedure of terminating and executing jobs was required.

HydroD allows the user to execute a list of successive jobs, but when HydroD is terminated during the first job, after all necessary results are generated, this successive execution of jobs it also terminated. A routine was developed to be able to run successive jobs automatically, even when terminating the program. The problem was solved by running HydroD from MATLAB, with a java script as input file. A *clean* java script input file can be generated from the HydroD model, but does not include the command to execute any of the jobs. For each job a copy of the java script file is made, and the execution command for the job is added. Before the HydroD analysis is executed, a separate MATLAB command window is opened automatically, and runs the script that will end HydroD once all relevant results are generated. This loop continue until the job for all wave directions are completed.

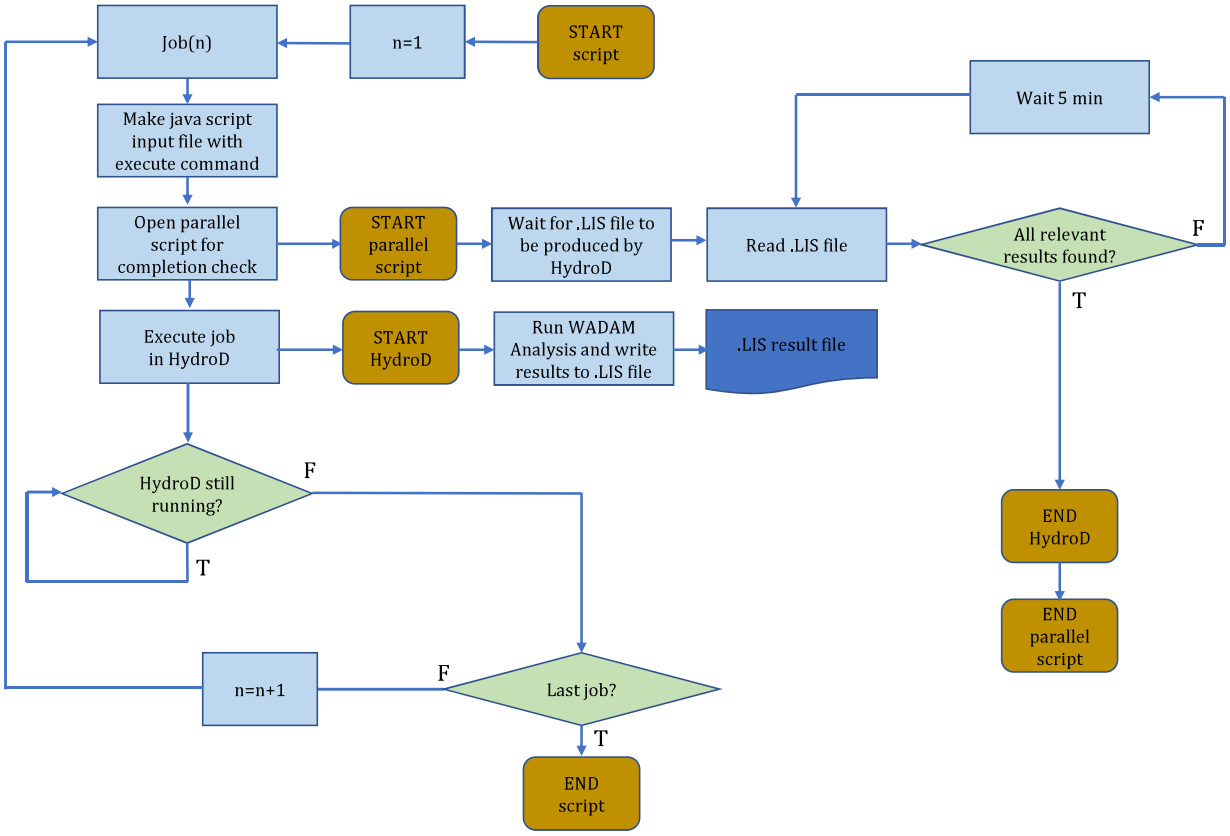

Figure C.4: Flowchart of how the efficient procedure in MATLAB works to reduce the estimation time of the second order transfer functions in HydroD.

Appendix D

Additional results

D.1 Additional flutter results

Mode number	Critical eigenvector ϕ_{Cr} $[-]$
Mode 30	-0.1160
Mode 107	-0.1127
Mode 29	-0.1093
Mode 32	-0.0978
Mode 118	-0.0977
Mode 85	0.0951
Mode 117	-0.0840
Mode 52	-0.0799
Mode 80	-0.0745
Mode 54	-0.0700
Mode 84	-0.0670
Mode 19	0.0654
Mode 45	0.0648
Mode 98	0.0616
Mode 71	-0.0605
Mode 104	-0.0539
Mode 51	0.0500
Mode 106	0.0496
Mode 61	0.0470
Mode 77	-0.0407

Table D.1: The table shows which eigenmodes the critical eigenvector weights to obtain the fluttering mode from a flutter analysis including 150 modes.

D.2 Mode shapes with frequency dependency of added mass accounted for

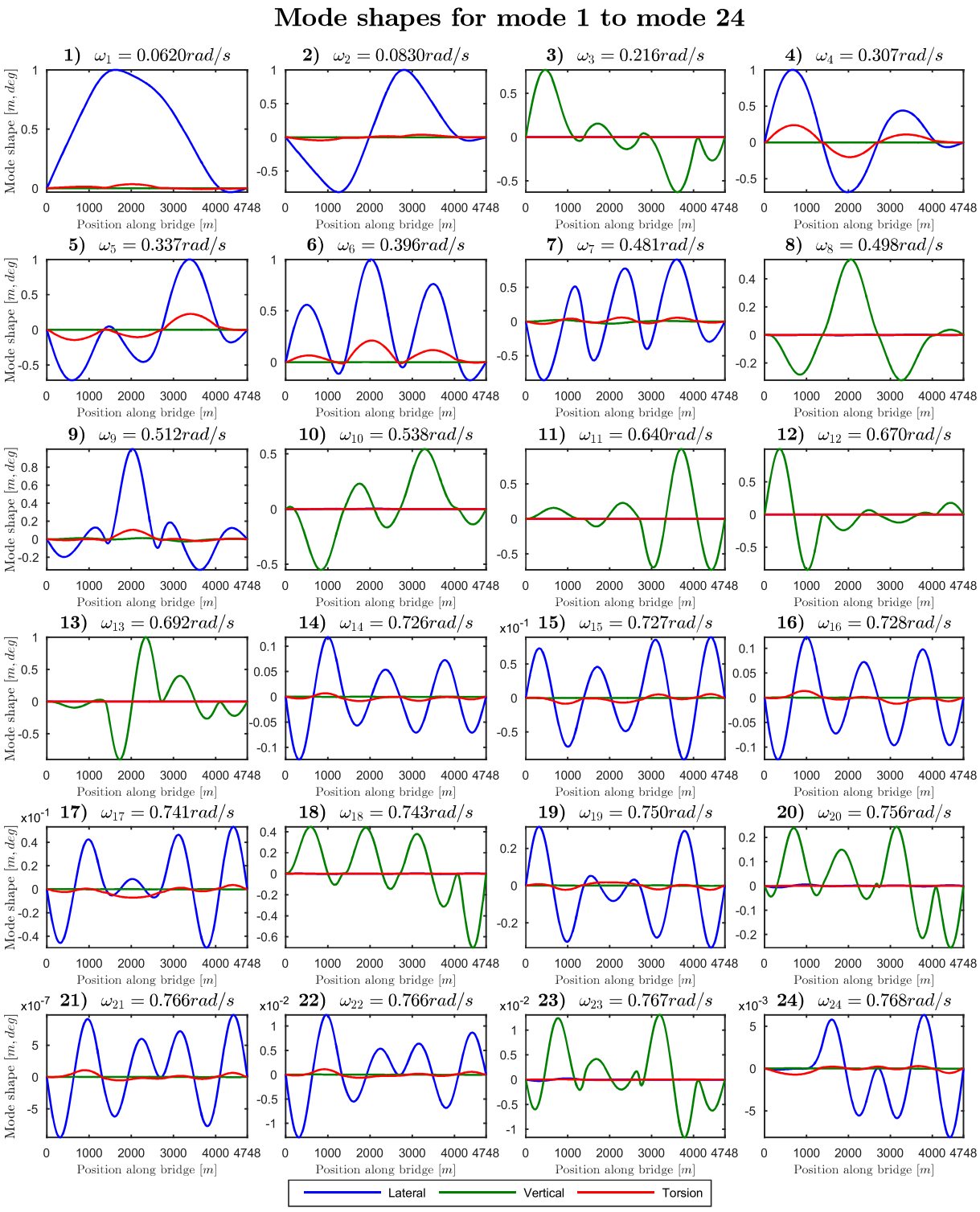

Figure D.1: Mode shapes for procedure B described in figure 7.4

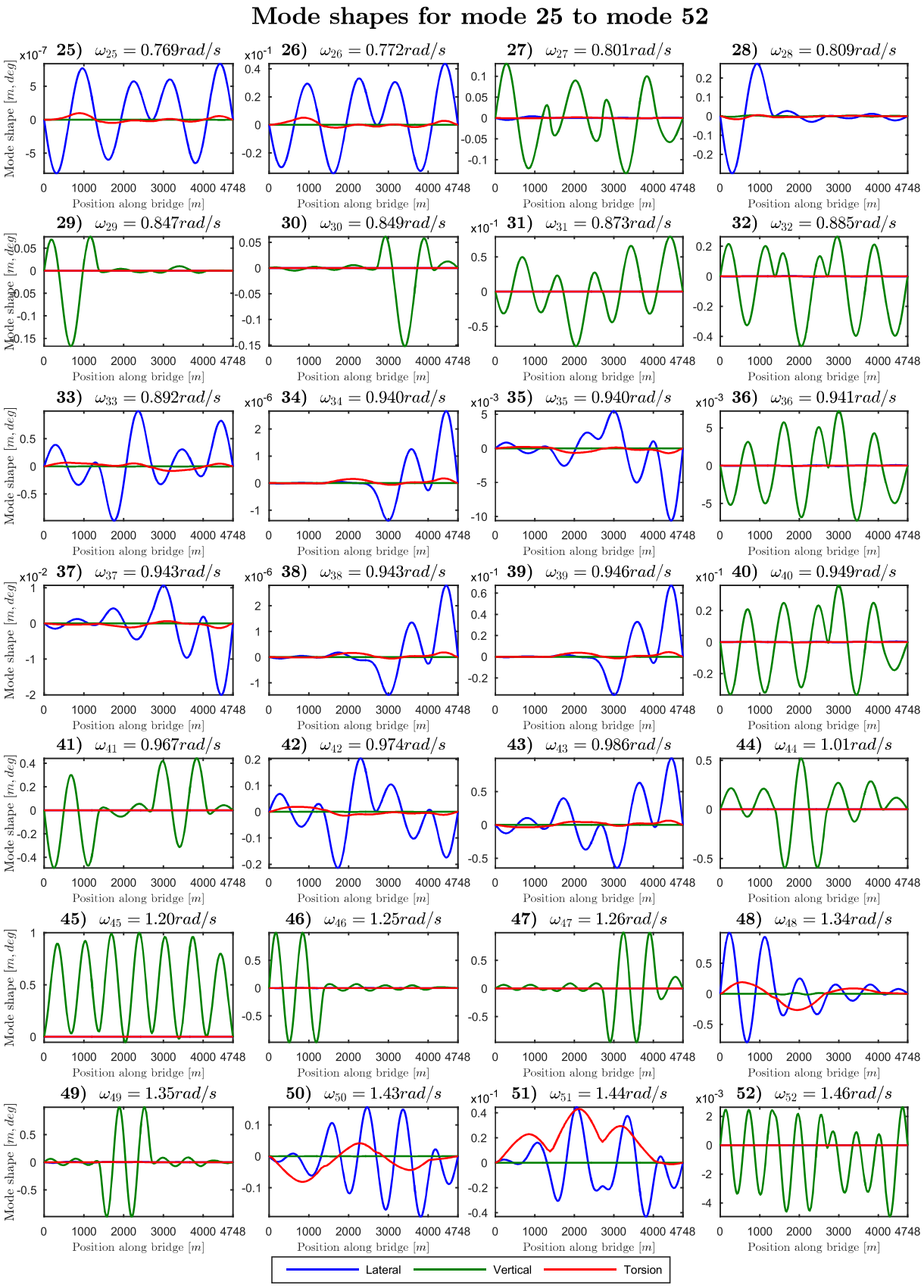

Figure D.2: Mode shapes for procedure B described in figure 7.4

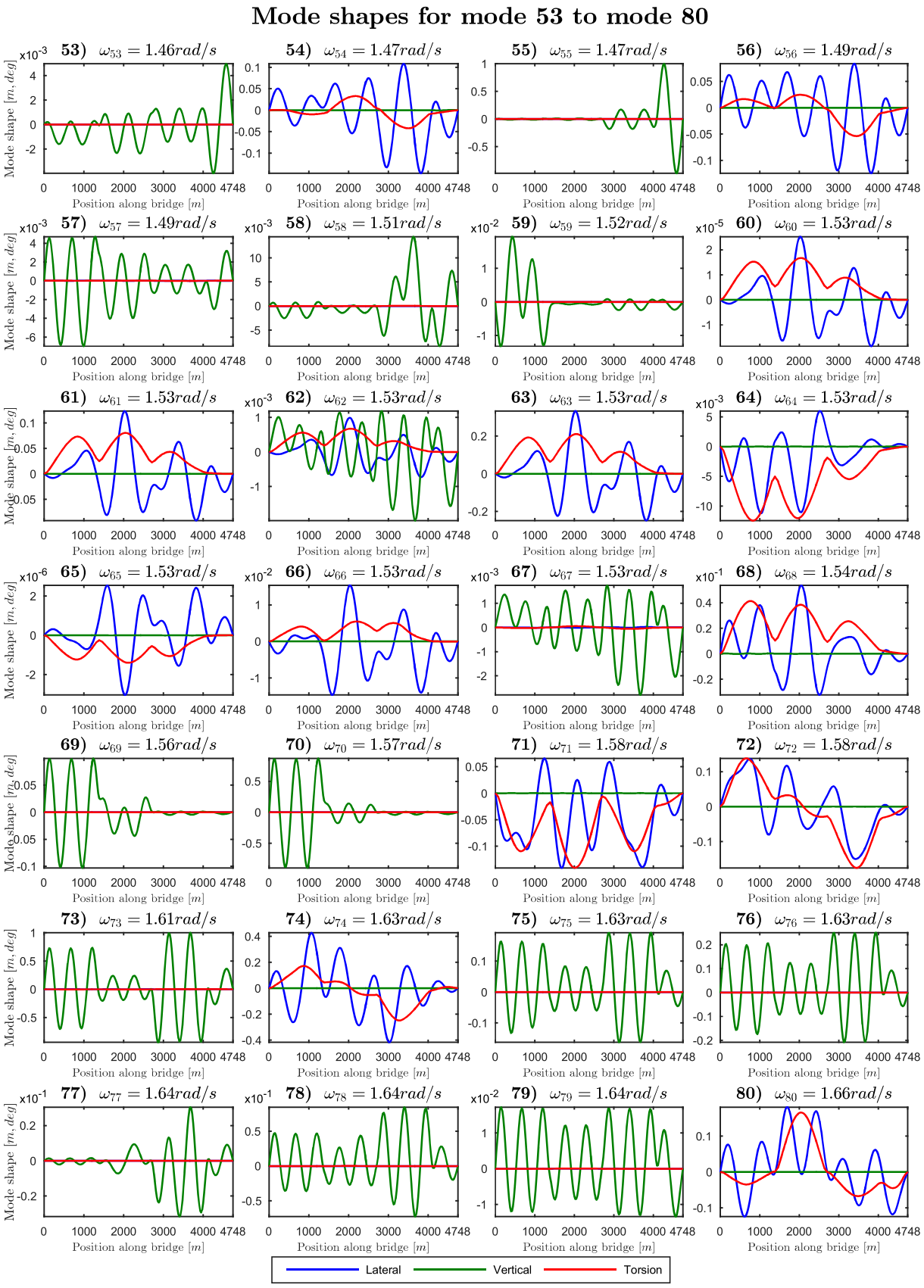

Figure D.3: Mode shapes for procedure B described in figure 7.4

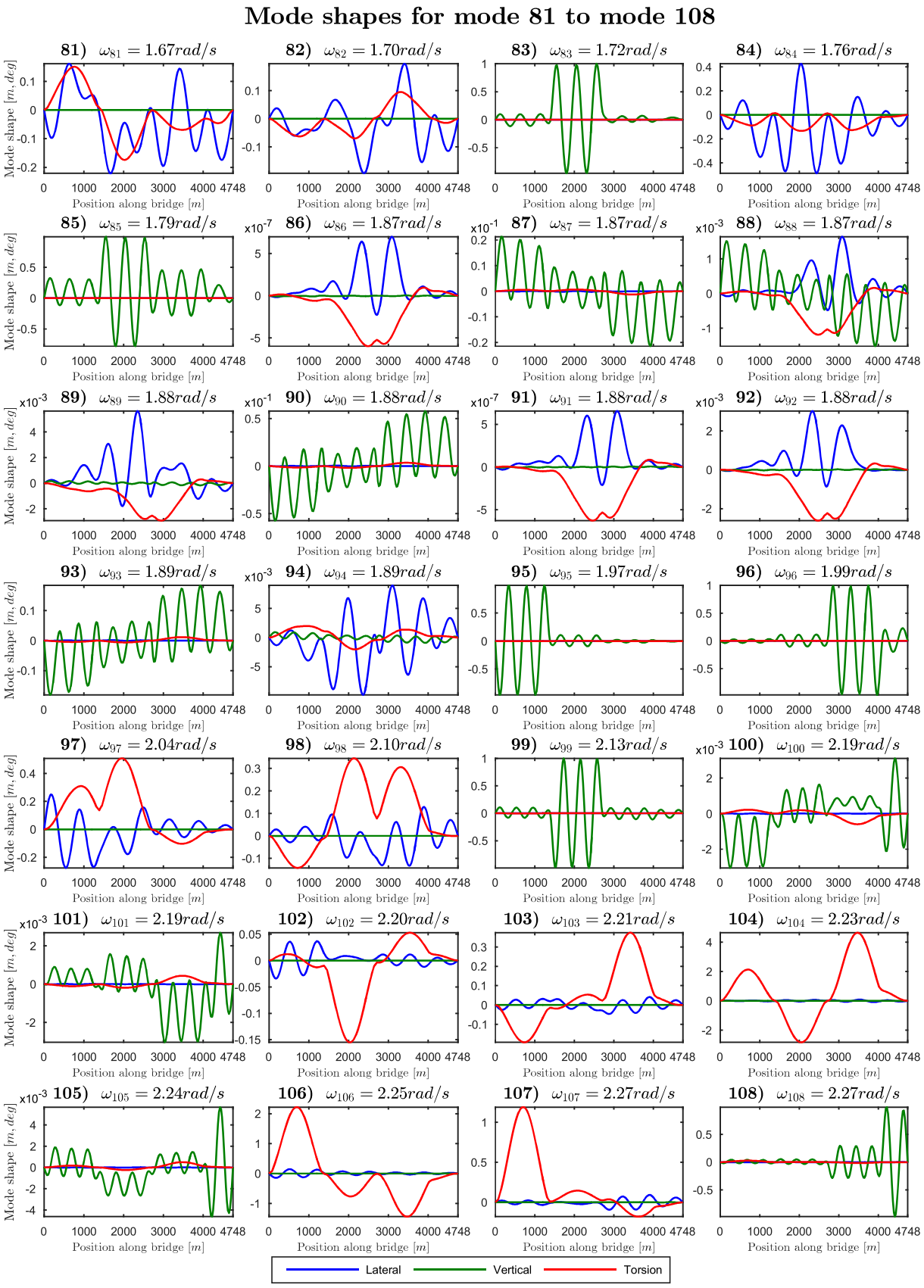

Figure D.4: Mode shapes for procedure B described in figure 7.4

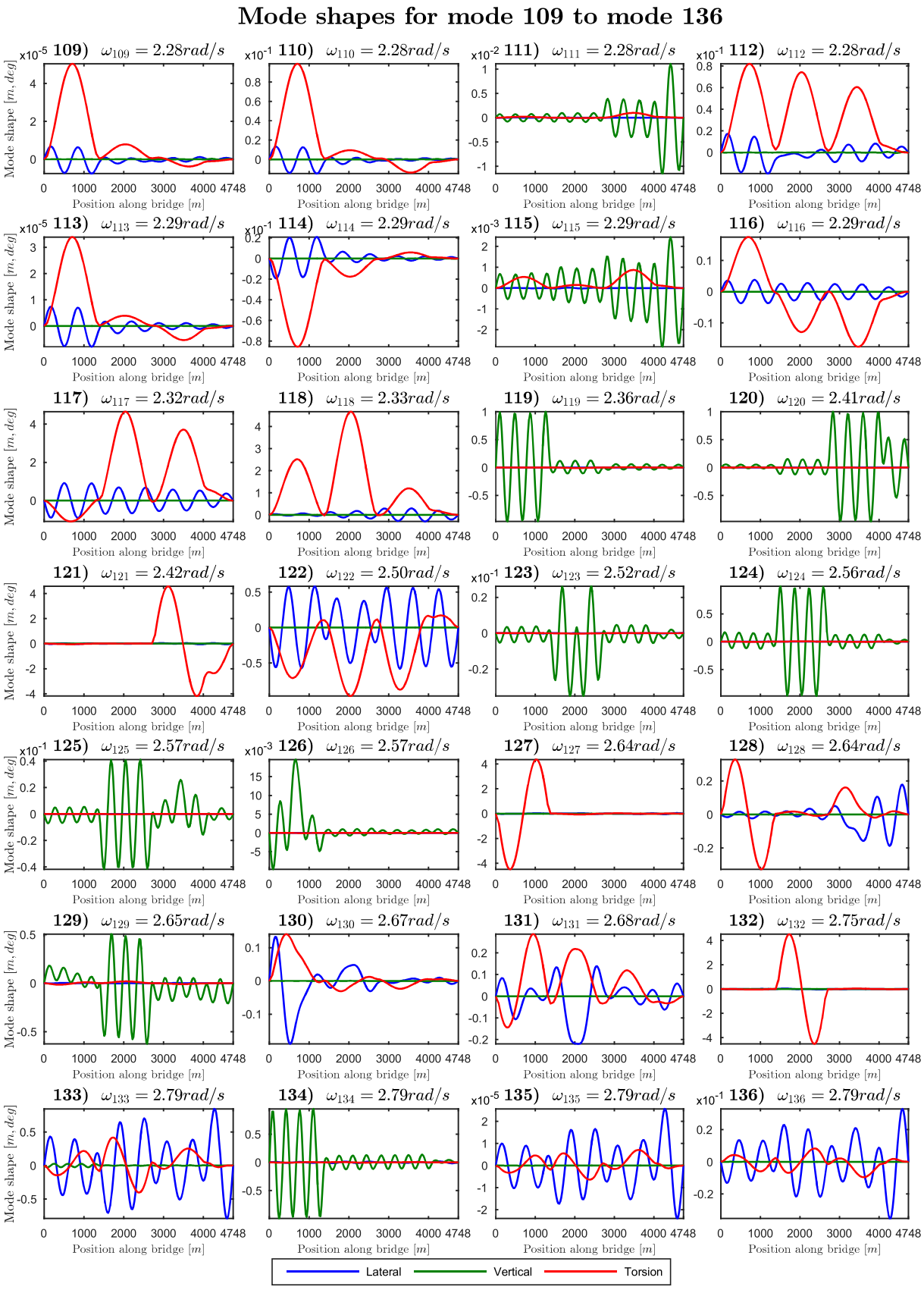

Figure D.5: Mode shapes for procedure B described in figure 7.4

D.3 Additional buffeting results

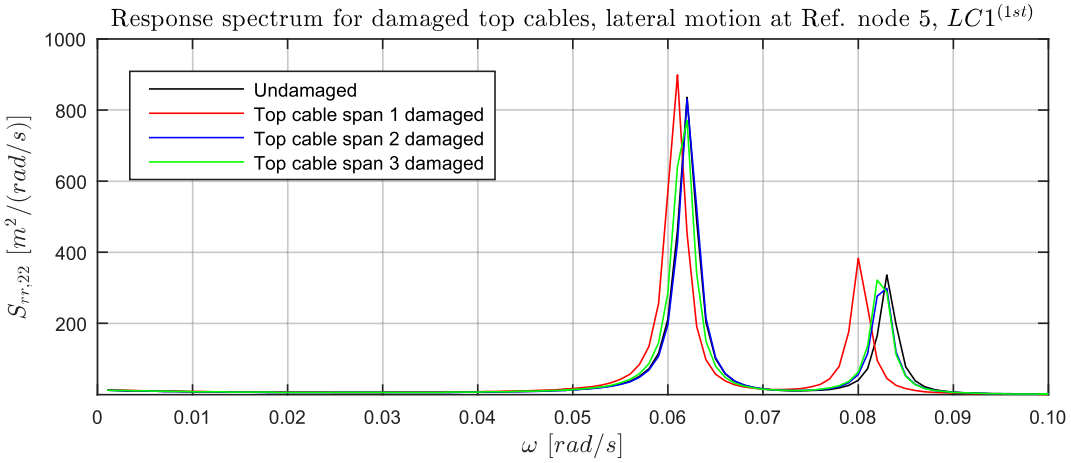

Figure D.6: Response spectrum for the case of damaged top cable. The lateral direction is considered and a linear axis is used.

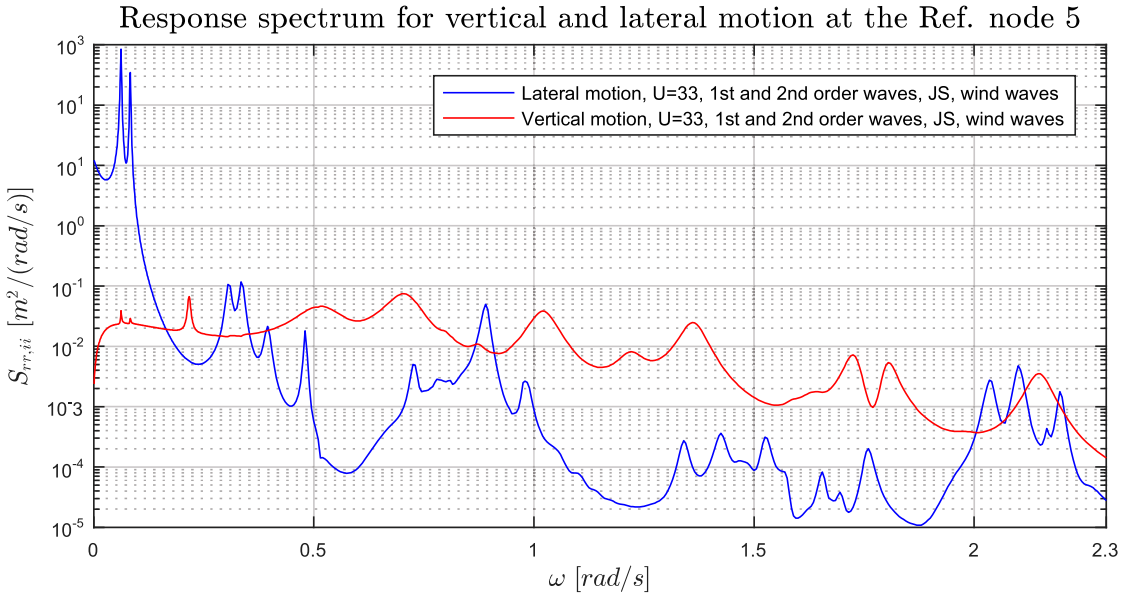

Figure D.7: The response spectrum for the lateral and vertical direction at Ref. node 5 for the bridge with the concrete pontoon alternative.

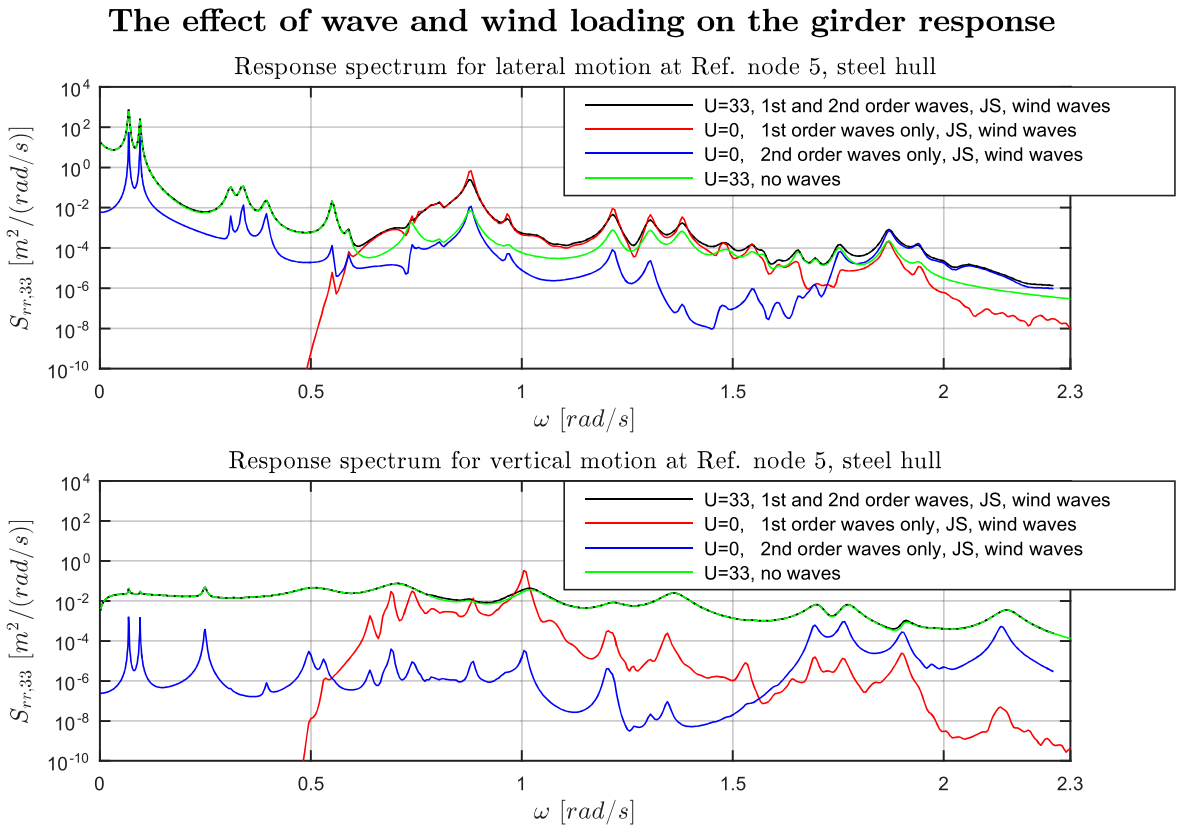

Figure D.8: The response spectrum for the steel hull alternative, for the lateral and vertical direction for Ref. node 5 plotted for various load cases.

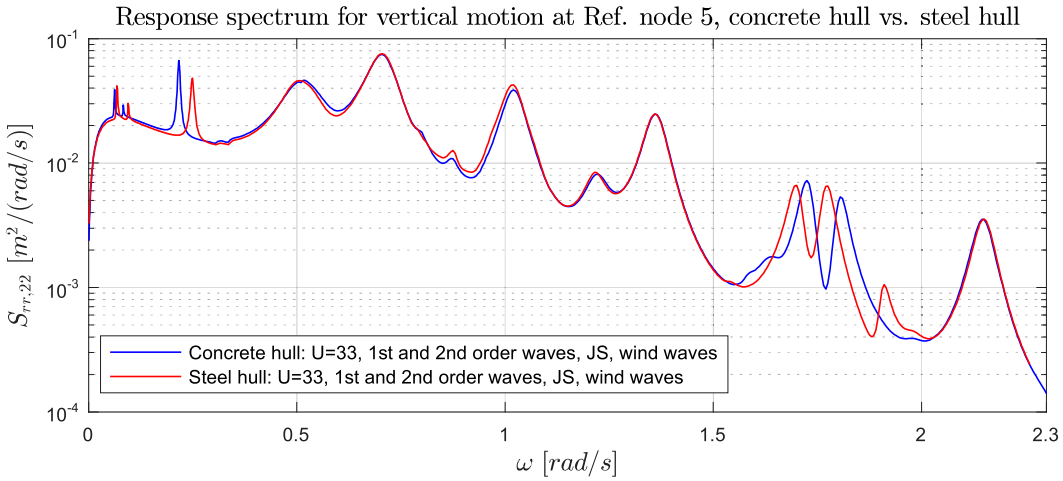

Figure D.9: A comparison of the response spectra of the bridge with the concrete hull alternative and the steel hull alternative at Ref. node 5. Vertical motion is presented.

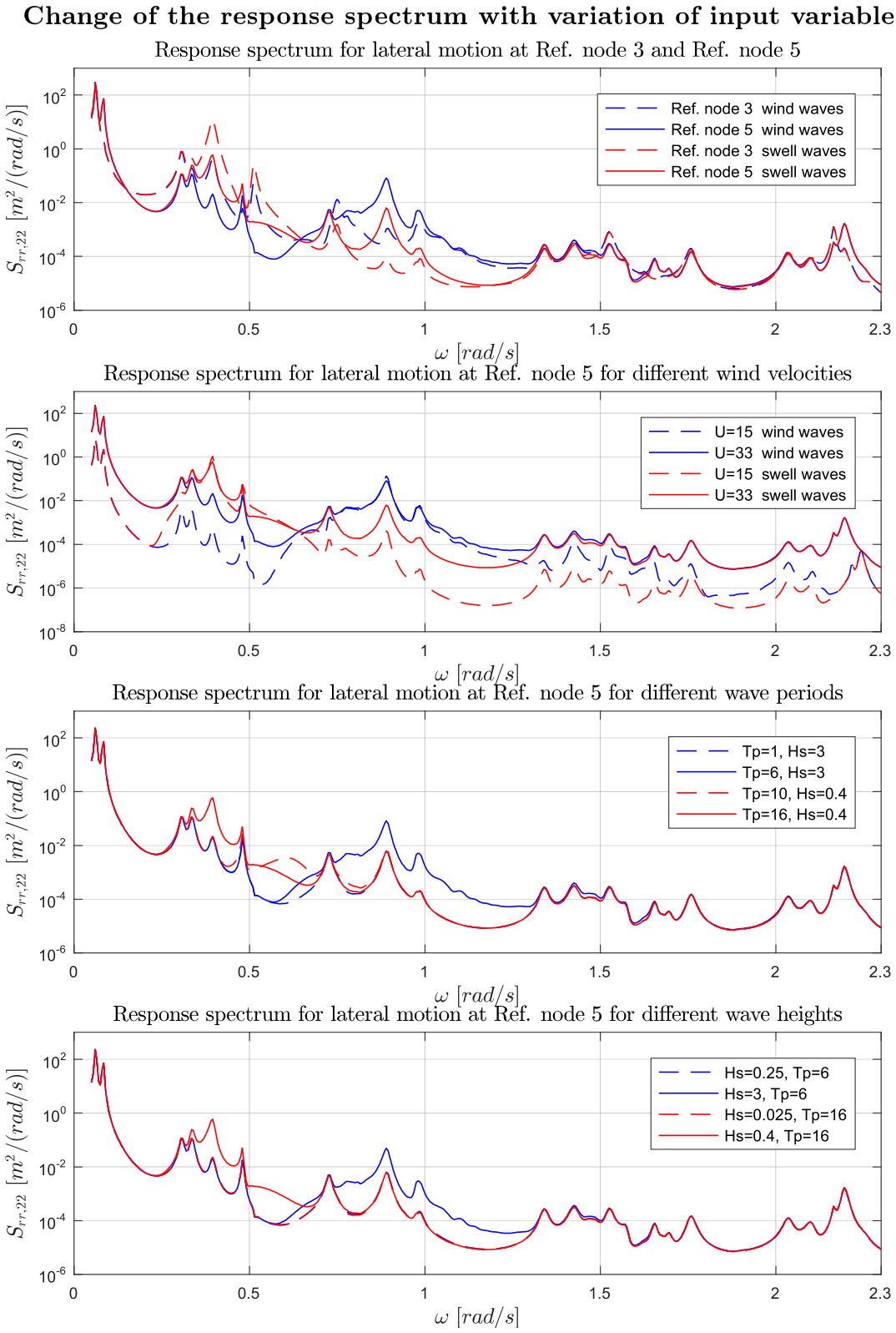

Figure D.10: Initial identification of the effect change of different variables might have on the response spectrum.

D.4 Additional results for damage to the tethers and the top cable

	Undamaged	Span 1		Span 2		Span 3	
	ω_n	ω_n	%	ω_n	%	ω_n	%
Mode 1	6.211E-02	6.094E-02	-1.88	6.220E-02	0.14	6.171E-02	-0.65
Mode 2	8.319E-02	8.026E-02	-3.52	8.264E-02	-0.66	8.251E-02	-0.82
Mode 3	2.200E-01	3.103E-01	41.09	2.204E-01	0.19	3.134E-01	42.50
Mode 4	3.076E-01	3.016E-01	-1.94	3.124E-01	1.55	3.076E-01	0.00
Mode 5	3.374E-01	3.300E-01	-2.19	3.392E-01	0.54	3.485E-01	3.28
Mode 6	3.972E-01	3.861E-01	-2.80	4.069E-01	2.45	4.040E-01	1.71
Mode 7	4.809E-01	4.755E-01	-1.12	4.833E-01	0.51	4.823E-01	0.28
Mode 8	4.973E-01	4.258E-01	-14.38	4.095E-01	-17.66	4.325E-01	-13.05
Mode 9	5.123E-01	4.855E-01	-5.23	5.147E-01	0.47	4.933E-01	-3.72

Table D.2: Eigenfrequencies calculated for the bridge when the top cable is damaged. All eigenfrequencies on the same row correspond to the same mode shape.

Standard deviation of the pontoon nodes for varying degree of tether damage						
	Surge		Sway		Heave	
	Pontoon 1	Pontoon 2	Pontoon 1	Pontoon 2	Pontoon 1	Pontoon 2
Undamaged bridge	0.1563	0.1515	1.7482	2.0709	0.0284	0.0281
1 tethers in group removed	0.1581	0.1530	1.7556	2.0718	0.0288	0.0279
2 tethers in group removed	0.1579	0.1520	1.7566	2.0716	0.0286	0.0278
3 tethers in group removed	0.1582	0.1502	1.7617	2.0719	0.0291	0.0277
4 tethers in group removed	0.1585	0.1455	1.7827	2.0701	0.0337	0.0273
	Roll		Pitch		Yaw	
	Pontoon 1	Pontoon 2	Pontoon 1	Pontoon 2	Pontoon 1	Pontoon 2
Undamaged bridge	1.741E-04	1.403E-04	2.320E-04	1.848E-04	1.476E-03	1.403E-03
1 tethers in group removed	1.907E-04	1.407E-04	2.684E-04	2.011E-04	1.385E-03	1.411E-03
2 tethers in group removed	2.265E-04	1.409E-04	2.802E-04	1.877E-04	1.377E-03	1.401E-03
3 tethers in group removed	3.139E-04	1.409E-04	3.136E-04	1.677E-04	1.359E-03	1.369E-03
4 tethers in group removed	5.386E-04	1.431E-04	4.143E-04	1.602E-04	1.376E-03	1.466E-03

Table D.3: The table shows the STDs at the pontoons from the damaged tether study. Surge, Sway, Heave are given in meters and Roll, Pitch and Yaw is given in radians.

Standard deviation of the pontoon nodes for dammage to the different top cables				
	Surge			
	Tower 1	Tower 2	Tower 3	Tower 4
Undammaged	1.081E-02	1.054E-02	1.113E-02	9.262E-03
Top calble in span 1 removed	1.269E-01	1.605E-01	1.569E-01	1.164E-01
Top calble in span 2 removed	1.286E-01	1.248E-01	1.615E-01	1.400E-01
Top calble in span 3 removed	5.320E-02	5.634E-02	5.873E-02	6.251E-02
	Sway			
	Tower 1	Tower 2	Tower 3	Tower 4
Undammaged	4.814E-03	4.431E-03	4.723E-03	4.735E-03
Top calble in span 1 removed	2.245E+00	2.352E+00	2.271E+00	2.291E+00
Top calble in span 2 removed	2.033E+00	2.134E+00	2.048E+00	2.053E+00
Top calble in span 3 removed	4.289E-03	4.300E-03	4.159E-03	3.797E-03
	Heave			
	Tower 1	Tower 2	Tower 3	Tower 4
Undammaged	2.052E-04	1.957E-04	2.019E-04	1.980E-04
Top calble in span 1 removed	2.834E-02	2.984E-02	2.778E-02	2.923E-02
Top calble in span 2 removed	2.809E-02	3.030E-02	2.714E-02	2.788E-02
Top calble in span 3 removed	2.359E-04	2.530E-04	2.432E-04	4.376E-04
	Roll			
	Tower 1	Tower 2	Tower 3	Tower 4
Undammaged	2.102E-05	1.975E-05	2.107E-05	2.128E-05
Top calble in span 1 removed	2.740E-04	2.225E-04	2.329E-04	2.717E-04
Top calble in span 2 removed	2.367E-04	2.353E-04	2.299E-04	2.071E-04
Top calble in span 3 removed	2.755E-05	2.637E-05	2.368E-05	2.468E-05
	Pitch			
	Tower 1	Tower 2	Tower 3	Tower 4
Undammaged	8.768E-05	8.530E-05	9.026E-05	7.341E-05
Top calble in span 1 removed	1.322E-03	2.419E-03	2.174E-03	1.684E-03
Top calble in span 2 removed	1.322E-03	1.763E-03	2.170E-03	2.286E-03
Top calble in span 3 removed	4.049E-04	4.268E-04	4.452E-04	4.813E-04
	Yaw			
	Tower 1	Tower 2	Tower 3	Tower 4
Undammaged	6.599E-04	7.191E-04	7.008E-04	7.122E-04
Top calble in span 1 removed	9.109E-04	1.918E-03	1.726E-03	8.901E-04
Top calble in span 2 removed	9.749E-04	9.893E-04	1.571E-03	1.844E-03
Top calble in span 3 removed	9.361E-04	9.440E-04	8.476E-04	9.061E-04

Table D.4: The table shows the STDs at the pontoons from the damaged top cable study. Surge, Sway, Heave are given in meters and Roll, Pitch and Yaw is given in radians.

D.5 The chi-squared goodness of fit test

H_s range	Observed	Expected	χ^2	p-value	p-value
0.00 - 0.01	788	785	0.0115		
0.01 - 0.02	95	93	0.043		
0.02 - 0.03	59	48	2.5208		
0.03 - 0.04	36	31	0.8065		
0.04 - 0.05	30	22	2.9091		
0.05 - 0.06	23	17	2.1176		
0.06 - 0.07	19	13	2.7692		
0.07 - 0.08	12	10	0.4		
0.08 - 0.09	9	9	0		0.239
0.09 - 0.10	7	7	0		Accepted
0.10 - 0.11	4	6	0.6667	0.063	
0.11 - 0.12	3	5	0.8	Accepted	
0.12 - 0.13	2	5	1.8		
0.13 - 0.14	1	4	2.25		
0.14 - 0.15	1	3	1.3333		
0.15 - 0.16	1	3	1.3333		
0.16 - 0.17	1	3	1.3333		
0.17 - 0.18	0	2	2		
0.18 - 0.19	0	2	2		
0.19 - 0.20	0	2	2		
0.20 - 0.21	0	2	2		
0.21 - 0.22	0	2	2		
0.22 - 0.23	0	2	2		

Table D.5: Chi-squared test assuming data comes from 1 swell sea measurement a day over approximately 3 years. (1091 measurements because of rounding of values). Outside the given range of H_s the expected value also goes to 0. p-values are found by interpolation of tabulated values

H_s range	Observed	Expected	χ^2	p-value	p-value	p-value
0.0 - 0.1	595	387	111.793			
0.1 - 0.2	1874	1863	0.065			
0.2 - 0.3	2021	2006	0.112			
0.3 - 0.4	1537	1516	0.291			
0.4 - 0.5	1026	1075	2.234			0.390
0.5 - 0.6	653	698	2.901		0.013	Accepted
0.6 - 0.7	406	416	0.240		Rejected	
0.7 - 0.8	249	229	1.747	< 0.005		
0.8 - 0.9	153	118	10.381	Rejected		
0.9 - 1.0	94	57	24.018			
1.0 - 1.1	58	26	39.385			
1.1 - 1.2	36	11	56.818			
1.2 - 1.3	22	5	57.800			
1.3 - 1.4	14	2	72			
1.4 - 1.5	9	1	64			
1.5 - 1.6	5	0	∞			

Table D.6: Chi-squared test assuming data comes from 24 wind sea measurements a day for a year. The p-values are given for the ranges represented by their column and are found by interpolation of tabulated values.